UNIVERSIDADE DE LISBOA
Faculdade de Medicina de Lisboa

Targeting cancer-related proteins: Rational design of covalent inhibitors and degraders for TEC kinases and serine hydrolases

Bárbara Beatriz da Costa Botelho Sousa

Orientador: Prof. Doutor Gonçalo José Lopes Bernardes

Tese especialmente elaborada para obtenção do grau de Doutor em Ciências Biomédicas – Especialidade em Bioquímica Médica

2023

UNIVERSIDADE DE LISBOA
Faculdade de Medicina de Lisboa

Targeting cancer-related proteins: Rational design of covalent inhibitors and degraders for TEC kinases and serine hydrolases

Bárbara Beatriz da Costa Botelho Sousa

Orientador: Prof. Doutor Gonçalo José Lopes Bernardes

Tese especialmente elaborada para obtenção do grau de Doutor em Ciências Biomédicas – Especialidade em Bioquímica Médica

Júri:

Presidente: Doutor Mário Nuno Ramos de Almeida Ramirez, Professor Associado com Agregação e Vice-Presidente do Conselho Científico da Faculdade de Medicina da Universidade de Lisboa.
Vogais:
- Doutora Maria Laura Bolognesi, Professoressa ordinária da Università di Bologna (Italy);
- Doutora Maria João Correia Pinto Carvalho de Matos, Professora Associada da Faculdade de Farmácia da Universidade de Santiago de Compostela (Espanha);
- Doutor Rui Ferreira Alves Moreira, Professor Catedrático da Faculdade de Farmácia da Universidade de Lisboa;
- Doutor João Pedro Taborda Barata, Professor Associado da Faculdade de Medicina da Universidade de Lisboa;
- Doutor Gonçalo José Lopes Bernardes, Professor Auxiliar Convidado da Faculdade de Medicina da Universidade de Lisboa (Orientador).

Aluna recipiente da bolsa de doutoramento FCT

2023

A impressão desta tese foi aprovada pelo Conselho Científico da Faculdade de Medicina de Lisboa em reunião de 26 de Setembro de 2023

ACKNOWLEDGEMENTS

I would like to acknowledge everyone who has helped throughout my thesis work including Dr Gonçalo José Lopes Bernardes, my supervisor, for his leadership, vision, and guidance, for the balance between giving and demanding, and for allowing me to grow as a person and a scientist.

I would like to extend my sincere gratitude to Dr Luís Miguel Afonso Carvalho, for his guidance and valuable insights. His contributions have been significant in helping me develop my research ideas and implement them effectively.

I am also grateful to Dr João Daniel Seixas for his constructive questions that have always challenged me to have a critical look regarding the results. His insightful feedback and suggestions have helped me to refine and improve my research work.

I would like to express my gratitude to Dr Daniel Zaidman, and all the collaborative teams involved in the animal and patient models used in this research and compound characterization. Their contribution was essential to the success of this research, and I am deeply grateful for their insights, expertise, and support.

Finally, I would also like to thank my colleagues, friends, and family who have supported me throughout this journey. Their constant encouragement and motivation have been a significant driving force in my academic pursuits.

Figures were created with BioRender.com.

RESUMO

A introdução da terapia-alvo tem transformado significativamente o panorama geral de terapia para cancro, oferecendo inúmeras vantagens relativamente à quimioterapia convencional. Dentro destas metodologias, pequenos inibidores covalentes e quimeras de alvo de proteólise (PROTACs) são utilizados para atingir especificamente proteínas causadoras de doenças em células malignas, sem afetar células saudáveis. Esta especificidade leva a que estas terapias sejam mais eficazes, reduzindo o risco de efeitos secundários. À vasta lista de proteínas passíveis de serem alvos deste tipo de tratamento químico, adicionam-se a tirosina quinase de Bruton (BTK) e a acil-proteína tioesterase 1 (APT1), que apresentam potencial terapêutico para o tratamento de tumores hematológicos e outras doenças relacionadas. Neste estudo, desenvolvemos uma abordagem racional para a identificação de pequenas moléculas covalentes que se ligam seletivamente à BTK e PROTACs para APT1. Posteriormente, avaliámos a sua relevância no tratamento de cancros do sangue.

Primeiro investigámos o potencial terapêutico de uma pequena molécula covalente (JS25) com atividade nanomolar contra BTK. A molécula JS25 foi derivada da estrutura base de BMX-IN-1, um inibidor de BTK recém-descoberto, por meio de um estudo direcionado a identificar regiões da molécula que pudessem ser modificadas de modo a aprimorar a sua eficácia e seletividade. Procurámos também caracterizar o modo de ligação de JS25 a BTK e confirmámos a sua seletividade contra um painel de diferentes proteínas relacionadas à via de sinalização de BTK ou com uma cisteína igualmente posicionada à cisteína 481 da BTK. A validação do seu efeito terapêutico foi realizada usando modelos de animais de linfoma de Burkitt e modelos derivados de pacientes de linfoma difuso de grandes células B e leucemia linfocítica crónica. Por último, explorámos a capacidade do JS25 atravessar a barreira hematoencefálica e tratar a infiltração de células tumorais no cérebro. JS25 apresentou uma alta eficácia de ligação à BTK e com seletividade e perfil inibitório mais desejáveis em comparação com outros inibidores de BTK clinicamente aprovados, nomeadamente Ibrutinib e Acalabrutinib. A previsão estrutural do complexo BTK/JS25 revelou uma importante interação com a tirosina 551, responsável por inativar BTK. JS25 também inibiu a proliferação de várias linhas celulares tumorais de linhagens mieloide e linfoide. Em modelos pré-clínicos de cancro de células B, o tratamento com JS25 induziu uma morte celular mais pronunciada no modelo animal de linfoma de Burkitt,

causando uma redução de 30 a 40% do tumor subcutâneo e uma redução geral na percentagem de metástases e formação de tumores secundários. Em modelos derivados de amostras de pacientes com linfoma difuso de grandes células B, a resposta terapêutica ao JS25 foi maior comparativamente à do Ibrutinib, gerando assim uma eficácia generalizada de 64%. Finalmente, em modelos de peixe-zebra, inoculados com amostras de pacientes com leucemia linfocítica crónica, o JS25 foi mais rápido e mais eficaz na diminuição da carga tumoral, produzindo efeitos terapêuticos superiores em comparação com Ibrutinib.

Na segunda parte deste estudo, foi feita a integração de plataformas computacionais e bioquímicas para acelerar a identificação de PROTACs com seletividade para APT1. O protocolo PRosettaC foi utilizado para prever o comprimento ideal do espaçador, configuração e eficácia de ligação prevista dos PROTACs à APT1 e E3 ubiquitina ligase. Em combinação, vários ensaios bioquímicos foram utilizados para monitorar a inibição e degradação de APT1 e caracterizar a seletividade dos PROTACs sintetizados. Para além disto, a atividade antitumoral do PROTAC mais promissor foi avaliada em linhas celulares de cancros do sangue. De acordo com os modelos computacionais gerados, os PROTACs com comprimentos de espaçador mais curtos tiveram eficácia mais limitada ou menor capacidade de degradar a APT1. Em contraste, PROTACs com espaçadores mais longos exibiram degradação mais significativa e em concentrações mais baixas, uma vez que mimetizam a estrutura de substratos específicos para esta enzima. Dentro de todas as moléculas geradas, destaca-se o PROTAC C8, que exibiu uma alta seletividade para APT1 e atividade em várias linhagens celulares de cancro do sangue. C8 exibiu seletividade notável para APT1, sem causar degradação significativa de outras hidrólases de serina, nomeadamente as ABHDs, que são frequentemente alvos de inibidores da APT1.

Em conclusão, este estudo reforça as vantagens de modelos putativos computacionais e da validação pré-clínica para gerar novos agentes terapêuticos que possam oferecer uma melhor eficácia e seletividade, combinadas com uma redução de efeitos secundários. Espera-se que estas descobertas e esforços aqui apresentados contribuam significativamente para o desenvolvimento de tratamentos inovadores para o cancro e outras doenças.

PALAVRAS-CHAVE: terapia-alvo, inibidores covalentes, PROTACs, cancros hematológicos

ABSTRACT

Targeted therapy has significantly transformed the landscape of cancer treatment by providing several advantages in contrast to conventional chemotherapy. Small covalent inhibitors and proteolysis targeting chimeras (PROTACs) are designed to specifically target disease-causing proteins in malignant cells, while leaving the healthy cells unaffected. This specificity makes these therapies more effective and reduces the risk of adverse side effects. Adding to the vast list of proteins amenable to targeting via these chemical routes, Bruton's tyrosine kinase (BTK) and acyl-protein thioesterase 1 (APT1), have shown therapeutic promise for the treatment of haematological cancers and other related diseases. Within this research, we employed a rational approach to develop covalent small molecules that selectively bind to BTK, and PROTACs for APT1. We subsequently evaluated their efficacy in treating blood cancers.

We first investigated the therapeutic potential of a small covalent molecule (JS25) with nanomolar activity against BTK. JS25 was obtained from the scaffold of BMX-IN-1 (a recently discovered BTK inhibitor), as part of our efforts to identify regions of the molecule that could be modulated for improved efficacy and selectivity. We sought to characterize the binding mode of JS25 to BTK and asserted its selectivity against a panel of proteins related to BTK's signalling pathway or with an equally placed cysteine as to the cysteine 481 of BTK. Validation of its therapeutic effect was conducted using xenograft mice models of Burkitt's lymphoma, and patient-derived models of diffuse large B-cell lymphoma and chronic lymphocytic leukaemia. Finally, we explored the capability of JS25 to cross the brain−blood barrier and treat infiltration of tumour cells in the brain. JS25 presented a high binding efficacy to BTK and with a more desirable selectivity and inhibitory profile compared to the clinically approved BTK inhibitors Ibrutinib and Acalabrutinib. Structural prediction of the BTK/JS25 complex revealed sequestration of tyrosine 551 responsible for rendering BTK to its inactive state. JS25 also inhibited the proliferation of myeloid and B-lymphoid cancer cell lines. In preclinical models of B-cell cancers, JS25 treatment induced a more pronounced cell death in a murine xenograft model of Burkitt's lymphoma, causing a 30–40% reduction of the subcutaneous tumour and an overall reduction in the percentage of metastasis and secondary tumour formation. In a patient model of diffuse large B-cell lymphoma, the drug response of JS25 was higher than

that of Ibrutinib, leading to a 64% on-target efficacy. Finally, in zebrafish patient-derived xenografts of chronic lymphocytic leukaemia, JS25 was faster and more effective in decreasing tumour burden, producing superior therapeutic effects compared to Ibrutinib.

In the second part, we integrated computational and biochemical platforms to help accelerate the identification of novel PROTACs with improved selectivity for APT1. PRosettaC protocol was utilized to predict the optimal linker length, configuration, and binding efficacy of designed PROTACs to APT1 and E3 ubiquitin ligase. Activity-based protein profiling and immunoblot assays were employed to monitor the inhibition and degradation of APT1 and to assert their selectivity. Additionally, the anti-tumour activity of the most promising APT1-targeting PROTAC was assessed in blood cancer cell lines. In accordance with the computer modelling, PROTACs with shorter linker lengths had limited or minimal effectiveness in degrading APT1. Conversely, PROTACs that comprehended linkers with long alkyl chains exhibited potent degradation in the nanomolar range, as these mimic the structure of substrates specific for this enzyme. Of particular interest is the PROTAC C8, which exhibited a high selectivity for APT1 and activity in several blood cancer cell lines. Notably, C8 displays remarkable selectivity for APT1, without causing significant disruption of other serine hydrolases, such as ABHDs, which are often the targets of APT inhibitors.

Overall, we endeavoured to harness the advantages of computational modelling and preclinical validation to create novel targeted therapeutic agents that could offer superior efficacy, selectivity, and safety profiles. It is hoped that the findings and efforts here presented will make a significant contribution to the expanding field of targeted therapy and pave the way for the development of innovative treatments for haematological cancers and other ailments with unmet clinical treatments.

KEY WORDS: targeted therapy, covalent inhibitors, PROTACs, haematological cancers

TABLE OF CONTENTS

LIST OF ABBREVIATIONS

ABC-DLBCL	Activated B-cell-diffuse large B-cell lymphoma
ABHD	α/β-Hydrolase domain
ABL	Tyrosine-protein kinase from ABL1 gene
ABPP	Activity-based protein profiling
ADMET	Absorption, distribution, metabolism, excretion, and toxicity
ADP	Adenosine diphosphate
AEs	Adverse effects
AKT	Protein kinase B/PKB
AML	Acute myeloid leukaemia
APML	Acute promyelocytic leukaemia
APT	Acyl-protein thioesterase
AR	Androgen receptor
ATP	Adenosine triphosphate
AZT	Azidothymidine
BBB	Brain-blood-barrier
BCAP	B-cell catabolite activator protein
BCL-2	B-cell lymphoma 2
BCL-XL	B-cell lymphoma XL
BCL10	B-cell lymphoma/leukemia 10
BCR	B-cell receptor
BH	BTK homology
BL	Burkitt’s lymphoma
BLK	B-lymphoid tyrosine kinase
BLNK	B-cell linker protein
BMX	Bone marrow kinase in the X chromosome
BOC	Tert-butyloxycarbonyl protecting group
BRD	Bromodomain-containing protein
BSA	Bovine serum albumin
BSF	Benzenesulfonyl fluoride
BTK	Bruton’s tyrosine kinase

BTKi	BTK inhibitor(s)
C	Cysteine
Ca^{2+}	Calcium
CaM	Calmodulin
CAR-T	Chimeric T-cell receptor
CARD11	Caspase recruitment domain-containing protein 11
CD	Cluster of differentiation
CDK	Cyclin-dependent kinase
cGVHD	Chronic graft versus host disease
$CHCl_3$	Chloroform
CI(s)	Covalent inhibitor(s)
cIAP	Cellular IAP
CLL	Chronic lymphocytic leukaemia
CNSL	Central nervous system lymphoma
CO_2	Carbon dioxide
COVID-19	Corona virus disease
CRBN	Cereblon
CR	Complete response
CRISPR-Cas9	Clustered Regularly Interspaced Short Palindromic Repeats-Cas9
CRLs	Cullin-RING ligases
Cs_2CO_3	Cesium carbonate
CS	Cysteine string
CUL	Cullin protein
$CuSO_4$	Copper(II) sulfate
CXCR	Chemokine receptor
Cys	Cysteine
D	Aspartic acid
DAG	Diglyceride
DAPI	4′,6-diamidino-2-phenylindole
DCAF	DDB1- and CUL4-associated factor
DCM	Dichloromethane
DDB1	Damage-specific DNA binding protein 1

DIPEA	N,N-Diisopropylethylamine
DLBCL	Diffuse large B-cell lymphoma
DMEM	Dulbecco's modified Eagle medium
DMF	Dimethylformamide
DMSO	Dimethyl sulfoxide
DNA	Deoxyribonucleic acid
DPBS	Dulbecco's phosphate-buffered saline
DTT	Dithiothreitol
E	Glutamic acid
ECGS	Endothelial cell growth supplement
EDTA	Ethylenediaminetetraacetic acid
EGFR	Epidermal growth factor receptor
EMA	European medicines agency
eNOS	Endothelial nitric oxide synthase
Eq.	Equivalents
ER	Estrogen receptors
ERK	Extracellular signal-regulated kinase
EtOAc	Ethyl acetate
EtOH	Ethanol
FAK	Focal adhesion kinase
FBS	Fetal bovine serum
FcR	Fc-receptors
FDA	Food and Drug Administration
FDR	False discovery rate
FGFR	Fibroblast growth factor receptor
FKBP12	FKBP-type peptidyl-prolyl cis-trans isomerase
FLT3	Fms related receptor tyrosine kinase 3
FP	Fluorophosphonate
G	Glycine
G-CSFR	Granulocyte colony stimulating factor receptor
GAPDH	Glyceraldehyde 3-phosphate dehydrogenase
GAP-43	Growth associated protein 43

GCB-DLBCL	Germinal center B-cell-diffuse large B-cell lymphoma
GDP	Guanosine diphosphate
Gsα	Gs alpha subunit
GSTP1	G1 to S phase transition 1
GTP	Guanosine triphosphate
H	Histidine
H/L	Heavy/Light
H_2O	Water
HATU	Hexafluorophosphate azabenzotriazole tetramethyl uronium
HBEC-5i	Human cerebral microvascular endothelial cells
HECT	Homologous to the E6-AP carboxyl terminus
HEF	Hemagglutinin-esterase-fusion
HER	Human epidermal growth factor receptor
HIV	Human immunodeficiency virus
HPLC	High-performance liquid chromatography
HRAS	Harvey rat sarcoma virus
IAP	Inhibitors of apoptosis proteins
Ib	Ibrutinib
IC_{50}	Half-maximal inhibitory concentration
IFN-γ	Interferon gamma
Ig	Immunoglobulin
IgH-IRF8	Immunoglobulin heavy chain-Interferon regulatory factor 8
IGHV	Immunoglobulin heavy chain variable region
IKZF	Ikaros zinc finger
IL	Interleukin
IMiD	Immunomodulatory imide drugs
IRAK1	Interleukin-1 receptor-associated kinase1
IRAK4	Interleukin-1 receptor-associated kinase 4
ITAMs	Immunoreceptor tyrosine-based activation motifs
ITIM	Immunoreceptor tyrosine-based inhibitory motif
ITK	Interleukin-2-inducible T-cell kinase
JAK	Janus kinase

K_2CO_3	Potassium carbonate
K_D	Dissociation constant
K_I	Initial non-covalent binding
k_{inact}/K_I	Rate of inactivation
k_{inact}	Rate of covalent bond formation
K_m	Michaelis constant
k_{obs}	Observed rate constant
KRAS	Kirsten rat sarcoma virus
L	Leucine
LE	Ligand efficiency
LYN	Lck/Yes novel tyrosine kinase
M	Methionine
M-CSF	Macrophage colony-stimulating factor
MALT1	Mucosa-associated lymphoid tissue lymphoma translocation protein 1
MAP2K7	Dual specificity mitogen-activated protein kinase 7
MAPK	Mitogen-activated protein kinase
MCL	Mantle cell lymphoma
MDM2	Mouse double minute 2 homolog
MEK	Mitogen-activated protein kinase
Mg	Magnesium
$MnCl_2$	Manganese(II) chloride
mTOR	Mammalian target of rapamycin
MYD88	Myeloid differentiation primary response 88
MZL	Marginal zone lymphoma
N	NEDD8
Na_2CO_3	Sodium carbonate
Na_3VO_4	Sodium orthovanadate
$NaBH_4$	Sodium borohydride
NaCl	Sodium chloride
NAE	N-activating enzyme
NaI	Sodium iodide
NaN_3	Sodium nitrate

NaOH	Sodium hydroxide
NEDD8	Neural precursor cell expressed developmentally down-regulated protein 8
NF-κB	Nuclear factor kappa B
NFAT	Nuclear factor of activated T-cells
NFKBIE	Nuclear factor of kappa light polypeptide gene enhancer in B-cells inhibitor, epsilon
NH_4Cl	Ammonium chloride
NH_4OH	Ammonium hydroxide
NHL	Non-Hodgkin lymphoma
NSCLC	Non-small cell lung cancer
ORR	Overall response rate
P	Phosphorylation
PAK	Serine/threonine-protein kinase
PAT	Protein acyl transferases
PBMCs	Peripheral blood mononuclear cells isolation
PBP(s)	Penicillin-binding protein (s)
PBS	Phosphate-buffered saline
$Pd(OAc)_2$	Palladium(II) acetate
PD-1	Programmed cell death 1
$PdCl_2(PPh_3)_2$	Bis(triphenylphosphine)palladium(II) dichloride
PDPK1	3-phosphoinositide-dependent protein kinase 1
PEG	Polyethylene glycol
PFS	Progression free survival
PH	Pleckstrin homology
Ph_2O	Diphenyl ether
PI3K	Phosphoinositide 3-kinase
PIP2	Phosphatidylinositol 4,5-bisphosphate
PIP3	Phosphatidylinositol (3,4,5)-trisphosphate
PKCβ	Protein kinase C beta
PLCγ2	Phospholipase C-γ2
POI	Protein of interest
POM	Pomalidomide

PR	Proline rich
PROTAC(s)	Proteolysis-targeting chimera(s)
R/R	Refractory and relapsed
R-BINAP	2,2′-bis(diphenylphosphino)-1,1′-binaphthyl
RANKL	Receptor activator of NF-kB ligand
RAS	Rat sarcoma virus
RBX1	RING box protein 1
RGS	G-protein signalling
RIPA	Radioimmunoprecipitation assay buffer
RMSD	Root-mean-square deviation
RNA	Ribonucleic acid
RNAi	RNA interference
RNF	Ring finger protein
RPT	Radiopharmaceutical therapy
RT	Radiotherapy
rt	Room temperature
S	Serine
SAR	Structure–activity relationship
SARS-CoV	Severe acute respiratory syndrome coronavirus
SARS1	Syndrome coronavirus 1
SDS-PAGE	Sodium dodecyl sulfate–polyacrylamide gel
Ser	Serine
SerH	Serine hydrolases
SFV	Semliki forest virus
SH	SRC homology
SHIP	Protein tyrosine phosphatase
SNAP-23	Synaptosomal-associated protein 23
$SnCl_2$	Tin(II) chloride
$SOCl_2$	Thionyl chloride
SRC	SRC-gene kinases
STAT	Statim protein
SYK	Spleen tyrosine kinase

T	Threonine
TBK	TANK-binding kinase
TCEP	Tris(2-chloroethyl) phosphate
TCR	T-cell receptor
TEA	Triethanolamine
TEAB	Triethylammonium bicarbonate
TEC	Tyrosine kinase expressed in hepatocellular carcinoma
TFA	Trifluoroacetic acid
TH	TEC homology
TH1	T-helper type 1 cell
TH2	T-helper type 2 cell
THF	Tetrahydrofuran
TLR	Toll-like receptors
TN	Treatment naïve
TNFAIP3	Tumor necrosis factor, alpha-induced protein 3
TrCP1	Transducin repeat-containing protein 1
TRIM24	Tripartite motif 24 protein
Tris-HCl	Tris-hydrochloride
TXK	Resting lymphocyte kinase/RLK
uMRD	Undetectable minimal residual disease
VAV	Guanine nucleotide exchange factors
VHL	Von Hippel−Lindau
VSV	Vesicular stomatitis virus
VTX	Venetoclax
WM	Waldenström’s macroglobulinemia
XLA	X-linked agammaglobulinemia
Y	Tyrosine
zPDX	Zebrafish patient-derived xenograft

LIST OF FIGURES

LIST OF SCHEMES

LIST OF TABLES

1

General Introduction

1. General Introduction

1.1 Hallmarks of cancer

Cancer is a condition involving the abnormal growth of cells with the potential to invade or spread to other parts of the body.[1] The set of functional capabilities acquired by the cells as they turn from normalcy to neoplastic growth rates is crucial for their ability to form malignant tumours and circumvent natural barriers.[1] These comprise for instance the capability to sustain proliferative signalling, to evade growth suppressors, epigenetic reprogramming, resist cell death, enable replicative immortality, induce vasculature, activate invasion and metastasis, and avoid immune destruction **(Fig. 1. 1)**.[1]

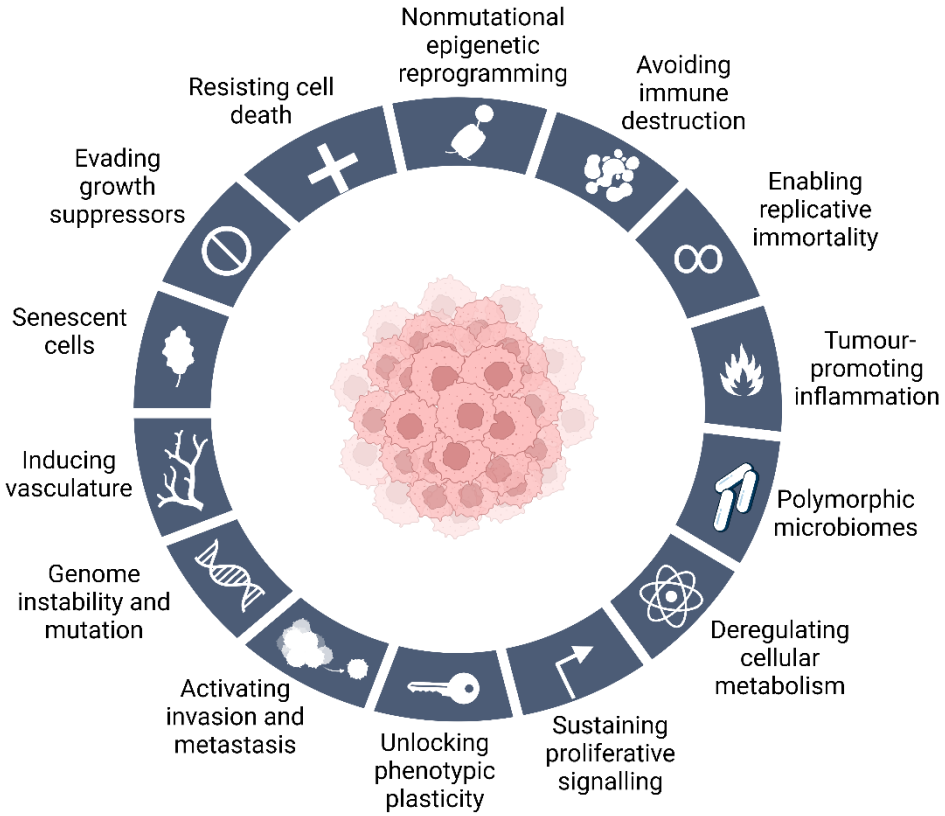

Fig. 1. 1. Hallmarks of cancer (adapted).[1]

1.2 Epidemiology

According to the World Health Organization, cancers impose the largest worldwide burden, with a 19 million incidence of new cases in 2020, also being one of the leading causes of death every year.[2] On the list of the most frequent cancers, breast cancer has the highest frequency (58.5/100 000), followed by prostate (36.0/100 000), lung (28.3/100 000), colorectal (24.8/100 000), cervix uteri (15.6/100 000), and stomach (14.0/100 000). Leukaemia (28.8%), lymphomas (13.8%) and nervous system cancers (11%) are the most prevalent malignant diseases in subjects aged 19 years or younger. The overall risk of developing cancer between the age of 0–74 years is 20.44%; with the highest risk of malignancy for lung (3.78%), prostate (3.86%) and colorectal (2.71%) in men and for breast (5.20%), colorectal (1.83%), and cervix uteri (1.39) in women.

Malignant diseases, such as cancer, have an enormous impact in public health-care, imposing a dramatic clinical and economic burden.[3] Hence, it is of foremost importance to reinforce the current strategies for cancer prevention, screening, diagnosis, and management.[3] These include (1) prebiopsy, to enable a more efficient screening, diagnosis, and therapeutic monitoring, (2) individualized medicine, to identify the interindividual tumour variability and outline personalized and more efficient treatments, (3) and the development of novel breakthrough therapies, to enhance efficacy and therapeutic benefits against malignant cells.[3]

1.3 Cancer treatment strategies

Treating cancer is a highly complex process. The choice of therapy depends upon the location and grade of the tumour, as well as in the general health status of the patient.[4] Given the heterogeneity of tumour cells, it is also unusual to have one single treatment. Therapies are often given in combination, depending on the tumour type and severity.[5] Conventional treatment approaches, such as surgery, chemotherapy, and radiotherapy, have been in use, while significant advances are being made in recent times, including in stem cell therapy and targeted therapy.[5] As new findings about the underlying biological processes of tumour development emerge, novel treatments are also further refined to improve clinical effectiveness and safety.[5] The most recommended conventional cancer treatment strategies include surgical removal of tumours, followed by radiotherapy and/or

chemotherapy as single treatments or in combination regimens.[5] At an early stage of disease progression, surgery can be the most effective among these modalities. Since its first use in 19th and early 20th centuries in cancer treatment, surgery has remained an important tool to treat localised tumours.[6] Nowadays, around 45% of cancer patients will undergo some type of surgery, to remove malignant tissue from affected areas (data from NHS). Radical prostatectomy is a surgical procedure that involves the removal of the prostate and nearby tissues, and it is used in combination with radiation therapy in low-risk prostate cancer patients.[7,8] In early-stage Burkitt's lymphoma, surgery is often used as first-line treatment, to remove most affected tissue in specific organs (*e.g.*, intestine) before or after the start of chemotherapy.[9] In other types of non-Hodgkin lymphoma, surgery may be useful in confirming or refuting disease diagnosis or, as splenectomy in the case of primary splenic marginal zone lymphoma.[10]

Radiotherapy is an important curative treatment modality for uncomplicated localized tumours.[11] Although the overall survival rates of radiotherapy have improved from about 30% to ~80% in the last two decades, cancer radiotherapy is limited by the maximum tolerated dose to adjacent normal tissues.[11] As an alternative, radiopharmaceutical therapy is emerging as a safer and more effective targeted approach.[12] Radiopharmaceutical therapy radiation is systemically or locally delivered using pharmaceuticals that either act preferentially in cancerous cells or accumulate by physiological mechanisms, thus resulting in a higher efficacy with minimal toxicity.[12]

For targeting both primary and metastatic cancers, stem cell transplantation has shown promising efficacy in regenerating and repairing diseased or damaged tissues. This modality is often used as a first-line treatment for many types of leukaemia and lymphomas.[5,9]

Chemotherapy and immunotherapy are products of the 20th century and have had a significant impact in the treatment of cancer.[6] Chemotherapy is a type of cancer treatment that uses one or more anti-cancer drugs to circumvent cancer cells from further growth and division.[13] This type of therapy can affect the target cells in distinct manners. Some of the treatments may directly alter the activity of cellular proteins, rendering them non-functional, and affecting major cellular physiological pathways. Other drugs may target some essential hormones and interfere with the body's overall metabolism.[13] Some of the the most promising inhibitor therapies which have been used to treat solid cancers are inhibitors of polyadenosine diphosphate-ribose polymerase, angiogenesis, histone

deacetylase, hedgehog pathway, and of tyrosine kinases.[13] Although chemotherapy has reduced morbidity and mortality, virtually all chemotherapeutic agents damage healthy cells, especially rapidly dividing and growing cells, such as those of the stomach and intestinal lining.[5,13] Drug resistance is also a major problem with chemotherapy, primarily causing reduced drug uptake and increased drug efflux.[5] Moreover, selecting dosage of chemotherapy can be quite difficult: if the dose is too low, it might be ineffective; but, if too excessive, the toxicity will be intolerable to the patient. Standardization of the optimal treatment effectiveness with minimum toxicity is also limited, as it is highly conditioned by the pharmacokinetic variability found amongst patients.[5,14]

Several new approaches have been developed in the last decade to modify and train a patient's immune system to directly act on tumour cells by recognizing multiple cell surface markers.[13] For instance, supplementing the treatment regime with immunotherapy (*e.g.*, antibodies) has significantly improved the success rate of the chemotherapeutic drugs in many cancer types, especially in triple-negative breast cancers and lymphomas.[9,13] rituximab is routinely used in the treatment of patients with blood malignancies, such as leukaemia and B-cell lymphomas, and can be safely added to chemotherapy regimens.[9,15] Tisagenlecleucel, a clinically approved drug, treats B-cell lymphoblastic leukaemia by effectively engineering the chimeric T-cell receptor (CAR-T) of the patient to target a transmembrane protein called CD19 expressed on B-cells.[13] Some other treatment plans include prophylactic and therapeutic vaccines, interferons and interleukins that help initiate tumour eradication by boosting the patient's immune system.[13]

Targeted therapy aims to deliver drugs (including antibodies) to specific genes or proteins that are unique to each type of cancer, or to the tissue environment surrounding it, inherently involved in tumour development.[16] This differs from traditional chemotherapy in which cytotoxic drugs attack rapidly dividing cells in general, without discriminating healthy tissue. Therefore, targeted cancer therapies are expected to be more effective than older forms of treatments and less harmful to normal cells.[16] The efficacy of this therapy depends on the precise release of therapeutics at the site of the disease, while minimizing the off-target effects on normal tissues. It is frequently used in combination with chemotherapy and other cancer treatments.[16] Small molecule inhibitors are one of the most extensively used types of targeted therapies in oncology.[17] Due to their high permeability, small molecule inhibitors can selectively block the activity of intracellular proteins and disrupt the related-downstream signalling cascades. In addition, their size usually conforms

to Lipinski's rule of five, which ensures their administration through the oral route.[17] PROteolysis-TArgeting Chimeras (PROTACs) work intracellularly by inducing selective degradation of the protein of interest, through recruitment of the ubiquitin-proteasome system.[17] Because PROTACs are only required to bind to their targets, rather than inhibiting their activity, many efforts have been made to redesigning previously ineffective inhibitor molecules as PROTACs for next-generation drugs.[17]

In the next sections, the fundamental aspects concerning the design and development of targeted therapy agents against cancer are reviewed. This review will focus particularly on the fundamentals of small covalent molecules and of PROTACs, and their respective therapeutic targets, as these are the primary interests of this thesis.

1.3.1 Covalent inhibitors

Historical impact and prevalence. Covalent inhibitors (CIs) are rationally designed molecules that block protein function by forming a covalent bond to their specific target **(Fig. 1. 2)**.[18] Despite generally being avoided by the pharmaceutical industry due to safety concerns, CIs have had a major impact in drug discovery and human health and can provide many pharmacological advantages **(Fig. 1. 3)**.[18]

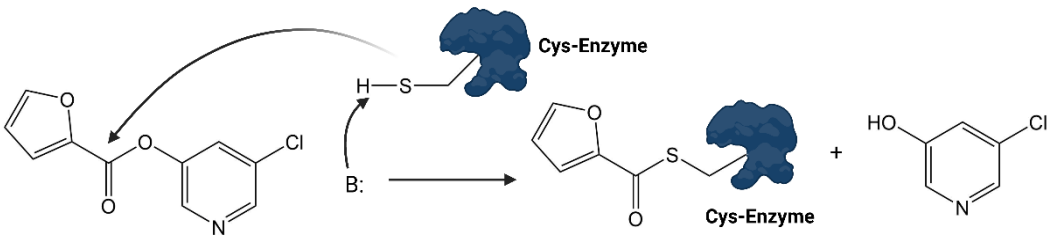

Fig. 1. 2. Mechanism of covalent bond formation.[19]

Aspirin, a non-steroidal anti-inflammatory drug that has been available on the market since 1899, is one of the most successful cases. The mechanism by which aspirin exerts its anti-inflammatory effects was not understood until 1971 when it was found to acetylate S530 in the substrate-binding channel, leading to the irreversible inactivation of cyclooxygenase 1 and suppression of prostaglandin production.[20,21] Covalent drugs, such as aspirin, were initially developed from or inspired by natural sources. β-Lactam

antibiotics, including penicillin, were originally extracted from Penicillium molds and bind to penicillin-binding proteins that are involved in bacterial cell wall synthesis, causing the disruption of the bacterial cell-wall formation. These antibiotics were among the first medications to prove effective against a broad range of bacterial infections caused by staphylococci and streptococci.[21] Within the first antiretroviral medications, Azidothymidine (AZT) belongs to the class of nucleoside reverse transcriptase inhibitors, and it is used in the treatment of the human immunodeficiency virus (HIV) infection.[22] AZT is a mimic of thymidine and binds covalently through a phosphodiester bond to the growing DNA chain. Since AZT lacks the 3'-hydroxyl group, it cannot participate in the formation of a covalent bond with the next nucleotide, thus inhibiting reverse transcription. This inhibition helps slow the progression of the disease, reduce viral load, and improve immune system function.[22] Omeprazole, a selective proton pump inhibitor approved for treating gastro-oesophageal reflux disease, and clopidogrel, an antiplatelet medication used to prevent strokes and heart attacks, are for instance two drugs that were approved for medical use before the full elucidation of their mechanism of action. Both omeprazole and clopidogrel are activated by cytochrome P450 enzymes, including CYP2C19, in the liver to produce bioactive thiol metabolites.[21] In cancer therapy, inhibitors of thymidylate synthase and ribonucleotide reductases, were frequently used to treat a wide range of cancers, including pancreatic and metastatic breast cancers.[21] In 2003, Bortezomib, a dipeptide boronic acid that covalently binds to the catalytic site of 26S proteasome, was approved for treating patients with multiple myeloma.[21]

Despite the fact that covalent inhibitors represent some of the most common and widely used drugs in the world, such as the aforementioned aspirin and penicillin, compounds that contain protein-reactive functional groups were often reluctantly used in drug screening collections owing to their lack of selectivity and concomitant undesired engagement of off-targets.[23] In addiction, successful CIs, such as omeprazole and clopidogrel, were often discovered serendipitously through biological assays/phenotypic screening with their target and brought to the market, with the mechanism of action only later elucidated.[21,23] It was only until recently that a shift towards a more target-based and structure-guided approaches to new ligand discovery were employed, with the inclusion of high-throughput screenings, *de novo* molecular design, *in silico* prediction of pharmacological profiles, DNA-encoded library technology, and fragment-based drug discovery.[23,24] These new approaches have led to a predictable means of creating a new generation of covalent drugs that display

controlled target-reactivity termed "targeted covalent inhibitor".[21] The advantages of targeted covalent warheads are numerous and significant. Targeted CIs present a high ligand efficiency and concomitant small size that results in favourable absorption, distribution, metabolism, excretion, and toxicity (ADMET) properties, improved potency and selectivity, enhanced ability to outcompete endogenous ligand binding, and sustained target engagement resulting in less frequent dosing.[23] The first successful examples of a targeted covalent drugs were the EGFR (epidermal growth factor receptor) inhibitors, Afatinib, Neratinib and Osimertinib, and the BTK (Bruton's tyrosine kinase) inhibitors, Ibrutinib and Acalabrutinib.[21]

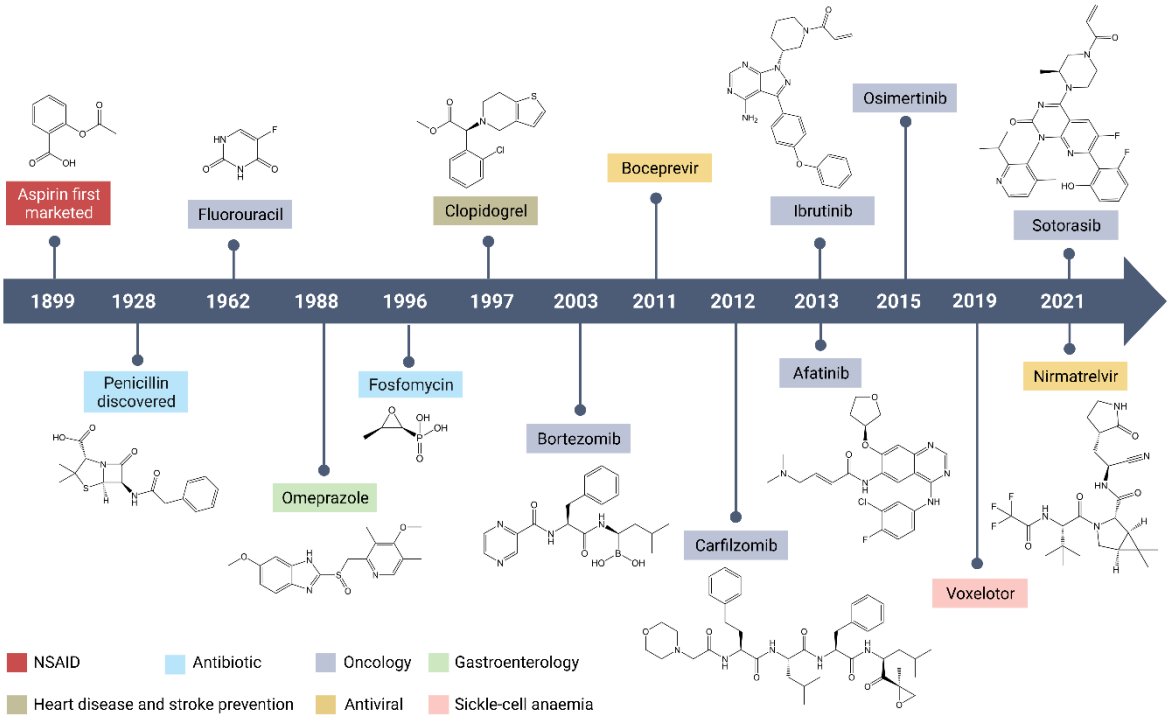

Fig. 1. 3. Timeline of the development of major covalent drugs (adapted).[21]

Mechanistic features and pharmacological advantages. Covalent modification of proteins is a two-step process governed by the affinity of the initial non-covalent binding, K_I, and the rate of covalent bond formation, k_{inact}. The rate of inactivation (k_{inact}/K_I) is a second-order event, which characterizes the efficacy of the covalent bond formation **(Fig. 1. 4)**.[18,25] The compound must first bind non-covalently to the target protein (K_I), placing its reactive electrophile close to the specific nucleophile on the protein. The resulting complex then undergoes covalent bond formation, which gives rise to the inhibited complex (k_{inact}).[18,25] In cases in which bond formation is effectively irreversible, k_{-2} will

essentially be zero, with their concentration and time-dependent target inhibition governed by K_I and k_{inact}.[18] Fully reversible inhibitors never form the covalent complex, and so k_{inact} is zero. For reversible covalent inhibitors, the covalent complex can dissociate and revert to the non-covalent complex, and so the covalent bond for formation exists on a continuum characterized by a range of values for both k_{inact} and k_{-2}.[23] This unique process allows rapid dissociation of the small molecules from common reactive groups while retaining persistent inhibition of the target.[21] However, a potential drawback of reversible inhibitors is that their efficiency and potency can be diminished by mass-action competition with endogenous substrates.[26] Irreversible inhibitors can overcome this problem, but selectivity requires optimization. When potential off-target liabilities are surpassed, irreversible inhibitors can display higher efficacy, since they provide a complete and permanent blockade of the target protein, and a prolonged pharmacodynamic effect, depending on the *de novo* resynthesis rate of the target protein.[21,26]

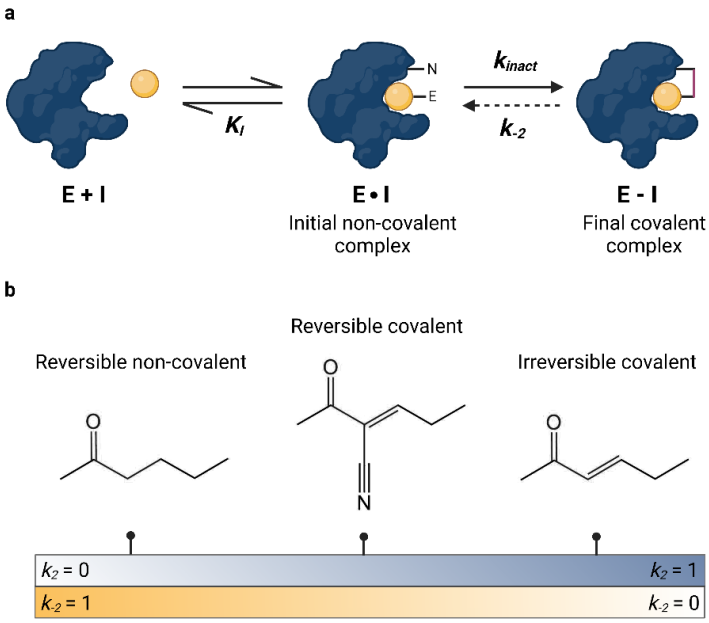

Fig. 1. 4. Kinetics of covalent bond formation. (a) Covalent bond formation: initial non-covalent binding, K_I, and final covalent reaction, k_{inact}. (b) The reversibility of covalent bond formation exists on a continuum characterized by a range of values for both k_{inact} and k_{-2} (adapted).[23]

Design and optimization. Design and optimization of CIs require a target that is amenable to specific covalent modification, and the optimization of both

the non-covalent binding affinity (K_I) and the reactivity of the electrophilic warhead

(k_{inact}).[21,26,27] These parameters allow the potency and selectivity of CIs to be fine-tuned. The non-covalent binding can be optimised though design of the overall compound structure.[27] However, the second part is optimised by a cautious selection of the covalent warhead to assure appropriate reactivity and orientation within the active site. The warhead should have sufficient reactivity to form the covalent bond to the residue in the active site, but insufficient reactivity to non-specifically react with residues in other proteins.[27] Serine and cysteine are two of the most targeted residues using covalent warheads **(Fig. 1. 5)** – although threonine, tyrosine, lysine, histidine and arginine residues may also be targeted.[27] The order of reactivity of the same warhead can change as it is directed to different residues. Serines are a much harder nucleophiles than cysteines and tend to react faster with harder electrophiles, such as benzoxaborole **(Fig. 1. 5, 4)** and sulfonyl fluoride **(Fig. 1. 5, 5)**.[27] In contrast, cysteines are much softer nucleophiles and rapidly react with softer electrophiles, such as Michael acceptors **(Fig. 1. 5, 1, 2, and 3)**. Owing to these different reactivities, covalent inhibitors can therefore be designed to target a nucleophile that is unique or rare across a protein family, thus ensuring that covalent bond formation does not occur with other related proteins, leading to a higher selectivity for the target protein.[27]

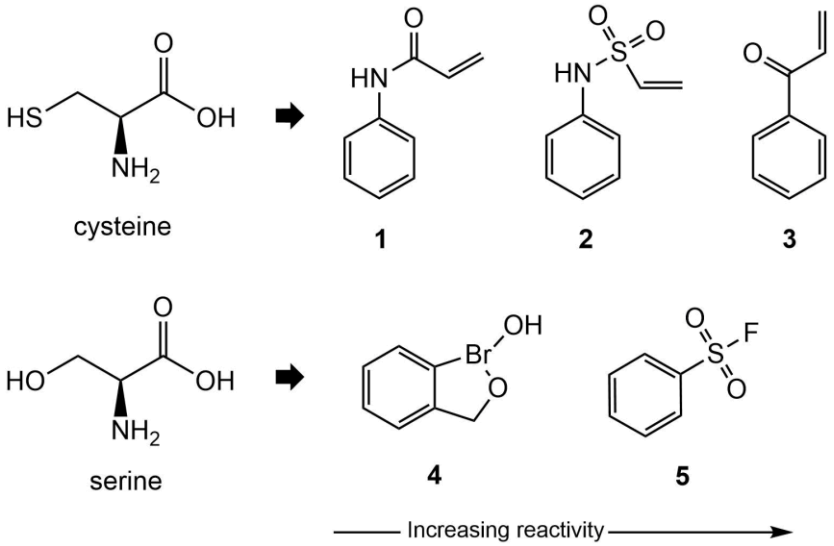

Fig. 1. 5. Covalent warheads against cysteine (1, 2, 3) and serine (4, 5).[27]

From the initial design stages, a small set of candidate compounds can be synthesized and screened for testing their ability to modify the target protein.[21] *De novo* molecular design and *in silico* predictions can also be used to identify innovative compounds in the early stages of drug discovery.[24] Other approaches comprise the incorporation of mildly reactive

electrophilic functional groups into known reversible ligands to enhance the inhibition of protein function.[21] The most active compounds are then characterized to determine their kinetic components (K_I and k_{inact}), thus allowing their activity to be optimized in a rational, data-driven way.[21,25] Small modifications are also introduced to the inhibitor structure that induce minor changes in the orientation of the electrophilic warhead relative to the nucleophile on the target protein. The success of these efforts is monitored through the increase in the rate of inactivation (k_{inact}/K_I) of the target protein.[21,27]

Clinical advances of targeted CI.

a) EGFR

Overexpressed EGFR is associated with the progression of a wide variety of cancers, including non-small cell lung cancer (NSCLC), making it a key drug target.[21] The identification of EGFR as an oncogene has led to the development of anticancer therapeutics directed against EGFR, including the first-generation reversible inhibitors Gefitinib and Erlotinib.[21] However, the disease in patients with NSCLC would eventually progress, mostly due to the acquisition of the T790M 'gatekeeper mutation'.[21] This mutation would not only diminish the binding affinity of reversible inhibitors, but it would also promote the binding affinity of the mutant EGFR for ATP.[21] To overcome this problem, a second-generation of covalent inhibitors were rationally designed to contain an acrylamide Michael acceptors that react with the cysteine residue (C797) in EGFR's ATP-binding site.[21] In addition to modest activity against T790M, covalent second-generation inhibitors provided prolonged pharmacological effects against EGFR signalling, thus being more efficacious than reversible first-generation inhibitors.[21] Afatinib was approved in 2013 as a first-line treatment for patients with metastatic NSCLC and with activating mutations in EGFR. Despite the increased potency derived from covalent engagement, the dose-limiting toxicity caused by inhibition of wild-type EGFR, prevented Afatinib from improving overall survival when compared head-to-head to platinum-based chemotherapy.[21] A third generation of EGFR covalent inhibitors followed. These compounds maintain the acrylamide group to covalently bind C797 but exchange the quinazoline moiety of first-generation and second-generation compounds for a pyrimidine

to promote selectivity for the mutant EGFR(T790M).[21] This approach not only increased the affinity for T790M over wild-type EGFR, but also contributed to an improved safety profile, even at high drug dosages, relative to Afatinib.[21]

b) Kinases with non-conserved residues

Kinases with non-conserved cysteine residues have been selectively targeted using CIs.[21] One main example is JAK3, a non-receptor tyrosine kinase that is mainly expressed in leukocytes and involved in cytokine signalling. Covalently targeting the non-conserved C909 in JAK3 has resulted in selective inhibition of JAK3 over other JAK family members for treating autoimmune diseases.[21] Several other covalent inhibitors of fibroblast growth factor receptor, FGFR4, target the non-conserved C552 residue, resulting in a high selectivity over FGFR1, FGFR2 and FGFR3.[21] The acrylamide-containing FGFR4 inhibitor Fisogatinib is currently the subject of a phase 2 clinical trial for the treatment of metastatic hepatocellular carcinoma (NCT04194801).

c) KRAS

KRAS is a crucial oncogene that encodes for the GTPase and is found to be mutated in approximately 25% of all cancers, especially pancreatic, colorectal, and lung cancers.[21] In its active form, wild-type KRAS binds to GTP and converts it to GDP. However, numerous KRAS mutations attenuates GTPase activity, which results in lower rates of GTP hydrolysis and higher RAS signalling, ultimately promoting tumorigenesis.[21,28] Since the discovery of the role of KRAS, attempts to drug it directly using traditional drug discovery methods were unsuccessful: KRAS does not possess an accessible pocket for drug targeting; competitive inhibitors have to overcome the picomolar binding affinities of GTP and GDP; and active drugs developed against wild-type KRAS may display on-target toxicity.[21,28] There were several reasons why developing covalent inhibitors against the KRAS(G12C) mutant was appealing: (1) it could enable selective cytotoxicity to cancer cells by targeting the mutant KRAS; (2) the affinity provided by covalent engagement would be beneficial as KRAS lacks a druggable pocket; (3) G12C mutations account for 12-14% of KRAS mutations in non-small cell lung cancer, providing a promising patient group for direct benefit from KRAS(G12C) inhibition; (4) and position 12 in KRAS is

located close to the effector-binding region and nucleotide-binding pocket, indicating that covalent modification of KRAS(G12C) would impair its function.[21] Sotorasib was the first selective KRAS(G12C) inhibitor to enter clinical trials in 2018. A phase 2 clinical trial investigating Sotorasib was successfully completed in 2020, and it was followed by FDA approval for the treatment of patients with locally advanced or metastatic NSCLC.[21,28] Other covalent KRAS(G12C) inhibitors have entered clinical trials. Adagrasib is being investigated for patients with previously treated advanced solid tumours, harbouring the KRAS(G12C) mutation (NCT05162443). JNJ-74699157 was also tested in patients with several types of advanced solid tumour that express KRAS(G12C), including NSCLC and colorectal cancer.[21,29] Based on dose-limiting skeletal muscle toxicities and the lack of efficacy at the 100 mg dose, JNJ-74699157 was not considered favourable for further clinical development, and treatments were ceased.[29]

d) SARS-CoV-2 main protease inhibitors

During the SARS-CoV-2 outbreak in 2021, a combination of nirmatrelvir and ritonavir was used to treat mild-to-moderate COVID-19 (caused by SARS-CoV-2), marking the first approved oral treatment for the disease.[21] Nirmatrelvir covalently inhibits a key enzyme responsible for viral replication and transcription, the M^{pro}. The discovery of other covalent inhibitors against SARS-CoV-2 M^{pro} emerged from extensive work on protease inhibitors for SARS-CoV-1, which is the causative virus for severe acute respiratory syndrome coronavirus 1 (SARS1).[21] During the 2002–2003 SARS1 outbreak, researchers made the discovery of rupintrivir, which is a mechanism-based inhibitor of the human rhinovirus M^{pro}. Because SARS-CoV-2 M^{pro} shares 96% sequence identity with SARS-CoV-1 M^{pro}, and there is 100% sequence overlap of the catalytic sites, rupintrivir was adapted into a SARS-CoV-2 M^{pro} inhibitor.[21] This in turn enabled the identification of the α-hydroxymethylketone-containing antiviral PF-00835231, which demonstrated potent inhibitory effects against SARS-CoV-2 M^{pro}. In later investigations, PF-00835231's oral bioavailability was enhanced through substitution of the α-hydroxymethylketone moiety with a nitrile group, which also functions as an electrophile.[21] As a result of further optimization from PF-00835231, a potent reversible covalent inhibitor of SARS-CoV-2 was developed and named nirmatrelvir (PF-07321332). This inhibitor does not seem to inhibit other human cysteine or serine proteases. The efficacy of nirmatrelvir was

demonstrated in an *in vivo* study using a mouse-adapted SARS-CoV-2 model.[21]

1.3.2 PROTACs

The concept of PROTACs was first described by Kathleen Sakamoto, Craig Crews and Ray Deshaies in 2001, under the premise that proteins could be intentionally pulled by a chemical handle to a ubiquitin ligase for degradation.[30] Since then, the field has grown exponentially and has moved from peptide-based tools to multiple classes of fully synthetic small molecules-based degraders, with major improvements in stability, cell permeability, solubility and tissue distribution **(Fig. 1. 6)**.[31]

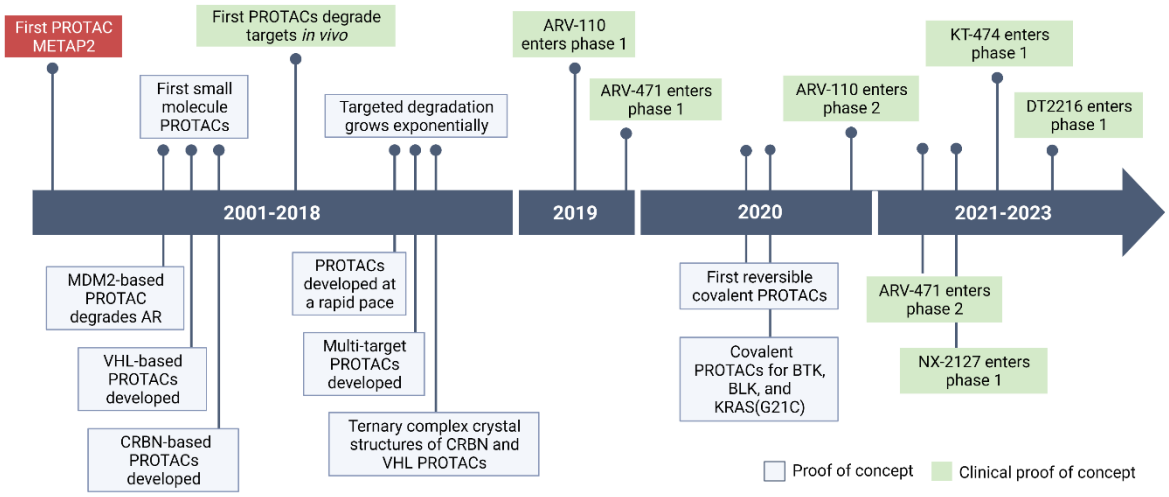

Fig. 1. 6. Timeline of PROTAC discoveries (adapted).[23,31]

Mechanistic features and pharmacological advantages. PROTACs are heterofunctional molecules that consist of a ligand for an E3 ubiquitin ligase, chemically tethered to a ligand for the protein of interest (POI).[23] The mechanism of PROTAC-mediated degradation occurs in three major steps. First, the ternary complex is formed by PROTAC-mediated proximity of the target protein to the E3 ubiquitin ligase. Second, the resultant ternary complex promotes the transfer of ATP-activated ubiquitin to the surface of the target protein by E2 ubiquitin-conjugating enzymes.[23,32] This transfer is accomplished via an isopeptide bond between the C-terminal glycine of ubiquitin and a lysine side chain on the

POI.[32] This cycle is repeated to poly-ubiquitinate the target, marking it for proteasomal degradation. Lastly, the poly-ubiquitinated protein is then recognized by the 26S proteasome and degraded **(Fig. 1. 7)**.[23]

A hook effect is commonly observed at high concentrations of PROTACs due to the bifunctional nature of the degrader.[23,33] This occurs when the PROTAC saturates the ligand-binding sites of both the POI and the E3 ubiquitin ligase, preventing the formation of ternary complexes and leading to reduced degradation of the target. The hook effect can limit the potency of a PROTAC and needs to be considered during the development of these molecules.[33]

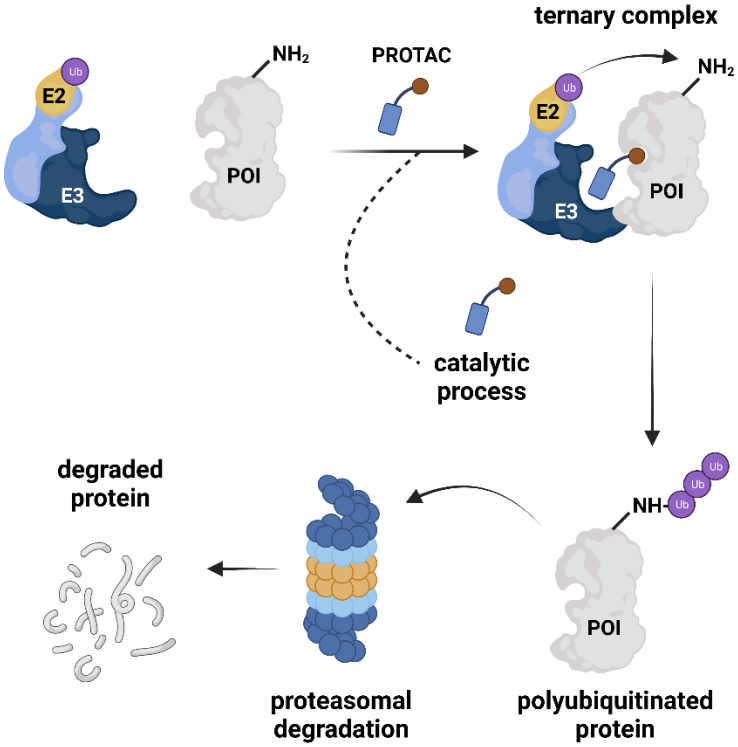

Fig. 1. 7. Catalytic mechanism of PROTAC-mediated degradation (adapted).[23]

PROTACs are designed to be substoichiometric target turnover molecules, meaning that one PROTAC molecule can degrade multiple molecules of the target protein, due to the PROTAC itself being recycled.[23,34] The advantage of this substoichiometric catalytic nature of PROTACs, offered by reversible engagement, is that it permits reduced dosage and mitigates undesirable off-target effects.[23]

Recruiters of the protein of interest. The ligand for POI can be easily adapted to target specific proteins, and this has enabled the rapid expansion of the PROTAC modality in

various diseases.[35] A significant proportion of targeted proteins are implicated in various types of cancers, although other diseases have also been represented, including the PROTACs targeting IRAK4 for the treatment of autoimmune and inflammatory disease;[36] and PROTAC degraders of viral proteins for inhibition of the hepatitis C virus;[37] and Tau degraders for the treatment of Alzheimer's disease.[38]

Ligands for the POI are not required to be functional or of high affinity, since PROTACs can convert non-functional or low-affinity ligands into functional, potent degraders.[23,39] This can be exemplified by a PROTAC which induced degradation of a multidomain co-regulator of transcription, TRIM24.[40] Inhibitors of the TRIM24 bromodomain had showed little to no phenotypic consequences in TRIM24-endogenously expressing cells, suggesting that inhibition alone was not sufficient as an anti-cancer strategy in TRIM24-dependent cancers.[39] Notably, the same ligand exhibiting lower affinity and selectivity towards TRIM24, afforded a selective and efficient VHL/E3-recruiting PROTAC.[39,40]

Having a reversible ligand for the POI offers many advantages. Reversible binding of the ligand means that the ligand can be released, and the protein's activity can be reinstated, allowing for the potential of on-off regulation.[23,41] The use of reversible ligands in PROTAC molecules also increases the stability of the molecule and prevents it from being degraded or removed from the system.[23] However, one of the key disadvantages of having a reversible warhead is that its reactivity can be difficult to control, as the binding and release of the ligand will depend on the concentration of the PROTAC molecule.[41] Furthermore, if the ligand is not reactive enough towards the POI, it can impair the formation of the ternary complex, and the subsequent target degradation.[41]

PROTACs with covalent warheads have become a popular alternative for degrading therapeutically challenging targets, due to the inherent advantages of CIs, such as their high ligand efficiency (LE), sustained target engagement, and ability to outcompete endogenous ligand binding.[23] These advantages of covalent bond formation are particularly attractive for PROTACs since, due to their large size ("beyond-rule-of-5"), their catalytic activity is at times dampened by poor cell permeability and an increased susceptibility to transporter-mediated efflux.[23,34] Covalent binding can potentially mitigate these disadvantages by allowing high affinity to be achieved, otherwise difficult to attain through non-covalent interactions alone.[23] Because CI can achieve a higher LE (*i.e.*, more binding energy per molecule's size) – and even for irreversible covalent inhibitors, where $k_{inact} = 0$,

the LE is essentially infinite – there is more opportunity to optimize the size and structure of the remainder PROTAC.[23,25] This can translate into a more favourable pharmacokinetic profile, with improved cell permeability and reduced susceptibility to efflux, and ultimately greater target degradation efficacy.[23]

There have been reported numerous PROTACs that exploit these kinetic properties of covalent warheads in PROTACs to degrade a range of targets.[41] The reversible covalent BTK PROTAC, RC-1, is a cyano-acrylamide-based molecule and has been found to have a higher target occupancy rate and efficient degradation, compared to its reversible noncovalent and irreversible covalent counterparts.[41] The DD-03-17 PROTAC, with pomalidomide and the reversible covalent BTK inhibitor CGI1746, not only caused selective degradation of wild-type BTK, but also the degradation of the Ibrutinib-resistant, C481S mutant BTK.[41,42] In addition, DD-03-171 significantly inhibited tumour growth and prolonged survival in mouse models of mantle cell lymphoma. The degrader MT-802 was developed based on thalidomide and the irreversible covalent BTK inhibitor, Ibrutinib. MT-802 exhibited activities in degradation of wild-type and mutant BTK and inhibited cell proliferation in Burkitt lymphoma and chronic lymphocytic leukaemia cells.[41,43] The KRAS(G12C)-targeting PROTAC (LC-2) is a small molecule designed to selectively bind and inhibit the mutant KRAS(G12C) protein.[44] LC-2 binds irreversibly to KRAS(G12C) through a MRTX849[45] warhead and recruits the VHL/E3 ligase, inducing rapid and sustained KRAS(G12C) degradation.[41] Preclinical data also showed that LC-2 selectivity engages KRAS(G12C), and it is effective against cancers associated with KRAS(G12C) mutations. This targeted approach holds several advantages over traditional inhibitors, including a greater selectivity and increased efficacy in targeting mutant proteins that would otherwise be considered "undruggable".[41,44]

In PROTACs, reversible covalent POI ligands are theorized to combine the benefits of covalent bond formation with the substoichiometric target turnover achieved by reversible engagement.[23] Conversely, irreversible engagement (where $k_{inact} = 0$) abrogates this fundamental concept of PROTAC's mechanism, along with the benefits associated.[23] However, very potent degradation has been observed with acrylamide PROTACs that bind irreversibly to BTK.[41] In this case, it was showed that the rate of covalent bond formation is slower relative to the rate of degradation, most likely due to the lower reactivity of substituted acrylamides, and therefore, the activity observed may have been derived from reversible binding.[41] Moreover, the degradation efficacy of the irreversible covalent

PROTACs did not significantly differ between the wild-type and C481S mutant BTK, suggesting that the covalent bond might not be a crucial factor in the PROTAC mode-of-action.[23,41] This data showcases that the measurement of the relative rates of covalent bond formation and degradation are required to estimate how covalent binding can affect PROTAC's activity.[41] Altogether, covalent warheads in PROTACs are a promising tool for degradation of more therapeutically challenging targets, but the choice of reversible *versus* irreversible should be evaluated on a case-by-case basis.[23]

Linker optimization. There are no generally accepted rules for *de novo* PROTAC linker design that can ensure the generation of potent degraders, and some degree of empirical trial and error is often required.[35] The most common motifs incorporated into PROTAC linker structures are PEGs and alkyl chains of varying lengths **(Fig. 1. 8)**. Modifications in the individual glycol units, through incorporation of additional methylene moieties, have also been reported. Other represented motifs include alkynes, triazoles and saturated heterocycles such as piperazine and piperidine.[35] Linker composition is important in PROTAC design since it influences the flexibility/rigidity of the molecule.[35,46] In addition, the linker must also have the appropriate length to allow both the target protein and the E3 ligase to come into proximity, without steric clashing of both entities with each other.[35,46]

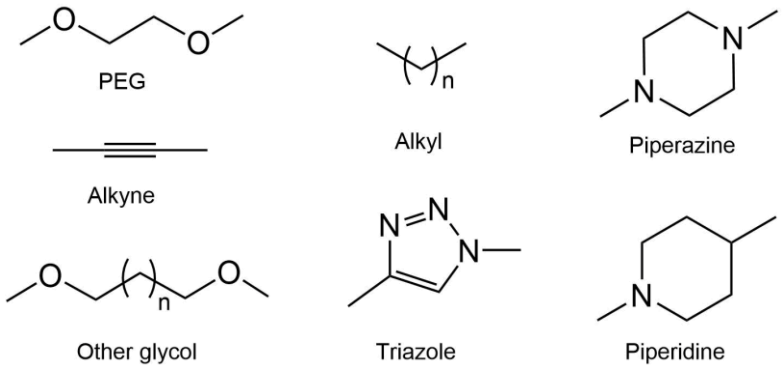

Fig. 1. 8. Chemical motifs most used in PROTAC-linker design.[35]

Selection of the optimal linker size to connect the two binding components is a key challenge in PROTAC design.[47] In some cases, it has been shown that arbitrary synthesized long linkers can successfully degrade their targets.[48] In other cases, a protein–protein interface between the target and the E3 ligase, supported by the presence of a shorter linker, is important for cooperativity of the specific ternary complex.[49–51] By

improving cooperativity, one can prevent targeting of other proteins, thus allowing for an increased selectivity.[34] Cooperativity (α) can be defined as the effect that POI:PROTAC association has on the affinity of the PROTAC:E3 pairing, and it is defined as $\alpha = K_D^{binary}/K_D^{ternary}$.[34,52] Positive cooperativity occurs when the $K_D^{ternary}$ is smaller than the K_D^{binary}. This is often accomplished by the addition of stabilizing interactions between the POI and the E3 ligase.[34] Conversely, negative cooperativity occurs when the $K_D^{ternary}$ is larger than the K_D^{binary} due to antagonizing interactions between the POI and E3 ligase. Increased cooperativity, in theory, stabilizes the ternary complex and can potentially decrease the magnitude of the hook effect.[34,52] Structural insights into the ternary complex structure of BRD4(BD2):MZ1:VHL/E3 revealed that MZ1, a PROTAC with a ten-atom linker, was significantly folded to allow proximity between the two proteins. Indeed, it was found that the surface complementarity of the two proteins plays a significant role in the newly formed ternary complex, facilitated by positive interactions between the linker and the two proteins.[51] With these insights from the ternary structure, a next-generation BRD4 degrader, AT1, was designed, composed of a shorter linker, which induced selective BRD4 degradation while sparing BRD2 and BRD3.[34,51] In subsequent studies, a macrocyclic PROTAC (macroPROTAC-1) was designed with the goal of similarly stabilizing the ternary complex. The crystal structure of macroPROTAC-1 showed it occupied a near-identical BRD4(BD2):MZ1:VHL/E3 conformation. As expected, an increase in cooperativity with BRD4(BD2) was observed, together with decreased cooperativity with other members of the BET family leading to equally potent, but more selective degradation of BRD4.[34,50] The solved structure of BCL-XL:PROTAC-6:VHL/E3 ternary structure, induced selective degradation of BCL-XL; despite the fact the PROTAC 6 incorporated a general BCL-2 family ligand, Venetoclax. The solved ternary complex structure showed PROTAC 6 also adopted a folded configuration, allowing for an extensive interface between BCL-XL and VHL/E3.[34,53] Conversely, successful degradation of BTK was achieved by employing longer linkers (PEG units ≥ 5) to alleviate steric clashes between BTK and CRBN/E3 observed with shorter linkers, demonstrating that increased PROTAC potency can also be achieved in the absence of thermodynamic cooperativity between POI:linker:E3.[48] Similar linker dependencies in TBK protein degradation have also been reported.[54] Thus, formation of ternary complexes, provided by positive cooperative interactions, are a strong indicator of successful target degradation.[34]

Recruiters of E3 ubiquitin ligase. E3 ligases are classified based on their mechanisms of action and divided into two main classes: RING E3 ligases, which recruit E2 ubiquitin conjugates via the RING domain and catalyse the transfer of ubiquitin directly to the substrate; and the HECT (homologous to the E6-AP carboxyl terminus) E3 ligases, which transfer ubiquitin to a substrate only after forming a thioester bond with ubiquitin.[32] Cullin-RING ligases (CRLs) are a type of RING E3 ligases that consist of a cullin protein (CUL), an E2-binding subunit, and a target-binding subunit.[32] The addition of the ubiquitin-like molecule NEDD8 (N) to target proteins via post-translational neddylation is initiated by N-activating enzyme (NAE), and it is essential for the activation of E3 ligases. MLN4924, a NAE-specific inhibitor was found to obstruct neddylation, thus deactivating CRL.[55,56] To date, of the ~600 E ligases encoded by the human genome, fewer than 10 have been recruited by successful protein degraders, and only four have been extensively exploited: Von Hippel−Lindau (VHL), cereblon (CRBN), cellular IAP (cIAP), and MDM2; with the remaining examples of β-TrCP1, DCAF15, DCAF16, RNF4, and RNF114 **(Fig. 1. 9)**.[23,39] It has been demonstrated all major classes of E3 ligases are amenable to targeted degradation, thus the recruitment of E3 ligases is only limited by the availability of small-molecules ligands.[57] PROTACs that have been commonly used all recruit their respective E3 ligase in a reversible way.[23,57] However, the discovery of PROTACs that covalently recruit E3 ligase has recently gained momentum, as these still retain the ability to act catalytically, if the POI ligand is reversible or reversible covalent.[23] They also have the advantage of simpler "pseudo-binary" kinetics since the binding is between E3:PROTAC and POI **(Fig. 1. 10)**.[23] Moreover, covalent engagement increases pharmacokinetics benefits since target degradation will depend upon the rate of E3 ligase and target turnover instead of PROTAC clearance.[23]

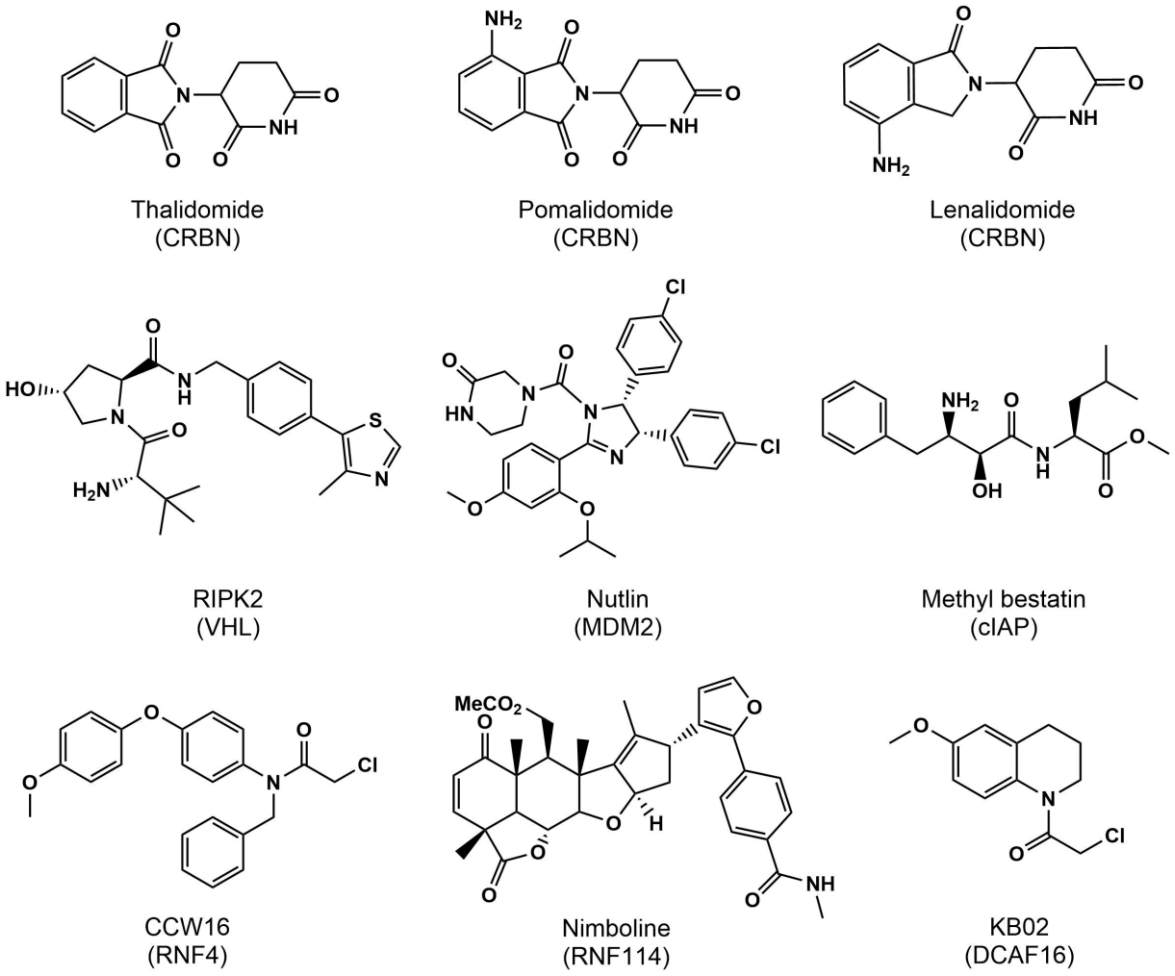

Fig. 1. 9. Examples of E3 recruiting elements and respective E3 ubiquitin ligases employed in recent years for PROTAC development.[39,58]

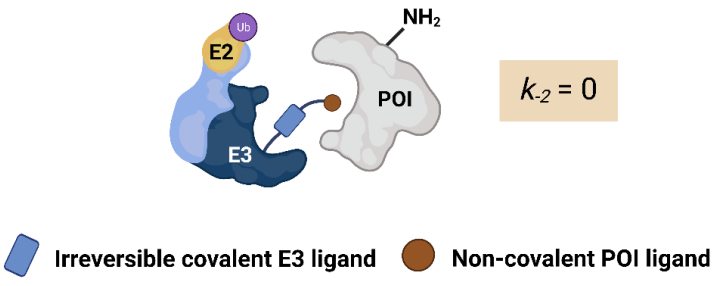

Fig. 1. 10. Schematic of PROTAC with irreversible covalent ligand for the E3 ligase (adapted).[23]

There are numerous factors to take into consideration when choosing which E3 ligase to recruit for effective PROTAC-mediated degradation. These include: (1) the subcellular location of both E3 ligase and its neosubstrate; (2) tissue expression levels of the E3 ligase; (3) its endogenous biological functions and the effects of perturbation; (4) the degree of engagement of the E3 ligand that still permits the E3 ligase to perform its endogenous functions; (5) the synergistic effects occurring from perturbing its endogenous function; (6) and an empirical discovery and optimization of compatible neosubstrate:E3 ligase pairing.[23,59] E3 ligases with a tissue-selective expression profile represent a particularly attractive therapeutic opportunity for disease-specific PROTACs to overcome on-target drug toxicity. Indeed, by recruiting an E3 ligase (containing CRBN) that is more abundantly expressed in senescent cells than in normal tissues, it was possible to achieve a 22-fold BCL-XL degradation selectivity over platelets and reduce on-target toxicity.[23,60] In addition, low fractional engagement of E3 ligases, as observed with RNF4 and DCAF16, avoids perturbing its endogenous functions. In some cases, as it has been reported for MDM2 and RNF114, antagonizing endogenous activity is desirable to elicit a therapeutically beneficial synergistic effect. In others, maintaining endogenous functions of other E3 ligases is important for mitigating off-target effects and potential toxicities.[23,61] Moreover, PROTACs with matching POI binding components but with different E3 ligase ligands (VHL *versus* CRBN) often show dramatic differences in potency for the targeted substrate proteins.[23,62] As reported, cells resistant to the VHL-based PROTAC remained sensitive to the CRBN-based PROTACs and *vice versa*. This absence of cross resistance suggests that acquired resistance can be surpassed by switching the recruited E3 ligase and that the proteasome degradation machinery can remain functional in these resistant cells.[23,62]

CRBN is one of the substrate receptors for the CRL ligases containing DDB1, CUL4A/B, and RBX1 **(Fig. 1. 11)**. CRBN recognizes neosubstrates upon binding to thalidomide and other less toxic immunomodulatory imide drugs (IMiD) analogues (*e.g.*, lenalidomide and pomalidomide) by engaging in ternary complexes, subsequently leading to the ubiquitination and proteasome-mediated degradation of these neosubstrates.[32,63] Thalidomide exerts its effects by directly binding to the highly conserved C-terminal region of CRBN. The conserved tyrosine residue at position 384 and tryptophan at position 386 are critical for the binding of thalidomide to CRBN, as alanine substitutions of these

residues abolish the ability of CRBN to bind thalidomide.[64,65] In 2015, Winter *et al*. demonstrated that CRBN recruiters could be linked to protein-targeting ligands to selectively degrade specific proteins in cells and slow tumour progression in mice.[66] They showed selective degradation of the transcriptional coactivator BRD4 and FKBP12 by linking phthalimide to their previously developed BET family protein ligand JQ1 and FKBP12 ligand SLF, respectively.[66] In the same year, Lu *et al*. published IMiD-based PROTACs for BRD4. Pomalidomide was used to hijack CRBN/E3 ligase.[32,67] The resultant molecule demonstrated a fast and permanent degradation of BRD4 in all Burkitt's lymphoma cell lines tested, and a higher efficacy in cell proliferation inhibition and apoptosis, relative to small molecules.[67] These results have opened-up the possibility for a fully synthetic drug-like heterobifunctional degraders that could be used to specifically degrade target proteins, and potentially advance into clinical development.[32]

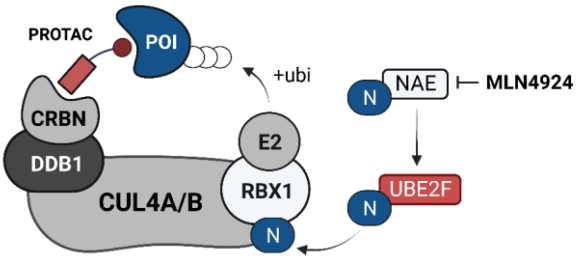

Fig. 1. 11. Schematic overview of cullin-RING E3 ligase. The substrate receptor protein (CRBN), docked into CRL complex through binding to the adaptor protein (DDB1), mediates neosubstrate degradation via ubiquitin conjugation. MLN4924 is a specific inhibitor of NAE, prohibiting NEDD8 conjugation and consequently inhibiting CRL activity.[55,56]

Pharmacological advantages. Targeted degradation through PROTACs offers numerous advantages relative to small molecule inhibitors.[17,23] First, the target proteins of small molecules require a druggable pocket or active site. In the entirety of the human proteome, only 25% of proteins possess active sites or pockets amenable to inhibitor modification. The remaining 75% include transcription factors, scaffolding proteins, and non-enzymatic proteins, considered undruggable using this strategy. Second, small molecule inhibitors operate via "occupancy-driven" pharmacology, where sustainably high systemic drug levels are required to maintain an adequate intracellular concentration for therapeutic

efficacy, which can elicit undesirable off-target effects. Third, small molecules generally only disrupt the activity of one domain in multidomain scaffolding proteins, while the functional activities of other domains and their interactions with other proteins and substrates remain intact.[17] In this way, the inhibition of multidomain proteins may lead to compensatory mechanisms via activation of other alternative routes.[68] Conversely, PROTACs can recapitulate phenotypes of protein knockdown expression generated with RNA interference (RNAi) and CRISPR-Cas9, combined with the temporal control, high cell permeability, and pharmaceutical properties of typical small-molecule inhibitors.[23] Because PROTACs do not require an accessible pocket for targeting, they are better suited for therapeutic targets in which inhibition alone is ineffective.[17] Importantly, PROTACs can be catalytically involved in multiple rounds of target protein degradation, possibly reducing systemic drug exposure in the clinic and potential associated toxic side effects.[17,23] They can also display intracellular picomolar potencies, where degradation of the protein target is fast achieved and sustained, as well as the inhibition of related-downstream signalling cascades. Moreover, PROTACs can avoid the compensatory target upregulation caused by constitutive administration of small-molecule inhibitors, observed in some clinical cases.[23]

Clinical advances. This foundational era of targeted degradation has been capped by the first rationally designed PROTACs entering clinical trials in 2019 – ARV-110 (NCT03888612) and ARV-471 (NCT04072952) – targeting the androgen and estrogen receptors (AR and ER), respectively.[31] Both of these degraders are currently in phase 2 trials, and have been followed into the clinic by degraders from Bristol Myers Squibb, Nurix Therapeutics, Kymera Therapeutics, Dialectic Therapeutics, Foghorn Therapeutics and others.[31] The AR degrader ARV-110 was evaluated in heavily pretreated patients with metastatic castration-resistant prostate cancer. Preliminary data indicated that doses of up to 420 mg of ARV-110 were well-tolerated.[69] Additionally, the data showed that ARV-110 caused degradation of the protein target in tumours and showed early signs of antitumor activity, as evidenced by decreased levels of prostate-specific antigen. These data supported the continued development of ARV-110 into phase 2 clinical trials.[31,69] ARV-471 entered clinical trials as a monotherapy for patients with locally advanced or metastatic breast cancer.[31] Preliminary data for ARV-471 revealed a manageable tolerability profile

with good clinical efficacy, a 42% clinical benefit rate in a heavily pretreated patients and evidence of greater ER degradation than fulvestrant and other clinical-stage selective ER degraders.[31] ARV-471 has now progressed to phase 2 (NCT04072952) in metastatic breast cancer, and to a phase 1b study evaluating ARV-471 in combination with the CDK4/CDK6 inhibitor, palbociclib.[31]

KT-474 is the first IRAK4 degrader to enter clinical trials (NCT04772885). The role of IRAK4 in inflammatory conditions, as well as in B-cell lymphomas, is well established, with several inhibitors currently under clinical investigation.[31] However, no IRAK4-targeting therapies have been approved yet. Alongside KT-474, NX-2127, a first-in-class oral BTK degrader with IMiD-like activity, has entered phase 1 clinical trial for relapsed and refractory B-cell malignancies (NCT04830137).[31]

Additionally, the clinical development of molecular glues (although non-heterofunctional degraders as PROTACs) such as CC-90009 and CC-92480, as well as molecular glues from C4 Therapeutics and Novartis, showcases the advances made in understanding and exploiting protein degradation as a therapeutic modality.[31] These new-generation CRBN modulators have been engineered to therapeutic target IKZF1/IKZF3 and GSPT1, and they can also induce or stabilize the interactions between an E3 ligase and the POI to form a ternary complex, resulting in protein degradation.[31]

Given the clinical progress in the past two decades, it is clear that targeted protein degradation could become a key therapeutic modality and it has the potential to offer patients new treatment options across diverse indications.[31]

1.4 Therapeutic targets

1.4.1 TEC kinases

TEC kinases are the second largest family of nonreceptor tyrosine kinases and present a cysteine residue of unique occurrence in their catalytic pocket, amenable to covalent modification.[70] This family is composed of five members, namely TEC (tyrosine kinase expressed in hepatocellular carcinoma), BTK (Bruton's tyrosine kinase), ITK (interleukin-2-inducible T-cell kinase), BMX (bone marrow kinase in the X chromosome) and TXK (resting lymphocyte kinase/RLK). TEC family proteins are abundantly expressed in

hematopoietic tissues and are essential for the growth and differentiation of normal and cancerous haematological cells.[71]

Comparable to other tyrosine kinases, TEC family of enzymes catalyze the transfer of the γ-phosphate from ATP to one or more amino acids in a protein substrate side-chains, resulting in conformational changes that affect protein activity.[72] TEC kinases present a very conserved core catalytic structure **(Fig. 1. 12)**, composed of an amino-terminal pleckstrin homology (PH) domain; a carboxy-terminal catalytic tyrosine kinase domain, preceded by proto-oncogene tyrosine kinase (SRC) homology 3 (SH3) and 2 (SH2) domains; and a TEC homology domain that includes one or two proline-rich regions that interact intramolecularly or intermolecularly with SH3 and contribute to kinase regulation – with the exception of TXK, which lacks a PH domain and instead contains a palmitoylated series of cysteines; and BMX that lacks the proline-rich region in the TH domain and contains a slightly different sequence in the SH3.[71,73]

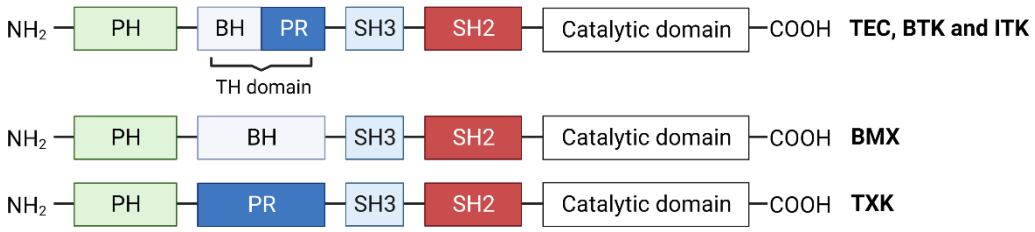

Fig. 1. 12. Core structure of TEC family members. PH, pleckstrin homology; CS, cysteine string; BH, BTK homology; PR, proline rich; TH, TEC homology; SH, SRC homology.[74]

TEC kinases are activated in response to cellular stimulation by antigen receptors, integrins, growth factors, cytokines, and G protein-coupled receptors. This activation is governed by two major steps: (1) membrane targeting, via interactions of their PH domains with phosphatidylinositol (3,4,5) trisphosphate (PIP3) or other proteins; and (2) tyrosine phosphorylation within the kinase activation loop. Protein interactions via the SH2 and SH3 domains may also be required to disrupt intramolecular interactions and to localize the kinases in signalling complexes.[71,75]

Protein kinases are the second most targeted group for drug therapy, after the G-protein-coupled receptors. Notably, TEC family kinases are involved in several pathologies, including haematological, cardiovascular, immunological, infectious, and inflammatory

diseases.[76–79] They may be abnormally activated or found overexpressed. The most well-known example is the targeting of BTK that has showed good prospects in the treatment of blood cancers and autoimmune diseases, with five inhibitors already commercially available, and many others currently in clinical trials.[80,81] Ibrutinib was the first confirmed irreversible inhibitor of BTK that binds to the C481 with outstanding clinical activity and tolerability in B-cell malignancies. It is also found to be effective for inhibition of other TEC family kinases, namely BMX and ITK.[80]

BMX is expressed in the endothelial and haematological lineages. It is found overexpressed in prostate[82], cervical[83], and breast cancers[84]. In prostate cancer, BMX is intimately related with androgen-receptor pathway, and it is involved in the adaptive compensatory mechanisms of castrate resistant prostate cancer.[82,85] Due to high sequence similarity to BTK, BMX inhibitors are typically dual BTK and BMX inhibitors.[86] BMX-IN-1 is the most well-known, selective, irreversible inhibitor of BMX that targets the functional C496 in the catalytic pocket.[70] BMX-IN-1 inhibits intracellularly BMX at two-digit nanomolar concentrations but requires single digit micromolar concentrations to inhibit the proliferation of prostate cancer cell lines.[70] In combinatorial regimens with the AKT inhibitor, MK2206, BMX-IN-1 is able to potentiate BMX inhibitor's antiproliferation efficacy against prostate cancer cells.[70] Additionally, BMX is inhibited by Ibrutinib and showed potential therapeutic effects in treating inflammatory and cardiovascular diseases.[87]

ITK is involved in T-cell receptor (TCR) signalling events essential for T-cell development and for controlled expression of pro-inflammatory cytokines.[88] ITK-deficiency impairs T-helper type 2 cell (TH2) responses associated with allergy and asthma, making ITK an attractive therapeutic target for such diseases.[89] Data from three highly selective ITK antagonists demonstrate putative therapeutic use for allergic-induced asthma. Several inhibitors of ITK have been described, including ibrutinib.[89–91]

TXK expression is mostly detected in some myeloid cell lines and T-cells.[72] Moreover, TXK is expressed in T-cell subsets, and was reported to act as a TH1 cell-specific transcription factor, regulating IFN-γ gene expression via binding to its promoter region, increasing transcriptional activity.[72]

Similar to BMX, TEC displays a much broader expression, even extending to normal somatic cells (*e.g.,* cardiac endothelium).[72] The overexpression of TEC has been found to be associated with tumorigenesis and liver cancer progression. Inhibiting TEC or

degrading its phosphorylation may therefore impair the progression and development of liver cancer.[72] A more recent study, identified TEC as a regulator in controlling pluripotent cell fate in human pluripotent stem cells, acting through the regulation of fibroblast growth factor-2 secretion.[72,92]

1.4.2 Serine Hydrolases

Serine hydrolases (SerH) are a large and diverse group of enzymes that play a key role in many pathophysiological processes, including blood clotting, digestion, nervous system signalling, inflammation and cancer.[93] A defining characteristic of SerH is the presence of a catalytic serine at the active site, which is used for the hydrolysis of substrates **(Fig. 1. 13)**. Many SerH have gained massive interest as therapeutic targets and are the focus of intense drug discovery studies.[93] Despite all recent efforts, most of the SerH remain poorly characterized with respect to their physiological functions, as well as their relevance in human diseases, and the majority lack selective, *in vivo*-active inhibitors.[93]

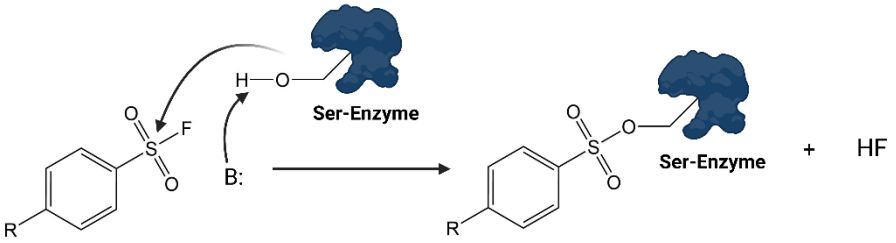

Fig. 1. 13. Schematic representation of the serine hydrolase catalytic cycle.[93]

There are around 240 serine hydrolases in the human proteome that can be divided into two subgroups: the serine proteases (~125) and the metabolic serine hydrolases (~115) **(Fig. 1. 14)**.[93,94] The metabolic SHs are composed of a range of lipases, peptidases, esterases, thioesterases and amidases that hydrolyse small molecules, peptides or post-translational ester (or thioester) protein modifications.[93] The majority of metabolic SerH have an α/β-hydrolase fold and a Ser-His-Asp catalytic triad, but this subfamily also includes structurally and mechanistically distinct enzyme classes, which use Ser-Asp dyads and Ser-Ser-Lys triads for catalysis.[93,95–97]

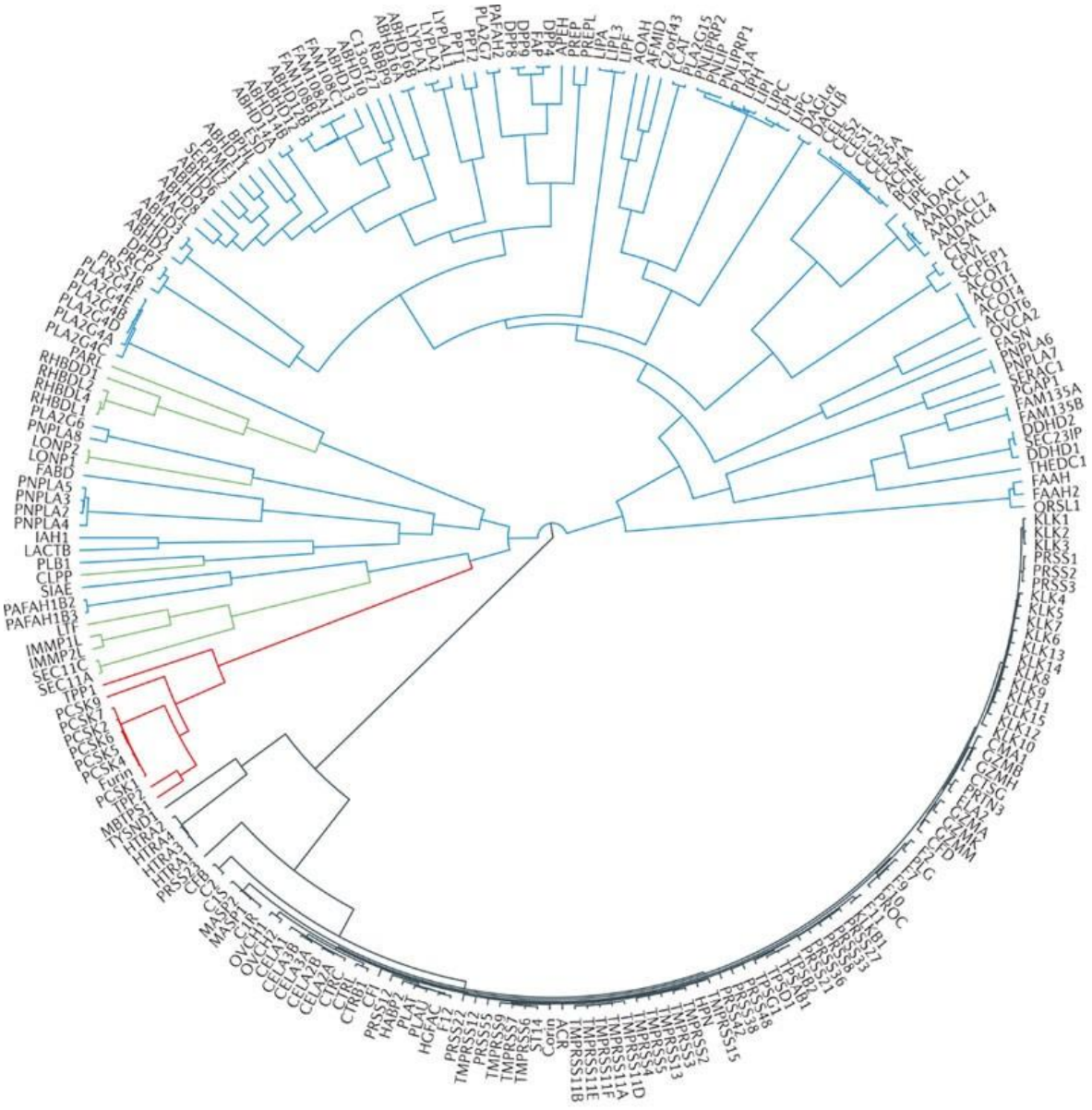

Fig. 1. 14. The human serine hydrolases. The metabolic serine hydrolases are depicted using blue lines. The remaining enzymes are serine proteases, with chymotrypsin-like enzymes depicted using grey lines, subtilisin-like enzymes depicted using red lines, and other smaller serine protease classes depicted using green lines.[93]

Although several members of the metabolic serine hydrolase family have been extensively characterized, including acetylcholinesterase, fatty acid amide hydrolase and dipeptidyl peptidase 4, the majority are still not annotated with respect to their physiological substrates and functions.[94] Serine proteases typically exist as inactive precursors (that is, zymogens), which are activated by limited proteolysis following

specific biological stimuli and are subsequently inactivated by endogenous protein inhibitors.[98,99] Serine proteases have a chymotrypsin-like or subtilisin-like folds, and a serine nucleophile that is activated by participating in a catalytic triad with conserved histidine and aspartic acid residues.[93,99] These enzymes include the well-studied digestive protease trypsin and the critical blood-clotting mediators, thrombin and activated factor Xa.[93,98,99]

The broad biological importance of serine hydrolases has encouraged numerous academic and industrial teams to design inhibitors for these enzymes, to be used as chemical probes to investigate enzymatic function and as potentially new therapeutic agents.[93] These compounds range from small molecules to peptides and antibodies, and they are being explored as potential treatments for various diseases.[93] Several inhibitors of SerH have been approved for clinical use, including inhibitors of thrombin, acetylcholinesterase, and dipeptidyl peptidase, which are used to treat clotting disorders, Alzheimer's disease-associated dementia, and diabetes, respectively.[93] Benzamidine is a small molecule that has been approved for the treatment of thromboembolic disorders and is also used to protect against tissue damage during cardiac surgery.[100] Aprotinin is a protease inhibitor that is used to reduce bleeding during surgery.[101] Acetylcholinesterase inhibitors, rivastigmine, donepezil, and galantamine, are used to treat dementia associated with Alzheimer's disease.[93] Furthermore, five dipeptidyl peptidase-4 inhibitors have been approved for clinical use for the treatment of type 2 diabetes: sitagliptin, saxagliptin, linagliptin, vildagliptin, alogliptin – although vildagliptin and alogliptin have not been approved in the United States.[93]

1.5 Thesis scope

Targeted therapy has revolutionized the field of cancer treatment by offering many advantages over traditional chemotherapy. In this thesis in particular, the fundamental aspects of developing covalent inhibitors and PROTACs for the treatment of blood cancers will be addressed.

Chapter 2 will focus on the therapeutic potential of a small covalent molecule (**JS25**) that inhibits BTK with nanomolar potency. Originally explored for treating prostate cancer,

JS25 was found to be highly selective for BTK and could be important in treating blood malignancies resulting from BTK's abnormal expression. In this study, we characterize the binding mode of **JS25** to BTK and demonstrate its potential to inhibit the proliferation of several haematological cancers and induce the degradation of BTK. The therapeutic effect was also validated in cancer models of Burkitt's lymphoma, diffuse large B-cell lymphoma, and chronic lymphocytic leukaemia.

In Chapter 3, computational and ABPP-based methods were combined for rational design and optimization of PROTACs that target with selectively the protein of interest, APT1. PRosettaC is used to predict optimal linker length, configuration, and binding efficacy, while immunoblot and ABPP-based assays were used to monitor APT1 degradation and selectivity. The most promising APT1-targeting PROTACs were evaluated for their anti-tumour activity in haematological cancer cell lines.

By leveraging the strengths of computational modelling and preclinical validation, this thesis aims to contribute to the ongoing efforts in developing effective BTK inhibitors and to advance the development of PROTACs, with the final goal of generating novel therapeutic agents with improved efficacy, selectivity, and safety profiles. Hopefully, all the efforts contained in this thesis will contribute to the growing field of targeted therapy, ultimately leading to the development of new and innovative therapies for cancer and other diseases.

2

Covalent targeting of BTK for the treatment of haematological cancers

Disclosures

The content of this chapter was published in the journal **RSC Chemical Biology**: "Structural and biophysical insights into the mode of covalent binding of rationally designed potent BMX inhibitors" **2020, 1, 251-262**; and in the journal **ACS Pharmacology and Translation Science**: "Selective inhibition of Bruton's tyrosine kinase by a designed covalent ligand leads to potent therapeutic efficacy in blood cancers relative to clinically used inhibitors" **2022, 5, 11, 1156–1168 (Annex)**. The findings in this chapter are also covered by a patent (number: WO2020245430A1).

The author also declares the following:

1. **Synthesis and optimization** of the compounds presented in this chapter were performed by Dr João Daniel Seixas, TargTex, Portugal.

2. **Initial biochemical assays (IC_{50}) of JS9-29 and kinome selectivity of JS25** were performed at Eurofins DiscoverX and KINOMEscan (United Kingdom), and Reaction Biology Corporation (Germany).

3. **Putative structures** of BTK in complex with Ibrutinib and JS25 were predicted by Dr Francisco Corzana from the Universidad de La Rioja, Spain.

4. **Mice model of Burkitt's lymphoma.** The histological analysis was performed by the teams of Dr. Pedro Faísca at the Histopathology Unit of Instituto Gulbenkian de Ciência, Portugal, and Comparative Pathology Unit at Instituto de Medicina Molecular, Portugal.

5. **Patient-models of DLBCL.** The experiments resulted from collaborative work with Dr Peter Neumeister and Dr Alexander Deutsch from Medical University of Graz, Austria, and with Dr Gregory I. Vladimer and Dr Nikolaus Krall from Exscientia company, United Kingdom.

6. **Zebrafish model of CLL**. The experiments were performed by Dr Cátia Rebelo de Almeida, Dr Ana F. Barahona, Dr Raquel Lopes, Dr Ana Martins-Lograd, Dr Cristina João, and Dr Rita Fior, at Champalimaud Foundation, Portugal.

2. Covalent targeting of BTK for the treatment of haematological cancers

2.1 Introduction

BTK is an essential component of multiple signalling pathways that regulate the functions of healthy or cancerous hematopoietic cells, making it a promising therapeutic target for blood cancers and autoimmune diseases.[80] This inspired the development of many BTK inhibitors (BTKi), including the first clinically approved agent, Ibrutinib. To overcome off-target effects and acquired resistance mechanisms to BTKi, significant efforts have been made over the years in developing highly selective and potent molecules.[80]

In this section we will address BTK's role in the pathophysiological context and the current progress in clinically approved BTKi for the treatment of haematological malignancies, and ultimately discuss our contribution in the discovery of a new BTKi (**JS25**) for the treatment of blood cancers.

2.1.1 Structure and pathophysiological functions

BTK was initially described as a critical mediator of B-cell receptor signalling in the development and functioning of adaptive immunity.[102] This protein was first discovered in 1993, and named after Ogden Bruton, who described X-linked agammaglobulinemia (XLA) in 1952.[102,103] XLA is a primary immunodeficiency disease caused by mutations of the BTK gene in the X chromosome, of which caused a defective maturation of B-cells in the bone marrow. BTK was thought to be expressed only in B-cells, since no other development and functional defects were observed in other immune cells of XLA patients.[80] BTK was also found overexpressed in cancerous B-cells. BTK overexpression inhibited the Fas/CD95-induced apoptosis, promoting the survival and continuous growth of cancer cells. It was then hypothesised that inhibitors of BTK would likely to enhance the drug sensitivity of B-lineage leukaemia/lymphoma cells.[104] Nowadays, it is well-known that BTK is expressed in a plethora of cells from the hematopoietic lineage, such as B- and T-cells, monocytes, neutrophils, and mast cells[81,105], and it has been shown to be an effective target against autoimmune and inflammatory diseases[106,107], and several haematological cancers.[81,108,109]

Similarly to other TEC kinases, BTK presents a highly conversed catalytic domain,

bearing a functional cysteine (481) permissive to covalent binding **(Fig. 2. 1)**.[81] BTK is generally located in the cytoplasm but is recruited to the cellular membrane upon binding of the PH domain to phosphatidylinositol lipids in the membrane.[80] After translocation, BTK is first activated by phosphorylation at the Y551 site in the catalytic pocket; followed by autophosphorylation of the Y223 in the SH3 domain as a result of Y551 phosphorylation, which can fully stabilize its active conformation.[80] Moreover, the TH domain possesses a zinc-finger motif which is essential for the optimal activity and stability of BTK.[80] BTK's activation is crucial for the development of healthy or malignant cells, and it modulates several signalling pathways including B-cell receptor (BCR), chemokine receptor, Toll-like receptors (TLR), and Fc-receptors (FcR) signalling **(Fig. 2. 2)**.

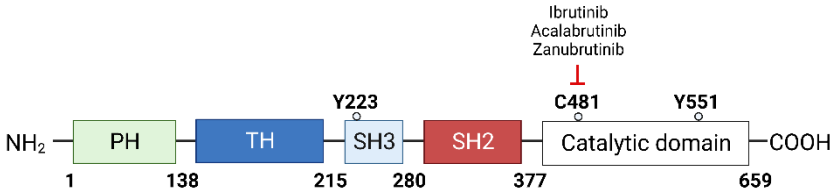

Fig. 2. 1. Structure and interactions of BTK (adapted).[80]

BCR signalling. BCR is a transmembrane protein located on the surface of B-cells.[81] Signalling via the BCR triggers a series of signal cascades that promote several physiological responses, including cell proliferation, differentiation, cytokine release and apoptosis.[80,81,110] There are two types of BCR signalling: tonic BCR and chronically activated BCR.[80,111] Activated BCR signalling is an antigen-dependent process utilizing the canonical nuclear factor-κB (NF-κB) pathway.[111,112] When BCR is stimulated by antigen binding, the signal triggers the phosphorylation ITAMs by SRC kinases, creating docking sites for the activation of SYK. This in turn can further phosphorylate BLNK to provide a scaffold for the recruitment and phosphorylation of various signalling molecules, including SYK, BTK and PLCγ2.[80] Simultaneously, LYN phosphorylates tyrosine residues in the cytoplasmic tail of CD19, which can then bind and activate PI3K and VAV family proteins. PI3K phosphorylates PIP2 to produce PIP3, attracting BTK to cell membranes and subsequently recruiting SYK and LYN to fully activate BTK.[80] Once activated, BTK can phosphorylate PLCγ2, leading to Ca^{2+} mobilization and activation of NF-κB and MAPK/ERK pathways.[80] Tonic BCR is an antigen-independent process that maintains B-cell survival through PI3K-AKT-mTOR signalling rather than NF-κB. PI3Kδ is a proximal

component of both tonic and chronic activated signalling. Tonic BCR signalling does not involve BTK.[111,113,114] The distinction between tonic and chronically activated BCR signalling is clinically relevant as it reflects disease sensitivity to BTKi.[80,111] For lymphoma-subtypes that are tonic BCR signalling-dependent, such as germinal center B-cell diffuse large B-cell lymphoma (GCB-DLBCL), BTK inhibition alone is ineffective, requiring additional therapeutic targets such as SYK and CXCR4. In contrast, lymphoma subtypes with chronic activated BCR signalling are sensitive to BTKi, and these include chronic lymphocytic leukaemia (CLL), mantle cell lymphoma (MCL), Waldenström's macroglobulinemia (WM), and activated B-cell (ABC)-DLBCL.[80]

Chemokine receptor signalling. Chemokine receptors are G-protein coupled receptors composed of seven transmembrane proteins (*e.g.,* CXC) and three subunits (Gα, Gβ, Gγ).[81] BTK can be directly or indirectly activated by the Gαβγ subunits, via the PH and TH domains, or even through its catalytic domain.[80,81] The chemokine receptors CXCR4 and CXCR5 are expressed on B-cells in different stages of their development and are important for trafficking, lymphocyte homing and homeostasis.[81] Due to its function downstream of CXCR4 and CXCR5, BTK is involved in integrin-mediated adhesion and migration of B-cells[115], and controls cellular responses to chemokines.[116,117]

TLR signalling. TLRs are a class of proteins that play a key role in the innate immune system and are expressed in B- and myeloid cells.[80,81] Upon activation, TLRs recruit the MYD88, which then induces the activation of the IRAK1, either alone or in combination with an adaptor molecule.[81] BTK interacts with all four proteins downstream of TLR signalling, and it is intimately involved in cell activation and proliferation, antibody secretion, class-switch recombination of immunoglobulins (*e.g.*, IgM to IgG) and proinflammatory cytokine production from B-cells.[81]

FcR signalling. BTK is an important modulator of FcR, whose balance regulates several myeloid cell processes including activation, polarization and phagocytosis.[81] FcεRI controls the activation of mast cells and subsequent histamine release; FcγRI activation enhances antigen presentation and the release of proinflammatory cytokines from myeloid cells.[80] BTK-dependent FcR activation is also required for osteoclast differentiation and osteoclastogenesis in response to RANKL. Therefore, constitutive activation of BTK is

linked to inflammatory diseases, such as rheumatoid arthritis and systemic lupus erythematosus.[80,107]

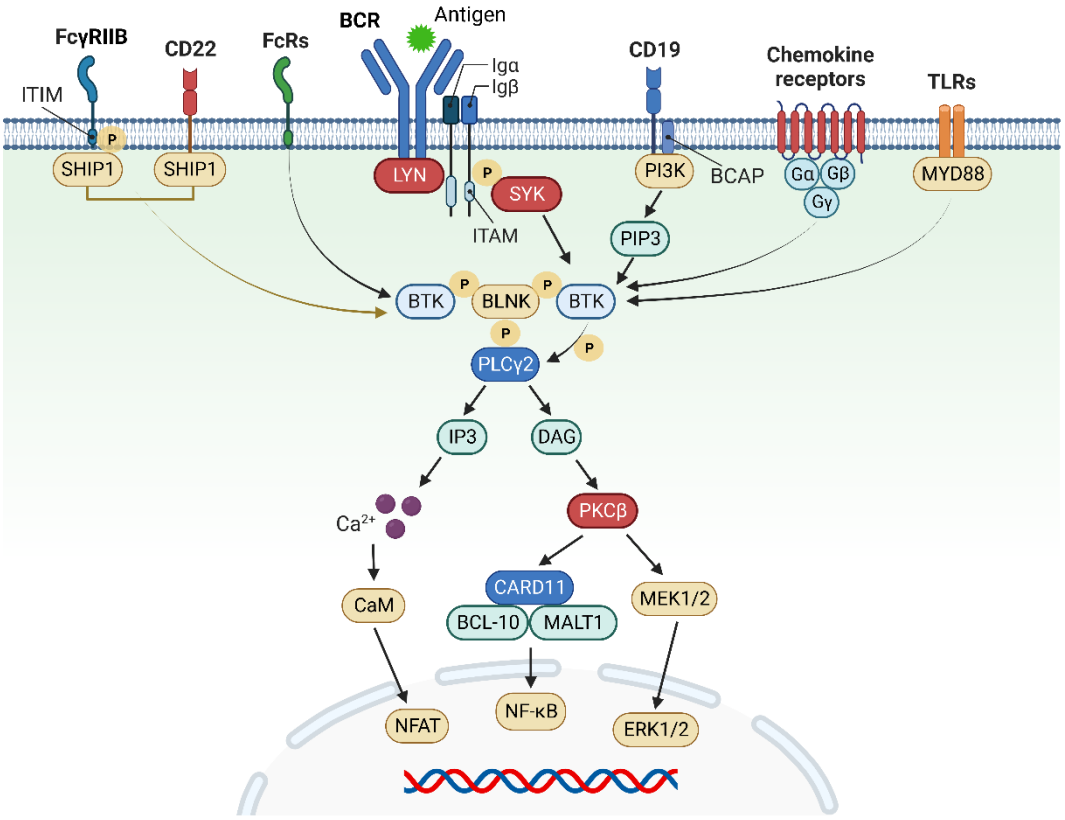

Fig. 2. 2. Role of BTK in BCR, TLR, chemokine receptor, and FcR signalling pathways (adapted).[80]

Growing evidence of BTK vital role in healthy and cancerous cells inspired the development of the first BTKi, LFM-A13, in 1999.[80] LFM-A13 was an effective inhibitor of JAK2 and of related downstream signalling molecules, such as BTK; also demonstrating synergistic anti-leukaemia effects *in vitro*, with ceramide or vincristine.[118] Since then, multiple BTKi have been gradually developed with improved selectivity and safety profiles, and with remarkable efficacy for the treatment of haematological diseases and autoimmune diseases.[119] BKTi can be divided into irreversible and reversible inhibitors according to different mechanisms of action and binding modes.[120] Irreversible inhibitors bind covalently via a Michael acceptor moiety to the wild type or mutant C481 present in the conserved catalytic pocket of BTK. Reversible molecules bind to a specific pocket in the SH3 domain through non-covalent interactions, such as hydrogen bonding or hydrophobic interactions.[120] All the current clinically approved BTKi are irreversible covalent molecules that induce permanent inhibition of BTK's enzymatic activity, with the exception of **Pirtobrutinib** which is a reversible non-covalent drug **(Fig. 2.3)**. Numerous

preclinical and clinical studies have initiated to evaluate the efficacy of novel BTKi as single agents or in combination with other standard chemotherapy, immunotherapy, or targeted agents, in order to expand indications to diseases with unmet clinical treatment.[119]

In the next sections, we will further address the role of BTK in haematological cancers, and the significant milestones in the preclinical discovery and clinical development of BTKi.

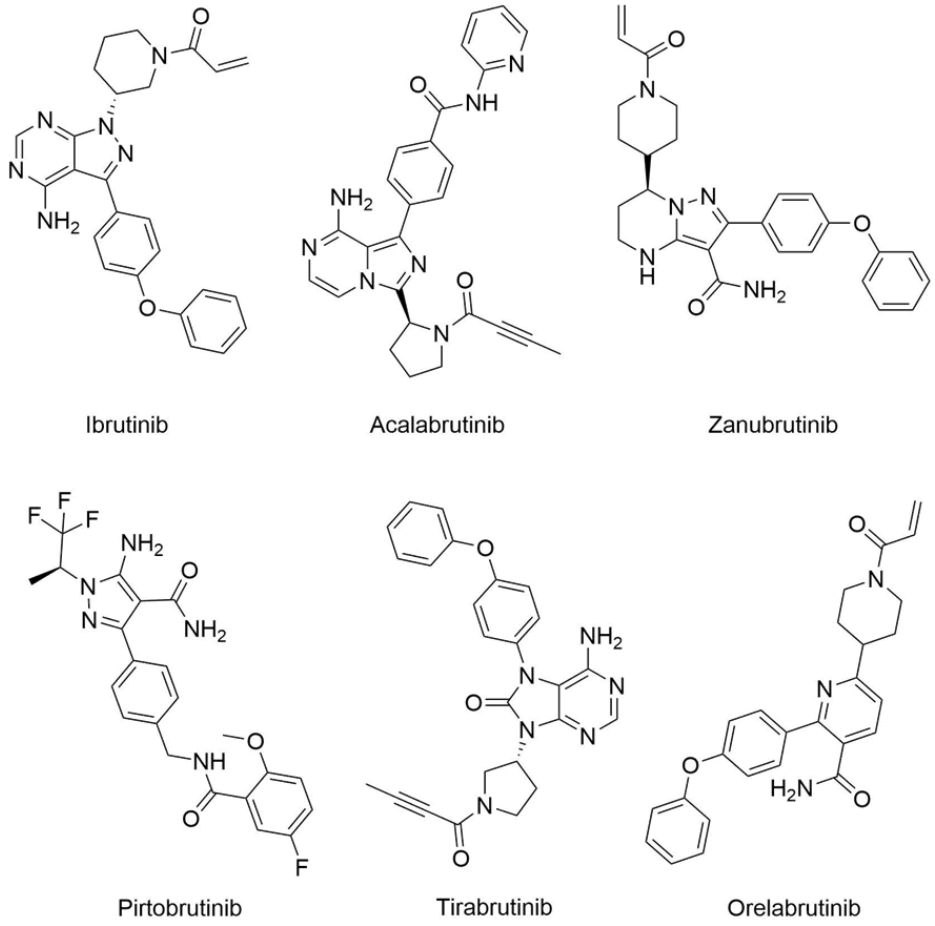

Fig. 2. 3. Chemical structures of the clinically approved BTK inhibitors.

2.1.2 Approved treatments against BTK

The irreversible BTKi, Ibrutinib, was the first to be FDA-approved and it is associated with high response rates in CLL, WM, and MCL and in chronic graft *versus* host disease (cGVHD).[121,122] However, with a broad selectivity profile, Ibrutinib inhibits the whole TEC family, EGFR, JAK3, HER2, BLK, and ITK kinases **(Table 2. 1)**. Ibrutinib's off-target binding is often associated with adverse effects such as rash, diarrhoea, bleedings,

infections, and atrial fibrillation, leading to treatment withdrawal in 9−23% of patients.[123] Ibrutinib can also antagonize rituximab-induced antibody dependent cellular cytotoxicity due to inhibition of its family member ITK, further limiting its use in combination regimens.[124] Despite the clinical success of Ibrutinib, further refinement was required in terms of adverse effects, fuelling the development of second-generation of compounds.

The second-generation BTKi are designed to maximize the potency and selectivity against BTK combined with reduced activity against off-target kinases.[80] These include Acalabrutinib, Zanubrutinib, Pirtobrutinib, Tirabrutinib and Orelabrutinib. Acalabrutinib was approved in 2017 for refractory and relapsed (R/R) MCL and in 2019 for CLL. With higher selectivity than Ibrutinib, Acalabrutinib inhibits BTK, TEC, BMX, ITK and TXK.[123,125] In previously treated CLL patients, treatment with Acalabrutinib demonstrated fewer AEs, including atrial fibrillation (9.4% *versus* 16.0%) and hypertension (9.4% *versus* 23.3%).[80] Overall, AEs-related treatment discontinuation was five times less likely to occur in patients administrated with Acalabrutinib, than with Ibrutinib. Zanubrutinib was approved to treat marginal zone lymphoma (MZL), MCL and WM between 2019-2021, and CLL in 2023.[123,126] Similar to Acalabrutinib, Zanubrutinib was less active against TEC and ITK, and displayed a higher potency and selectivity for BTK than Ibrutinib, with fewer toxicity effects.[123] Tirabrutinib was approved in Japan in 2020 for the treatment of refractory primary central nervous system lymphoma (CNSL) and is in clinical development in the United States and Europe for autoimmune disorders, CLL, Sjogren's syndrome, pemphigus, and rheumatoid arthritis.[80,127,128] However, Tirabrutinib also significantly inhibits TEC kinase. The co-occupation of both BTK and TEC leads to the hindrance of osteoclast differentiation and fosters bone loss that is propelled by M-CSF and RANKL.[129] Orelabrutinib has received approval in China for the treatment of patients with R/R MCL and CLL in 2020, and for R/R MZL in 2022.[130] Orelabrutinib showed excellent safety profiles and tolerability after long-term administration on patients.[80,131,132] Pirtobrutinib, the first non-covalent BTKi, was granted FDA-approval in January 2023 for the treatment of R/R MCL following two or more prior lines of systemic therapy. Pirtobrutinib inhibits both BTK and BTK-C481 substitute mutants with similar potencies.[133] Patients with BTK-C481 mutations for whom previous BTK treatments had failed, benefited from Pirtobrutinib treatment.[134]

Table 2. 1. Selectivity values (IC_{50}/nM) for approved BTKi.[135,136]

	Ib	Aca	Zan	Pirt	Tira	Ore
BTK	**1.5**	**5.1**	**0.5**	**1.8**	**5.6**	1.6
BMX	**0.8**	46	**1.4**	70	**4.3**	n/r
TEC	10	126	44	65	77	n/r
TXK	**2**	368	**2.2**	20	116	n/r
ITK	**4.9**	>1000	50	103	>1000	n/r
EGFR	**5.3**	>1000	21	61	>1000	n/r
BLK	**0.1**	>1000	**2.5**	82	>1000	n/r
JAK3	32	>1000	>1000	97	>1000	n/r
HER2	**6.4**	~1000	88	66	>1000	n/r
Approval	CLL, MCL, WM, cGVHD	CLL, R/R MCL	MZL, MCL, CLL, WM	R/R MCL	CNSL (Japan)	CLL, R/R MCL and MZL (China)

Ib: Ibrutinib; Aca: Acalabrutinib; Zan: Zanubrutinib; Pirt: Pirtobrutinib; Tira: Tirabrutinib; Ore: Orelabrutinib; n/r: not reported; Bold numbers correspond to IC_{50} < 10 nM.

2.1.3 BTK inhibitors in haematological diseases

Burkitt's lymphoma (BL) is characterized by a fast-growing of tumour cells in the lymphatic system, commonly associated with the infection of B-cells with the Epstein–Barr virus.[137] BL cells are mostly dependent on the tonic BCR signalling (PI3K-AKT-mTOR) for proliferation and survival. However, in high-grade BL, it has been reported chronic activation of the BCR (NF-κB) signalling, rendering the cells more sensitive to Ibrutinib treatment.[138] Besides, knockdown expression of BCR-related proteins, such as SYK and BTK, in specific BL-subsets, followed the same pattern of drug sensitivity, confirming dual BL cell-dependence on both tonic and active BCR signalling.[139]

BL patients can achieve remission in 70-90% of the cases, but the cure rate is lower in low-income countries.[9] BL treatment include the combination of rituximab with chemotherapy agents (*e.g.*, cyclophosphamide, doxorubicin), or dose-adjusted EPOCH

(etoposide, prednisone, vincristine, cyclophosphamide, doxorubicin) with rituximab, in case of older patients. Other forms of treatment include stem cell transplantation and radiotherapy.[9] While some patients with chemotherapy-sensitive disease may achieve long-term remissions, a few others will relapse soon after treatment completion and generally within the first 6 months of follow-up.[9] Current treatment responses in R/R BL are extremely poor, and new options are urgently needed. BTKi monotherapy has been proven ineffective for the treatment of BL or R/R BL, but these molecules still retain sustainable interest, as they could offer an improved efficacy and safety in combined regimens.[140] In a phase 3 trial, treatment responses to Ibrutinib-combined regimens with RICE (rituximab, ifosfamide, carboplatin, and etoposide), or RVICI (rituximab, vincristine, ifosfamide, carboplatin, and idarubicin), fell within the range previously reported with most rituximab-based regimens in R/R non-Hodgkin lymphomas (NHL), thus showing no apparent benefit of adding Ibrutinib to standard chemotherapy.[141] The lack of identification of disease subsets and overrepresentation of patients with non-BL pathologies, such as DLBCL, contributed partly to the poor result outcome.[141] Despite being both non-Hodgkin lymphomas, BL and DLBCL are two heterogeneous and distinct pathologies, and may require additional treatment options and checkpoints. A more balanced representation of B-cell NHL subtypes and their molecular variability in clinical trials, would be beneficial to fully understand the advantages of using BTKi to treat B-cell NHL, specifically R/R BL.[141] Most recently, clinical trials have started in order to investigate the therapeutic benefits of the novel BTKi, JNJ-64264681[142], in patients with R/R B-cell NHL, including R/R BL (NCT04210219).

Diffuse large B-cell lymphoma is the most prevalent type of aggressive NHL and can be categorized into two main subtypes that are defined by distinct genetic patterns and mechanisms of oncogenic activation: germinal centre B-cell (GCB) and activated B-cell (ABC). ABC-DLBCL is mainly dependent on BCR signalling.[80,119] Mutations in the CARD11, MYD88, or other NF-κB pathway components are present in about 40% of cases, while around 20% of cases have mutations in CD79A/B, leading to downstream kinase activation of SYK, BTK, PI3K, and PKCβ. In GCB-DLBCL, PI3K/AKT activation is relied upon primarily instead of NF-κB activation.[80,119] The dissimilar genetic signatures between ABC- and GCB-variants explain their differential response to chemotherapy.

Additionally, it has been observed that ABC-variants are more responsive to Ibrutinib than GBC-variants, with a 35% *versus* 5% complete or partial response rate reported in phase 1/2 clinical trials. However, the effectiveness of BTKi is modest in ABC-DLBCL when compared to other currently available treatments, with an overall response rate (ORR) of approximately 40%.[80,143] Patients diagnosed with ABC-DLBCL have a poorer prognosis compared to GBC-variants following standard treatment, with reported OS rates of 31-56% and 79-80%, respectively.[80,144] Ibrutinib is under investigation in combining regimens with other chemotherapy or immunotherapy agents, with ORR of 38-90% in early clinical trials but requires further exploration.[80] The combination of Ibrutinib with R-CHOP (rituximab, cyclophosphamide, doxorubicin, vincristine, and prednisone) was effective to a certain extent.[145] However, this combination did not meet its primary endpoint in untreated ABC-DLBCL patients, and the increased toxicity lead to treatment cessation.[146] As for the second-generation BTKi, Acalabrutinib monotherapy showed an ORR of 33% in ABC-patients in a phase 2 study;[147] and the ORR for Zanubrutinib monotherapy was similar (29.3%), showing no major improvements. Most patients with the ABC- phenotype had a lower survival outcome.[148] On this account, single-agent BTKi or combination regimens in DLBCL are limited. The ratio of added toxic effects *versus* the therapeutic benefit in combinatory regimens should be carefully balanced.[80] Further studies are needed to explore the molecular mechanisms underlying the resistance and poor outcomes, in order to identify the patients that would benefit from mono- or combined therapy with BTKi.[80]

Chronic lymphocytic leukaemia is the most common leukaemia in the western world, with a five-year survival rate, after the first diagnosis. It is characterized by the clonal proliferation and accumulation of CD5+ mature B cells in the bone marrow, peripheral blood, and lymphoid organs.[80,149] CLL-cell survival and proliferation are maintained through overexpression and constitutive phosphorylation of LYN, SYK, PKCβ, BTK, and PI3K.[119] Previously, medications such as fludarabine, cyclophosphamide, and rituximab were the initial treatment for CLL. As of 2021, the BTKi are often recommended for first-line treatment, as these demonstrate a higher efficacy in managing CLL and a more acceptable toxicity profile than conventional therapies.[80,83] Ibrutinib was the first licensed BTKi for CLL.[80] The approval of Ibrutinib was based on promising data from randomized clinical trials. Long-term follow up revealed the ORR of Ibrutinib would remain relatively

high (>70%) after six years of continuous treatments, with a complete response (CR) rate increasing overtime. However, Ibrutinib monotherapy presented some disadvantages, including a low complete remission, drug resistance and toxicity, and an undetectable minimal residual disease (uMRD) – complete MRD eradication was hardly obtained with Ibrutinib in CLL patients.[80,150,151] Besides, continuous treatment with Ibrutinib in R/R CLL patients increased the possibility of long-term toxicities, undesirable drug interactions and the development of acquired resistance.[80,150] These limitations urged the exploration of Ibrutinib-combinatory regimens with immunotherapy, chemoimmunotherapy (CIT), CART-T cell therapy, and other targeted agents, in order to further improve the efficacy.[80] The most extensively investigated combined regimens with Ibrutinib, include anti-CD20 agents, such as ofatumumab, obinutuzumab, ublituximab, and rituximab.[80] Combination of Ibrutinib with ublituximab or ofatumumab was highly tolerable and resulted in a rapid and high response rate (ORR > 83%) in R/R CLL patients.[80,152,153] In a phase 3 trial, Ibrutinib-obinutuzumab therapy showed a 30-month progression free survival (PFS) of 79% in previously untreated CLL patients, including high-risk patients with mutated and unmutated immunoglobulin heavy chain variable region (IGHV).[154] Based on the promising results, Ibrutinib-obinutuzumab therapy has been approved for the management of treatment naïve (TN) CLL patients in 2019. Ibrutinib-rituximab combination exhibited superior PFS in both IGHV and IGHV mutated CLL patients.[155] This finding promoted the approval of this combination strategy for previously TN CLL patients in 2020. However, it has been reported that the addition of rituximab provides no additional benefits to Ibrutinib immunotherapy.[80] The addition of Ibrutinib has also been reported to enhance the efficacy of CIT strategies, with an improved PFS and without additional toxicities for high-risk patients, in a phase 3 study.[156] The OS with Ibrutinib also appeared comparable to more intensive CIT regimens in studies that included younger and fit patients. These results strongly supported the combination of Ibrutinib with CIT regimens, to achieve prolonged survival and remission in CLL patients.[80] Ibrutinib combined with targeted therapeutics, such as BCL-2 inhibitor (Venetoclax), PI3K inhibitor (umbralisib), and STAT-1 inhibitor (fludarabine), improved CR rates in both TN and R/R CLL patients.[80] Ibrutinib-Venetoclax induced relatively high rate of uMRD (75% in peripheral blood and 68% in bone marrow), and CR (46%). In patients without confirmed uMRD, continuous therapy achieved a prolonged PFS (30-month: > 95%). This demonstrates favourable survival outcomes with good tolerability in R/R patients.[157] CART-T cell therapy has shown excellent responses in

some CLL patients. It was observed that Ibrutinib treatment increased the expansion of CD19-directed CART-T cells, in association with reduced expression of immunosuppressive molecules, including PD-1 on T-cells and CD200 on B-cells. Ibrutinib exposure also promoted CART-T cell engraftment, improved tumour clearance, and survival in human xenograft models of resistant acute lymphocytic leukaemia and CLL.[158]

Acalabrutinib, a second-generation BTKi known for its high selectivity, demonstrated encouraging efficacy and safety profiles in different subgroups of patients with CLL. Prolonged dosing of Acalabrutinib was well tolerated and induced a high ORR (95.8%) and PFS (24 months: 94%).[159] In previous treated CLL patients, Acalabrutinib showed no improvements in the survival outcomes, but demonstrated fewer cardiovascular toxicities than Ibrutinib in a randomized phase 3 clinical trial.[160] In R/R patients intolerable to Ibrutinib, Acalabrutinib exhibited a high ORR (81%) and favourable safety profiles.[161,162] Combination of Acalabrutinib with obinutuzumab was beneficial with longer PFS in the first-line treatment. However, a higher frequency of AEs was observed with this regime, rendering this combination unacceptable for patient administration.[163,164] Acalabrutinib, Venetoclax, and obinutuzumab combination also induce dose and durable remissions with acceptable toxicities. Approximately 38% patients achieved a high CR with uMRD in the bone marrow, after a median follow-up of 27.6 months.[165] These results promoted the evolution of this combination in an ongoing phase 3 trial (NCT03836261).[80]

Zanubrutinib demonstrated a promising activity with a low rate of serious toxicities, with an ORR of 78.3%, against Ibrutinib's ORR of 62.5%, in a 15-month follow-up period.[80,166,167] No long-term adverse effects (AEs) were observed in four years of dosing escalation study. Zanubrutinib *versus* Ibrutinib treatment was associated with lower rates of atrial fibrillation (2.5% *versus* 10.1%) and AEs-caused discontinuation (7.8% *versus* 13.0%).[80] Zanubrutinib combined therapies with immunotherapy or targeted therapy, are also being investigated. In phase 1b study, Zanubrutinib-obinutuzumab treatment yield a CR of 28% and 30% in TN and R/R CLL patients, respectively – a considerable improvement from previous reported ORR for Zanubrutinib monotherapy (~3%).[168] Triplet combination of Zanubrutinib, obinutuzumab, and Venetoclax showed promising efficacy as the initial treatment for CLL and reached a high uMRD rate of > 89% in both peripheral blood and bone marrow after 25.8 months. Additional observation after treatment and clinical trials involving more patients are required to verify the benefits of the three-drug combination strategy in CLL patients.[80,168]

Orelabrutinib, Pirtobrutinib, and Tirabrutinib monotherapy has also shown promising results in early-phase clinical trials in patients with R/R CLL, with ORR of respectively 91.3%[131,132], 62%[169] and 96%[170]. Pirtobrutinib also showed efficacy in pretreated and Ibrutinib-resistant CLL patients, suggesting a wide therapeutic index and strong efficacy.[169] Combination of Tirabrutinib and idelalisib or entospletinib, with or without obinutuzumab, also showed therapeutic effects and acceptable safety profile, although CR rates remained relatively low ($\leq 10\%$).[171,172] Multiple phase 3 clinical trials have been launched to compare the efficacy and safety of Pirtobrutinib (NCT05023980, NCT04965493, NCT05254743, NCT04666038) and Orelabrutinib (NCT04578613) to other conventional CLL therapies, including Ibrutinib.[80] Moreover, the novel BTKi, DTRMWXHS-12 and Fenebrutinib are also currently under clinical investigation to treat R/R CLL patients (NCT04305444, NCT01991184).[80]

Although preclinical and clinical data have shown promising results, further studies are required to confirm the therapeutic benefits of the novel BTKi and their combinatorial strategies in treating CLL patients.[80]

Central nervous system lymphoma is a rare subset of non-Hodgkin lymphoma, affecting mostly the brain, spinal cords, meninges, cerebrospinal fluids, and eyes.[173,174] CNS involvement is detected in < 5% of patients at initial diagnosis, with 4 months of median survival.[175,176] Amongst lymphoma subtypes, DLBCL accounts for 90% of the cases of both primary and secondary CNSL, with the remainder consisting of T-cell lymphomas, MCL, BL, CLL, MZL, and other poorly characterized low-grade lymphomas.[173] Due to the blood–brain barrier, patients with CNSL respond poorly to most available therapies. However, more recently BTKi have been extensively investigated as first-line treatments for CNSL, either as a single-agents or in combination, for their ability to cross the blood-brain-barrier.[80] In primary CNSL-DLBCL, Tirabrutinib induced an ORR of 63.6% and a median PFS of 2.9-5.8 months, in a phase 1/2 study conducted in Japan.[128] Similarly, Ibrutinib showed desirable efficacy in a phase 2 study.[80,177] Approximately 70% of the patients with primary CNSL-DLBCL receiving Ibrutinib treatment, presented median PFS and OS of 4.8 months and 19.2 months, respectively – much higher than what has been reported for Tirabrutinib. The combination of Ibrutinib with anthracycline-based chemotherapy significantly improved the CR (86%) for CNSL-DLBCL patients.[80,178]

However, this combination was met with undesirable toxicity, including a higher risk for invasive fungal infections by Aspergillus *spp*. A combination of Ibrutinib-rituximab, plus methotrexate[179,180] or lenalidomide[15] also induced lasting antitumor response, even in patients with poor prognosis, with an ORR ranging from 57% to 83%. In CNSL-MCL, the use of Ibrutinib monotherapy was associated with higher response rates and longer PFS and OS than the standard CNSL-directed chemotherapy (methotrexate, cytarabine, and ifosfamide).[175] The median OS was 16.8 months in treated patients, representing a substantial improvement over the 4.4 months reported for other regimens. As for other inhibitors, switching from Ibrutinib to Acalabrutinib has been shown not to affect the quality of the response to R/R CNSL-MCL.[176,181] A 57-year-old patient achieved a complete clinical radiological remission for almost 2 years after initiation with Acalabrutinib.[176] Therefore, the application of BTKi is a promising strategy in CNSL patients, either as monotherapy or in combination.[80]

Acute myeloid leukaemia (AML) is the most common leukaemia in older adults, with a five-year survival rate of 29.5% and is characterized by uncontrolled proliferation of abnormal myeloid progenitor cells in the bone marrow and blood.[182] In primary AML, BTK is found upregulated and constitutively phosphorylated.[183,184] BTK phosphorylation is induced by CD117 receptor signalling[185] or activating mutations in the G-CSFR[186] or FLT3[109], and can stimulate CXCR4 signalling, being therefore intrinsically involved in AML cell survival, migration and adhesion to stroma cells.[116,117] First-line treatment of AML consists primarily of chemotherapy, divided into induction and consolidation phases.[187] Induction therapy often includes cytarabine and an anthracycline, such as daunorubicin or idarubicin, to achieve complete cancer remission. Consolidation typically involves an additional three to five courses of intensive chemotherapy with cytarabine, to eliminate the remaining small numbers of AML cells that go on undetected (uMRD remission).[187] Hematopoietic stem cell transplantation is usually considered as an alternative in case induction chemotherapy fails or even after cancer relapse, and it can also be used as first-line therapy for patients with high-risk disease.[187] Because of the toxic effects of chemotherapy and a greater chance of AML acquired resistance, different treatments, such as BTKi, have been considered.[184] Among these, one phase 2 trial is evaluating the potential of Ibrutinib in preventing AML relapse after reduced-intensity

conditioning (chemo- and immune suppressing therapy) and hematopoietic cell transplantation for AML.[184] Another phase 2/3 aims to investigate the efficacy of Ibrutinib in combined regimens with decitabine, aclacinomycin, cytarabine, G-CSF and sorafenib, and with or without FLT3 inhibitor, in order to overcome drug-resistance in R/R FLT3 mutant AML.[184] The novel BTKi, Nemtabrutinib and Abivertinib, have shown promising anti-tumour activity against acute myeloid leukaemia in preclinical models.[184] Nemtabrutinib is an orally administered reversible and non-covalent inhibitor of both wild type BTK and Ibrutinib-resistant BTK-C481S mutant.[80] In xenograft models, Nemtabrutinib showed a superior antitumor activity in CLL, DLBCL, and AML, compared to Ibrutinib.[80] One phase 2/3 study showed a sustained anti-tumour activity and manageable safety profile of Nemtabrutinib in B-cell malignancies, but no other follow-up studies were performed to evaluate the efficacy in AML.[188] Abivertinib also showed anti-leukaemia effects, especially in FLT3 mutated AML cells, and was found to be more sensitive than Ibrutinib.[189] Furthermore, in cell and animal models, Abivertinib presented synergistic efficacy with homoharringtonine, a natural plant alkaloid commonly used in China, in both non- and mutated FLT3 AML cells.[189]

2.1.4 Adverse effects of BTK inhibitors

The AEs associated with BTKi are diverse and may include bleeding, infections, haemorrhage, atrial fibrillation, and headache.[119,190] Adverse events associated with Ibrutinib often include infections, bleeding, and atrial fibrillation. Although the prevalence of most AEs tends to decrease over time, long-term use of BTKi may lead to an increased prevalence of hypertension. Therefore, Ibrutinib is not recommended for patients with a high risk of cardiovascular and cerebrovascular diseases.[119,191] Acalabrutinib has a comparable rate of infections and bleeding to Ibrutinib, but a lower incidence of atrial fibrillation. However, it can lead to frequent headaches, making it unsuitable for patients with a history of headaches or migraines. Prolonged use of Acalabrutinib has been linked to a higher incidence of ventricular arrhythmias and sudden deaths, with a median time to event of 14.9 months. The incidence was higher in patients previously treated with Ibrutinib.[119,164] In alternative, Zanubrutinib showed a higher incidence of haematological AEs, but the reports of rash, atrial fibrillation, or bleeding are rare, suggesting a more favourable safety profile.[119] The most common AEs of Zanubrutinib were contusion,

airway infection, neutropenia, and diarrhoea.[119,192] Patients with MCL who received Zanubrutinib treatment experienced grade ≥ 3 adverse events, but the treatment was only discontinued by 9.3% of the patients. The study's long-term follow-up confirmed the effectiveness and durability of the response, with an average progression-free survival of 33 months and good tolerability.[80,119] BTKi are given continuously until unacceptable adverse events occur, which may lead to treatment cessation.[119] As a result, careful monitoring of adverse events and prompt interventions are necessary when administering BTKi. Meanwhile, combination therapy is recommended as it helps to decrease the duration of BTKi therapy and discontinuation of treatment before the onset of life-threatening adverse events.[80,119]

2.1.5 Acquired resistance in BTK inhibition

Although BTKi-based treatments have been proven to be one of the most effective strategies for several malignancies, cases of primary and secondary resistance often occur and result in poor clinical outcomes. These merging mechanisms of resistance have underlined the need for clinical biomarkers to predict sensitivity or resistance to BTKi.[80,119] Mutated IGHV in WM or MYD88 mutations with CD79 in ABC-DLBCL are associated with primary resistance to Ibrutinib.[119,144] Clinical analysis of R/R ABC-DLBCL samples also revealed several genetic aberrations in CARD11, NFKBIE, TNFAIP3, and an IgH-IRF8 translocation, all potentially enhancing NF-κB signalling.[193] Amongst patients continuously treated with Ibrutinib, mutations in C481, T474, and T316 residues in BTK are the most reported.[80,119] Cysteine to serine mutations at the 481 site not only weakens the ability of Ibrutinib to form a covalent bond with BTK, but also allows downstream signalling, including the activation of PLCγ2 and CARD11, hence bypassing the inactive BTK promoting distal BCR signalling activation, and consequently promoting the survival and proliferation of cancer cells.[119] Strategies to overcome acquired resistance include the development of non-covalent BTKi that do not dependent on C481 binding. Some representatives of these include Fenebrutinib, Pirtobrutinib, Nemtabrutinib, Vecabrutinib, and HMPL-760.[80] Combinatorial regimens of BTKi with inhibitors of other BCR-related proteins, such as PI3K, SYK, or BCL-2, also offer a great alternative to prevent the activation of bypassing signalling pathways.[80,194] Besides, BTKi can be combined with immunotherapy and CAR-T cell therapy to enhance treatment response and durable

remission, thus eliminating the requirement of continuous treatment with BTKi and reducing the possibility of developing drug resistance.[80,158] Most importantly, and especially for BTKi resistant patients, prebiopsy with detection of mutations is crucial to guide individualized treatment, and to guarantee the efficacy of BTKi in the appropriate disease context.[80,119]

2.2 Aim of the project

In this study, we investigate the therapeutic potential of a small covalent molecule (**JS25**) with nanomolar potency against BTK (5.8 nM). **JS25** was obtained from the scaffold of **BMX-IN-1**[70], a recently discovered molecule shown to also inhibit BTK, as part of our efforts to identify regions of the molecule that could be modulated for improved efficacy and selectivity. Initially, we had explored **JS25** potential to target BMX for the treatment of prostate cancer, but later experiments revealed that **JS25** was highly selective for BTK, and therefore, it could have therapeutic importance in blood malignancies that arise from BTK's abnormal expression. Following the preliminary data, we sought to characterize the binding mode of **JS25** to BTK and asserted its selectivity against a panel of proteins related to BTK's signalling pathway or with an equally placed cysteine as to the C481 of BTK. We further demonstrate that the lead compound has potential to inhibit the proliferation of several haematological cancers and to induce the degradation of BTK. Validation of its therapeutic effect was conducted in xenograft murine models of Burkitt's lymphoma, and in patient-derived models of diffuse large B-cell lymphoma and chronic lymphocytic leukaemia. Finally, we explore the capability of **JS25** to cross the brain−blood barrier and treat infiltration of tumour cells in the brain.

2.3 Results

2.3.1 Discovery of a single-digit nanomolar BMX/BTK inhibitors

To evaluate substituent tolerability at each position and to establish an optimal vector through positioning of different functionalities, a structure–activity relationship (SAR) study was used to establish the limitations of the tool chemotype **BMX-IN-1 (Fig. 2. 4)**. A total of 24 analogues were synthesized in an attempt to both enhance potency and optimize

physicochemical properties within the allowable SAR study **(Fig. 2. 5)**. Upon systematic evaluation, we found that analogues with substituents in position R^3 **(Table 2. 2)** of the quinoline moiety had only marginal effects on BMX inhibition. Furthermore, any change of the electrophilic warhead (position R^1) for cysteine covalent ligation resulted in loss of potency as illustrated for instance by the introduction of the enamide substituents in **JS10** and **JS11 (Table 2. 2)**. The substituents in the aromatic ring bearing the amide functionality play an unexpected relevant role for the activity, affording different reactivity patterns arising from non-covalent interactions. Introducing a strong electron-donating group such as a methoxy group (OMe) (**JS9E**) in R^2 decreases potency by 4-fold. In contrast, the use of a weak electron-donating group, such as a methyl substituent, has different effects depending on the positioning. Thus, moving the methyl group to the ortho position abolishes target inhibition (**JS9C**), while a methyl positioning in the meta position slightly improved inhibition by 2-fold. Even more striking is the effect of no substituent in the ring (**JS9D**), which increased inhibition by 6-fold. Since the electronic influence of the methyl substituents in the different positions is not expected to account for these differences, we consider that a conformational effect may play an important role. The ortho substitution may increase the constraints for fitting into the pocket, while the removal of the methyl groups affords less spatial restriction. Interestingly, substituents in position R^4 were found to significantly enhance BTK inhibition relative to **BMX-IN-1**.

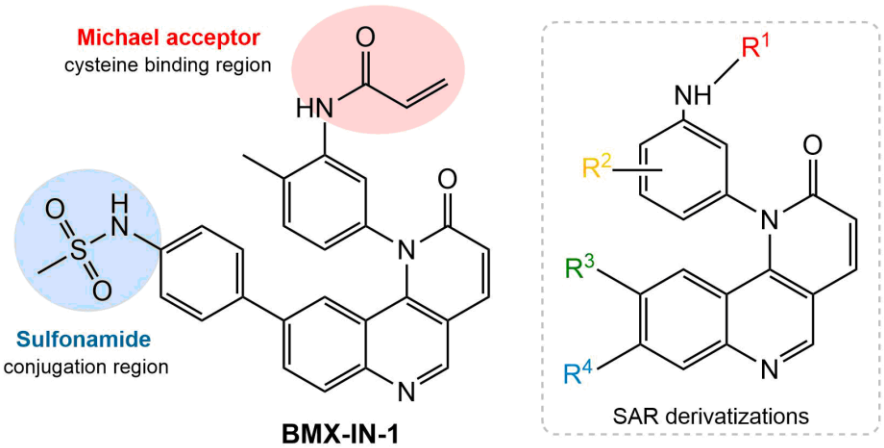

Fig. 2. 4. Structures of **BMX-IN-1** and SAR explored derivatizations.

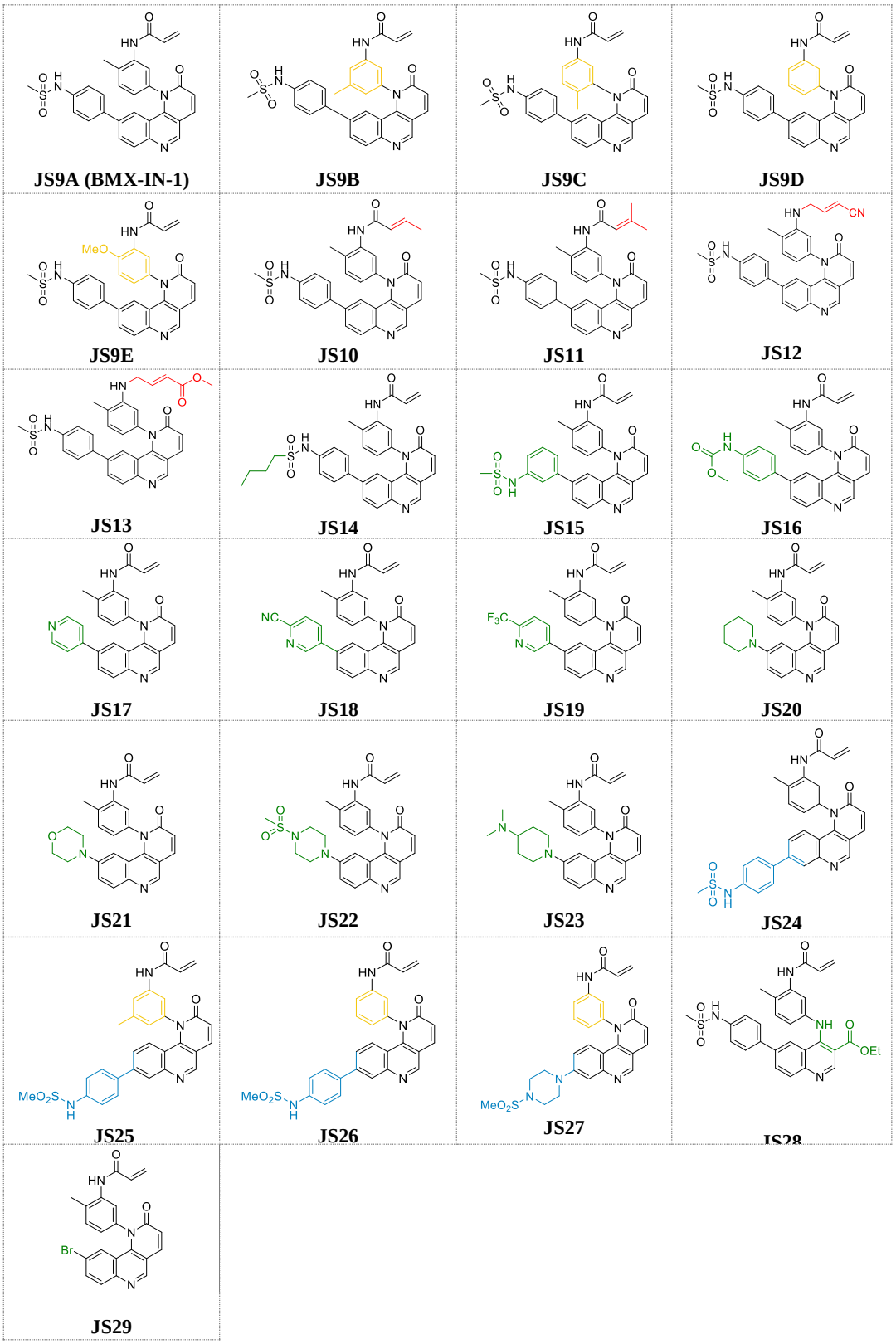

Fig. 2. 5. Structure of the 24 analogues prepared. The modified regions in each analogue are highlighted in red, yellow, green, and blue.

With this SAR information in hand, we decided to prepare **JS24–JS27** that were designed to include substituents at position R^4 of the quinoline and incorporated features from previous analogues that afforded a preferred overall profile, varying methyl positioning in R^2 and retaining the acrylamide electrophilic warhead for cysteine covalent binding. Compound **JS24**, which features a methyl sulfonamide at position 7, showed considerable gain of inhibition potency from IC_{50} 50 to 7.5 nM relative to the parent molecule **BMX-IN-1**. Further derivatives that presented changes in the aniline core (R^2) with a methyl in the meta position (**JS25**) and without any substituent in this position (**JS26**), but that featured the same methyl sulfonamide at R^4, were designed and prepared. Both compounds showed significantly improved activity **(**IC_{50} of 3.5 and 9.1 nM, respectively). Similarly, in **JS27** we installed a substituted piperazine in the R^4 position that affords less restraint relative to the aromatic phenyl-sulfonamide ring, but which renders it the least active analogue of the series (13.7 nM) albeit considerably more potent (~4-fold) relative to **BMX-IN-1**.

To date, all the reported BMX inhibitors also display the ability to inhibit BTK. To determine if our leads were also binders of BTK, we evaluated inhibitory capacity of our compounds against BTK. For the BTK IC_{50} assay, we selected **BMX-IN-1**, the two analogues with higher BMX inhibitory capacity: **JS24**, **JS25** and **JS27**. The results showed that all the leads are also potent BTK inhibitors, in the low nanomolar range **(Table 2. 2)**. The same inhibitory trend is observed with an increase of 62-, 33- and 15-fold potency gain with **JS25**, **JS24** and **JS27**, respectively, relative to **BMX-IN-1**.

2.3.2 JS25 is a selective TEC family inhibitor

To investigate in which targets the new BTKi could have an effect, we tested **JS25** against a panel of 36 kinases in the Eurofins DiscoverX's KINOMEscan® platform at a concentration of 1 μM. It is important to note that from the extensive number of accessible cysteine residues distributed across the whole kinome, not all are available for covalent modification.[195–197] BTK belongs to a restricted group that includes 10 other kinases that share an equivalently placed cysteine in the ATP binding pocket. This group comprises members from the TEC family (BMX, ITK, TXK and TEC), the EGFR family (EGFR, HER2, HER4), JAK3, BLK and MAP2K7. Therefore, we included the whole TEC, EGFR and JAK family in our screening, and the SRC family and LKB1, which also have a

cysteine within the same sequence alignment. We also included kinases involved in the signal cascades of TEC family kinases. The KINOMEscan® platform is a binding assay and the screening showed that **JS25** displays a strong binding affinity against all the members of TEC family that share an equivalently placed cysteine **(Table 2. 3)**.

Table 2. 2. Biochemical IC_{50} determination of compounds **JS9–29**.

BMX inhibition IC_{50} (nM)[a]				BTK inhibition IC_{50} (nM)[b]	
JS9A	360 ± 24	**JS18**	140 ± 12	**JS24**	11.1 ± 0.8
JS9B	240 ± 25	**JS19**	470 ± 179	**JS25**	5.8 ± 0.04
JS9C	6900 ± 2925	**JS20**	42 ± 13	**JS27**	24.3 ± 0.3
JS9D	59 ± 5.0	**JS21**	43 ± 5	**BMX-IN-1**	362 ± 2.4
JS9E	1300 ± 206	**JS22**	93.8 ± 0.87		
JS10	21000 ± 7250	**JS23**	41 ± 6		
JS11	n.d.	**JS24**	7.5 ± 0.4		
JS12	n.d.	**JS25**	3.5 ± 0.02		
JS13	n.d.	**JS26**	9.1 ± 0.3		
JS14	890 ± 27	**JS27**	13.7 ± 0.7		
JS15	118.7 ± 11.4	**JS28**	410 ± 35		
JS16	50 ± 62	**JS29**	44 ± 2		
JS17	45 ± 10	**BMX-IN-1**	50.2 ± 0.7		

n.d. - not determined; [a]average of triplicates, showing mean ± S.D.; [b]average of duplicates, showing mean ± S.D.

As stated above, the TEC family has high sequence similarity and in particular residues in the ATP binding kinase domain share 40–65% identity and 60–80% similarity. The ATP binding sites are also highly conserved between the TEC and SRC families with 14 identical residues out of 18 that comprise the ATP binding pocket. In fact, one of the key determinants of kinase selectivity – the gatekeeper residue – is a threonine in both the SRC family and the TEC family members, except ITK. **JS25** also binds BLK (and JAK3) whereas no affinity was observed with other potential targets. These results reveal **JS25** as a selective probe for TEC kinases and suggest that any cellular activity mediated by **JS25** is probably a result of inhibition of any of the TEC kinases rather than any off-target inhibition of upstream and downstream regulators.

Table 2. 3. Kinome selectivity of **JS25** over 36-related kinases in the KINOMEscan® platform. The results for primary screen binding interactions at 1 μM concentration are reported as % DMSO control.

Family	Target	% Ctrl	Family	Target	% Ctrl
TEC	BMX	1.3	SRC	FYN	99
	BTK	0		SRC	92
	ITK	4.7		YES1	85
	TEC	0.4		BLK	16
	TXK	3.4		FGR	93
EGFR	EGFR	87		LCK	80
	HER2	89		HCK	95
	HER3	91		LYN	100
	HER4	66	mTOR	mTOR	100
JAK	JAK1	93	LKB1	STK11	52
	JAK2	81	PKB	AKT1	100
	JAK3	21		AKT2	94
	TYK2	100		AKT3	99
FAK	PTK2	93	PAK1	PAK1	100
PI3K	PIK3CA	79	TAM	AXL	93
	PIK3CB	89		MERTK	89
	PIK3CG	64	ABL	ABL1-phosphorylated	100
	PIK3CD	100	PDPK1	PDPK1	92

2.3.3 JS25 presents a more favourable selectivity profile

Compound intracellular selectivity is a crucial factor to take into consideration in drug discovery, as in many cases, a lack of selectivity can translate into an increased toxicity in clinical trials.[198] To determine whether **JS25** is a selective binder, we evaluated its intracellular inhibitory capability against BTK, BMX, ITK, TXK, and TEC, and against other BTK pathway-related proteins (BLK, EGFR, HER2, and JAK3). The selectivity of **JS25** was measured using the NanoBRET™ technology and defined as IC_{50} kinase/IC_{50} BTK **(Table 2. 4)**. **JS25** showed an IC_{50} value of 28.5 nM against BTK, and the value for BMX was 49.0 nM, representing a ~2-fold increase in the selectivity towards BTK. Within the TEC family kinases, **JS25** presented a ~7-, ~8-, 15-, and 100-fold higher selectivity for

BTK, relative to TXK, TEC, ITK, and BLK, respectively. Importantly, the values of IC_{50} for EGFR, HER2, and JAK3 were higher than 3 μM. Overall, our data reveal that **JS25** is very selective for both BMX and BTK, but with lower reactivity for other proteins within the TEC family, as well as for other proteins in BTK's signalling pathways, possibly mitigating the chances for off-target effects in the clinical stages.

Table 2. 4. Kinome selectivity of **JS25** values obtained in the NanoBRET™-based assays.

Kinase	IC_{50} (M)[a]	Selectivity (kinase/BTK)
BTK	$2.85 \times 10^{-8} \pm 0.55$	1
BMX	$4.90 \times 10^{-8} \pm 0.40$	1.7
TXK	$1.90 \times 10^{-7} \pm 0.50$	6.7
TEC	$2.20 \times 10^{-7} \pm 0.30$	7.7
ITK	$4.40 \times 10^{-7} \pm 0.10$	15.4
BLK	$2.60 \times 10^{-6} \pm$ n.d.	104
EGFR	$> 3 \times 10^{-6}$	n.d.
HER2	$> 3 \times 10^{-6}$	n.d.
JAK3	$> 3 \times 10^{-6}$	n.d.

n.d. – not determined; [a]average of duplicates, showing mean ± S.D.

2.3.4 JS25 exhibits higher potency in inhibiting BTK compared to Ibrutinib, Acalabrutinib and BMX-IN-1

Covalent modification of BTK is a two-step process that covers the affinity of the initial non-covalent binding, K_I, and the rate of covalent bond formation, k_{inact}.[25] The rate of inactivation (k_{inact}/K_I) is a second-order event, which describes the efficacy of the covalent bond binding event. To characterise the covalent interactions of **JS25** with BTK, evaluation of the irreversible binding efficacy was performed as reported[25]. Additionally, we included **Ibrutinib**, **Acalabrutinib** and **BMX-IN-1**. The calculated kinetic parameters K_I, k_{inact}, *and* k_{inact}/K_I, are shown in **Table 2. 5**. The data demonstrated similar binding affinity between **JS25**, **Ibrutinib**, and **BMX-IN-1** for BTK, as indicated by their respective K_I values: 0.77 nM, 0.59 nM, and 1.29 nM. Out of the 4 compounds, **Acalabrutinib** presented the weakest binding affinity for BTK (K_I = 15.07 nM). Most importantly, the rate of covalent bond formation, K_{inact}, of **JS25** is 10-fold faster (0.401 min^{-1}), compared with **Ibrutinib** (0.041 min^{-1}), **Acalabrutinib** (0.038 min^{-1}), and **BMX-IN-1** (0.038 min^{-1}); consequently, **JS25** efficiently inactivated BTK with a k_{inact}/K_I of 8.72

μM $^{-1}s^{-1}$, displaying an increased rate of inactivation of approximately 8-fold relative to **Ibrutinib** (1.17 μM $^{-1}s^{-1}$), 200-fold relative to **Acalabrutinib** (0.04 μM $^{-1}s^{-1}$), and 18-fold relative to **BMX-IN-1** (0.49 μM $^{-1}s^{-1}$). The differences in kinetic properties between the tested compounds, highlight the variances in their specific binding modes, and suggest an improved complementarity of **JS25** with the target protein.

Table 2. 5. Comparison of the kinetic parameters.

Compound	K_I [nM]	k_{inact} [min^{-1}]	k_{inact}/K_I [μM $^{-1}s^{-1}$]
JS25	0.77 ± 0.06	0.401 ± 0.064	8.72 ± 1.02
Ibrutinib	0.59 ± 0.03	0.041 ± 0.004	1.17 ± 0.13[a]
Acalabrutinib	15.07 ± 0.51	0.038 ± 0.005	0.04 ± 0.01[b]
BMX-IN-1	1.29 ± 0.50	0.038 ± 0.008	0.49 ± 0.15[c]

[a]Value with a 0.17 deviation from published results[199]
[b]Value with a 0.002 deviation from published results[199]
[c]Value with a 0.29 deviation from published results[200]

2.3.5 Selectivity and inhibition is induced by hijacking M477, L408, and Y551

The putative 3D structure of **JS25** covalently bound to BTK was generated. *Autodock* 4.2 software was used to predict the region where **JS25** binds to BTK (noncovalent docking). The crystal structure of this protein, reported together with an inhibitor (PDB: 6TFP), was used for the docking studies. Interestingly, the best 10 docking poses in terms of binding affinity interact with BTK in the same region as other reported inhibitors[125] **(Fig. 2. 6, a)**. Detailed analysis of the different poses shows that pose #10 localises the Michael acceptor moiety near C481. Therefore, we covalently linked **JS25** with this 3D orientation to this cysteine residue of BTK and performed 0.5 μs MD simulations in explicit water **(Fig. 2. 6, b)**. The simulations show that the complex is stable due to the occurrence of hydrogen bonds and hydrophobic contacts between the ligand and the receptor. Hydrogen bonds are established between the oxygen atoms of the sulfonamide and the main chain of M477 (which occupies about 30% of the total trajectory time). Equally, the aromatic ring containing the sulfonamide group is engaged in a CH/π interaction with the sidechain of L408, which is maintained throughout the simulation time. We also analysed the dynamics of Y551, as BTK inhibitors can be classified according to their ability to trigger the 'sequestration' of this tyrosine residue. In cells, sequestration of Y551 was shown to render it inaccessible for phosphorylation[125]. According to our calculations, Y551 is sequestrated

around 60% of the whole trajectory (χ^1 torsional angle close to 180 degrees). To validate our simulation protocol, we performed MD simulations for the complex of BTK with **Ibrutinib (Fig. 2. 6, c)**, using the X-ray structure as the initial coordinates (PDB: 5P9J). As in the X-ray structure, the MD simulations show a hydrogen bond between the $–NH_2$ group of the ligand and the main chain of E475 (with a population of about 32%). As for the dynamics of Y551, our calculations showed that this residue is inaccessible about 72% of the time, which is consistent with the X-ray structure and experimental data.

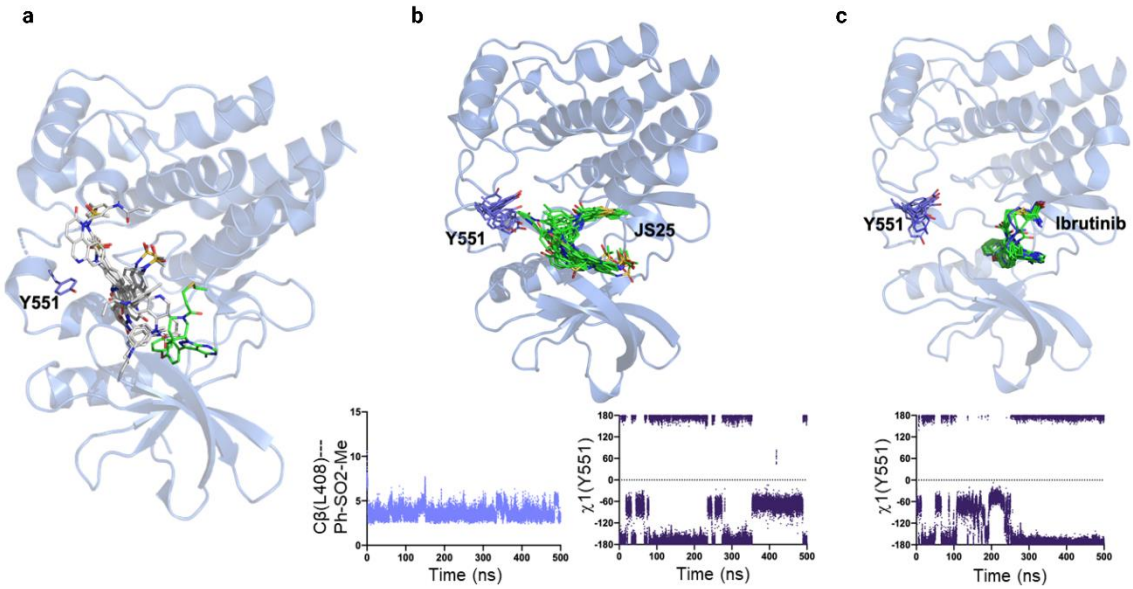

Fig. 2. 6. Putative structure of BTK covalently inhibited. (a) The energetically best poses for BTK as determined by docking calculations. (b) Overlay of 10 frames of BTK/**JS25** complex sampled from 0.5 μs MD simulations, together with the distance between sidechain of L408 and the aromatic ring (Ph-SO_2Me) of **JS25**, and the geometry of the sidechain (χ1 dihedral angle) of Y551 throughout MD simulations. (c) Overlay of 10 frames of BTK/**Ibrutinib** complex sampled from 0.5 μs MD simulations, together with geometry of the sidechain (χ1 dihedral angle) of Y551 through MD simulations. BTK is shown as blue ribbons and carbon atoms of the ligand and Y551 are shown in green and purple, respectively.

2.3.6 JS25 has a wide spectrum of activity in blood cancer cells

Having demonstrated **JS25** is a potent inhibitor of BTK in biochemical assays, we turned to its characterisation in standard cell lines of haematological cancers, related with an

abnormal expression of BTK, including BL, DLBCL, CLL, AML, and acute promyelocytic leukaemia (APML). **Acalabrutinib** and **Ibrutinib** were also included to validate the therapeutic relevance of **JS25** in these cell lines. The results presented in **Fig. 2. 7, a-f** show that **JS25** has a significant effect on viable cell growth in all the tested cells, and it has the capability to inhibit the proliferation with similar or greater potency than the clinically approved BTKi, **Acalabrutinib** and **Ibrutinib**. **JS25** presented a 15-fold greater efficacy than **Ibrutinib**, to inhibit the proliferation of Raji cells (BL), with an IC_{50} value of 2.3 µM. In DoHH-2 (DLBCL), Mo1043 (CLL), and MOLM-13 (AML) cell lines, there were no major improvements; however, in WA-C3CD5+ cells (CLL), the antiproliferative potency of **JS25** (3.5 µM) was approximately 7-fold greater than **Ibrutinib** (25.9 µM). In addition, **JS25** also presented a better efficacy than **Ibrutinib** in HL-60 cells (APML) with an IC_{50} value of 1.95 µM. Importantly, other non-B-cell lines (JURKAT, HEK293T, and HBEC-5i), were not as sensitive to the treatment **(Fig. 2. 7, g-i)**.

Degradation of BTK was also investigated by treating wild-type Raji cells with a 10 µM concentration of **JS25** and **Ibrutinib**. Western blot analysis showed that BTK degradation was evident at 4h of treatment, and it was almost completed at 15h **(Fig. 2. 7, j)**. These results validate **JS25** as a potential therapeutic candidate with applicability against haematological cancers and demonstrates its ability to inhibit both the catalytic activity and the expression of BTK in tumour cells.

2.3.7 JS25 effectively crosses the blood-brain-barrier

The permeability of **JS25** on the blood-brain-barrier (BBB) was evaluated using an *in vitro* HBEC-5i cell model. **Ibrutinib** and **Acalabrutinib** were included as controls. As shown in **Fig. 2. 8**, **JS25** and **Acalabrutinib** showed similar permeability to the BBB at 24h (28.5% and 29.2%, respectively). However, this was comparatively lower than the permeability of **Ibrutinib** (51.9%), due to higher retention rates of **JS25** and **Acalabrutinib** in the cells. Depending on the intracellular mechanism involved, a higher retention of the compound in the BBB could result in its degradation, or in a greater durability of the treatment. These findings suggest a potential avenue for the application of **JS25** in treating more aggressive forms of hematological cancers.

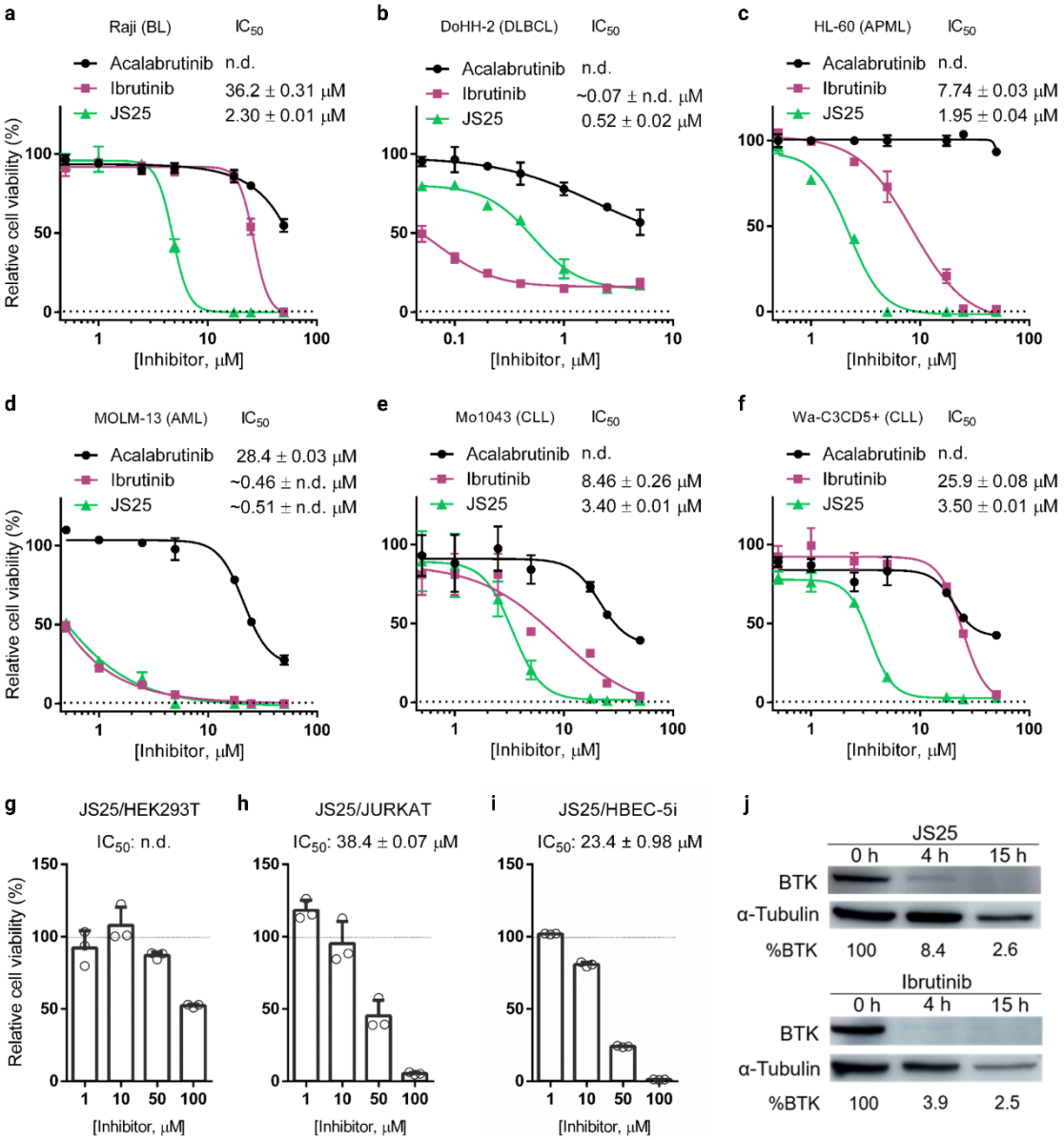

Fig. 2. 7. Cell viability assays. (a) Raji. (b) DoHH-2. (c) HL-60. (d) MOLM-13. (e) Mo1034. (f) WA-C3CD5+. (g) HEK293T. (h) JURKAT. (i) HBEC-5i. Cells were treated with serial doses of **Acalabrutinib**, **Ibrutinib**, and **JS25** for 72h. Error bars correspond to the standard deviation of the mean, n=3 technical replicates. (j) Degradation analysis of BTK after treating Raji cells with **JS25** and **Ibrutinib**.

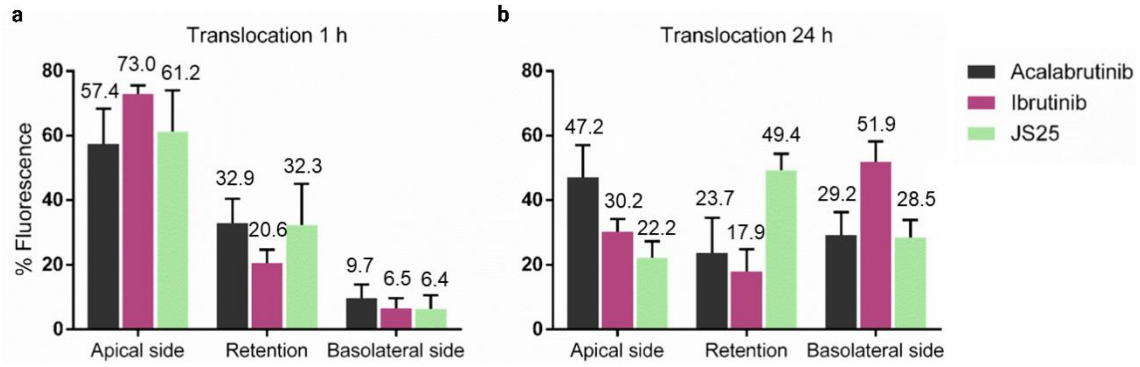

Fig. 2. 8. Translocation profile of different compounds (15 μM) at 1h (a) and 24h (b). Error bars correspond to the standard deviation of the mean, n=3 technical replicates.

2.3.8 JS25 has a superior therapeutic effect relative to Ibrutinib in a mice model of Burkitt's lymphoma

To further validate its therapeutic potency, **JS25** was examined in a mouse xenograft model inoculated subcutaneously with human lymphoma Raji cells (BL). This study comprised a vehicle control group, and three treatment groups, including one dose of **Ibrutinib** (10 mg/Kg), and two doses of **JS25** (10 and 20 mg/Kg). The compounds were administered through intraperitoneal injection once every two days for 14 days, and tumour sizes were measured periodically **(Fig. 2. 9, a)**. As shown in **Fig. 2. 9, b**, **JS25** caused significant reduction in the solid tumour sizes (around 30-40% in both dosages), while **Ibrutinib**–treated groups did not show significant changes relative to the control. Additionally, no weight fluctuations were observed by the end of the treatment **(Fig. 2. 9, c)**. Considering that drug dosing strongly influences the existing number of metastases, we sought out to determine the overall percentage in each experimental group **(Fig. 2. 9, d-f)**. Our quantitative analysis revealed that mice treated with **JS25** had a significant reduction in their secondary tumour formation (71-88%) **(Fig. 2. 9, d)**; however, only mice treated with the highest dose of **JS25** (20 mg/Kg), presented a significant lower percentage of metastases (70% reduction) **(Fig. 2. 9, e-f)**. For both **Ibrutinib** and **JS25** (10mg/Kg doses), the reduction was similar and around 30% **(Fig. 2. 9, e)**. Invasion of tumour cells was not observed in the heart and kidneys; and drug-induced necrosis of normal cells was also not observed. Our data shows **JS25** has potential therapeutic effect in this mouse xenograft model of BL, supported by the generalised reduction in the size of the primary tumours, and in the reduction of secondary tumours and metastasis.

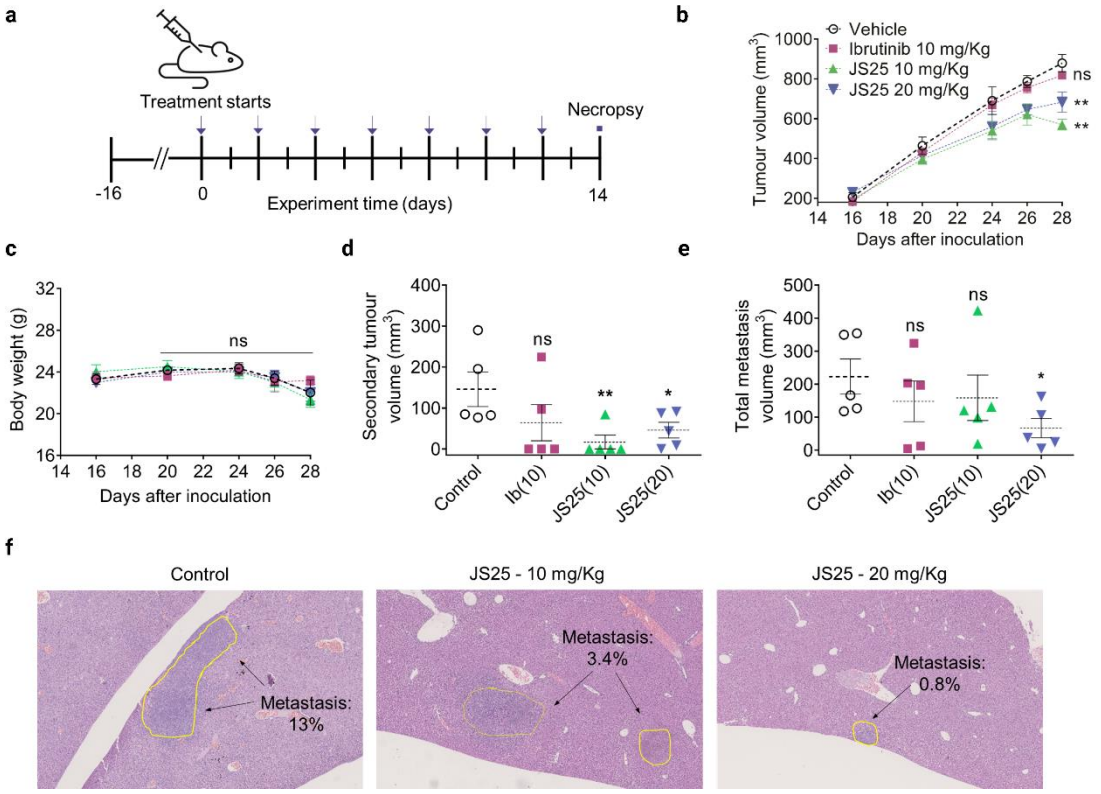

Fig. 2. 9. JS25 treatment inhibits tumour growth of Burkitt's lymphoma. (a) Schematic representation of the *in vivo* assay. Blue arrows indicate days of treatment. (b) Tumour size and (c) body weight were monitored periodically. (d, e) Quantification and analysis of the metastases and tumour formation observed (n = 5/group), (b, $**p = 0.0018$ and 0.0090, d, $**p = 0.0086$, $*p = 0.0418$, e, $*p = 0.0386$). Statistical analysis was conducted by one-way ANOVA, followed by Dunnett's test for significance: not significant (ns) $p > 0.05$; $*p < 0.05$ (*); $**p < 0.01$. (f) Example of neoplastic cells observed in the liver of the control and **JS25**-treated groups.

2.3.9 JS25 demonstrates selective on target activity in patient samples of diffuse large B-cell lymphoma

On the basis of its kinetic and cytotoxic efficiency, we tested the ability of **JS25** to induce targeted cell cytotoxicity on viable DLBCL tumour tissues, by collecting lymph node samples from patients with the pathology **(Fig. 2. 10, a)**. Solid tissues were dissociated, cells were treated with **JS25** and **Ibrutinib**, then fixed and permeabilised, and the resulting monolayers were stained with fluorescent antibodies against surface markers: CD19 (clone

HIB19), CD20 (clone L27), and CD79a (clone HM47), along with DAPI. Imaging of the primary cell monolayer was carried out and the viability and identity (cancer *versus* non-cancer) of individual cells evaluated using deep learning driven image analysis. The on-target cytotoxicity was identified by calculation of the DRS, which has been shown to correlate with the clinical response for late-stage haematological cancer patients. This score is measured by dividing the fraction of live cancer cells under treatment[201] by the fraction of live cancer cells of total cells under controls, averaging across multiple concentrations. As shown in **Fig. 2. 10, c**, **JS25** had on-target effect in 7 out of 11 patients (~64%), and in 4 patients the "killing" was off-target or non-specific (~36%). **Ibrutinib** presented an on-target toxicity in 5 out of 10 patients (50%) **(Fig. 2. 10, b)**. Overall, **JS25** presented a greater pharmacologic effect at the target of interest than **Ibrutinib**, supported by the number of samples that were more sensitive to the treatment with **JS25**.

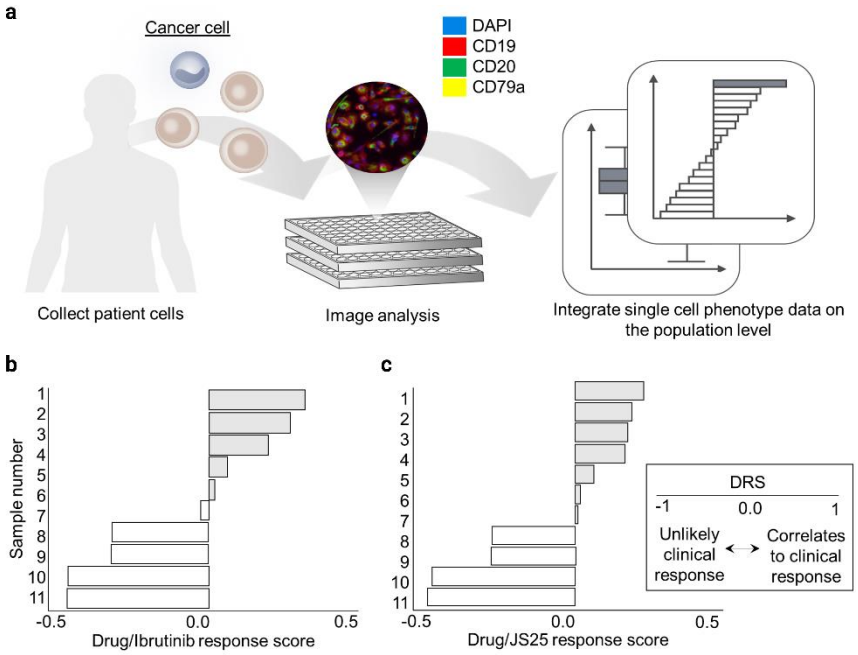

Fig. 2. 10. Patient-derived model of DLBCL. (a) Schematic representation of the *ex vivo* experiment. (b) **Ibrutinib** and (c) **JS25**/drug response score (DRS) calculated as 1-mean of the RCF. Each concentration point for each sample was performed in 4 replicates, at 72h hour incubation time point. Grey indicates a DRS > 0, white indicates DRS < 0. DRS scores > 0 indicates on-target cytotoxic response, < 0 indicates general cytotoxicity or off-target cytotoxic response.

2.3.10 JS25 is more effective than Ibrutinib in patient-derived model of chronic lymphocytic leukaemia

To evaluate the efficacy of **JS25** in CLL patient samples, PBMCs were collected and used to generate zebrafish patient-derived xenografts (zPDX). Here we compared **JS25**'s efficacy with **Ibrutinib**, and **Venetoclax** was also included as a positive control. **Venetoclax** is a BH3-mimetic BCL-2 inhibitor that induces significant cell death[202], and it is highly efficient for treating CLL; however, the rapid onset of apoptosis often leads to tumour lysis syndrome complications.[203] In contrast, **Ibrutinib** has a different dynamics, and therefore is less prone to induce tumour lysis syndrome.[204] CLL zPDXs with tumour cells in circulation were randomly distributed into four conditions immediately following injection: DMSO (control), **Ibrutinib** (Ib), **JS25** and **Venetoclax** (VTX). After 48h of treatment, all zPDXs were fixed and analysed by confocal microscopy to evaluate tumour burden and incidence **(Fig. 2. 11)**. Tumour incidence is the percentage of zPDXs with tumours by the end of the assay, while tumour burden is the area occupied by PBMCs from the cloaca region until the end of the tail **(Fig. 2. 12, a-a')**. In 2 out of the 3 CLL-zPDX, **JS25** was more efficient than **Ibrutinib** in reducing CLL disease burden **(Fig. 2. 12, b-m)**. In the CLL zPDX(2) (del17p+), **JS25** treatment led to a reduction of the tumour burden of 45% when compared to **Ibrutinib (Fig. 2. 12, f-i, and Fig. 2. 13, c-d)**, whereas in CLL zPDX(3), **JS25** reduces the incidence of zPDXs with tumours in 27% relative to **Ibrutinib** and 25% in relation to DMSO controls and a tendency to reduce tumour burden **(Fig. 2. 12, j-m, and Fig. 2. 13, e-f)**. In all the zPDXs, **Venetoclax** has a major impact on tumour incidence and burden, being able to induce a massive cell death of all CLL cells within 48h **(Fig. 2. 12)**, which is in accordance with the fast CLL cells killing effect observed in patients. Altogether, our results suggest that **JS25** has a higher therapeutic impact in CLL, being faster and more effective than its counterpart **Ibrutinib**.

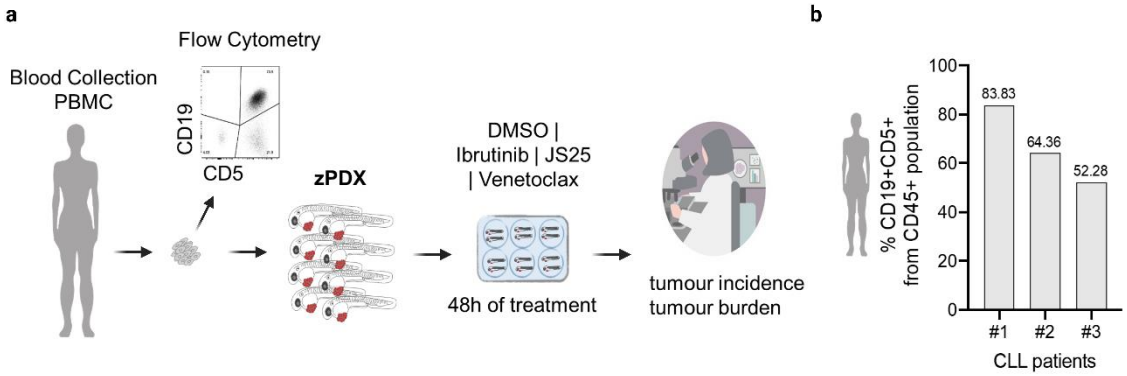

Fig. 2. 11. Zebrafish patient-derived model of CLL. (a) Representative scheme of the zPDX assay. (b) Percentage of CD19+CD5+ cells within CD45+ population from PBMCs of each CLL patient.

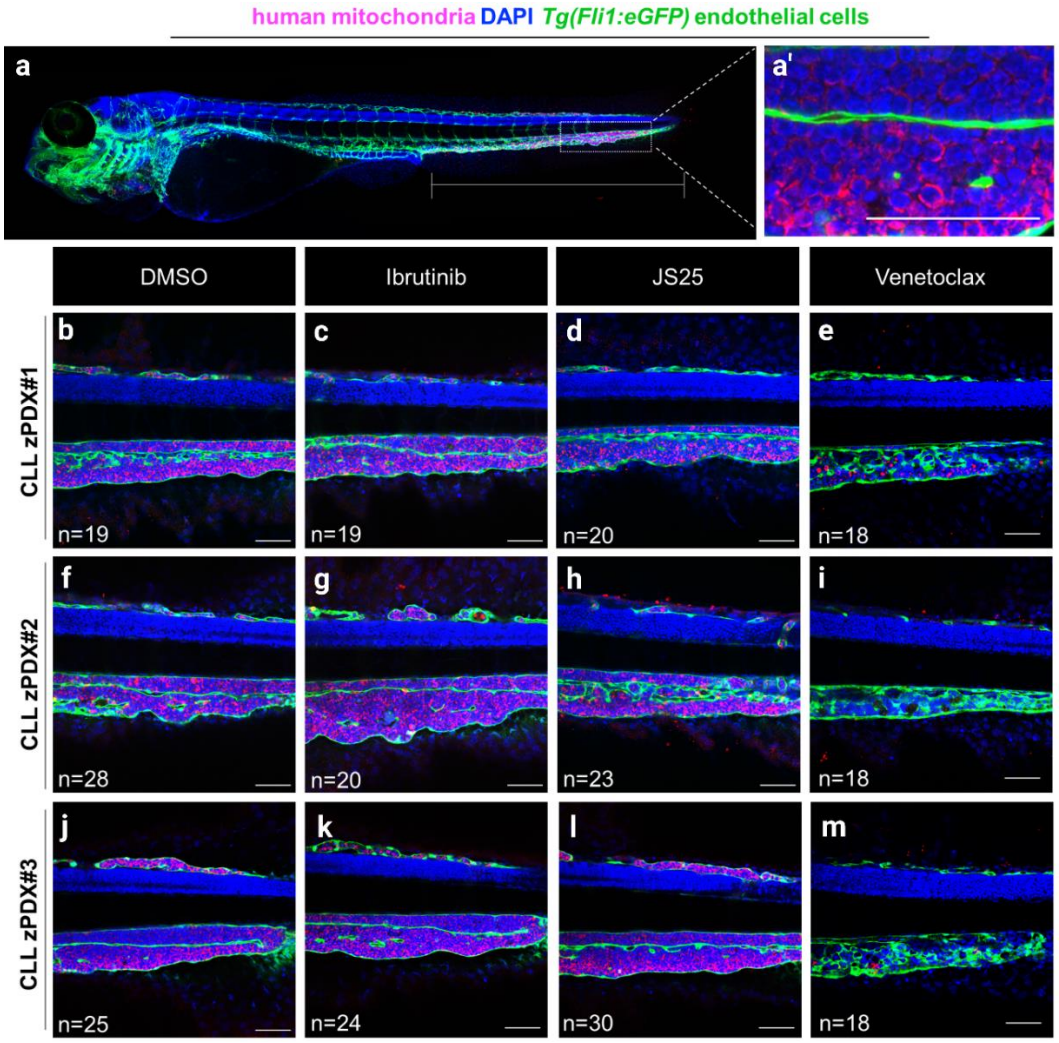

Fig. 2. 12. Therapeutic effects of BTKi in zebrafish patient-derived xenografts of CLL. (a-a') Representative zPDX confocal image on where the therapeutic effects of the different compounds were analysed. (b-m) Representative confocal images for each zPDX. Scale bar represents 50 μm.

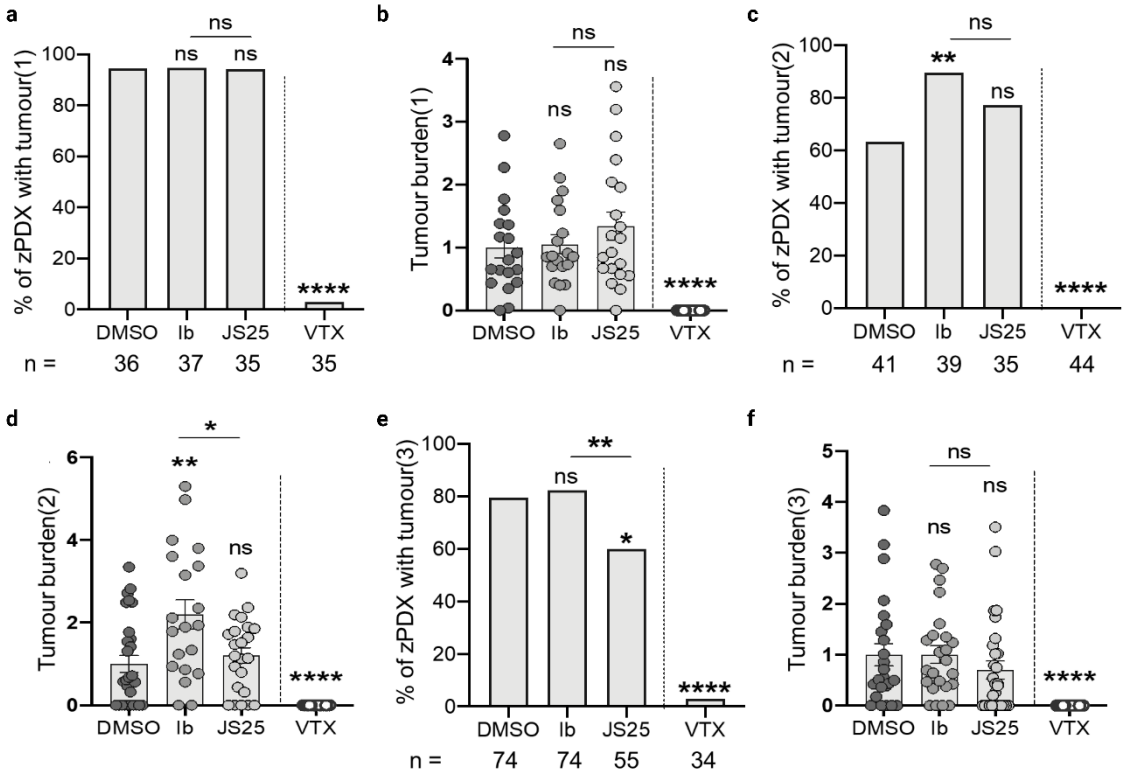

Fig. 2. 13. Analysis of the anti-tumour activity of BTKi in zebrafish patient-derived xenografts of CLL. Percentage of zPDXs with tumour (a, ****$p < 0.0001$, c, **$p = 0.0080$, ****$p < 0.0001$, e, *$p = 0.0183$, **$p = 0.0054$, ****$p < 0.0001$) and tumour burden (b, ****$p < 0.0001$, d, *$p = 0.0188$, **$p = 0.0045$, ****$p < 0.0001$, f, ****$p < 0.0001$). The outcomes are expressed as mean (a, c, and e) and mean ± SEM (b, d, f). Data are from one independent experiment and the number of xenografts analysed for tumour burden is indicated in the representative images. The number of total zPDXs analysed at the end of the assay is indicated below the respective charts. Each dot represents one zebrafish xenograft. Statistical analysis was performed using Fisher's exact test (tumour incidence) and an unpaired t-test (tumour burden). Statistical results: ns > 0.05, *$p \leq 0.05$, **$p \leq 0.01$, ***$p \leq 0.001$, and ****$p \leq 0.0001$.

2.4 Discussion

Selective inhibition of Bruton's tyrosine kinase is as a promising therapy for multiple haematological cancers and autoimmune diseases. The first-in-class BTK inhibitor,

Ibrutinib, has shown durable clinical responses, but its clinical efficacy has been limited by off-target effects and the development of resistance. This prompted the development of second-generation BTKi with improved therapeutic effects. In this context, we report the discovery of a new inhibitor, **JS25**, a covalent small molecule with high potency and selectivity for BTK.

We first explored a chemical scaffold that contains an archetypal tricyclic core of a quinoline with a fused pyridinone, which is present in the covalent inhibitor **BMX-IN-1**. We sought to introduce a chemical handle that may be used for further derivatization whilst simultaneously tuning the physicochemical properties. We found that rational modification introduced at the position 7 of the quinoline moiety leads to potent, single-digit nanomolar inhibition of BMX and BTK. We characterised the covalent modification of BTK of the most potent compound **JS25** using kinetic analysis. An improvement in the covalent binding efficiency of **JS25** to BTK was observed when compared to **Ibrutinib**, **Acalabrutinib**, and **BMX-IN-1**, with an increase of ~8-200 fold in the rate of protein inactivation ($8.72 \pm 1.02\ \mu M^{-1}s^{-1}$). The mechanism of target-specific covalent inhibition is governed by an initial non-covalently binding event that places the reactive electrophile close to the specific nucleophile on the target protein.[25] The success of this initial fitting dictates the rate of covalent bond-formation. Therefore, inhibitors' structural variations can affect covalent bond formation and consequent target inhibition, as observed in this study. Moreover, the combined effect of a higher potency and faster rate of covalent bond formation seen with **JS25**, can directly translate into less compound required to achieve the same pharmacologic effect and therefore reducing the probability of side effects.[205]

Our MD simulation studies of BTK covalently linked to **JS25**, demonstrated Y551 is sequestrated around 60% of the whole trajectory, possibly rendering BTK inaccessible for phosphorylation and causing its inactivation. Consistently, inactivation of BTK is usually achieved through blocking of Y551 phosphorylation within the SH1 domain by SRC kinases, consequently hindering autophosphorylation of Y223.[206] Many BTKi, both covalent and non-covalent, act directly within the SH1 domain, thereby interfering with cell survival and proliferation.

JS25 is also a dual inhibitor of BMX and BTK, and presented a lower reactivity for TEC, ITK, and TXK, and non-reactivity towards EGFR, BLK, JAK3, and HER2. Additionally, we showed that **JS25** does not react with other SRC kinases. When comparing **JS25** selectivity profile with other BTKi, **JS25** is less reactive than **Ibrutinib**

for TEC, TXK, ITK, EGFR, JAK3, BLK, and HER2; less reactive for TEC and TXK than **Acalabrutinib**; less reactive towards EGFR, JAK3 and HER2 than **Zanubrutinib**; and less reactive towards TEC, TXK and BLK than **Tirabrutinib**, although slightly more reactive against ITK. The BTKi **Acalabrutinib**, **Zanubrutinib**, and **Tirabrutinib**, are second-generation inhibitors, and relatively to **Ibrutinib**, these molecules have fewer off-target effects in early clinical trials. Dermatitis is a known adverse side effect attributed to **Ibrutinib**'s off-targeting of EGFR[207]; and bleeding is attributed to the off-targeting of TEC protein, although a recent study suggested it may be caused by inhibition of SRC (*e.g.*, BLK)[119]. In clinical studies, patients treated with BTKi that have no off-target effect for TEC kinase (*e.g.,* **Branebrutinib, Evobrutinib and Fenebrutinib**)**,** reported less or no bleeding events.[208] For this reason, it is desirable that newly developed BTKi, such as **JS25**, have a higher selectivity for BTK and a lower reactivity towards this particular group of kinases, as shown in this study. Overall, **JS25** off-target profile suggests a more favourable therapeutic index in comparison to other BTKi. However, some clarification within clinical context is required to understand whether the **JS25** selectivity profile will translate into a higher efficacy and safety, particularly in combinatorial regimens with other drugs.

In a cellular context, **JS25** presented a wide spectrum of activity against several myeloid/lymphoid B-cell cancers dependent on BTK expression. In addition to inducing degradation of BTK, **JS25** effectively crosses the BBB, but with higher retention rates than **Ibrutinib**. However, this does not devaluate the therapeutic potential of **JS25** in brain cancers, since higher retention rates can result in longer pharmacological effects, depending on the intracellular metabolism involved. Besides, clinical treatment with **Acalabrutinib** (which showed a similar retention rate to **JS25**), did not affect the quality of the response to MCL-cells infiltration in the brain.[176]

As a proof of concept of the therapeutic potential, mice with BL were treated with **JS25** and presented a reduction of 30-40% in the size of their solid tumours, and an overall reduction in metastasis and secondary tumour formation, relative to **Ibrutinib**. The percentage of metastatic cells present in the liver, lungs, brain/meninges, and spinal cord/bone marrow, was similar between treated groups (30% reduction), although lower with a higher **JS25** dosage (70% reduction). Naturally, a variety of factors can impact **JS25**'s distribution throughout the body and even decrease its availability in specific organs.[205] Thus, within these conditions, a higher drug dosage was more impactful in

impairing tumour spread and growth in the mice. Nevertheless, in consistency with the *in vitro* experiments performed here, treatment-induced cell death was significantly more pronounced with **JS25**. Additionally, no weight fluctuations were observed by the end of the treatment, even at the highest dose (20 mg/Kg), suggesting a safe and tolerable profile for **JS25** in animal models, within the doses tested.

The drug response score of **JS25**, in a DLBCL patient-model, was slightly higher than **Ibrutinib**, proven by the overall increased cell death, leading to a 64% on-target efficacy. Although the efficacy of BTKi in DLBCL has been shown, patient prognosis is still poor, and several inhibitors are still struggling for indications expansion.[119] Several genetic variations are in the basis of cellular resistance to **Ibrutinib** in B-cell cancers such as DLBCL.[193] Mutations that lead to acquired resistance to **JS25** are still unknown and will be important when evaluating its effectiveness and safety in the clinical stages. Nonetheless, comprehensive drug responsive profiles such as those generated here, directly translate the clinical outcome of **JS25** efficacy, thus being a useful route to understand its potential relevance in the clinic.

In zebrafish patient-model of CLL, in 2 out of 3 zPDXs, **JS25** was more effective and/or faster than **Ibrutinib**, reducing tumour incidence and tumour burden, thus suggesting a competitive potential of **JS25** over **Ibrutinib** as a promising anti-cancer therapy. CLL is a heterogeneous oncological disease of mature B-cells, in which BTKi are largely prescribed both as first-line and relapse therapy.[209] The responses to the currently clinically approved therapies are diverse and commonly lead to a pathological partial response with incomplete management of the symptoms.[210,211] Therefore, there is an unmet need to develop more effective and faster BTKi that produce higher anti-tumoral responses.

2.5 Outlook

Small covalent inhibitors, when combined with prolonged inhibition and high selectivity to the target protein, are a promising tool for the treatment of various diseases, including cancer and autoimmune disorders. Among these inhibitors, **JS25**, a novel covalent inhibitor of BTK, has shown significant potential in preclinical studies. The ability of **JS25** to bind covalently to BTK at C481, a key amino acid residue, provides prolonged inhibition and high selectivity to the target protein. Moreover, the efficacy of **JS25** binding

was showed to be more efficient than other BTKi in the market. Measurement of selectivity-IC_{50} values, showed an improved selectivity pattern against EGFR and TEC kinases, compared to **Ibrutinib** and the second-generation inhibitors, **Acalabrutinib**, **Tirabrutinib**, and **Zanubrutinib**. **JS25** also presented a broad spectrum of activity in myeloid and lymphoid B-cell cancers, and demonstrated improved therapeutic efficacy against **Ibrutinib**, in patient-derived DLBCL and CLL models, as well as in xenograft models of BL, making it a promising drug candidate for clinical use. One of the most significant findings in the preclinical studies of **JS25** is its ability to cross the blood-brain barrier, which indicates its potential to treat primary or metastatic forms of blood cancers in the brain. Taken together, the results of these preclinical studies establish **JS25** as a promising candidate for clinical use, and we envisage its clinical application against haematological cancers and other B-cell malignancies where patients may benefit from BTK inhibition, such as in autoimmune diseases.

3

Rationally designed PROTACs to target APTs

Disclosures

The author declares the following:

Synthesis and chemoproteomic analysis of the compounds presented in this chapter were performed with the help of Dr Luís Miguel Afonso Carvalho from the University of Cambridge, UK.

Putative structures of APTs in complex with PROTAC and CRBN were predicted with the help of Dr Daniel Zaidman from the University of Cambridge, UK.

3. Rationally designed PROTACs to target APTs

3.1 Introduction

Acyl-protein thioesterases 1 and 2 (APT1 and APT2), are crucial in regulating protein S-acylation, a reversible post-translational modification that controls protein recruitment to membranes. Dysregulation of APT1 and APT2 is implicated in the development of several diseases, including cancer and neurodegenerative disorders.[212,213] Although PROTACs have shown therapeutic potential in many diseases, the development of these molecules is accompanied by various challenges, and their potential against serine hydrolases has remained mostly underexplored.[214] The combination of computational and biochemical platforms can help accelerate the identification of novel PROTACs that exhibit enhanced efficacy and selectivity against desirable targets.

In this section we will cover the role of acyl-protein thioesterases and how computational and biochemical platforms can assist in designing and optimizing PROTACs for their degradation.

3.1.1 Pathophysiological roles and structure

S-Palmitoylation is a post-translational modification that directs the membrane localization and trafficking of a wide range of cellular proteins.[215] This process involves a coordinated palmitoylation cycle that relies on the action of both protein acyl transferases (PATs) and APTs to redistribute S-palmitoylated proteins across different cellular membrane compartments.[215] APT enzymes are responsible for removing palmitoyl modifications on cysteine residues of proteins, leading to redistribution of the substrate **(Fig. 3. 1)**.[216,217] In particular, APT2 interacts with membranes by deforming the lipid bilayer, extracting the acyl chain, capturing it in a hydrophobic pocket, and allowing for hydrolysis and subsequent substrate removal.[218] Although the function of APTs remains poorly understood, APTs have been found to be conserved individually across all vertebrates, suggesting distinct functional roles for each enzyme.[215] APT1 is a member of the α/β-hydrolase family of serine hydrolases encoded by the LYPLA1 gene.[219] Its crystal

structure reveals the presence of the catalytic triad S199-H209-D174, a unique feature of α/β-hydrolases, and essential for its enzymatic activity.[220] Originally identified as a lysophospholipase[221], APT1 was later recognized as a thioesterase[222]. *In vitro* studies demonstrate that APT1 can depalmitoylate various proteins, including Gsα, RGS, HRAS[217], eNOS[223], and SNAP-23[224]. APT1 also deacylates the G-protein of vesicular stomatitis virus (VSV), HEF and hemagglutinin proteins of influenza virus, and the E2 glycoprotein of Semliki Forest virus (SFV), but not the E1 glycoprotein of SFV, indicating its substrate specificity.[225] APT1 is expressed in neuronal dendrites at the mRNA level and regulates dendritic spine size in hippocampal neurons.[226,227] Knockdown or inhibition of APT1 decreases dendritic spine volume.[226] APT2, encoded by the LYPLA2 gene, was first discovered in mouse embryos and described as a lysophospholipase.[228] It shares 67.7% amino acid sequence identity with APT1 and contains a similar catalytic triad, S122-H210-D176.[228] Overexpression of APT2, but not APT1, leads to rapid depalmitoylation of GAP-43, indicating the substrate specificity of APT2.[216]

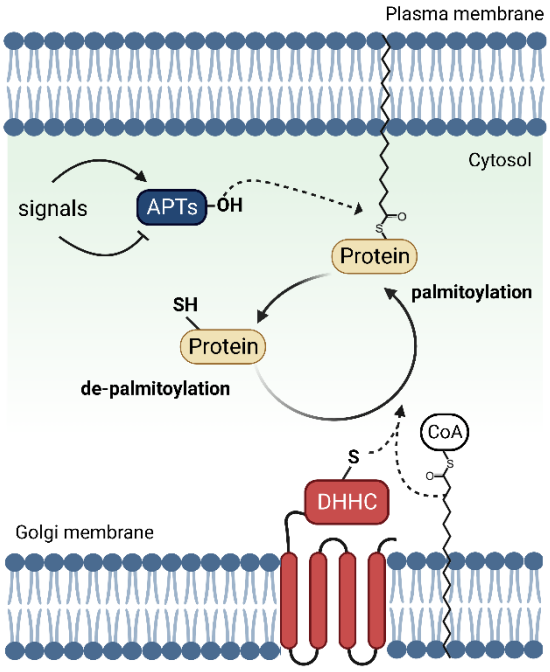

Fig. 3. 1. APTs as probes of dynamic S-palmitoylation. Palmitoylated cysteine residues are hydrolysed by APTs in response to specific stimuli. This hydrolysis process leads to de-palmitoylation of the protein, enabling it to detach from the plasma membrane and move to the cytosol. The protein can then undergo re-palmitoylation by DHHC palmitoyl transferases that are present in the Golgi membrane, transported back to the plasma membrane, and then re-establish associations with signalling partners (adapted).[229]

In oncology, APTs are described as important regulators of the palmitoylation cycle of the oncogene Ras – critical for its trafficking and oncogenic signalling[230,231] – although one study has pointed to other enzymes being involved in this process.[232] Moreover, both APT1 and APT2 have shown to promote tumour growth and metastasis of melanoma cells.[233] Suppressing their activity has proven effective in decreasing cancer cell proliferation and survival, as well as impeding the migration and invasion of cancer cells in both *in vitro* and *in vivo* settings.[234,235] Additionally, APTs have been shown to regulate apoptosis mediated by CD95 in primary chronic lymphocytic leukemia cells.[227] These enzymes were found to promote depalmitoylation of CD95 by directly interacting with it, resulting in impaired CD95-mediated apoptosis. Specific downregulation or inhibition of APTs reversed this impairment.[227] In neurodegenerative disorders, APTs were identified as regulators of the palmitoylation of disease-associated proteins.[213,236] In a murine model of Huntington's disease, APT1 inhibition (which prevents removal of palmitoyl modifications) has been shown to increase brain palmitoylation, restoring axonal transport, synapse homeostasis, and survival signalling to wild-type levels without toxicity.[213]

3.1.2 Selective inhibition and degradation

Selective inhibitors for APTs have been developed that target their hydrophobic substrate pocket, the catalytic serine, or both, and have shown promising results in preclinical studies.[215,231,237] Palmostatin B and M were the first probes found to effectively target APTs in cells. Specifically, palmostatin B is a selective inhibitor of APT1, whereas palmostatin M has been shown to target both APT1 and APT2 **(Fig. 3. 2)**.[237] Optimization of a potent triazole urea inhibitor, resulted in the discovery of a dual APT1/APT2 inhibitor ML211, and of two reversible compounds ML348 and ML349 that act as selective inhibitors for APT1 and APT2, respectively **(Fig. 3. 2)**.[215,238] Inhibitors of APTs have been widely used to monitor the biological effects associated with the inhibition of APTs in cells and to extrapolate the biological functions of these proteins.[215,227,231,237,238] In their latest work, Seneviratne and colleagues selectively degraded APT-2 against a panel of ~40 serine hydrolases using degraders composed of fluorophosphonate-based warheads and pomalidomide (*e.g.*, **FP-PROTAC**), which act via a CRBN-mediated mechanism **(Fig. 3. 2)**.[229] It is important to note that achieving selectivity against APT-1 or APT-2 is challenging due to their high sequence similarity.

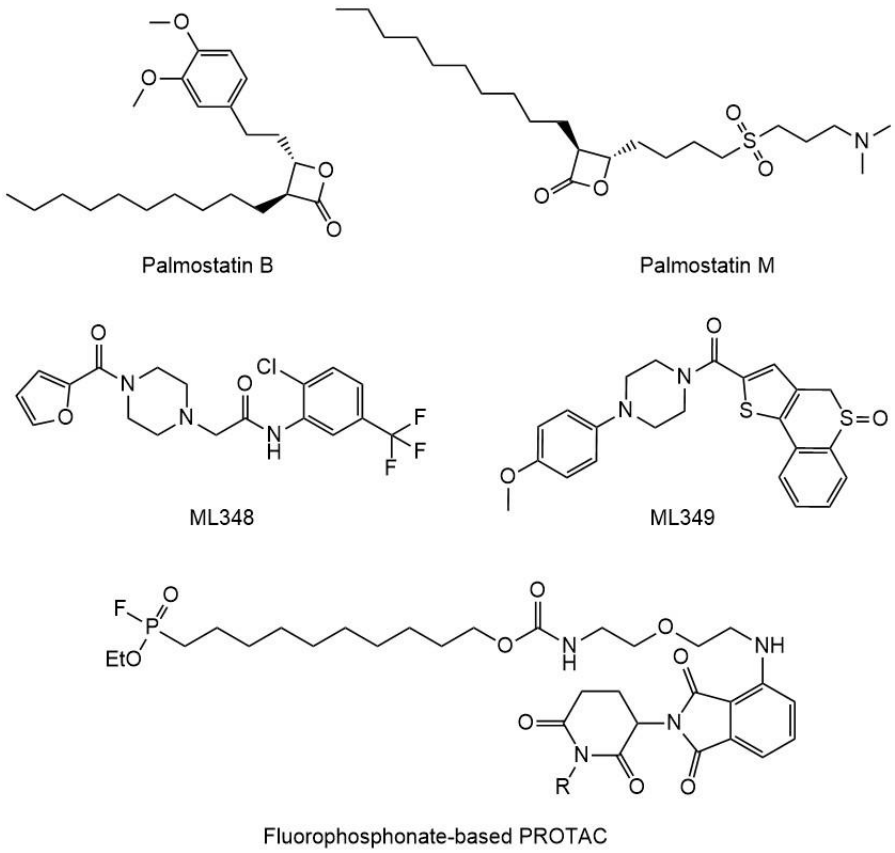

Fig. 3. 2. Chemical structures of selective inhibitors and degraders for APT1 or APT2.

3.1.3 Biochemical tools: Activity-based protein profiling

Developing drugs is a complex process that entails thorough characterization and precise fine-tuning of a drug's efficacy and selectivity towards a desired target. To tackle these hurdles, biochemical and proteomic approaches have been introduced to aid in profiling targets within complex proteomes.[93,239] Within this field, activity-based protein profiling (ABPP) surges an invaluable tool to study protein functions, as it enables researchers to rapidly record changes in enzyme activity directly in native biological systems.[93] Changes in the enzyme activity are directly monitored by ABPP using small-molecule probes.[239] These chemical probes are designed to bind and covalently label a specific subset or family of catalytically related enzymes at their active sites, and consist of two components: a reactive group that is directed towards the active site of the enzyme; and a reporter tag, such as a fluorophore or biotin, for detection, quantification, and/or enrichment/identification of labelled enzymes.[239–241] The selectivity of ABPP probes for

active enzymes allows for monitoring of changes in enzyme activities resulting from post-translational modification and/or protein-protein/protein-small molecule interactions without corresponding changes in protein abundance or mRNA expression, as inactive forms of the enzyme are not labelled by the probes.[239]

To conduct competitive ABPP, a native proteome is incubated with a small molecule and then labelled with a fluorescent probe.[93,242] The proteins are separated by SDS-PAGE, and the fluorescence intensity of probe-labelled enzymes is quantified relative to a control proteome, which is known as gel-based competitive ABPP.[242] For protein identification, a complementary mass spectrometry-based platform may be introduced.[243] However, it requires more time, larger amounts of samples compared to gel-based ABPP assays, and more advanced equipment, thus it is usually reserved for more detailed analysis of lead inhibitors.[93] Regardless of whether gel-based or mass spectrometry-based format is used, competitive ABPP has the benefit of enabling optimization of the potency and selectivity of inhibitors in a cellular environment, without the need for protein purification **(Fig. 3. 3)**.[93] Several types of ABPP probes are used to study serine hydrolase activity. These include fluorophosphonate (FP)-based probes, which covalently label the active site of serine hydrolases; and clickable ones such as desthiobiotin-FP probes, which can be used to isolate and identify labelled serine hydrolases by affinity purification.[243,244]

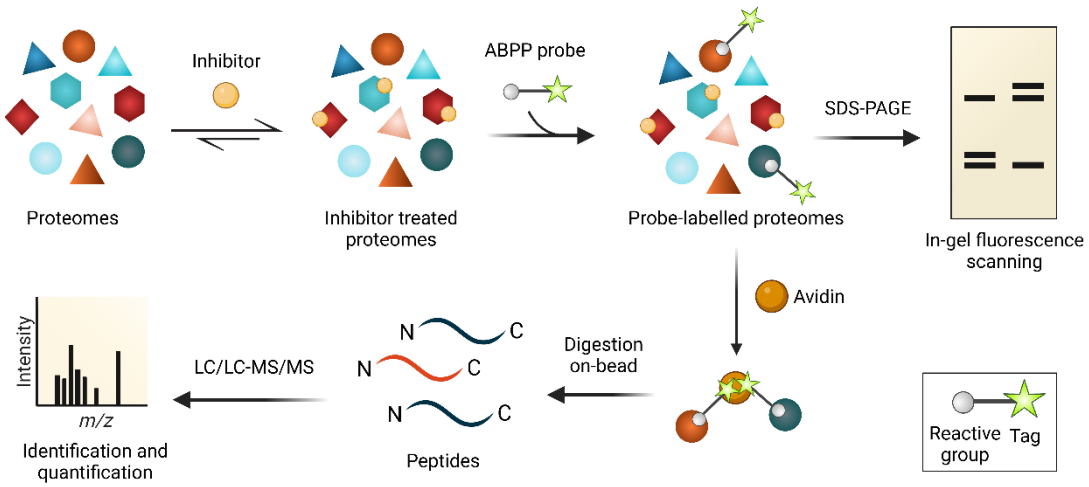

Fig. 3. 3. Competitive activity-based approach for the discovery of inhibitors for serine hydrolases (adapted).[93]

ABPP has been used to investigate the activity of serine hydrolases involved in the metabolism of small molecules such as fatty acids and cholesterol, leading to the discovery

of novel substrates and regulatory mechanisms.[245,246] Furthermore, ABPP studies can help investigate the effects of mutations on the activity of serine hydrolases, by elucidating how changes in the amino acid sequence of an enzyme can alter its activity and its role in the cell.[93] In drug discovery, the application of ABPP can prove advantageous in identifying novel therapeutic targets and producing compounds that are more selective and effective than traditional drugs.[93] Overall, ABPP is an important tool for studying serine hydrolases and has numerous applications in drug discovery and understanding biological processes.[93]

3.1.4 Computational tools: PRosettaC

Despite the growing popularity of PROTACs, a significant amount of empirical screening and optimization is often required to identify a suitable POI:PROTAC:E3 triad and to optimize linker composition and length, to ultimately achieve successful protein degradation.[47,247] The ability to model such ternary complexes through Rosetta-based protocol (PRosettaC) could aid in the design of more potent PROTACs, significantly reducing the number of linker designs required for efficient degradation and rationalizing the structure-activity relationship of existing PROTAC series **(Fig. 3. 4)**.[47,247]

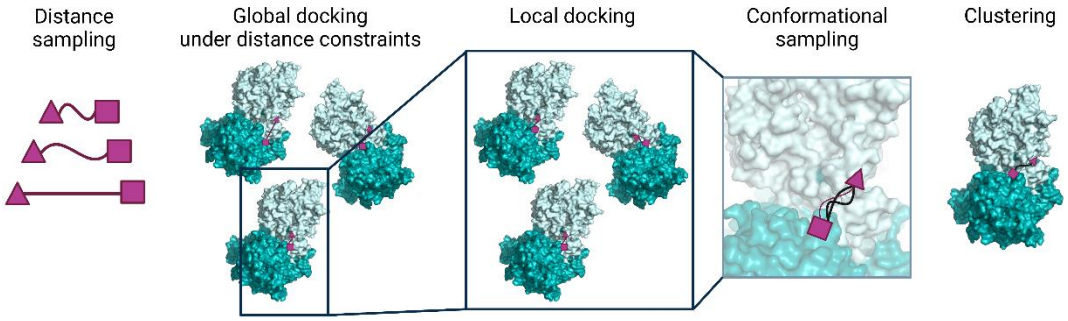

Fig. 3. 4. An overview of the PRosettaC protocol. The protocol consists of the following consecutive steps: (1) sampling of the distance between the two ligand anchor points; (2) constrained global protein–protein docking with PatchDock; (3) local docking with RosettaDock; (4) generating constrained PROTAC conformations compatible with the local docking solutions; (5) clustering of the top scoring results (adapted).[47]

The PRosettaC software is a computational platform that can help in the discovery and optimization of PROTACs.[47] The software is designed to predict the ternary structure of

POI:PROTAC:E3 pairing, as well as the likely efficacy of a given PROTAC to induce ternary complex formation. PRosettaC can also help to identify potential problems or limitations with a given design. This includes issues with linker length or flexibility, as well as potential clashes or steric hindrances that could interfere with the binding of the PROTAC to its target.[47] This computational platform has been successfully employed for modelling and predicting protein structures and interactions in various proteins, with the ability to recover published structures of ternary complexes to near atomic resolution and recapitulate experimental trends for two model systems with high accuracy.[47] Indeed, PRosettaC has been successfully applied in the design of degraders for the blood-cancer related protein BTK[47], and the cell apoptotic-regulator proteins BCL-XL and BCL-2.[248] The protocol involves multiple consecutive steps aimed at reducing the large conformational search space, which includes the degrees of freedom for protein-protein interaction, PROTAC internal conformation, and its relative pose to the protein-protein complex.[47] The input consists of the crystal structures of the POI and E3 ligase, each with its own binding ligand, and a SMILES string representing the entire PROTAC.[47] The protocol uses two anchor atoms in the two ligands, which are defined as part of the input. The distance between the two anchor atoms in a PROTAC is estimated by generating 200 random pairs of ligand positions for each value starting from 1Å and in increments of 1Å.[47] For each pair of ligand positions, a random conformation of the entire PROTAC is generated which incorporates the "fixed" ligand positions. Successful generated PROTAC conformations for each distance bin are summed-up, and their distribution is used to select distance constraints. Geometrical constraints of the molecule can cause some pairs to fail to generate a valid PROTAC conformation.[47] The protein-protein interaction space is sampled, with the bound ligands present, to generate docking solutions for the final ternary complex, with the ability to model up to 100 random linker conformations that could connect the two ligands, given their position in the docking solution.[47] After sampling the protein-protein interaction space and generating conformations for the proposed PROTAC, potential ternary complexes are selected based on optimal linker conformations that avoid steric clashes with the protein-protein interaction. The ternary complexes are scored and clustered assuming that near-native solutions are sampled multiple times. Clusters are then ranked based on the number of models and other parameters, with the top cluster containing a near-native solution, defined as a structure with a Cα average distance of less than 4Å to the crystallographic conformation.[47] Importantly, this computational model

does not consider a PROTAC's cell penetrance, efflux, kinetics of ternary complex formation, ubiquitination efficiency, or rate of proteasomal degradation.[247] This implies that the model's ability to induce ternary complex formation is the main determinant of a PROTAC's activity, and other factors are not directly incorporated into the model.[247] Nevertheless, creating a productive ternary complex remains a crucial starting point for enhancing PROTAC activity, particularly by improving cooperativity in ternary complex formation.[47,247] Therefore, this computational strategy focuses on binding modes where there is intrinsic affinity between the two proteins, likely to exhibit positive cooperativity, neglecting modes where protein-protein interactions do not contribute favourably to the ternary complex.[47,247]

Overall, the PRosettaC software can help to accelerate the discovery and optimization of PROTACs by allowing researchers to quickly evaluate the likely efficacy of potential designs and identify promising candidates for further testing and development.[47] By streamlining the drug discovery process, the software can help to accelerate the development of new treatments for a wide range of diseases and conditions.[47]

3.2 Aim of the project

In this study, we have integrated computational and ABPP-based methodologies to design and optimize PROTACs for serine hydrolases, focusing on APT1 as a model target. PRosettaC was utilized to predict the optimal linker length, configuration, and binding affinity of the PROTAC to APT1. ABPP-based approaches were employed to monitor the inhibition of APT1 in cell lysates treated with PROTACs, and to characterize the selectivity of the PROTACs by comparing their activity towards APT1 with other closely related enzymes. Additionally, degradation activity was evaluated through immunoblot assays, and the anti-tumour activity of the most promising APT1-targeting PROTACs in haematological cancer cell lines was also assessed.

3.3 Results

3.3.1 PRosettaC-guided design of PROTACs

In this study, computational modelling was employed to predict the potential for ternary complex formation of PROTACs and to guide the synthetic tasks. A sulfonyl fluoride-warhead was selected due to its established ability to label serine residues. Moreover, given the selectivity of APTs for substrates bearing longer alkyl chains, we hypothesized that PROTACs with linkers bearing alkyl linkers would exhibit a higher probability to engage APTs and form the tertiary complexes needed for PROTAC-mediated degradation. To this end, we first generated a molecule with an eight-carbon chain linker, **C8**, which comprises a benzenesulfonyl fluoride-warhead for APT binding, and a pomalidomide moiety for CRBN recruitment **(Fig. 3. 5, a)**. Using a proprietary pipeline to create models of the APT1:**C8**:CRBN complex, we were able to predict nonclashing models for PROTAC design. This run produced over 200 models, including a promising first cluster, with 53% of the results. In PRosettaC, each model represents a possible solution for the ternary complex found by the software. The clusters are ordered by the number of solutions they include and the similarity between these model solutions. Clustering is performed by applying the DBSCAN density-based clustering method, while using the RMSD between a pair of models, to group neighbouring models together with a threshold of 4Å. The first cluster is therefore the most populated one **(Fig. 3. 5, b)**. Every other cluster included less than 3% of the results. Therefore, the first cluster was promising as an initial hypothesis for the correct ternary complex formation. The likelihood of APT1:**C8**:CRBN pairing was compared with the one for the aforementioned, **FP-PROTAC (Fig. 3. 2)**. Even though only APT2 is degraded by **FP-PROTAC**, the two proteins are very similar, and by indication of the number of clusters produced and the similarity between the generated results (RMSD: 0.17Å), it suggests the previously obtained models have the potential to be the foremost ones for tripartite formation **(Fig. 3. 6)**. Clusters from different runs that corresponded to the same overall solution (**C8** and **FP-PROTAC**) were combined, and reclustered to 1Å and again to 0.5Å RMSD, yielding the top 5 subclusters **(Fig. 3. 5, c)**.

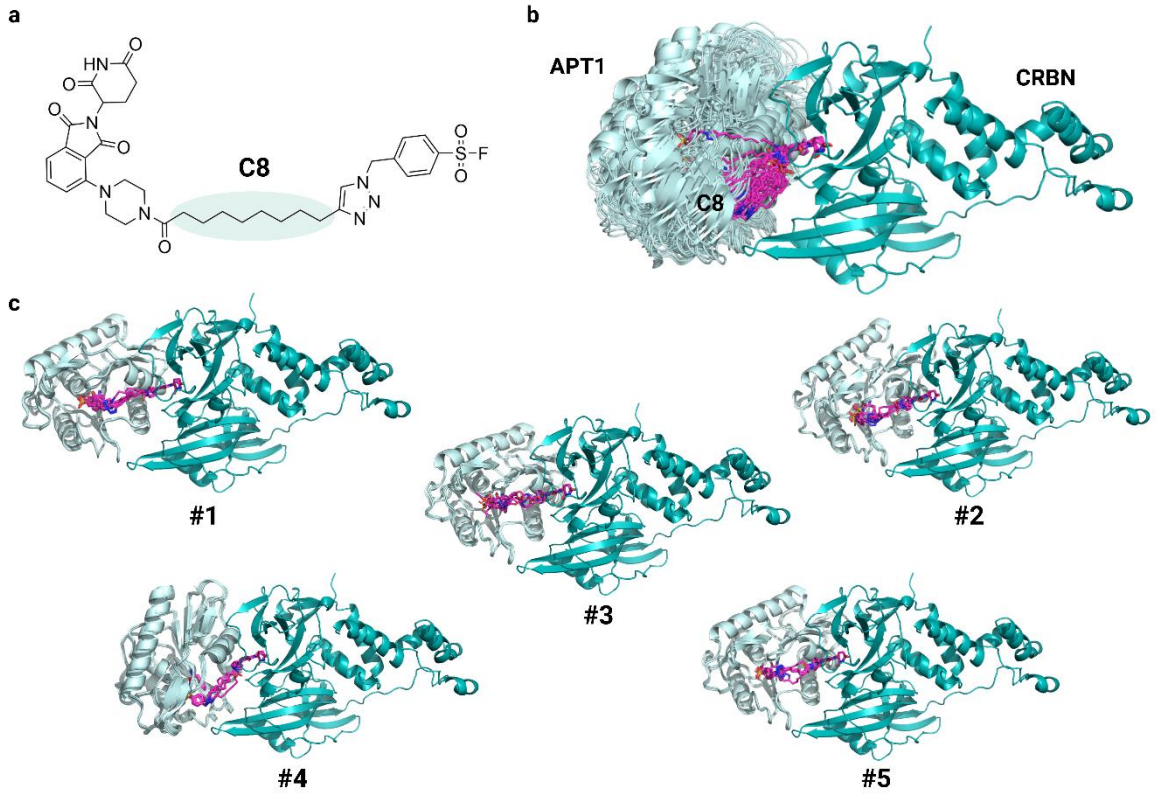

Fig. 3. 5. Results from the PRosettaC with **C8**.

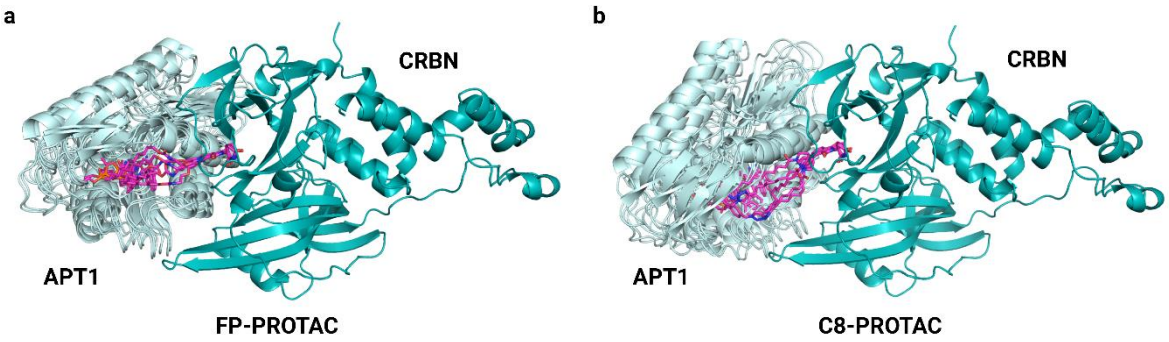

Fig. 3. 6. Results from the PRosettaC with **FP-PROTAC** (a) and **C8** (b).

Next, we aimed to determine the minimal linker length that would result in the cessation of PROTAC-mediated degradation of APT1 *in silico* **(Fig 3. 7 and 3. 8, a-c)**. We generated a series of PROTACs with varying linker lengths (**R1**, **C-1**-**C7**), while maintaining the ligands for APT1 and CRBN. To assess the ability of the chosen models to accommodate the newly generated PROTACs, RDKit and Rosetta were used to compute the molecules into models #1-5. This resulted in the generation up to 500 clusters, demonstrating that

almost all pairs of PROTAC-model did produce tripart complex formation without destructive steric interactions. However, molecules with shorter/rigid linkers, such as **R1**, **C-1**, and **C0**, were unable to generate any results, suggesting their linker length is potentially too short to allow adequate formation of a ternary complex **(Fig. 3. 8)**.

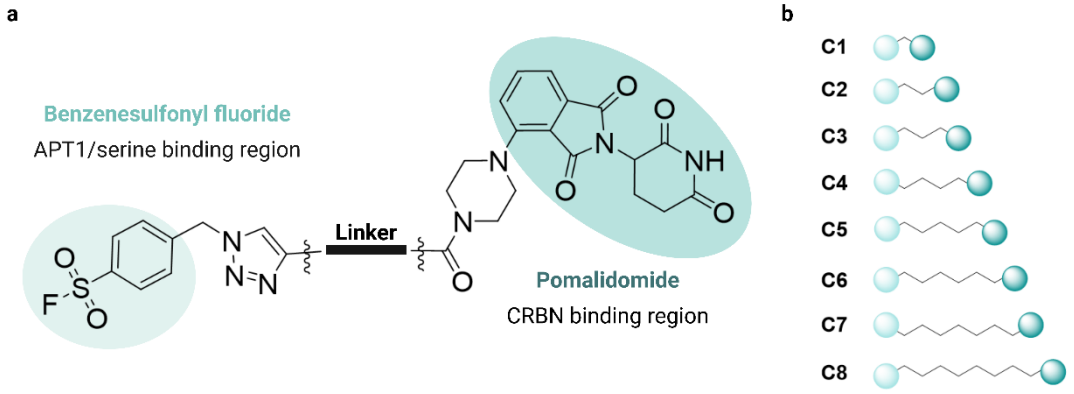

Fig. 3. 7. PROTAC design for APT1. (a) General chemical structures of the designed molecules. (b) Linker lengths explored in this study.

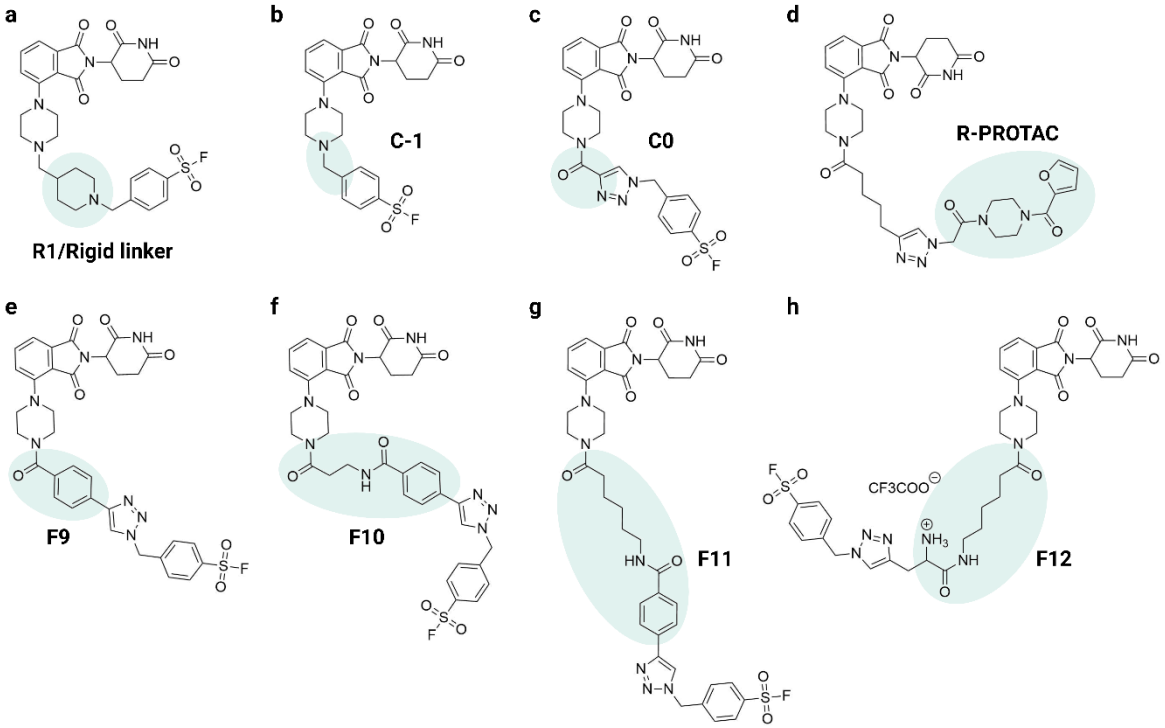

Fig. 3. 8. Chemical structures of designed and synthesised PROTACs for APT1. The linkers are highlighted in blue.

3.3.2 Benzenesulfonyl fluoride-based PROTAC induces degradation of APT1 via CRBN-mediated proteolysis

To validate PROTAC-activity of designed molecules we first synthesized the **C8** molecule. We evaluated the effects of **C8** in endogenous levels APT1, by treating a human Burkitt's lymphoma cell line (Raji) for 0-18h and with increasing concentrations of **C8 (Fig. 3. 9, a, and b)**. Pronounced loss of APT1 (> 80%) was observed at 4h for concentrations of **C8** as low as 0.5 µM. Marked depletion of APT1 was observed at 4 and 6h, with a partial recovery in APT1 abundance at 18h. Next, we test the ability of **C8** to induce CRBN-mediated degradation of APT1. First, we confirmed that treatment with either benzenesulfonyl fluoride (BSF) or pomalidomide (Pom) alone was insufficient to induce APT1 degradation in Raji cells as demonstrated in **Fig. 3. 9, c**. The degradation by **C8** was dependent on proteasome function, as evidenced by the rescue of APT1 degradation upon treatment with the proteasome inhibitor carfilzomib **(Fig. 3. 9, d)**. Engagement of both APT1 and CRBN was demonstrated by the abolition of **C8**-induced APT1 degradation upon pretreatment with excess benzenesulfonyl fluoride or pomalidomide, respectively **(Fig. 3. 9, e)**. The dependence of APT1 degradation on CRL activity was rescued through pretreatment with the NAE1 inhibitor MLN4924[249] **(Fig. 3. 9, f)**, as expected for E3 ubiquitin ligases that rely on neddylation for effective E3 ligase activity[250,251]. Finally, to confirm cellular requirement for CRBN recruitment, we used a CRBN-deficient human MOLT-4 cell line (MOLT-4-CRBN$^{-/-}$). Whereas treatment of wild-type MOLT-4 cells with **C8** promoted degradation of APT1, exposure of MOLT-4-CRBN$^{-/-}$ cells to **C8** had no effect **(Fig. 3. 9, g)**. These data provide mechanistic evidence for CRBN-dependent proteasomal degradation of APT1 by **C8**.

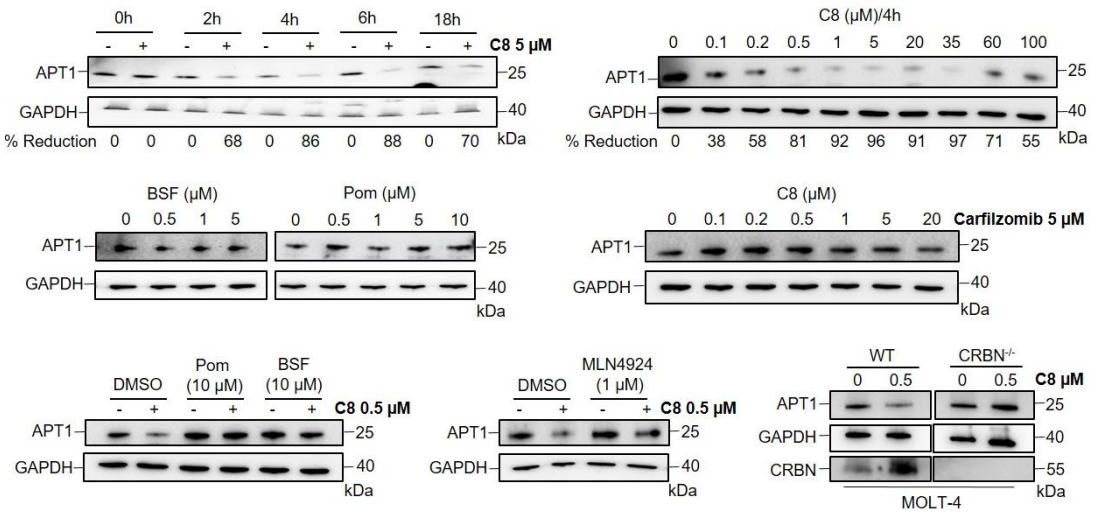

Fig. 3. 9. Activity characterization, and chemical/genetic-rescue of **C8**-mediated degradation. (a) Immunoblot for APT1 and GAPDH after treatment of Raji cells with 5 µM **C8** for the indicated time exposures. (b) Immunoblot for APT1 and GAPDH after 4h of treatment of Raji cells with the indicated concentrations of **C8**. (c) Immunoblot for APT1 and GAPDH after a 4h treatment with the indicated concentrations of benzenesulfonyl fluoride (BSF) and pomalidomide (Pom) in Raji cells. (d) Immunoblot for APT1 and GAPDH after a 1h pretreatment with carfilzomib (5 µM), followed by a 4h-**C8** treatment in Raji cells. (e) Immunoblot for APT1 and GAPDH after a 1h pretreatment with the indicated concentrations of benzenesulfonyl fluoride and pomalidomide, followed by a 4h-**C8** treatment in Raji cells. (f) Immunoblot for APT1 and GAPDH after a 1h pretreatment with MLN4924, followed by a 4h **C8** treatment (0.5 µM) in Raji cells. (g) Immunoblot for APT1, GAPDH and CRBN after treatment of MOLT-4-WT or MOLT-4-CRBN$^{-/-}$ cells with **C8** (0.5 µM) for 4h.

3.3.3 Extended linkers correlate with a more favourable degradation profile

To validate the computed models, we synthesized all designed PROTACs previously described (**R1**, **C-1**-**C7**). Moreover, we synthesized other molecules with a more complex linker composition (**F9-F12**), to evaluate the significance of linker interactions with adjacent residues to S199 of APT1, and the overall effects of flexibility and rigidity on the binding mode. The modifications included the introduction of aromatic rings and free amine groups, in addition to alkyl chains with various lengths **(Fig. 3. 8, e-h)**. Finally, we synthesized a PROTAC with a reversible warhead (**R-PROTAC**), and with similar structure to the aforementioned APT1 inhibitor, ML348 **(Fig. 3. 2 and 3. 8, d)**. To quickly

obtain a small library of compounds for testing we designed a straightforward pathway to derivatize pomalidomide and append the different linkers in a quick and simple synthetic route. The synthesis started with attachment of piperazine to pomalidomide using boc-piperazine. After boc deprotection the piperazine-derivatized pomalidomide was coupled to different alkyl chains containing an alkyne and carboxylic acids at opposite ends using HATU, yielding a series of pomalidomide alkynes containing a pyrazine linker and a series of alkyl chains differing in size by one carbon. Click chemistry was then used to attach the sulfonyl fluoride reactive group. A few compounds required additional steps to append additional elements to the linkers. For example, compounds with extended linkers had an additional HATU step to include the small flexible alkyl chains. Additionally, since the PRosettaC modelling suggested that even the one carbon linker could be enough to generate a ternary complex, we sought shorter compounds by using propiolic acid in the HATU step and also directly attaching the pomalidomide-piperazine to the sulfonyl fluoride building block to create shorter compounds that could act as inactive derivatives in terms of degradation. For the non-covalent compound, the triazole urea was first formed via an HATU coupling of 2-furoic acid with a piperazine derivative containing an azide. This compound was then clicked to an alkyle-derivatized pomalidomide derivative.

APT1 PROTAC-engagement was first assessed by determining the inhibitory potential for all compounds through a gel-based competitive ABPP assay **(Fig. 3. 10 and 3. 14, a)**. All synthesized degraders displayed binding efficacy to APT1 within the micromolar range, apart from **C0** and **C1**, which showed to inhibit APT1 at concentrations lower than 1 µM. The inhibitory potential was not impaired by linker length, as evidenced by the calculated average percentage of inhibited protein for shorter *versus* longer PROTACs **(Fig. 3. 11)**. Complex linker compositions (**F9-12**) impaired the engagement to APT1, relative to the "simpler" alkyl-linker PROTACs (**C0-C8**). However, partial recovery of the inhibitory potential was observed when increasing linker length to include an alkyl chain with 2 or 5 carbons, in **F10** and **F11**, relative to the short and non-alkyl linker molecule **F9 (Fig. 3. 14, a)**. The **R-PROTAC** is a reversible molecule, therefore the inhibitory potential could not be observed in this type of experimental set-up.

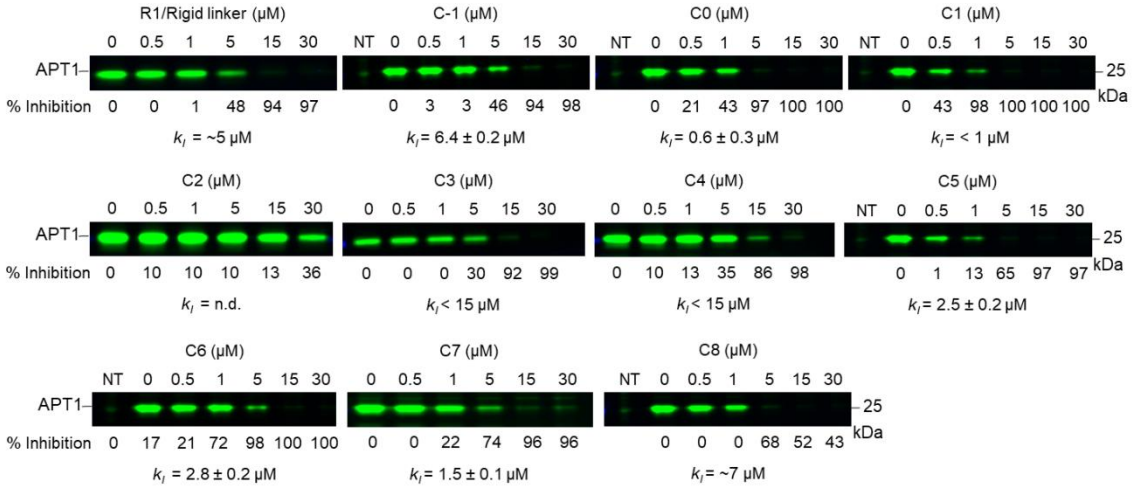

Fig. 3. 10. Gel competitive ABPP assays for APT1. The proteome of HEK293T cells overexpressing APT1, was treated with the indicated concentrations of PROTACs for 30 min, followed by 1h incubation with FP-Rhodamine. The green signal intensity correlates to the remaining active protein present in the sample mixture.

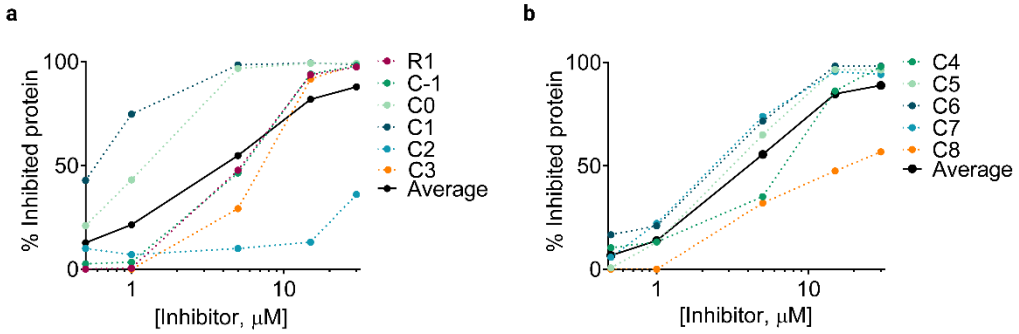

Fig. 3. 11. Percentage of protein inhibited with (a) **R1**, **C-1-C3** and (b) **C4-C8** from activity-based SDS-gel. The values correspond to the measured band intensity of experimental conditions relative to the control (DMSO).

To determine the efficacy of the synthesized PROTACs in degrading APT1, western blot analysis was performed on Raji cells treated for 4h **(Fig. 3. 12 and 3. 14, b)**. The results revealed that PROTACs with shorter linker lengths (**R1**, **C-1**, **C0, C2**) induced only modest degradation or were overall ineffective in degrading APT1, while linkers with extended alkyl chains showed potent degradation of the target protein **(Fig. 3. 12 and 3. 13)**. Interestingly, extended linker PROTACs that previously exhibited only mild inhibitory potential in the micromolar range (**C5**, **C6**, **C8**) were found to degrade endogenous APT1 by 50%, at concentrations as low as 200 and 500 nM. Furthermore, PROTACs with complex linker compositions (**F9-F10**) did not show any significant

improvements in target degradation, indicating that simpler and more flexible linkers may be more effective in this context **(Fig. 3. 14, b)**. In addition, substituting the irreversible covalent warhead with a reversible one did not lead to any significant improvements relative to **C5**, **C6** and **C8 (Fig. 3. 14, b)**. Moreover, the hook effect, which is commonly observed in molecules that form ternary complexes, such as PROTACs, becomes apparent at higher concentrations of 60 and 100 µM. This effect prevents the formation of ternary complexes and leads to reduced degradation of the target protein as observed **(Fig. 3. 12)**.

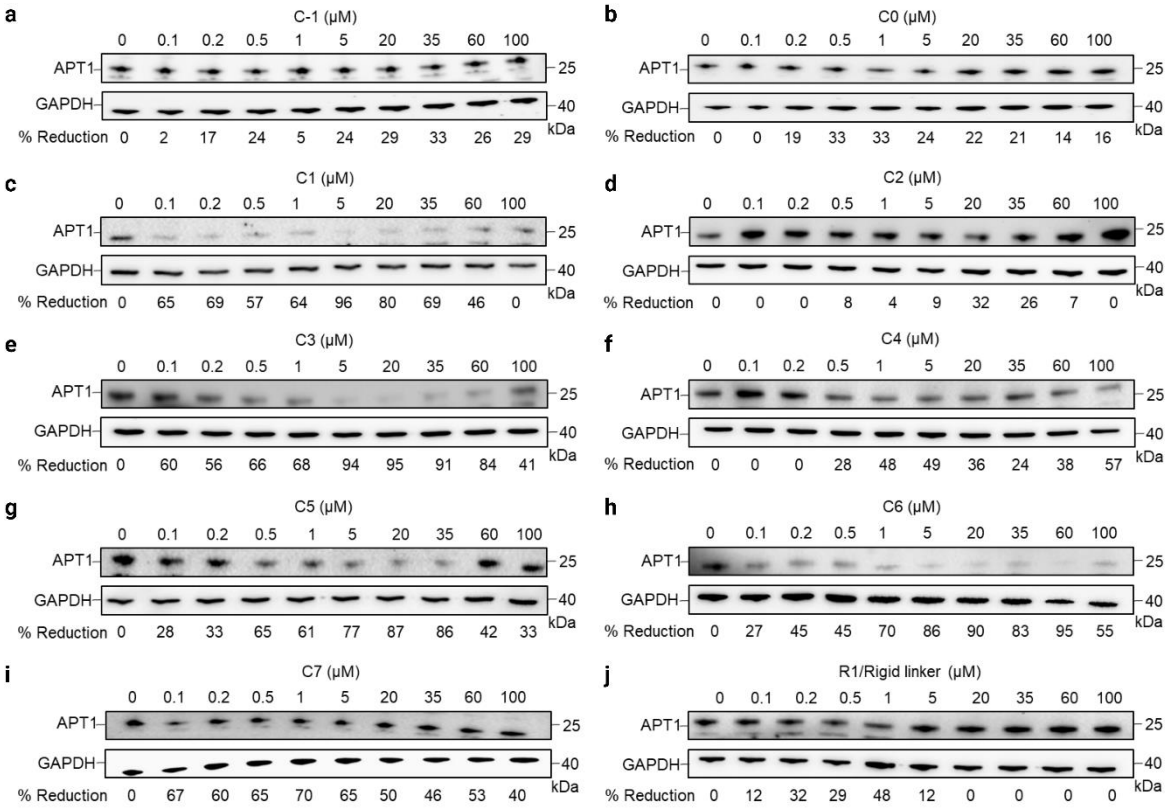

Fig. 3. 12. Immunoblot analysis of APT1 degradation in Raji cells treated with the indicated concentrations of PROTACs for 4h.

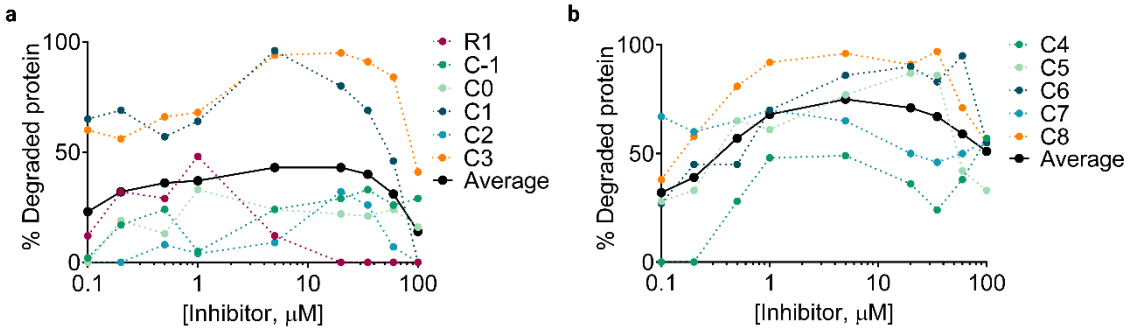

Fig. 3. 13. Percentage of protein degraded with (a) **R1**, **C-1-C3** and (b) **C4-C8** from immunoblot analysis. The values correspond to the measured band intensity of experimental conditions relative to the control (DMSO).

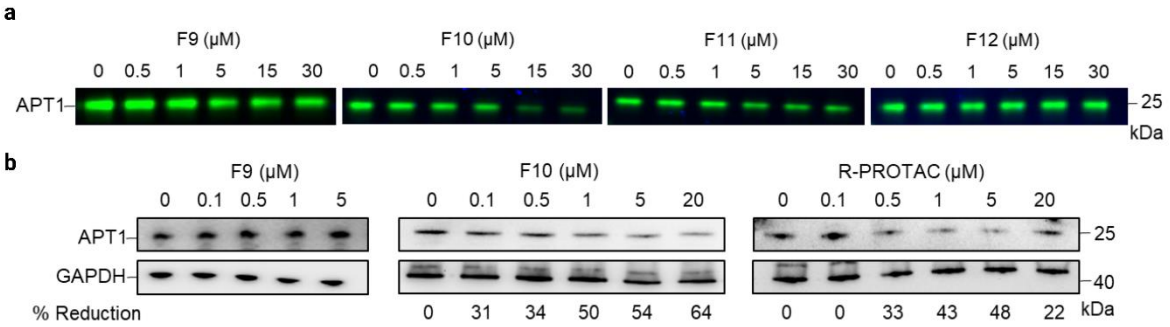

Fig. 3. 14. Activity characterization of **F9**-**F12** and **R- PROTACs**. (a) Gel competitive ABPP assays for APT1. The proteome of HEK293T cells overexpressing APT1, was treated with the indicated concentrations of PROTACs for 30 min, followed by 1h incubation with FP-Rhodamine. (b) Immunoblot analysis of APT1 degradation in Raji cells treated with the indicated concentrations of PROTACs for 4h.

To exclude potential issues with cell permeability that could hinder the efficacy of PROTACs, we ascertain the extent of compound internalization in Raji cells, treated with 100 μM of four different PROTAC degraders: **C-1**, **C8**, **F9**, and **F12**. Cells were lysed after medium removal, and the fluorescence signal intrinsic to all PROTACs, was measured both in cells and in the media. Results demonstrated that all four PROTACs were detected within the cells, thereby indicating their ability to cross cell membrane and access the intracellular environment **(Table 3. 1)**. Overall, our findings suggest that the lack of degrader efficiency observed in our earlier experiments for **C-1**, **F9**, and **F12**, is unlikely to be attributed to issues with cell permeability.

Table 3. 1. Detected fluorescence of **C-1**, **C8**, **F9**, and **F12**.

	C-1	C8	F9	F12
Cell lysate	1.5×10^6	36×10^6	67×10^6	1.5×10^6
Medium	18×10^6	0.06×10^6	0.17×10^6	10×10^6

3.3.4 Selectivity for APT1 is conditioned by a linker

After the promising results observed in the gel-based ABPP assays, we were interested in a more in-depth analysis of the proteome and to get the IDs of proteins being inhibited and degraded by our compounds. To achieve this, a mass-spectrometry based ABPP was run. Due to the challenged inherent to analysing an entire proteome we decided to start by analysing the serine hydrolase family of enzymes by again using a fluorophosphonate probe, in this case a desthiobiotin-containing fluorophosphonate probe. Briefly, cells were treated with the corresponding PROTAC molecules for 4h and then harvested. Each sample preparation was done together with a paired control sample treated only with DMSO. Sample pairs were lysed, and general serine hydrolase labelling was then done with fluorophosphonate-desthiobiotin for both samples. The samples were denatured, reduced, and alkylated. Serine hydrolases that were labelled by the fluorophosphonate probe were enriched using streptavidin-coated agarose beads and the remaining protein content was eliminated by thoroughly washing the beads. Streptavidin-enriched proteins were digested overnight with trypsin. Tryptic peptides were isotopically labelled with light and heavy formaldehyde for protein quantification using a reductive dimethylation technique. Each sample pair was combined and analysed by LC-MS/MS. Importantly, PROTAC treated samples were labelled with light formaldehyde and DMSO-treated samples were labelled with heavy formaldehyde. After data processing, heavy/light ratios were calculated. If a serine hydrolase was inhibited/degraded, the light channel signal will be decreased, resulting in a higher heavy/light ratio. Using this method, we identified ~32 serine hydrolases. For simplified analysis of the results, only the most relevant labelled proteins for each molecule are represented **(Fig. 3. 15)**. The full list of labelled serine hydrolases can be found in **Annex 1**. From data analysis, **C8** showed significant degradation of APT1 with high statistical significance. APT2 and other lipid metabolizing enzymes, such as ABHD6 and ABHD11 were also labelled, with a $\%\log_2$FC of 35, 54, and 22 respectively, further suggesting the preference of **C8** for these enzymes. It is worth noting that **C8** exhibits a high selectivity for APT1 while causing minimal disruption to other ABHDs, which are frequently targeted by APT inhibitors. Conversely, **F10** and **R-PROTAC** display a lack of selectivity towards APTs and degrade ABHD enzymes non-specifically.

The effect of benzenesulfonyl fluoride or pomalidomide alone on APT1 activity was

analysed in a competitive ABPP gel-based experiment utilizing lysates derived from transfected HEK293T cells. As observed, both benzenesulfonyl fluoride and pomalidomide alone are uncapable to specifically target APT1 **(Fig. 3. 16)**, suggesting the inhibition and degradation observed for APT1 is not derived solely by the presence of a highly reactive sulfonyl fluoride or the E3 ligase binder, pomalidomide.

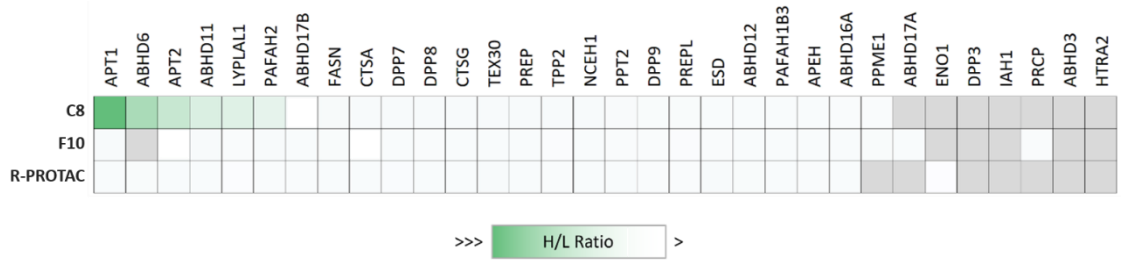

Fig. 3. 15. Mass spectrometry-based ABPP of Raji cells treated with selected PROTACs; serine hydrolases were enriched using a fluorophosphonate-biotin probe. A higher H/L ratio, depicted in green, represents a higher level of inhibition and/or degradation. Raji cells were treated for 4h with 5 µM of each compound.

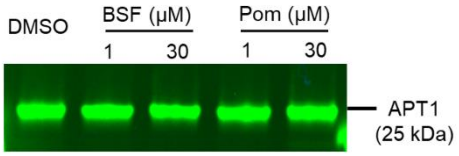

Fig. 3. 16. Gel-competitive ABPP assay for APT1. The proteome of HEK239T transfected cells, was treated with 1 and 30 µM concentrations of benzenesulfonyl fluoride (BSF) and pomalidomide (Pom) for 30 min, followed by 1h incubation with FP-Rhodamine.

3.3.5 C8 presents anti-tumour activity in blood cancer cells

We next evaluated the efficacy of **C8** in cell lines of haematological cancers, including ones from lymphoid and myeloid lineages. In published studies, inhibition of APT1 and APT2 has shown to be effective against leukemic cells.[236] Thus, we hypothesized **C8** would have similar anti-tumour effect in blood cancer cell lines, where APTs are expressed. In this study we included cell lines for BL, DLBCL, CLL, AML, APML, and acute lymphoblastic leukaemia (ALL). As expected, **C8** presented a pronounced effect in inhibiting the proliferation of MOLT-4 (ALL) and MOLM-13 (AML), with IC_{50} values of

2.92 and 9.74 µM, respectively **(Table 3. 2)**. In diffuse large B-cell lymphoma (DoHH-2) the value was 9.7 µM and 10.8 µM for acute promyelocytic leukaemia (HL-60). However, the antiproliferative consequences of APTs degradation were not as evidenced in chronic lymphocytic cell lines, WA-C3CD5+ and Mo1043 (IC_{50}: 34.3 and 19.3 µM). Importantly, non-tumoral HEK293T cells were less sensitive to the treatment with a IC_{50} value of ~ 43 µM. In addition, pomalidomide, which is used for the treatment of multiple myeloma and under investigated for certain lymphoma cancers, was not active in Raji cells, suggesting that any cellular activity mediated by **C8** is likely a result of direct interaction with APT1 rather than any off-target inhibition of the pomalidomide warhead present in the PROTAC molecule. Also, the lack of anti-tumour activity of **F10** and **R-PROTAC**, helps to exclude additional anti-tumour activity of pomalidomide. Furthermore, all PROTACs described in this study incorporate a secondary amine as an exit vector in the pomalidomide warhead. This chemical modification has been shown to be highly effective in mitigating off-target effects, thus increasing the specificity and safety profile of pomalidomide-based PROTACs.[252]

Table 3. 2. Viable cell growth inhibition of compounds (IC_{50}: µM), 72h**.**

	C8	F10	R-PROTAC	Pomalidomide
Raji (BL)	16.8 ± 0.01	n.d.	n.d.	n.d.
DoHH-2 (DLBCL)	9.74 ± 0.06			
WA-C3CD5+ (CLL)	34.3 ± 0.04			
Mo1043 (CLL)	19.3 ± 0.11			
HL-60 (APML)	10.8 ± 0.03			
MOLT-4 (ALL)	2.92 ± 0.02			
MOLM-13 (AML)	10.6 ± 0.03			
HEK293T (embryonic cells)	~ 43 ± n.d.			

n.d. – not determined

3.4 Discussion

While the fundamental components of a PROTAC structure may appear straightforward, the actual development of PROTACs is a complex and multifaceted process.[253] One of the most critical aspects of PROTAC development is the linker design, which must be of

appropriate length, flexibility, and stability to allow for efficient proximity-induced degradation while avoiding steric hindrance and other potential complications.[47,253] However, determining the optimal linker length and composition can be a laborious and time-consuming process that requires substantial empirical screening, chemical synthesis, and iterative optimization.[47] Rosetta-based models, such as PRosettaC, provide a promising, structure-based approach to circumvent this rate-limiting step of PROTAC development.[47]

In this study, we employed PRosettaC for guided design of serine hydrolase degraders, specifically for APT1. Based on predictive scoring and likelihood for inducing target protein degradation, eleven PROTACs with varying alkyl linker chains were synthesized and tested for intracellular activity. An additional five molecules were synthesized to assess substituent functionalities by altering linker composition and substituting the covalent warhead for the POI with a reversible one. Results from immunoblot analysis, showed that PROTACs with shorter linker lengths had limited or minimal effectiveness in degrading APT1, while those with extended alkyl chains exhibited potent degradation. Moreover, PROTACs with more complex linker compositions did not result in any significant improvement in target degradation, and their potential for APT1 degradation was relatively lower than that of alkyl-PROTACs. APT enzymes, which are responsible for catalysing reactions involving fatty acid derivatives[254], are more reactive towards long chain fatty alkyl substrates. This suggests that shorter alkyl chains may not provide enough free energy to counteract the entopic penalty of binding (increasing K_m) or bind too deep in the channel.[215] Besides, linker length and vector (the direction in which an E3 ligase is recruited to a protein) can influence the overall cooperativity within the ternary complex formation, affecting the rate of protein degradation.[34] Consequently, in the extent of APT1 degradation, longer linkers were accompanied with a greater cooperativity, yielding a more efficient cellular degradation. This was also supported by PRosettaC modelling, where longer alkyl linkers provided the best clustering results. PROTAC engagement through the hydrophobic channel is not surprising, since APT1 and APT2 react exceptionally fast with aliphatic fluorophosphonate and hexadecylfluorophosphonate probes, but much slower with PEG-fluorophosphonate probes.[215] In addition, APT1 and APT2 are known to be inhibited by compounds with long fatty motifs, such as Palmostatin B and M, demonstrating a clear preference of these enzymes for aliphatic substrates.[237] Predictably, the compound **C8**, due to having a long alkyl linker, similar to the structural motifs found

in lipids, showed a distinct activity for APTs. On the other hand, by using linkers that do not have this hydrophobic characteristic, as in the case of **F9-F12**, the activity and selectivity are lost. Consistently, **C8** surfaced as a robust and specific APT1 degrader in an initial proteomic analysis. Given the high selectivity for APT1 observed in this experiment, it is possible to extrapolate that **C8**'s selectivity may be attributed not only to the reactive moiety but also on the composition and length of the linker, which reinforced the selectivity for APT1. However, the biochemical/proteomic approach here presented has limitations, since the probes used are specific for enrichment of serine hydrolases and these preliminary results can therefore only report on the selectivity within this enzymatic family. As the benzenesulfonyl fluoride is a broadly reactive moiety that can also bind to tyrosine and histidine residues[255], it is possible that other proteins could also be affected by **C8**'s activity. Currently, a more extensive proteomics is being run to establish the full degradome of selected compounds of the PROTAC library to gain a more comprehensive understanding of the full range of targets being degraded.

In the cellular context, **C8** presented a wide spectrum of activity against several myeloid/lymphoid cancers. The same activity was not observed in HEK293T cells or with single-treatment with pomalidomide in Raji cells, excluding the cellular activity that may advent from off-target reactivity of the pomalidomide warhead. APTs are involved in post-translational modifications of proteins, which can alter protein function and localization, specifically of those related with cancer pathogenesis. However, the precise role of APTs in cancer remains somehow conflicting, as some studies have suggested that other enzymes, such as ABHDs, might be implicated.[256] The discovery of **C8** as a potent and selective molecule of APT1, with less selectivity for ABHDs, provides an exciting opportunity to investigate the effects of APTs degradation on cancer cells. Nonetheless, further research is required to learn about the full scope of **C8** target specificity and to further establish APTs as promising therapeutic targets for cancer treatment.

3.5 Outlook

The field of targeted protein degradation using PROTACs has rapidly emerged in recent years as a promising strategy for the development of novel therapeutics. As demonstrated in this study, computational modelling can significantly accelerate the discovery process of

PROTACs by prioritizing biochemical screens and providing insights into linker design. Additionally, advances in artificial intelligence may further enhance the accuracy and speed of computational modelling for PROTAC discovery. Moreover, our findings suggest that PROTACs with longer alkyl chains can exhibit highly potent degradation effects on APT1, presumably by having a similar structure to that of substrates specific for these enzymes. Of particular interest is the potent APT1 degrader, **C8**, which exhibited a high selectivity factor compared to other serine hydrolases. The potential clinical applications of **C8** as a tool for evaluating the consequences of potent APT1 degradation in blood cancer cells are promising. Furthermore, the identification of selective degraders such as **C8** for specific targets highlights the potential for PROTACs to be used as precision therapeutics, offering a promising avenue for the development of novel cancer therapies. However, further optimization will be required to improve its pharmacological properties and increase its efficacy and safety profiles.

4

Conclusions

4. Conclusions

In recent years, small covalent inhibitors and PROTACs have gained significant attention in the field of targeted therapy due to their promising pharmacological advantages. These classes of drugs enable high potency against target proteins that are important for cancer development, while causing minimum damage to healthy cells. This in turn can increase therapeutic efficacy and minimize off-target effects.

The primary advantage of covalent inhibitors lies in their exceptional target selectivity and potency. These properties are particularly crucial when tackling challenging diseases, such as cancer, where precision and durability of therapeutic effects are vital to improve clinical outcomes.

Despite the clinical approval of some BTK inhibitors, there remains a strong demand for the development of this class of inhibitors for several reasons: (1) the need to expand their potential clinical applications; (2) the imperative to investigate alternative molecules with distinct selectivity profiles; (3) and the urgency to address drug resistance, which can reduce their long-term efficacy of BTKi in treating diseases such as leukemia and lymphoma.

The discovery of the novel covalent inhibitor **JS25** contributes to this continuous pursuit of precision medicine and addresses the ongoing demand for the development of more effective BTK inhibitors. **JS25** showed significant potential in preclinical models of BL, CLL, and DLBCL, with prolonged inhibition and high selectivity for BTK. This selectivity is crucial as it could minimize off-target effects, enhancing the safety profile of the drug candidate, especially when combined with other therapeutic molecules. Most importantly, **JS25**'s potency and selectivity profile sets it apart from existing BTK inhibitors, potentially providing a more effective and well-tolerated treatment option for patients with haematological cancers and autoimmune diseases.

The ability of **JS25** to cross the blood-brain barrier also indicates its potential to treat primary and secondary forms of haematological cancers in the brain – a relatively rare but significant occurrence among patients afflicted by these malignancies.

In the ongoing development of **JS25** as a potential drug candidate, it will become increasingly important to gain a comprehensive understanding of the resistance profile exhibited by tumor cells when exposed to this inhibitor. As with many targeted therapies, including BTKi, the emergence of resistance mechanisms can pose a significant challenge

to long-term treatments. Thus, investigating how tumor cells may adapt or gain resistance to **JS25** will be crucial for future treatment strategies, and to also establish safer combination regimens.

Overall, **JS25**'s distinct properties position it as a promising candidate for clinical development, and it may offer a new approach to address BTK-related diseases, particularly those with unmet clinical needs.

PROTACs, by utilizing the body's inherent protein degradation and stabilization mechanisms, represent an innovative and promising frontier in drug discovery that has advanced into clinical development. Protein degradation can offer superior efficacy compared to mere inhibition, especially for proteins that lack well-defined binding sites suitable for traditional small molecule inhibitors and possess complex scaffold functions that are challenging to inhibit directly. Nevertheless, the design of PROTACs can be complex, often demanding extensive empirical screening and iterative refinement. Computational models can play a crucial role in expediting this critical phase of their development.

The primary objective of this project was to devise a comprehensive methodology for modelling POI:PROTAC:E3 ligase ternary complexes, using computational strategies (PRosetaC) and combined it with activity-based biochemical assays. Utilizing this approach, we have identified the first potent and highly selective APT1 degrader: **PROTAC C8**. This study effectively demonstrated the usefulness of the software PRosettaC in PROTAC design, successfully predicting the optimal linker type. The employment of ABPP in evaluating PROTACs proved invaluable in showcasing the selectivity of our compounds within the serine hydrolase family and other lipid-metabolizing enzymes. Western blot analysis confirmed efficient degradation of APT1 for multiple compounds in the library. A comparison of our findings with existing literature and clinical trial PROTACs underscores the challenge of generalizing linker design, indicating that an individualized approach supported by computational modeling tools may be the key to success. It's important to note that targeted protein degradation hinges not only on target engagement and linker design but also on effective E3 ligase recruitment and efficient ubiquitination, which depends on appropriately positioned lysine/ubiquitin accepting residues. This complexity underscores the dynamic nature of this evolving field in chemical biology.

Notably, APT1 protein has been associated with the progression of several cancers, Huntington’s and Alzheimer’s diseases, all of which continue to require substantial

advancements in treatment options. The discovery of **C8** introduces an exciting prospect for the advancement of innovative blood cancer therapies, boasting distinct advantages over conventional small molecules. **C8** not only exhibited exceptional target specificity and potency (within serine hydrolases), but also leverages the unique mechanisms of PROTACs, which include the ability to induce degradation of disease-associated proteins. This innovative approach not only allows for a prolonged target suppression, but it also addresses issues related to drug resistance.

Future work will aim to characterise the phenotypic effects of PROTAC-mediated APT1 degradation in mice, evaluate the kinetics of ternary complex formation and degradation using biophysical techniques. Moreover, performing global quantitative proteomics would enable the full scope of degraded targets to be elucidated, which would be important for mitigating off-target toxicity.

Overall, we highlighted how the integration of computational modelling protocols, such as PRosettaC, can confer a high degree of assurance to our experimental findings, thus reducing the time expended in the production of PROTACs for novel targets.

In summary, this thesis contributes with valuable insights into the rational design of small covalent inhibitors and PROTACs for the treatment of heamatological malignancies. As we delve through the exploration of these two distinct drug modalities, the discovery of covalent molecules and PROTACs served as a pivotal point for a meaningful comparison. This comparison not only highlights their distinctive mode of action, but it also underscores the potential advantages that they each bring to the field of targeted therapy. Furthermore, the rational design of these novel compounds holds the promise of delivering safer and more effective treatment options, representing a significant step forward in the ongoing battle against cancer and other debilitating diseases.

5

Materials and methods

5. Materials and methods

5.1 Covalent targeting of BTK

5.1.1 Synthesis

Compound synthesis was performed by Dr João Seixas **(Scheme 5. 1 - 5. 4)**. Building blocks and solvents were purchased from Sigma Aldrich, Alfa Aesar, Acros, or Fluka and used without further purification. Proton and carbon nuclear magnetic resonance (^{1}H and ^{13}C NMR) spectra were recorded on a Bruker AVANCE 300 or 400 MHz spectrometers. All chemical shifts are quoted on the δ scale in ppm with TMS as an internal reference. Coupling constants (*J*) are reported in Hz with the following splitting abbreviations: s = singlet, d = doublet, t = triplet, m = multiplet. All compounds present ≥ 95% purity.

6-bromo-4-hydroxyquinoline-3-carboxylate (1)

Diethyl 2-(ethoxymethylene) malonate (11.7 ml; 58.13 mmol) and 4-bromoaniline (10 g; 58.13 mmol) were heated to 145ºC. After 23h, the solvent was evaporated affording an off-white solid. Ph_2O (25 ml) was added, and the reaction heated to 245ºC. After 6h, no more intermediate was detected by TLC (EtOAc:Hexane 20:80). Upon cooling to rt, a precipitate was formed, and hexane was added to induce more precipitation. The precipitate was filtered, washed with EtOAc and dried in vacuum to afford the title compound as an off-white solid (6.9 g; 40% yield). ^{1}H NMR (300 MHz, d^{6}-DMSO): δ 8.60 (s, 1H), 8.22 (d, *J* = 2.4 Hz, 1H), 7.82 (dd, *J* = 8.7, 2.4 Hz, 1H), 7.58 (d, *J* = 8.7 Hz, 1H), 4.20 (q, *J* = 7.1 Hz, 2H), 1.27 (t, *J* = 7.1 Hz, 3H).

Ethyl 6-bromo-4-chloro-3-quinolinecarboxylate (2)

6-bromo-4-hydroxy-3-quinolinecarboxylate (13.4 g; 45.25 mmol) was suspended in $SOCl_2$ (130 ml; 1.792 mol) and the mixture heated to 80ºC. After 5h, a clear yellow solution was obtained. The solvent was evaporated and the solid co-evaporated with DCM (5x) to remove residual HCl. It was dried in vacuum to afford the title compound as a light-yellow solid (14.4 g; 100% yield). ^{1}H NMR (300 MHz, $CDCl_3$): δ 9.37 (s, 1H), 8.71 (d, *J* = 2.0 Hz, 1H), 8.56 (d, *J* = 9.0 Hz, 1H), 8.12 (dd, *J* = 9.0, 2.0 Hz, 1H), 4.53 (q, *J* = 7.1 Hz, 2H), 1.47 (t, *J* = 7.1 Hz, 3H).

Ethyl 6-bromo-4-((4-methyl-3-nitrophenyl)amino)quinoline-3-carboxylate (3a)

Ethyl 6-bromo-4-chloro-3-quinolinecarboxylate **2** (800 mg; 2.543 mmol**)** and 4-methyl-5-nitroaniline (387 mg; 2.543 mmol) were mixed in dioxane (15 ml) and heated to 90ºC. After 7h, TLC analysis (50% EtOAc/Hexane) no longer detected starting materials. The yellow suspension was cooled to rt, diluted with H_2O and NaOH (1M) added until pH=8 was reached. EtOAc was added and the phases were separated. The aqueous phase was further extracted with EtOAc (2x), and the combined organics were washed with brine and dried over $MgSO_4$. After filtration, the solvent was evaporated to afford the title compound as a bright-yellow solid (980 mg; 90% yield). ^{1}H NMR (300 MHz, $CDCl_3$): δ 10.38 (s, 1H), 9.29 (s, 1H), 7.90 (d, *J* = 9.4 Hz, 1H), 7.74 (dq, *J* = 4.3, 2.2 Hz, 2H), 7.65 (d, *J* = 2.5 Hz, 1H), 7.25 (d, *J* = 8.3 Hz, 1H), 7.08 (dd, *J* = 8.3, 2.5 Hz, 1H), 4.45 (q, *J* = 7.1 Hz, 2H), 2.58 (s, 3H), 1.46 (t, *J* = 7.1 Hz, 3H).

Ethyl 6-bromo-4-((3-methyl-5-nitrophenyl)amino)quinoline-3-carboxylate (3b)

Prepared using General Procedure A, reacting intermediate **2** with with 3-methyl-5-nitroaniline. Compound **3b** was isolated as a yellow solid (730 mg; 89% yield). ^{1}H NMR (300 MHz, $CDCl_3$): δ 10.35 (s, 1H), 9.30 (s, 1H), 7.92 (d, J = 8.8 Hz, 1H), 7.79-7.73 (m, 3H), 7.61 (s, 1H), 7.11 (s, 1H), 4.45 (q, J = 7.1 Hz, 2H), 2.39 (s, 3H), 1.45 (t, J = 7.1 Hz, 3H). ^{13}C NMR (75.5 MHz, $CDCl_3$): δ 167.9, 151.5, 150.2, 149.6, 149.0, 143.5, 141.2, 135.1, 132.1, 128.4, 127.5, 120.8, 119.7, 119.2, 113.2, 109.1, 61.9, 14.4. HRMS (ESI): *m/z* $[M + H]^+$ calc. for $C_{19}H_{17}BrN_3O_4$: 430.0397; found: 430.0401.

Ethyl 6-bromo-4-((2-methyl-5-nitrophenyl)amino)quinoline-3-carboxylate (3c)

Prepared using General Procedure A, reacting intermediate **2** with 2-methyl-5-nitroaniline. The reaction required heating at 90ºC during 23h followed by 4h at 110ºC. Compound **3c** was isolated as a yellow solid (730 mg, 89% yield). ^{1}H NMR (300 MHz, d^6-DMSO): δ 9.29 (s, 1H), 8.87 (s, 1H), 8.52 – 8.47 (m, 1H), 7.98 – 7.90 (m, 3H), 7.66 (d, J = 2.4 Hz, 1H), 7.60 (d, J = 8.5 Hz, 1H), 3.85 (q, J = 7.1 Hz, 2H), 2.44 (s, 3H), 1.04 (t, J = 7.1 Hz, 3H). HRMS (ESI): *m/z* $[M + H]^+$ calc. for $C_{19}H_{17}BrN_3O_4$: 430.0397; found: 430.0400. ^{13}C NMR could not be acquired because the compound is not sufficiently soluble in d^6-DMSO, d^6-acetone, d^3-acetonitrile, or d^4-methanol.

Ethyl 6-bromo-4-((3-nitrophenyl)amino)quinoline-3-carboxylate (3d)

Prepared using General Procedure A, reacting intermediate **2** with with 3-nitroaniline. Reaction time was 8h. Compound **3d** was isolated as an orange solid (640 mg: 81% yield). ^{1}H NMR (300 MHz, $CDCl_3$): δ 10.41 (s, 1H), 9.32 (s, 1H), 8.01 – 7.91 (m, 2H), 7.86 (t, J = 2.2 Hz, 1H), 7.79 – 7.70 (m, 2H), 7.51 – 7.42 (m, 1H), 7.28 – 7.23 (m, 1H), 4.47 (q, J = 7.1 Hz, 2H), 1.47 (t, J = 7.2 Hz, 3H). ^{13}C NMR (75.5 MHz, $CDCl_3$): δ 167.9, 151.5, 150.1, 149.5, 149.0, 143.7, 135.1, 132.1, 130.0, 128.3, 126.6, 120.8, 119.4, 119.0, 115.9, 109.4, 62.0, 14.3. HRMS (ESI): *m/z* $[M + H]^+$ calc. for $C_{18}H_{15}BrN_3O_4$: 416.0240; found: 416.0245.

Ethyl 6-bromo-4-((4-methoxy-3-nitrophenyl)amino)quinoline-3-carboxylate (3e)

Prepared using the General Procedure A, reacting intermediate **2** with 4-methoxy-3-nitroaniline. Compound **3e** was isolated as an orange solid (780 mg; 92% yield). ^{1}H NMR (300 MHz, $CDCl_3$): δ 10.43 (s, 1H), 9.26 (s, 1H), 7.88 (d, J = 9.3 Hz, 1H), 7.73 – 7.70 (m, 2H), 7.59 (d, J = 2.7 Hz, 1H), 7.22 – 7.18 (m, 1H), 7.04 (d, J = 9.0 Hz, 1H), 4.45 (q, J = 7.1 Hz, 2H), 3.98 (s, 3H), 1.46 (t, J = 7.1 Hz, 3H). ^{13}C NMR (75.5 MHz, $CDCl_3$): δ 168.2, 151.7, 151.1, 150.4, 149.7, 139.7, 135.2, 134.9, 132.1, 128.4, 128.1, 120.4, 119.7, 118.9, 114.6, 107.8, 61.8, 57.1, 14.4. HRMS (ESI): *m/z* $[M + H]^+$ calc. for $C_{19}H_{17}BrN_3O_5$: 446.0346; found: 446.0347.

Ethyl 7-bromo-4-(4-methyl-3-nitrophenylamino)quinoline-3-carboxylate (3a')

Prepared using General Procedure A, reacting intermediate **2'** with 4-methyl-5-nitroaniline. Reaction was completed after 3h. Compound **3f** was isolated as a yellow solid (1.85 g; 85% yield). ^{1}H NMR (300 MHz, $CDCl_3$): δ 10.54 (s, 1H), 9.31 (s, 1H), 8.26 (d, *J* = 2.0 Hz, 1H), 7.69 (d, *J* = 2.4 Hz, 1H), 7.48 (d, *J* = 9.1 Hz, 1H), 7.34 (dd, *J* = 9.1, 2.0 Hz, 1H), 7.28 (m, 1H), 7.13 (dd, *J* = 8.3, 2.4 Hz, 1H), 4.48 (q, *J* = 7.1 Hz, 2H), 2.60 (s, 3H), 1.49 (t, *J* = 7.1 Hz, 3H). ^{13}C NMR (75.5 MHz, $CDCl_3$): δ 168.0, 152.1, 151.8, 151.3, 149.6, 141.5, 133.7, 132.4, 129.6, 128.8, 127.3, 126.4, 126.2, 117.9, 117.7, 108.0, 61.9, 20.1, 14.4. HRMS (ESI): *m/z* $[M + H]^+$ calc. for $C_{19}H_{17}BrN_3O_4$: 430.0397; found: 430.0393.

Ethyl 7-bromo-4-(3-methyl-5-nitrophenylamino)quinoline-3-carboxylate (**3b'**)

Prepared using General Procedure A, reacting intermediate **2'** with with 3-methyl-5-nitroaniline. Reaction time was 17h.The crude was washed with cold EtOAc to remove unreacted aniline. Compound **3b'** was isolated as an orange solid (740 mg: 58% yield). ^{1}H

NMR (300 MHz, $CDCl_3$) δ 10.41 (s, 1H), 9.31 (s, 1H), 8.35 – 8.08 (m, 1H), 7.79 (s, 1H), 7.63 (s, 1H), 7.46 (d, *J* = 9.1 Hz, 1H), 7.37 – 7.28 (m, 1H), 7.10 (s, 1H), 4.46 (q, *J* = 7.0 Hz, 2H), 2.39 (s, 3H), 1.46 (t, *J* = 7.1 Hz, 3H). HRMS (ESI): *m/z* $[M + H]^+$ calc. for $C_{19}H_{17}BrN_3O_4$: 430.0397; found: 430.0390.

Ethyl 7-bromo-4-(3-nitrophenylamino)quinoline-3-carboxylate (3d')

Prepared using General Procedure A, reacting intermediate **2'** with with 3-nitroaniline. Reaction time was 17h. Compound **3d'** was isolated as an orange solid (2.52 g: 95% yield). ^1H NMR (300 MHz, $CDCl_3$): δ 10.41 (s, 1H), 9.31 (s, 1H), 8.24 (brs, 1H), 7.79 (s, 1H), 7.63 (s, 1H), 7.46 (d, *J* = 9.1 Hz, 1H), 7.34 – 7.28 (m, 1H), 7.10 (s, 1H), 4.46 (q, *J* = 7.1 Hz, 2H), 2.39 (s, 3H), 1.46 (t, *J* = 7.1 Hz, 3H). ^{13}C NMR (75.5 MHz, $CDCl_3$): δ 168.0, 152.3, 151.7, 151.2, 149.1, 144.0, 132.9, 130.3, 129.0, 127.2, 126.9, 126.3, 119.0, 118.2, 116.0, 108.8, 62.0, 14.4. HRMS (ESI): *m/z* $[M + H]^+$ calc. for $C_{18}H_{15}BrN_3O_4$: 416.0240; found: 416.0244.

(6-bromo-4-((4-methyl-3-nitrophenyl)amino)quinolin-3-yl)methanol (4a)

Sodium borohydride (5.44 g; 143.99 mmol; 15 equiv.) was added portionwise to a stirred solution of **3a** (4.13 g; 9.599 mmol) in EtOH (35 ml) at 0ºC. After 15h, TLC analysis (50% EtOAc/Hexane) showed disappearance of starting material. The orange solution was cooled in an ice-bath and quenched with NH_4Cl aq.. The mixture was partitioned between H_2O and EtOAc. The phases were separated and the aqueous phase further extracted with EtOAc (2x). The combined organics were washed with brine, dried over $MgSO_4$ and evaporated to dryness to afford the title compound as an orange solid (3.73 g; 100% yield).

(6-bromo-4-((3-methyl-5-nitrophenyl)amino)quinolin-3-yl)methanol (4b)

Prepared using the procedure described for **4a**. Compound **4b** was obtained as an orange solid (630 mg; 100%). ^1H NMR (300 MHz, d^6-DMSO): δ 9.07 (s, 1H), 9.00 (s, 1H), 8.24 (s, 1H), 8.00 (d, J = 8.9 Hz, 1H), 7.87 (d, J = 8.9 Hz, 1H), 7.48 (s, 1H), 7.28 (s, 1H), 6.85 (s, 1H), 5.47 (t, J = 5.4 Hz, 1H), 4.48, (d, J = 5.4 Hz, 2H), 2.31 (s, 3H). ^{13}C NMR (75.5 MHz, d^6-DMSO): δ 152.2, 148.6, 146.9, 146.1, 140.6, 139.9, 132.3, 131.7, 128.7, 125.5, 125.3, 121.3, 119.6, 114.3, 106.5, 58.2, 20.9. HRMS (ESI): *m/z* $[M + H]^+$ calc. for $C_{17}H_{15}BrN_3O_3$: 388.0291; found: 388.0293.

(6-bromo-4-((2-methyl-5-nitrophenyl)amino)quinolin-3-yl)methanol (4c)

Prepared using the procedure described for **4a**. Compound **4c** was obtained as an orange solid (250 mg; 68% yield). ^{1}H NMR (300 MHz, d^{6}-DMSO): δ 9.03 (s, 1H), 8.20 (d, J = 2.1 Hz, 1H), 8.09 (s, 1H), 8.00 (d, J = 8.9 Hz, 1H), 7.87 (dd, J = 8.9, 2.2 Hz, 1H), 7.68 (dd, J = 8.3, 2.3 Hz, 1H), 7.50 (dd, J = 8.3, 0.9 Hz, 1H), 6.88 (d, J = 2.4 Hz, 1H), 5.47 (t, J = 5.5 Hz, 1H), 4.39, (d, J = 5.5 Hz, 2H), 2.50 (s, 3H). ^{13}C NMR (75.5 MHz, d^{6}-DMSO): δ 152.0, 147.0, 146.5, 144.4, 141.5, 134.5, 132.4, 131.7, 131.5, 128.2, 125.7, 125.2, 119.5, 115.0, 109.2, 58.3, 18.4. HRMS (ESI): *m/z* [M + H]$^{+}$ calc. for $C_{17}H_{15}BrN_3O_3$: 388.0291; found: 388.0293.

(6-bromo-4-((3-nitrophenyl)amino)quinolin-3-yl)methanol (4d)

Prepared using the procedure described for **4a**. Purification was carried out by column chromatography over silica-gel (eluent: MeOH:DCM 0:100 to 5:95) to give compound **4d** as a yellow solid (250 mg; 42% yield). ^{1}H NMR (300 MHz, d^{6}-DMSO): δ 9.06 (d, J = 5.4 Hz, 2H), 8.21 (d, J = 2.0 Hz, 1H), 7.99 (d, J = 8.9 Hz, 1H), 7.87 (d, J = 8.9 Hz, 1H), 7.64 (d, J = 8.0 Hz, 1H), 7.49 – 7.42 (m, 2H), 7.00 (d, J = 8.0 Hz, 1H), 5.47 (t, J = 5.1 Hz, 1H), 4.48 (d, J = 5.1 Hz, 2H). ^{13}C NMR (75.5 MHz, d^{6}-DMSO): δ 152.3, 148.6, 147.0, 146.3, 139.9, 132.4, 131.7, 130.5, 128.8, 125.5, 125.3, 120.9, 119.7, 113.7, 109.1, 58.2. HRMS (ESI): *m/z* [M + H]$^{+}$ calc. for $C_{16}H_{13}BrN_3O_3$: 374.0135; found: 374.0134.

(6-bromo-4-((4-methoxy-3-nitrophenyl)amino)quinolin-3-yl)methanol (4e)

Prepared using the procedure described for **4a**. Compound **4e** was obtained as an orange solid (600 mg; 93% yield). ^{1}H NMR (300 MHz, d^{6}-DMSO): δ 8.97 (s, 1H), 8.67 (s, 1H), 8.26 (d, J = 2.1 Hz, 1H), 7.94 (d, J = 8.9 Hz, 1H), 7.83 (dd, J = 8.9, 2.1 Hz, 1H), 7.32 – 7.18 (m, 2H), 7.00 (dd, J = 9.0, 2.8 Hz, 1H), 5.40 (t, J = 5.4 Hz, 1H), 4.42 (d, J = 5.4 Hz, 2H), 3.85 (s, 3H). ^{13}C NMR (75.5 MHz, d^{6}-DMSO): δ 152.2, 147.0, 146.0, 141.1, 139.3, 138.2, 132.1, 131.7, 131.7, 126.5, 125.5, 124.6, 122.3, 119.2, 115.5, 112.3, 58.5, 56.9. HRMS (ESI): *m/z* [M + H]$^{+}$ calc. for $C_{17}H_{15}BrN_3O_4$: 404.0240; found: 404.0244.

(7-bromo-4-(4-methyl-3-nitrophenylamino)quinolin-3-yl)methanol (**4a'**)

Prepared using the procedure described for **4a**. Compound **4a'** was isolated as an orange solid (770 mg; 100% yield). ^{1}H NMR (300 MHz, d^{6}-DMSO): δ 9.00 (s, 1H), 8.83 (s, 1H), 8.23 (d, *J* = 2.0 Hz, 1H), 7.88 (d, *J* = 9.0 Hz, 1H), 7.68 (dd, *J* = 9.0, 2.1 Hz, 1H), 7.32 – 7.21 (m, 2H), 6.86 (dd, *J* = 8.4, 2.5 Hz, 1H), 5.43 (t, *J* = 5.4 Hz, 1H), 4.51 (d, *J* = 5.4 Hz,

2H), 2.39 (s, 3H). ^{13}C NMR (75.5 MHz, d^6-DMSO): δ 152.9, 149.2, 149.1, 144.2, 141.7, 133.4, 131.3, 129.2, 127.8, 125.8, 123.0, 122.5, 122.4, 120.2, 110.6, 58.3, 18.9. HRMS (ESI): *m/z* $[M + H]^+$ calc. for $C_{17}H_{15}BrN_3O_3$: 388.0291; found: 388.0293.

(7-bromo-4-(3-methyl-5-nitrophenylamino)quinolin-3-yl)methanol (4b')

Prepared using the procedure described for **4a**. Compound **4b'** was isolated as a yellow solid (620 mg; 96% yield). ^{1}H NMR (300 MHz, d^6-DMSO): δ 9.03 (s, 1H), 8.94 (s, 1H), 8.24 (d, *J* = 2.0 Hz, 1H), 7.88 (d, *J* = 9.0 Hz, 1H), 7.68 (dd, *J* = 9.0, 2.0 Hz, 1H), 7.48 – 7.45 (m, 1H), 7.25 (m, 1H), 6.84 (brs, 1H), 5.47 (t, *J* = 5.4 Hz, 1H), 4.52 (d, *J* = 5.4 Hz, 2H), 2.29 (s, 3H). HRMS (ESI): *m/z* $[M + H]^+$ calc. for $C_{17}H_{15}BrN_3O_3$: 388.0291; found: 388.0294.

(7-bromo-4-(3-nitrophenylamino)quinolin-3-yl)methanol (4d')

Prepared using the procedure described for **4a**. Compound **4d'** was isolated as an orange solid (810 mg; 91% yield). ^{1}H NMR (300 MHz, d^6-DMSO): δ 9.03 (s, 2H), 8.25 (d, *J* = 2.0 Hz, 1H), 7.87 (d, *J* = 9.0 Hz, 1H), 7.69 (dd, *J* = 9.0, 2.1 Hz, 1H), 7.62 (ddd, *J* = 8.1, 2.2, 0.9 Hz, 1H), 7.48 – 7.44 (m, 1H), 7.41 (d, *J* = 8.1 Hz, 1H), 5.82 (s, 1H), 5.51 (t, *J* = 5.5 Hz, 1H), 4.52 (d, *J* = 5.5 Hz, 2H). HRMS (ESI): *m/z* $[M + H]^+$ calc. for $C_{16}H_{13}BrN_3O_3$: 374.0135; found: 374.0134.

6-bromo-4-((4-methyl-3-nitrophenyl)amino)quinoline-3-carbaldehyde (5a)

The alcohol **4a** (2.34 g; 6.029 mmol) was suspended in DCM (150 ml) and the mixture cooled to 0ºC. DMP (3.83 g; 9.041 mmol; 1.5 equiv.) was added portionwise and the reaction warmed to rt. After 2h, TLC analysis (5% MeOH in DCM) showed that the reaction was completed. The solution was cooled to 0ºC, and NaOH (1 M) was slowly added. The mixture was stirred for 15 min at rt. H_2O was added and the phases were separated. The aqueous phase was further extracted with DCM (3x). The combined organics were washed with brine, dried over MgSO4 and taken to dryness to afford the title compound as a yellow solid (1.75 g; 75% yield).

6-bromo-4-((3-methyl-5-nitrophenyl)amino)quinoline-3-carbaldehyde (5b)

Prepared using the procedure described for **5a**. Compound **5b** was obtained as an orange solid (420 mg; 72% yield). ^{1}H NMR (300 MHz, $CDCl_3$): δ 11.26 (s, 1H), 10.10 (s, 1H), 8.90 (s, 1H), 7.97–7.88 (m, 2H), 7.83–7.74 (m, 2H), 7.66 (d, *J* = 2.1 Hz, 1H), 7.34–7.27

(m, 1H), 2.46 (s, 3H). ^{13}C NMR (75.5 MHz, $CDCl_3$): δ 193.4, 155.0, 150.2, 149.7, 149.0, 141.6 (2), 136.0, 132.2, 129.5, 128.7, 121.4, 119.2, 118.9, 115.3, 113.7, 21.5. HRMS (ESI): *m/z* $[M + H]^+$ calc. for $C_{17}H_{13}BrN_3O_3$: 386.0135; found: 386.0142.

6-bromo-4-((2-methyl-5-nitrophenyl)amino)quinoline-3-carbaldehyde (5c)

Prepared using the procedure described for **5a**. Compound **5c** was obtained as a yellow solid (165 mg; 72% yield). ^{1}H NMR (300 MHz, d^6-DMSO): δ 10.18 (s, 1H), 9.94 (s, 1H), 8.97 (s, 1H), 8.07-8.02 (m, 2H), 7.93-7.88 (m, 3H), 7.67 (m, 1H), 2.42 (s, 3H). ^{1}H NMR (300 MHz, $CDCl_3$): δ 11.28 (s, 1H), 10.11 (s, 1H), 8.90 (s, 1H), 8.11 (dd, J = 8.4, 2.1 Hz, 1H), 7.91 (d, J = 8.9 Hz, 2H), 7.75 (dd, J = 9.0, 2.1 Hz, 1H), 7.55 (d, J = 8.4 Hz, 1H), 7.45 (d, J = 1.9 Hz, 1H), 2.48 (s, 3H). HRMS (ESI): *m/z* $[M + H]^+$ calc. for $C_{17}H_{13}BrN_3O_3$: 386.0135; found: 386.0136.

6-bromo-4-((3-nitrophenyl)amino)quinoline-3-carbaldehyde (5d)

Prepared using the procedure described for **5a**. Compound **5d** was obtained as an orange solid (200 mg; 65% yield). ^{1}H NMR (300 MHz, $CDCl_3$): δ 11.27 (s, 1H), 10.12 (s, 1H), 8.93 (s, 1H), 8.14 (dd, J = 8.1, 2.2 Hz, 1H), 8.03 (t, J =2.2 Hz, 1H), 7.93 (d, J = 9.0 Hz, 1H), 7.78 (dd, J = 9.0, 2.1 Hz, 1H), 7.64 (d, J = 2.1 Hz, 1H), 7.60-7.53 (m, 1H), 7.45 (d, J = 8.0 Hz, 1H). ^{13}C NMR (75.5 MHz, $CDCl_3$): δ 193.4, 154.9 150.1, 149.7, 149.1, 142.0, 136.0, 132.2, 130.6, 128.8, 128.6, 120.8, 119.2, 119.1, 118.0, 113.9. HRMS (ESI): *m/z* $[M + H]^+$ calc. for $C_{16}H_{11}BrN_3O_3$: 371.9978; found: 371.9986.

6-bromo-4-((4-methoxy-3-nitrophenyl)amino)quinoline-3-carbaldehyde (5e)

Prepared using the procedure described for **5a**. Compound **5e** was obtained as an orange solid (370 mg; 70% yield). ^{1}H NMR (300 MHz, $CDCl_3$): δ 11.33 (s, 1H), 10.07 (s, 1H), 8.84 (s, 1H), 7.88 (dd, J = 8.9, 2.1 Hz, 1H), 7.77-7.70 (m, 2H), 7.63 (d, J = 2.1 Hz, 1H), 7.38 (dd, J = 8.8, 2.7 Hz, 1H), 7.14 (d, J = 8.9 Hz, 1H), 4.02 (s, 3H). ^{13}C NMR (75.5 MHz, $CDCl_3$): δ 193.3, 155.2, 151.6, 151.0, 149.7, 139.7, 135.8, 133.0, 132.1, 129.9, 128.7, 121.5, 119.0, 118.8, 114.8, 112.9, 57.1. HRMS (ESI): *m/z* $[M + H]^+$ calc. for $C_{17}H_{13}BrN_3O_4$: 402.0084; found: 402.0088.

7-bromo-4-(4-methyl-3-nitrophenylamino)quinoline-3-carbaldehyde (5a')

Prepared using the procedure described for **5a**. Compound **5a'** was obtained as a brown solid (220 mg; 85% yield). ^{1}H NMR (300 MHz, $CDCl_3$): δ 11.29 (s, 1H), 10.06 (s, 1H),

8.85 (s, 1H), 8.18 (d, *J* = 2.0 Hz, 1H), 7.80 (d, *J* = 2.4 Hz, 1H), 7.40 - 7.32 (m, 2H), 7.30 – 7.24 (m, 2H), 2.62 (s, 3H). ^{13}C NMR (75.5 MHz, $CDCl_3$): δ 193.3, 155.9, 151.8, 151.6, 149.7, 139.8, 134.1, 132.9, 131.4, 128.8, 127.9, 127.5, 127.4, 119.5, 116.6, 113.3, 20.2. HRMS (ESI): *m/z* $[M + H]^+$ calc. for $C_{17}H_{13}BrN_3O_3$: 386.0135; found: 386.0135.

7-bromo-4-(3-methyl-5-nitrophenylamino)quinoline-3-carbaldehyde (5b')

Prepared using the procedure described for **5a**. Compound **5b'** was obtained as an orange solid (480 mg; 82% yield). ^{1}H NMR (300 MHz, d^6-DMSO): δ 10.37 (s, 1H), 10.11 (s, 1H), 9.03 (s, 1H), 8.22 (d, *J* = 2.1 Hz, 1H), 7.92 (d, *J* = 9.1 Hz, 1H), 7.78 – 7.75 (m, 2H), 7.67 (dd, *J* = 9.0, 2.1 Hz, 1H), 7.38 (s, 1H), 2.34 (s, 3H). HRMS (ESI): *m/z* $[M + H]^+$ calc. for $C_{17}H_{13}BrN_3O_3$: 386.0135; found: 386.0127.

7-bromo-4-(3-nitrophenylamino)quinoline-3-carbaldehyde (5d')

Prepared using the procedure described for **5a**. Compound **5d'** was obtained as a brown solid (790 mg; 99% yield). ^{1}H NMR (300 MHz, $CDCl_3$): δ 11.32 (s, 1H), 10.10 (s, 1H), 8.92 (s, 1H), 8.23 (d, *J* = 2.0 Hz, 1H), 8.17 – 8.05 (m, 1H), 8.03 – 8.01 (m, 1H), 7.55 (t, *J* = 8.1 Hz, 1H), 7.50 – 7.41 (m, 1H), 7.38 (d, *J* = 9.1 Hz, 1H), 7.29 (dd, *J* = 9.1, 2.0 Hz, 1H). HRMS (ESI): *m/z* $[M + H]^+$ calc. for $C_{16}H_{11}BrN_3O_3$: 371.9978; found: 371.9975.

9-bromo-1-(4-methyl-3-nitrophenyl)benzo[h][1,6]naphthyridin-2(1H)-one (6a)

The aldehyde **5a** (1.74 g; 4.505 mmol), triethylphosphonoacetate (894 µL; 4.505 mmol) and K_2CO_3 (1.87 g; 13.516 mmol; 3 equiv.) were mixed in dry EtOH (30 ml) in a sealed tube under Argon. The mixture was heated to 100ºC overnight. After 16h, the reaction was cooled to rt and the solvent evaporated. The crude was partitioned between H_2O and EtOAc. The aqueous phase was further extracted with EtOAc (3x) and the combined organics washed with brine, dried over $MgSO_4$ and taken to dryness to afford the title compound as a dark brown solid (1.62 g; 88% yield).

9-bromo-1-(3-methyl-5-nitrophenyl)benzo[h][1,6]naphthyridin-2(1H)-one (6b)

Prepared using the procedure described for **6a**. Compound **6b** was obtained as a brown solid (320 mg; 74% yield). ^{1}H NMR (300 MHz, $CDCl_3$): δ 8.97 (s, 1H), 8.33 (s, 1H), 8.09 – 7.88 (m, 3H), 7.67 (dd, *J* = 8.9, 2.1 Hz, 1H), 7.53 (s, 1H), 6.95 (d, *J* = 9.5 Hz, 1H), 6.80 (d, *J* = 2.1 Hz, 1H), 2.58 (s, 3H). ^{13}C NMR (75.5 MHz, $CDCl_3$): δ 162.9, 150.8, 149.4, 148.2, 142.7, 141.2, 140.6, 139.7, 135.6, 133.5, 132.6, 127.5, 125.1, 122.9, 121.4, 120.3,

118.44, 113.8, 21.5. HRMS (ESI): *m/z* $[M + H]^+$ calc. for $C_{19}H_{13}BrN_3O_3$: 410.0135; found: 410.0132.

9-bromo-1-(2-methyl-5-nitrophenyl)benzo[h][1,6]naphthyridin-2(1H)-one (6c)

Prepared using the procedure described for **6a**. Compound **6c** was obtained as a dark brown solid (165 mg; 68% yield). ^{1}H NMR (300 MHz, $CDCl_3$): δ 9.02 (s, 1H), 8.45 (dd, *J* = 8.5, 2.4 Hz, 1H), 8.11 – 7.97 (m, 3H), 7.74 – 7.68 (m, 2H), 7.00 (d, *J* = 9.5 Hz, 1H), 6.80 (d, *J* = 2.0 Hz, 1H), 2.21 (s, 3H). HRMS (ESI): *m/z* $[M + H]^+$ calc. for $C_{19}H_{13}BrN_3O_3$: 410.0135; found: 410.0133.

9-bromo-1-(3-nitrophenyl)benzo[h][1,6]naphthyridin-2(1H)-one (6d)

Prepared using the procedure described for **6a**. Compound **6d** was obtained as a dark brown solid (150 mg; 71% yield). ^{1}H NMR (300 MHz, $CDCl_3$): δ 9.01 (s, 1H), 8.53 (dd, *J* = 8.3, 2.1 Hz, 1H), 8.21 (t, *J* = 2.1 Hz, 1H), 8.00 (dd, *J* = 10.4, 9.2 Hz, 2H), 7.87 (t, *J* = 8.1 Hz, 1H), 7.80 – 7.64 (m, 2H), 6.97 (d, *J* = 9.5 Hz, 1H), 6.80 (d, *J* = 2.1 Hz, 1H). HRMS (ESI): *m/z* $[M + H]^+$ calc. for $C_{18}H_{11}BrN_3O_3$: 395.9978; found: 395.9976.

9-bromo-1-(4-methoxy-3-nitrophenyl)benzo[h][1,6]naphthyridin-2(1H)-one (6e)

Prepared using the procedure described for **6a**. Compound **6e** was obtained as a dark brown solid (255 mg; 65% yield). ^{1}H NMR (300 MHz, d^6-DMSO): δ 9.17 (s, 1H), 8.32 (d, *J* = 9.5 Hz, 1H), 8.17 (d, *J* = 2.5 Hz, 1H), 7.98 (d, *J* = 8.9 Hz, 1H), 7.82 (m, 2H), 7.69 (d, *J* = 9.0 Hz, 1H), 6.96 (d, *J* = 9.4 Hz, 1H), 6.83 (d, *J* = 2.0 Hz, 1H), 4.07 (s, 3H). HRMS (ESI): *m/z* $[M + H]^+$ calc. for $C_{19}H_{13}BrN_3O_4$: 426.0084; found: 426.0090.

8-bromo-1-(4-methyl-3-nitrophenyl)benzo[h][1,6]naphthyridin-2(1H)-one (6a')

Prepared using the procedure described for **6a**. Compound **6a'** was obtained as a brown solid (220 mg; 96% yield). ^{1}H NMR (300 MHz, d^6-DMSO): δ 9.17 (s, 1H), 8.31 (d, *J* = 9.5 Hz, 1H), 8.23 (m, 2H), 7.81 – 7.68 (m, 2H), 7.39 (dd, *J* = 9.4, 2.3 Hz, 1H), 6.94 (d, *J* = 9.5 Hz, 1H), 6.73 (d, *J* = 9.4 Hz, 1H), 2.68 (s, 3H). HRMS (ESI): *m/z* $[M + H]^+$ calc. for $C_{19}H_{13}BrN_3O_3$: 410.0135; found: 410.0134.

8-bromo-1-(3-methyl-5-nitrophenyl)benzo[h][1,6]naphthyridin-2(1H)-one (6b')

Prepared using the procedure described for **6a**. Compound **6b'** was obtained as a brown solid (345 mg; 81% yield). ^{1}H NMR (300 MHz, d^6-DMSO): δ 9.18 (s, 1H), 8.36 – 8.27 (m,

3H), 8.24 (d, *J* = 2.3 Hz, 1H), 7.76 (brs, 1H), 7.36 (dd, *J* = 9.5, 2.3 Hz, 1H), 6.95 (d, *J* = 9.4 Hz, 1H), 6.69 (d, *J* = 9.4 Hz, 1H), 2.48 (s, 3H). HRMS (ESI): *m/z* $[M + H]^+$ calc. for $C_{19}H_{13}BrN_3O_3$: 410.0135; found: 410.0132.

8-bromo-1-(3-nitrophenyl)benzo[h][1,6]naphthyridin-2(1H)-one (6d')

Prepared using the procedure described for **6a**. Compound **6d'** was obtained as a brown solid (500 mg; 60% yield). ^{1}H NMR (300 MHz, d^6-DMSO): δ 9.18 (s, 1H), 8.49 (m, 2H), 8.32 (d, *J* = 9.5 Hz, 1H), 8.24 (d, *J* = 2.3 Hz, 1H), 7.91 – 7.89 (m, 2H), 7.34 (dd, *J* = 9.4, 2.3 Hz, 1H), 6.95 (d, *J* = 9.5 Hz, 1H), 6.65 (d, *J* = 9.4 Hz, 1H). HRMS (ESI): *m/z* $[M + H]^+$ calc. for $C_{18}H_{11}BrN_3O_3$: 395.9978; found: 395.9975

N-(4-(1-(4-methyl-3-nitrophenyl)-2-oxo-1,2-dihydrobenzo[h][1,6]naphthyridin-9-yl)phenyl)methanesulfonamide (7a)

The bromo-quinoline **6a** (280 mg; 0.683 mmol), 4-(methanesulfonylamino) phenyl boronic acid pinacol ester (243 mg; 0.819 mmol; 1.2 equiv.), $PdCl_2(PPh_3)_2$ (48 mg; 0.068 mmol; 0.1 equiv.) and Na_2CO_3 (1.025 ml; 2 M, 2.049 mmol; 3 equiv.) were mixed in dioxane (3 ml) under Argon. The mixture was heated to 90ºC overnight. After 16h, TLC analysis (MeOH:DCM 5:95) showed that the reaction was completed. The mixture was cooled to RT and filtered through a Celite pad. The pad was further washed with EtOH and MeOH/DCM (10%) until no more product was detected by TLC. The solvent was evaporated and the crude applied in a silica column with a gradient up to 2% MeOH in DCM. The desired fractions were collected and evaporated to dryness to afford the title compound as a yellow solid (455 mg; 69%).

N-(4-(1-(3-methyl-5-nitrophenyl)-2-oxo-1,2-dihydrobenzo[h][1,6]naphthyridin-9-yl)phenyl)methanesulfonamide (7b)

Prepared using the procedure described for **7a**. Compound **7b** was obtained as a dark yellow solid (160 mg: 64% yield). ^{1}H NMR (300 MHz, d^6-DMSO): δ 9.92 (brs, 1H), 9.15 (s, 1H), 8.45 – 8.28 (m, 3H), 8.10 (d, *J* = 8.6 Hz, 1H), 7.98 (dd, *J* = 8.7, 1.9 Hz, 1H), 7.89 (s, 1H), 7.20 (d, *J* = 8.6 Hz, 2H), 7.15 – 7.02 (m, 3H), 6.95 (d, *J* = 9.5 Hz, 1H), 3.03 (s, 3H), 2.5 (s, 3H). ^{1}H NMR (300 MHz, $CDCl_3$): δ 9.01 (s, 1H), 8.29 (s, 1H), 8.19 (d, *J* = 8.7 Hz, 1H), 8.09 (m, 1H), 8.03 (d, *J* = 9.5 Hz, 1H), 7.86 (dd, *J* = 8.7, 1.9 Hz, 1H), 7.59 (s, 1H), 7.19 (d, *J* = 8.6 Hz, 2H), 7.12 (d, *J* = 1.9 Hz, 1H), 7.04 (d, *J* = 8.6 Hz, 2H), 6.96 (d, *J*

= 9.4 Hz, 1H), 6.57 (s, 1H), 3.07 (s, 4H), 2.56 (s, 3H). HRMS (ESI): *m/z* $[M + H]^+$ calc. for $C_{26}H_{21}N_4O_5S$: 501.1227; found: 501.1224.

N-(4-(1-(2-methyl-5-nitrophenyl)-2-oxo-1,2-dihydrobenzo[h][1,6]naphthyridin-9-yl)phenyl)methanesulfonamide (7c)

Prepared using the procedure described for **7a**. Compound **7c** was obtained as an orange solid (145 mg; 77% yield). ^{1}H NMR (300 MHz, d^6-acetone): δ 9.14 (s, 1H), 8.74 (brs, 1H), 8.53 – 8.44 (m, 2H), 8.34 (d, *J* = 9.5 Hz, 1H), 8.15 (d, *J* = 8.6 Hz, 1H), 8.03 – 7.91 (m, 2H), 7.38 – 7.31 (m, 2H), 7.23 – 7.13 (m, 3H), 6.95 (d, *J* = 9.5 Hz, 1H), 3.04 (s, 3H), 2.23 (s, 3H). HRMS (ESI): *m/z* $[M + H]^+$ calc. for $C_{26}H_{21}N_4O_5S$: 501.1227; found: 501.1223.

N-(4-(1-(3-nitrophenyl)-2-oxo-1,2-dihydrobenzo[h][1,6]naphthyridin-9-yl)phenyl) methanesulfonamide (7d)

Prepared using the procedure described for **7a**. Compound **7d** was obtained as a yellow solid (85 mg; 51% yield). ^{1}H NMR (300 MHz, d^6-DMSO): δ 9.93 (s, 1H), 9.15 (s, 1H), 8.62 (s, 1H), 8.58 – 8.47 (m, 1H), 8.34 (d, *J* = 9.5 Hz, 1H), 8.10 (d, *J* = 8.7 Hz, 1H), 7.97 (m, 3H), 7.18 (d, *J* = 8.2 Hz, 2H), 7.10 – 6.99 (m, 3H), 6.96 (d, *J* = 9.4 Hz, 1H), 3.03 (s, 3H). HRMS (ESI): *m/z* $[M + H]^+$ calc. for $C_{25}H_{19}N_4O_5S$: 487.1071; found: 487.1071.

N-(4-(1-(4-methoxy-3-nitrophenyl)-2-oxo-1,2-dihydrobenzo[h][1,6]naphthyridin-9-yl)phenyl)methanesulfonamide (7e)

Prepared using the procedure described for **7a**. Compound **7e** was obtained as a dark yellow solid (120 mg; 42% yield). ^{1}H NMR (300 MHz, d^6-acetone): δ 9.06 (s, 1H), 8.83 – 8.74 (brs, 1H), 8.24 (d, *J* = 9.5 Hz, 1H), 8.15 – 8.09 (m, 2H), 7.99 (dd, *J* = 8.7, 1.9 Hz, 1H), 7.82 (dd, *J* = 8.9, 2.6 Hz, 1H), 7.64 (d, *J* = 9.0 Hz, 1H), 7.40 (d, *J* = 8.6 Hz, 2H), 7.30 (d, *J* = 2.2 Hz, 1H), 7.27 (d, *J* = 2.1 Hz, 1H), 7.21 (dd, *J* = 1.9, 0.6 Hz, 1H), 6.88 (d, *J* = 9.5 Hz, 1H), 4.14 (s, 3H), 3.06 (d, *J* = 0.9 Hz, 3H). HRMS (ESI): m/z [M + H]+ calc. for $C_{26}H_{21}N_4O_6S$: 517.1176; found: 517.1176.

N-(4-(1-(4-methyl-3-nitrophenyl)-2-oxo-1,2-dihydrobenzo[h][1,6]naphthyridin-8-yl) phenyl)methanesulfonamide (7a')

Prepared using the procedure described for **7a**. Compound **7a'** was obtained as an orange solid (76 mg; 21%). ^{1}H NMR (300 MHz, d^6-DMSO): δ 9.97 (s, 1H), 9.16 (s, 1H), 8.33 – 8.30 (m, 2H), 8.26 (s, 1H), 7.84 – 7.77 (m, 4H), 7.57 (dd, *J* = 9.3, 2.2 Hz, 1H), 7.30 (d, *J* =

8.7 Hz, 2H), 6.92 – 6.86 (m, 2H), 3.04 (s, 3H), 2.69 (s, 3H). HRMS (ESI): *m/z* $[M + H]^+$ calc. for $C_{26}H_{21}N_4O_5S$: 501.1227; found: 501.1227.

N-(4-(1-(3-methyl-5-nitrophenyl)-2-oxo-1,2-dihydrobenzo[h][1,6]naphthyridin-8-yl)phenyl)methanesulfonamide (7b')

Prepared using the procedure described for **7a**. Compound **7b'** was obtained as an orange solid (400 mg; 95%). HRMS (ESI): *m/z* $[M + H]^+$ calc. for $C_{26}H_{21}N_4O_5S$: 501.1227; found: 501.1232.

N-(4-(1-(3-nitrophenyl)-2-oxo-1,2-dihydrobenzo[h][1,6]naphthyridin-8-yl)phenyl)methanesulfonamide (7d')

Prepared using the procedure described for **7a**. Compound **7d'** was obtained as an orange solid (90 mg; 31%). ^{1}H NMR (300 MHz, d^6-DMSO): δ 9.92 (brs, 1H), 9.16 (s, 1H), 8.52 – 8.49 (m, 2H), 8.34 – 8.29 (m, 2H), 7.95 – 7.93 (m, 2H), 7.79 (d, *J* = 8.8 Hz, 2H), 7.52 (dd, *J* = 9.3, 2.2 Hz, 1H), 7.29 (d, *J* = 8.8 Hz, 2H), 6.91 (d, *J* = 9.4 Hz, 1H), 6.76 (d, *J* = 9.3 Hz, 1H), 3.03 (s, 3H). HRMS (ESI): *m/z* $[M + H]^+$ calc. for $C_{25}H_{19}N_4O_5S$: 487.1071; found: 487.1069.

Ethyl 4-(4-methyl-3-nitrophenylamino)-6-(4-(methylsulfonamido)phenyl)quinoline-3-carboxylate

Prepared using the procedure described for **7a**, from intermediate **3a**. Compound **INT1** was obtained as a yellow solid (265 mg; 73%). ^{1}H NMR (300 MHz, $CDCl_3$): δ 10.52 (s, 1H), 9.29 (s, 1H), 8.10 (d, *J* = 8.7 Hz, 1H), 7.87 (dd, *J* = 8.7, 2.0 Hz, 1H), 7.72 (d, *J* = 2.0 Hz, 1H), 7.67 (d, *J* = 2.5 Hz, 1H), 7.59 – 7.41 (m, 2H), 7.20 - 7.16 (m, 5H), 4.46 (q, *J* = 7.1 Hz, 2H), 3.03 (s, 3H), 2.58 (s, 3H), 1.47 (t, *J* = 7.1 Hz, 3H). HRMS (ESI): *m/z* $[M + H]^+$ calc. for $C_{26}H_{25}N_4O_6S$: 521.1489; found: 521.1486.

N-(4-(1-(4-methyl-3-nitrophenyl)-2-oxo-1,2-dihydrobenzo[h][1,6]naphthyridin-9-yl)phenyl)butane-1-sulfonamide (7f – precursor of 14)

Prepared using General Procedure E, reacting intermediate **6a** with 4-(butylsulfonamido)phenylboronic acid. Compound **7f** was isolated as a yellow solid (200 mg; 53% yield). ^{1}H NMR (300 MHz, d^6-DMSO): δ 9.98 (s, 1H), 9.13 (s, 1H), 8.44 – 8.26 (m, 2H), 8.09 (d, *J* = 8.7 Hz, 1H), 7.98 (d, *J* = 8.6 Hz, 1H), 7.82-7.74 (m, 2H), 7.24 (d, *J* = 8.2 Hz, 2H), 7.09 (d, *J* = 8.2 Hz, 2H), 6.95 (d, *J* = 8.2 Hz, 2H), 3.12 (t, *J* = 7.9 Hz, 3H),

2.65 (s, 3H), 1.65 (m, 2H), 1.36 (m, 2H), 0.84 (t, *J* = 7.2 Hz, 3H). HRMS (ESI): *m/z* [M + H]$^+$ calc. for $C_{29}H_{27}N_4O_5S$: 543.1697; found: 543.1694.

N-(3-(1-(4-methyl-3-nitrophenyl)-2-oxo-1,2-dihydrobenzo[h][1,6]naphthyridin-9-yl) phenyl)methanesulfonamide (7g – precursor of 15)

Prepared using General Procedure E, reacting intermediate **6a** with 3-(methanesulfonylamino)phenylboronic acid pinacol ester. Compound **7g** was isolated as an orange solid (235 mg; 67% yield). ^{1}H NMR (300 MHz, d^6-DMSO): δ 9.81 (s, 1H), 9.16 (s, 1H), 8.34 (d, *J* = 9.5 Hz, 1H), 8.29 (m, 1H), 8.15 (d, *J* = 8.6 Hz, 1H), 7.91 (dd, *J* = 8.7, 1.9 Hz, 1H), 7.79 (d, *J* = 1.3 Hz, 2H), 7.35 (t, *J* = 7.8 Hz, 1H), 7.27 – 7.15 (m, 2H), 7.05 (d, *J* = 1.8 Hz, 1H), 6.95 (d, *J* = 9.4 Hz, 1H), 6.58 (dt, *J* = 8.0, 1.2 Hz, 1H), 3.00 (s, 3H), 2.66 (s, 3H). HRMS (ESI): *m/z* [M + H]$^+$ calc. for $C_{26}H_{21}N_4O_5S$: 501.1227; found: 501.1228.

Methyl 4-(1-(4-methyl-3-nitrophenyl)-2-oxo-1,2-dihydrobenzo[h][1,6]naphthyridin-9-yl)phenylcarbamate (7h – precursor of 16)

Prepared using General Procedure E, reacting intermediate **6a** with 4-(methoxycarbonylamino)benzeneboronic acid. Compound **7h** was isolated as an orange solid (166 mg; 50% yield). ^{1}H NMR (300 MHz, d^6-DMSO): δ 9.82 (s, 1H), 9.13 (s, 1H), 8.33 (dd, *J* = 9.4, 1.5 Hz, 2H), 8.08 (dd, *J* = 8.6, 1.4 Hz, 1H), 8.04 – 7.93 (m, 1H), 7.86 – 7.72 (m, 2H), 7.56 – 7.46 (m, 2H), 7.06 (dd, *J* = 8.7, 1.5 Hz, 2H), 7.03 – 6.91 (m, 2H), 3.69 (s, 3H), 2.68 (s, 3H). HRMS (ESI): *m/z* [M + H]$^+$ calc. for $C_{27}H_{21}N_4O_5$: 481.1506; found: 481.1507.

1-(4-methyl-3-nitrophenyl)-9-(pyridin-4-yl)benzo[h][1,6]naphthyridin-2(1H)-one (7i – precursor of 17)

Prepared using General Procedure E, reacting intermediate **6a** with pyridine-4-boronic acid hydrate. Compound **7i** was isolated as an orange solid (90 mg; 45% yield). ^{1}H NMR (300 MHz, d^6-DMSO): δ 9.21 (s, 1H), 8.64 – 8.56 (m, 2H), 8.40 – 8.31 (m, 2H), 8.20 – 8.14 (m, 1H), 8.11 (dd, *J* = 8.7, 1.9 Hz, 1H), 7.87 – 7.75 (m, 3H), 7.15 – 7.12 (m, 2H), 6.98 (d, *J* = 9.5 Hz, 1H), 2.66 (s, 3H). HRMS (ESI): *m/z* [M + H]$^+$ calc. for $C_{24}H_{17}N_4O_3$: 409.1295; found: 409.1293.

5-(1-(4-methyl-3-nitrophenyl)-2-oxo-1,2-dihydrobenzo[h][1,6]naphthyridin-9-yl)picolinonitrile (7j – precursor of 18)

Prepared using General Procedure E, reacting intermediate **6a** with 6-(cyanopyridin-3-yl)boronic acid. Compound **7i** was isolated as an orange solid (92 mg; 44% yield). ^{1}H NMR (300 MHz, d^6-DMSO): δ 9.22 (s, 1H), 8.50 (m, 1H), 8.36 (d, *J* = 9.5 Hz, 1H), 8.29 (s, 1H), 8.20 (d, *J* = 8.6 Hz, 1H), 8.16 - 8.14 (m, 1H), 7.80 (m, 2H), 7.65 – 7.52 (m, 3H), 6.98 (d, *J* = 9.5 Hz, 1H), 2.66 (s, 3H). HRMS (ESI): *m/z* $[M + H]^+$ calc. for $C_{25}H_{16}N_5O_3$: 434.1248; found: 434.1245.

1-(4-methyl-3-nitrophenyl)-9-(6-(trifluoromethyl)pyridin-3-yl)benzo[h][1,6]naphthyridin-2(1H)-one (7k – precursor of 19)

Prepared using General Procedure E, reacting intermediate **6a** with 2-Trifluoromethyl(pyridin-5-yl)boronic acid. Compound **7i** was isolated as an orange solid (110 mg; 47% yield). ^{1}H NMR (300 MHz, d^6-DMSO): δ 9.22 (s, 1H), 8.53 (d, *J* = 2.1 Hz, 1H), 8.36 (d, *J* = 9.5 Hz, 1H), 8.29 (s, 1H), 8.20 (d, *J* = 8.7 Hz, 1H), 8.13 (dd, *J* = 8.7, 1.9 Hz, 1H), 7.95 (d, *J* = 8.2 Hz, 1H), 7.83 (m, 1H), 7.65 – 7.54 (m, 3H), 6.97 (s, 1H), 2.62 (s, 3H). HRMS (ESI): *m/z* $[M + H]^+$ calc. for $C_{25}H_{16}F_3N_4O_3$: 477.1169; found: 477.1168.

1-(4-methyl-3-nitrophenyl)-9-(piperidin-1-yl)benzo[h][1,6]naphthyridin-2(1H)-one (7l - precursor of 20)

The bromo-quinoline **6a** (250 mg; 0.609 mmol), piperidine (180 µL; 1.827 mmol; 3 equiv.), $Pd(OAc)_2$ (8.4 mg; 37.4 µmol; 0.06 equiv.), R-BINAP (46 mg: 73.1 µmol; 0.12 equiv.) and Cs_2CO_3 (595 mg,1.827 mmol; 3 equiv.) were mixed in dioxane (5 ml) under Argon. The mixture was heated to 90ºC overnight. After 24h, LCMS analysis showed that the reaction was completed. The mixture was cooled to rt and the solvent evaporated. The crude was partitioned between EtOAc and sat $NaHCO_3$. The phases were separated and the aqueous phase further extracted with EtOAc (2x). The combined organics were washed with brine and dried over $MgSO_4$. After filtration, the solvent was evaporated to afford the title compound as a yellow solid. The compound was used without further purification (180 mg; 71% yield). ^{1}H NMR (300 MHz, d^6-DMSO): δ 8.87 (s, 1H), 8.26 – 8.18 (m, 2H), 7.84 (d, *J* = 9.2 Hz, 1H), 7.76 (d, *J* = 8.2 Hz, 1H), 7.70 (dd, *J* = 8.2, 2.1 Hz, 1H), 7.50 - 7.46 (m, 1H), 6.85 (d, *J* = 9.4 Hz, 1H), 6.23 (d, *J* = 2.6 Hz, 1H), 2.74 (m, 4H), 2.60 (s, 3H),

1.45 (m, 6H). HRMS (ESI): *m/z* $[M + H]^+$ calc. for $C_{24}H_{23}N_4O_3$: 415.1765; found: 415.1763.

1-(4-methyl-3-nitrophenyl)-9-morpholinobenzo[h][1,6]naphthyridin-2(1H)-one (7m – precursor of 21)

Prepared using General Procedure F, using morpholine as amine. Compound **7m** was isolated as an orange solid (290 mg; 95% yield). ^{1}H NMR (300 MHz, d^6-DMSO): δ 8.91 (s, 1H), 8.35 – 8.17 (m, 2H), 7.89 (d, *J* = 9.2 Hz, 1H), 7.81 – 7.65 (m, 2H), 7.53 (dd, *J* = 9.2, 2.6 Hz, 1H), 6.87 (d, *J* = 9.4 Hz, 1H), 6.23 (d, *J* = 2.6 Hz, 1H), 3.62 (m, 4H), 2.68 (m, 4H), 2.58 (s, 3H). HRMS (ESI): *m/z* $[M + H]^+$ calc. for $C_{23}H_{21}N_4O_4$: 417.1557; found: 417.1557.

1-(4-methyl-3-nitrophenyl)-9-(4-(methylsulfonyl)piperazin-1-yl)benzo[h][1,6]naphthyridin-2(1H)-one (7n– precursor of 22)

Prepared using General Procedure F, using 1-(Methylsulfonyl)piperazine as amine. Compound **7n** was isolated as a yellow solid (285 mg; 95% yield). ^{1}H NMR (300 MHz, $CDCl_3$): δ 8.83 (s, 1H), 8.10 – 7.86 (m, 3H), 7.69 – 7.52 (m, 2H), 7.35 (dd, *J* = 9.3, 2.6 Hz, 1H), 6.90 (d, *J* = 9.3 Hz, 1H), 6.36 (d, *J* = 2.6 Hz, 1H), 3.25 (t, *J* = 5.0 Hz, 4H), 2.95 – 2.89 (m, 2H), 2.85 – 2.82 (m, 2H), 2.82 (s, 3H), 2.71 (s, 3H).HRMS (ESI): *m/z* $[M + H]^+$ calc. for $C_{24}H_{24}N_5O_5S$: 494.1493; found: 494.1492.

9-(4-(dimethylamino)piperidin-1-yl)-1-(4-methyl-3-nitrophenyl)benzo[h][1,6]naphthayridin-2(1H)-one (7o – precursor of 23)

Prepared using General Procedure F, using N,N-dimethylpiperidin-4-amine as amine. Compound **7o** was isolated as a yellow solid (215 mg; 77% yield). ^{1}H NMR (300 MHz, d^6-DMSO): δ 8.87 (s, 1H), 8.23 (m, 2H), 7.85 (d, *J* = 9.2 Hz, 1H), 7.77 (d, *J* = 8.4 Hz, 1H), 7.70 (dd, *J* = 8.1, 2.1 Hz, 1H), 7.51 (m, 1H), 6.85 (d, *J* = 9.4 Hz, 1H), 6.25 (d, *J* = 2.6 Hz, 1H), 3.23 – 3.18 (m, 2H), 2.62 (s, 3H), 2.44 – 2.37 (m, 2H), 2.15 (s, 3H), 2.15 (m, 1H), 1.66 – 1.62 (m, 2H), 1.28 – 1.23 (m, 2H). HRMS (ESI): *m/z* $[M + H]^+$ calc. for $C_{26}H_{28}N_5O_3$: 458.2187; found: 458.2185.

8-(4-(methylsulfonyl)piperazin-1-yl)-1-(3-nitrophenyl)benzo[h][1,6]naphthyridin-2(1H)-one (7d'n'- precursor of 27)

Prepared using the General Procedure F, reacting intermediate **6d** with 1-(Methylsulfonyl)piperazine. Compound **7d'n'** was obtained as a brown solid (355 mg; 98%). HRMS (ESI): *m/z* $[M + H]^+$ calc. for $C_{23}H_{22}N_5O_5S$: 480.1336; found: 480.1330.

N-(4-(1-(3-amino-4-methylphenyl)-2-oxo-1,2-dihydrobenzo[h][1,6]naphthyridin-9-yl) phenyl)methanesulfonamide (8a)

Intermediate **7a** (335 mg; 0.669 mmol) was suspended in EtOH (40 ml) and heated to reflux. Fe (224 mg; 4.016 mmol; 6 equiv.) and NH_4Cl (215 mg; 4.016 mmol; 6 equiv.) in H_2O (20 ml) were added and the mixture heated to reflux. After 2h, TLC analysis (MeOH:DCM 1:9) showed that the reaction was completed. The hot mixture was filtered through a Celite pad and the pad further washed with EtOH and MeOH:DCM (2:8). The solvent was evaporated and the crude partitioned between H_2O and EtOAc. The phases were separated and the aqueous phase was further extracted with EtOAc (3x). The combined organics were washed with brine, dried over $MgSO_4$ and taken to dryness to afford the title compound as an off-white solid (330 mg; 100% yield).

N-(4-(1-(3-amino-5-methylphenyl)-2-oxo-1,2-dihydrobenzo[h][1,6]naphthyridin-9-yl) phenyl)methanesulfonamide (8b)

Prepared using the procedure described for **8a**. Compound **8b** was obtained as a bright-yellow solid (85 mg; 70% yield). ^{1}H NMR (300 MHz, d^6-DMSO): δ 9.90 (s, 1H), 9.07 (s, 1H), 8.25 (d, *J* = 9.4 Hz, 1H), 8.03 (q, *J* = 8.9 Hz, 2H), 7.70 (s, 1H), 7.35 – 7.21 (m, 4H), 6.87 (d, *J* = 9.5 Hz, 1H), 6.66 (s, 1H), 6.48 (s, 1H), 6.29 (s, 1H), 5.40 (s, 2H), 3.04 (s, 3H), 2.25 (s, 3H). HRMS (ESI): *m/z* $[M + H]^+$ calc. for $C_{26}H_{23}N_4O_3S$: 471.1485; found: 471.1484.

N-(4-(1-(5-amino-2-methylphenyl)-2-oxo-1,2-dihydrobenzo[h][1,6]naphthyridin-9-yl) phenyl)methanesulfonamide (8c)

Prepared using the procedure described for **8a**. Compound **8c** was obtained as an orange solid (70 mg; 68% yield). ^{1}H NMR (300 MHz, d^6-DMSO): δ 9.91 (s, 1H), 9.11 (s, 1H), 8.30 (d, *J* = 9.5 Hz, 1H), 8.12 – 7.97 (m, 2H), 7.53 (d, *J* = 1.8 Hz, 1H), 7.32 (d, *J* = 8.7 Hz, 2H), 7.27 – 7.16 (m, 3H), 6.92 (d, *J* = 9.4 Hz, 1H), 6.79 (dd, *J* = 8.2, 2.3 Hz, 1H), 6.45 (d, *J*

= 2.3 Hz, 1H), 5.29 (s, 2H), 3.05 (s, 3H), 1.80 (s, 3H). HRMS (ESI): *m/z* $[M + H]^+$ calc. for $C_{26}H_{23}N_4O_3S$: 471.1485; found 471.1485.

N-(4-(1-(3-nitrophenyl)-2-oxo-1,2-dihydrobenzo[h][1,6]naphthyridin-9-yl)phenyl)methanesulfonamide (8d)

Prepared using the procedure described for **8a**. Compound **8d** was obtained as a dark yellow solid (60 mg; 92% yield). ^{1}H NMR (300 MHz, d^6-DMSO): δ 9.91 (s, 1H), 9.09 (s, 1H), 8.27 (d, *J* = 9.5 Hz, 1H), 8.11 – 7.95 (m, 2H), 7.60 (d, *J* = 1.9 Hz, 1H), 7.36 – 7.27 (m, 3H), 7.23 (d, *J* = 8.8 Hz, 2H), 6.92 – 6.79 (m, 2H), 6.57 (dd, *J* = 6.7, 1.2 Hz, 2H), 5.55 (brs, 2H), 3.04 (s, 3H). HRMS (ESI): *m/z* $[M + H]^+$ calc. for $C_{25}H_{21}N_4O_3S$: 457.1329; found: 457.1328.

N-(4-(1-(3-amino-4-methoxyphenyl)-2-oxo-1,2-dihydrobenzo[h][1,6]naphthyridin-9-yl)phenyl)methanesulfonamide (8e)

Prepared using the procedure described for **8a**. Compound **8e** was obtained as an orange solid (85 mg; 78% yield). ^{1}H NMR (300 MHz, d^6-DMSO): δ 9.93 (s, 1H), 9.07 (s, 1H), 8.26 (d, *J* = 9.5 Hz, 1H), 8.05 (d, *J* = 8.7 Hz, 1H), 7.97 (dd, *J* = 8.7, 1.9 Hz, 1H), 7.37 (d, *J* = 1.9 Hz, 1H), 7.32 – 7.18 (m, 4H), 7.05 (d, *J* = 8.3 Hz, 1H), 6.88 (d, *J* = 9.4 Hz, 1H), 6.67 – 6.53 (m, 2H), 5.11 (s, 2H), 3.91 (s, 3H), 3.04 (s, 3H). HRMS (ESI): *m/z* $[M + H]^+$ calc. for $C_{26}H_{23}N_4O_4S$: 487.1435; found: 487.1433.

N-(4-(1-(3-amino-4-methylphenyl)-2-oxo-1,2-dihydrobenzo[h][1,6]naphthyridin-8-yl)phenyl)methanesulfonamide (8a')

Prepared using the procedure described for **8a**. Compound **8a'** was obtained as a bright-yellow solid (80 mg; 71% yield). ^{1}H NMR (300 MHz, d^6-DMSO): δ 9.96 (s, 1H), 9.10 (s, 1H), 8.26 – 8.23 (m, 2H), 7.84 (d, *J* = 8.7 Hz, 2H), 7.52 (dd, *J* = 9.4, 2.2 Hz, 1H), 7.30 (d, *J* = 8.7 Hz, 2H), 7.15 (m, 2H), 6.84 (d, *J* = 9.4 Hz, 1H), 6.56 (d, *J* = 2.1 Hz, 1H), 6.48 (dd, *J* = 7.8, 2.1 Hz, 1H), 5.20 (s, 2H), 3.04 (s, 3H), 2.21 (s, 3H). HRMS (ESI): *m/z* $[M + H]^+$ calc. for $C_{26}H_{23}N_4O_3S$: 471.1485; found: 471.1483.

N-(4-(1-(3-amino-5-methylphenyl)-2-oxo-1,2-dihydrobenzo[h][1,6]naphthyridin-8-yl)phenyl)methanesulfonamide (8b')

Prepared using the procedure described for **8a**. Compound **8b'** was obtained as an orange solid (295 mg; 70% yield). ^{1}H NMR (300 MHz, d^6-DMSO): δ 9.99 (s, 1H), 9.09 (s, 1H),

8.25 – 8.22 (m, 2H), 7.86 - 7.81 (m, 4H), 7.54 (dd, *J* = 9.4, 2.3 Hz, 1H), 7.30 (d, *J* = 8.5 Hz, 2H), 7.21 (d, *J* = 9.3 Hz, 1H), 6.84 (d, *J* = 9.4 Hz, 1H), 6.61 (s, 1H), 6.34 (s, 2H), 3.04 (s, 3H), 2.22 (s, 3H). HRMS (ESI): *m/z* $[M + H]^+$ calc. for $C_{26}H_{23}N_4O_3S$: 471.1485; found: 471.1483.

N-(4-(1-(3-aminophenyl)-2-oxo-1,2-dihydrobenzo[h][1,6]naphthyridin-8-yl)phenyl)methanesulfonamide (8d')

Prepared using the procedure described for **8a**. Compound **8d'** was obtained as a brown solid (140 mg; 85% yield). ^{1}H NMR (300 MHz, d^6-DMSO): δ 9.09 (s, 1H), 8.26 – 8.22 (m, 2H), 7.79 – 7.77 (m, 2H), 7.50 (dd, *J* = 9.3, 2.2 Hz, 1H), 7.29 – 7.23 (m, 3H), 7.12 (d, *J* = 9.3 Hz, 1H), 6.85 – 6.78 (m, 2H), 6.53 – 6.50 (m, 2H), 5.42 (s, 2H), 2.97 (s, 3H). HRMS (ESI): *m/z* $[M + H]^+$ calc. for $C_{25}H_{21}N_4O_3S$: 457.1329; found: 457.1329.

Ethyl 4-(3-amino-4-methylphenylamino)-6-(4-(methylsulfonamido)phenyl)quinoline-3-carboxylate

Prepared using the procedure described for **8a**. Compound **INT2** was obtained as a yellow solid (190 mg; 88%). ^{1}H NMR (300 MHz, d^6-DMSO): δ 10.14 (s, 1H), 9.88 (s, 1H), 8.94 (s, 1H), 8.08 (d, *J* = 2.0 Hz, 1H), 8.04 – 7.96 (m, 1H), 7.92 (d, *J* = 8.7 Hz, 1H), 7.67 – 7.50 (m, 2H), 7.39 (d, *J* = 8.7 Hz, 2H), 7.23 (d, *J* = 8.7 Hz, 2H), 6.97 (d, *J* = 7.9 Hz, 1H), 6.45 (d, *J* = 2.2 Hz, 1H), 6.33 (dd, *J* = 7.9, 2.2 Hz, 1H), 4.19 (q, *J* = 7.1 Hz, 2H), 3.02 (s, 3H), 2.11 (s, 3H), 1.29 (t, *J* = 7.1 Hz, 3H). HRMS (ESI): *m/z* $[M + H]^+$ calc. for $C_{26}H_{27}N_4O_4S$: 491.1753; found: 491.1748.

N-(4-(1-(3-amino-4-methylphenyl)-2-oxo-1,2-dihydrobenzo[h][1,6]naphthyridin-9-yl) phenyl)butane-1-sulfonamide (8f – precursor of 15)

Prepared using the procedure described for **8a**. Compound **8f** was obtained as a bright-yellow solid (163 mg; 91% yield). ^{1}H NMR (300 MHz, d^6-DMSO): δ 9.92 (s, 1H), 9.06 (s, 1H), 8.25 (d, *J* = 9.5 Hz, 1H), 8.04 (d, *J* = 8.6 Hz, 1H), 7.96 (dd, *J* = 8.7, 1.9 Hz, 1H), 7.70 – 7.48 (m, 2H), 7.39 (d, *J* = 1.9 Hz, 1H), 7.30 – 7.13 (m, 5H), 6.87 (d, *J* = 9.4 Hz, 1H), 6.61 (d, *J* = 2.1 Hz, 1H), 6.51 (dd, *J* = 7.8, 2.1 Hz, 1H), 3.12 (t, *J* = 7.4 Hz, 2H), 2.25 (s, 3H), 1.76 – 1.58 (m, 2H), 1.47 – 1.29 (m, 2H), 0.85 (t, *J* = 7.3 Hz, 3H). HRMS (ESI): *m/z* $[M + H]^+$ calc. for $C_{29}H_{29}N_4O_3S$: 513.1955; found: 513.1954.

N-(3-(1-(3-amino-4-methylphenyl)-2-oxo-1,2-dihydrobenzo[h][1,6]naphthyridin-8-yl) phenyl)methanesulfonamide (8g – precursor of 16)

Prepared using the procedure described for **8a**. Compound **8g** was obtained as a bright-yellow solid (75 mg; 94% yield). HRMS (ESI): *m/z* $[M + H]^+$ calc. for $C_{26}H_{23}N_4O_3S$: 471.1484; found: 471.1485.

Methyl 4-(1-(3-amino-4-methylphenyl)-2-oxo-1,2-dihydrobenzo[h][1,6]naphthyridin-9-yl)phenylcarbamate (8h – precursor of 17)

Prepared using the procedure described for **8a**. Compound **8h** was obtained as a bright-yellow solid (147 mg; 100% yield). ^{1}H NMR (300 MHz, d^6-DMSO): δ 9.77 (s, 1H), 9.06 (s, 1H), 8.25 (d, *J* = 9.4 Hz, 1H), 8.08 – 7.91 (m, 2H), 7.51 (d, *J* = 8.3 Hz, 2H), 7.43 (d, *J* = 1.8 Hz, 1H), 7.22 – 7.18 (m, 3H), 6.87 (d, *J* = 9.4 Hz, 1H), 6.61 (d, *J* = 2.1 Hz, 1H), 6.51 (dd, *J* = 7.8, 2.1 Hz, 1H), 5.25 (brs, 2H), 3.70 (s, 3H), 2.27 (s, 3H). HRMS (ESI): *m/z* $[M + H]^+$ calc. for $C_{27}H_{23}N_4O_3$: 451.1765; found: 451.1763.

1-(3-amino-4-methylphenyl)-9-(pyridin-4-yl)benzo[h][1,6]naphthyridin-2(1H)-one (8i – precursor of 18)

Prepared using the procedure described for **8a**. During phase separation, the aqueous phase (pH~5) was adjusted to pH 7 with $NaHCO_3$. Compound **8i** was obtained as an orange solid (75 mg; 100% yield). ^{1}H NMR (300 MHz, d^6-DMSO): δ 9.14 (s, 1H), 8.64 – 8.55 (m, 2H), 8.28 (d, *J* = 9.5 Hz, 1H), 8.11 (s, 2H), 7.51 (s, 1H), 7.31 – 7.23 (m, 2H), 7.20 (d, *J* = 8.2 Hz, 1H), 6.90 (d, *J* = 9.4 Hz, 1H), 6.66 (d, *J* = 2.1 Hz, 1H), 6.49 (dd, *J* = 7.8, 2.1 Hz, 1H), 5.33 (s, 2H), 2.25 (s, 3H). HRMS (ESI): *m/z* $[M + H]^+$ calc. for $C_{24}H_{19}N_4O$: 379.1553; found: 379.1552.

5-(1-(3-amino-4-methylphenyl)-2-oxo-1,2-dihydrobenzo[h][1,6]naphthyridin-9-yl)picolinonitrile (8j – precursor of 19)

Prepared using the procedure described for **8a**. Compound **8j** was obtained as an orange solid (79 mg; 97% yield). HRMS (ESI): *m/z* $[M + H]^+$ calc. for $C_{25}H_{18}N_5O$: 404.1506; found: 404.1507.

1-(3-amino-4-methylphenyl)-9-(6-(trifluoromethyl)pyridin-3-yl)benzo[h][1,6]naphthyridin-2(1H)-one (8k – precursor of 20)

Prepared using the procedure described for **8a**. Compound **8k** was obtained as an orange solid (99 mg; 100% yield). ^{1}H NMR (300 MHz, d^6-DMSO): δ 9.15 (s, 1H), 8.67 (d, *J* = 2.1 Hz, 1H), 8.29 (d, *J* = 9.5 Hz, 1H), 8.13 (brs, 2H), 7.95 (m, 1H), 7.88 (m, 1H), 7.33 (s, 1H), 7.19 (d, *J* = 7.8 Hz, 1H), 6.92 (d, *J* = 9.4 Hz, 1H), 6.64 (d, *J* = 2.1 Hz, 1H), 6.51 (dd, *J* = 7.7, 2.1 Hz, 1H), 5.33 (s, 2H), 2.21 (s, 3H). HRMS (ESI): *m/z* [M + H]$^+$ calc. for $C_{25}H_{18}F_3N_4O$: 447.1427; found: 447.1426.

1-(3-amino-4-methylphenyl)-9-(piperidin-1-yl)benzo[h][1,6]naphthyridin-2(1H)-one (8l – precursor of 21)

Prepared using the procedure described for **8a**. Compound **8l** was obtained as a yellow solid (134 mg; 85% yield). HRMS (ESI): *m/z* [M + H]$^+$ calc. for $C_{24}H_{25}N_4O$: 385.2023; found: 385.2025.

1-(3-amino-4-methylphenyl)-9-morpholinobenzo[h][1,6]naphthyridin-2(1H)-one (8m – precursor of 22)

Prepared using the procedure described for **8a**. Compound **8m** was obtained as an orange solid (141 mg; 95% yield).HRMS (ESI): *m/z* [M + H]$^+$ calc. for $C_{23}H_{23}N_4O_2$: 387.1816; found: 387.1817.

Synthesis of 1-(3-amino-4-methylphenyl)-9-(4-(methylsulfonyl)piperazin-1-yl)benzo[h][1,6]naphthyridin-2(1H)-one (8n)

Prepared using the procedure described for **8a**. Compound **8n** was obtained as a yellow solid (285 mg; 88% yield). ^{1}H NMR (300 MHz, $CDCl_3$): δ 8.79 (s, 1H), 7.94 (dd, *J* = 16.9, 9.3 Hz, 2H), 7.33 (dd, *J* = 9.2, 2.6 Hz, 1H), 7.27 (m, 1H), 6.90 (d, *J* = 9.4 Hz, 1H), 6.78 (d, *J* = 2.6 Hz, 1H), 6.68 (d, *J* = 6.4 Hz, 2H), 3.83 (s, 2H), 3.26 – 3.22 (m, 4H), 2.99 – 2.96 (m, 4H), 2.82 (s, 3H), 2.26 (s, 3H). HRMS (ESI): *m/z* [M + H]$^+$ calc. for $C_{24}H_{26}N_5O_3S$: 464.1751; found: 464.1748.

1-(3-amino-4-methylphenyl)-9-(4-(dimethylamino)piperidin-1-yl)benzo[h][1,6]naphthayridin-2(1H)-one (8o – precursor of 23)

Prepared using the procedure described for **8a**. The reaction required 12 eq. of Fe and NH_4Cl and 5h reaction time at 80ºC. During phase separation, the aqueous phase (pH~5)

was adjusted to pH 8 with $NaHCO_3$. Compound **8o** was obtained as a yellow solid (85 mg; 46% yield). ^{1}H NMR (300 MHz, d^6-DMSO): δ 8.81 (s, 1H), 8.16 (d, *J* = 9.4 Hz, 1H), 7.79 (d, *J* = 9.1 Hz, 1H), 7.46 (dd, *J* = 9.4, 2.4 Hz, 1H), 7.13 (d, *J* = 7.8 Hz, 1H), 6.79 (d, *J* = 9.4, 1H), 6.71 (brs, 1H), 6.57 (d, *J* = 1.8 Hz, 1H), 6.49 – 6.37 (m, 1H), 5.22 (s, 2H), 3.34 – 3.30 (m, 2H), 2.50 (s, 3H), 2.42 – 2.36 (m, 2H), 2.16 (s, 6H), 2.16 (m, 1H), 1.70 – 1.66 (m, 2H), 1.30 – 1.22 (m, 2H). HRMS (ESI): *m/z* $[M + H]^+$ calc. for $C_{26}H_{30}N_5O$: 428.2445; found: 428.2442.

1-(3-aminophenyl)-8-(4-(methylsulfonyl)piperazin-1-yl)benzo[h][1,6]naphthyridin-2(1H)-one (8d'n' – precursor of JS27)

Prepared using the procedure described for **8a**. Compound **8d'n'** was obtained as an orange solid (225 mg; 71% yield). ^{1}H NMR (300 MHz, $CDCl_3$): δ 8.92 (s, 1H), 8.14 (d, *J* = 9.4 Hz, 1H), 7.28 – 7.21 (m, 2H), 7.03 – 6.96 (m, 1H), 6.86 (d, *J* = 9.8 Hz, 1H), 6.77 – 6.68 (m, 2H), 6.46 (brs, 2H), 5.43 (s, 2H), 3.43 (m, 4H,) 3.20 (m, 4H), 2.89 (s, 3H). HRMS (ESI): *m/z* $[M + H]^+$ calc. for $C_{23}H_{24}N_5O_3S$: 450.1594; found: 450.1600

1-(3-amino-4-methylphenyl)-9-bromobenzo[h][1,6]naphthyridin-2(1H)-one

Intermediate **6a** (1.03 g; 2.511 mmol) was suspended in EtOAc (50 ml) and $SnCl_2$ (2.86 g; 15.065 mmol; 6 equiv.) was added. The mixture was heated to 85ºC and after 2h, the reaction cooled to rt and saturated $NaHCO_3$ aq. was added. The phases were separated and the aqueous phase further extracted with ethyl acetate (2x). The combined organics were washed with brine, dried over MgSO4, taken to dryness to afford **INT3** as a brownish solid (650 mg; 68% yield). ^{1}H NMR (300 MHz, d^6-DMSO): δ 9.11 (s, 1H), 8.25 (d, *J* = 9.4 Hz, 1H), 7.91 (d, *J* = 8.9 Hz, 1H), 7.78 (dd, *J* = 8.9, 2.1 Hz, 1H), 7.18 (d, *J* = 7.8 Hz, 1H), 6.99 (d, *J* = 2.1 Hz, 1H), 6.90 (d, *J* = 9.4 Hz, 1H), 6.53 (d, *J* = 2.1 Hz, 1H), 6.45 (dd, *J* = 7.7, 2.1 Hz, 1H), 5.24 (s, 2H), 2.22 (s, 3H). HRMS (ESI): *m/z* $[M + H]^+$ calc. for $C_{19}H_{15}BrN_3O$: 380.0393; found: 380.0390.

N-(2-methyl-5-(9-(4-(methylsulfonamido)phenyl)-2-oxobenzo[h][1,6]naphthyridin-1(2H)-yl)phenyl)acrylamide (9a; BMX-IN-1)

A stirred solution of **8a** (90 mg; 0.191 mmol) in dry THF (20 ml) was cooled in an ice-bath to -10ºC for 20 min. DIPEA (133 uL; 0.765 mmol; 4 equiv.) was added and the mixture stirred for 10 min at T < 4ºC. After 10 min, acryloyl chloride was added and the mixture further stirred at -10ºC for 10 min. and then 1h at rt. THF was then evaporated and the

crude redissolved in EtOAc and washed three times with $NaHCO_3$ (4%). The organics were dried over $MgSO_4$ and taken to dryness. The crude was applied in a silica column and eluted with a gradient from 100:0 to 96:4 in DCM:MeOH. The desired fractions were collected and taken to dryness to afford the title compound as a white solid. (20 mg; 20% yield). ^{1}H NMR (300 MHz, d^6-DMSO): δ 9.85 (s, 1H), 9.78 (s, 1H), 9.11 (s, 1H), 8.30 (d, *J* = 9.4 Hz, 1H), 8.08 (d, *J* = 8.7 Hz, 1H), 7.98 (dd, *J* = 8.7, 1.9 Hz, 1H), 7.69 (s, 1H), 7.52 (d, *J* = 8.1 Hz, 1H), 7.23-7.20 (m, 6H), 6.91 (d, *J* = 9.4 Hz, 1H), 6.57 (dd, *J* = 17.2, 10.2 Hz, 1H), 6.19 (d, *J* = 17.2 Hz, 1H), 5.74 (d, *J* = 10.2 Hz, 1H), 3.01 (s, 3H), 2.42 (s, 3H). HRMS (ESI): *m/z* $[M + H]^+$ calc. for $C_{29}H_{25}N_4O_4S$: 525.1591; found: 525.1586. HPLC Purity: 98.9%.

NOTE: BMX-IN-1 was also acquired from Calbiochem and the commercial compound was used for *in vitro* experiments (including BMX and BTK IC_{50} determination, kinetic measurements, target engagement and cellular assays).

N-(3-methyl-5-(9-(4-(methylsulfonamido)phenyl)-2-oxobenzo[h][1,6]naphthyridin-1(2H)-yl)phenyl)acrylamide (9b)

Prepared using the procedure described for **9a**. Compound **9b** was obtained as a light-yellow solid (8 mg; 10% yield). ^{1}H NMR (300 MHz, d^6-DMSO): δ 10.42 (s, 1H), 9.92 (s, 1H), 9.12 (s, 1H), 8.31 (d, *J* = 9.5 Hz, 1H), 8.08 (d, *J* = 8.8 Hz, 1H), 8.00 (dd, *J* = 8.8, 1.9 Hz, 1H), 7.78 (s, 1H), 7.57 (brs, 1H), 7.44 (d, *J* = 1.9 Hz, 1H), 7.20 (brs, 4H), 7.09 (s, 1H), 6.92 (d, *J* = 9.4 Hz, 1H), 6.39 (dd, *J* = 17.0, 10.0 Hz, 1H), 6.22 (dd, *J* = 17.0, 2.2 Hz, 1H), 5.73 (dd, *J* = 9.9, 2.1 Hz, 1H), 3.03 (s, 3H), 2.36 (s, 3H). HRMS (ESI): *m/z* $[M + H]^+$ calc. for $C_{29}H_{25}N_4O_4S$: 525.1591; found: 525.1576. HPLC Purity: 93.1%.

N-(4-methyl-3-(9-(4-(methylsulfonamido)phenyl)-2-oxobenzo[h][1,6]naphthyridin-1(2H)-yl)phenyl)acrylamide (9c)

Prepared using the procedure described for **9a**. Compound **9c** was obtained as a light-yellow solid (40 mg; 55% yield). ^{1}H NMR (300 MHz, d^6-DMSO): δ 10.40 (s, 1H), 9.91 (brs, 1H), 9.14 (s, 1H), 8.35 (d, *J* = 9.5 Hz, 1H), 8.10 (d, *J* = 8.7 Hz, 1H), 8.01 (dd, *J* = 8.7, 1.9 Hz, 1H), 7.83 (dd, *J* = 8.4, 2.2 Hz, 1H), 7.72 (d, *J* = 2.1 Hz, 1H), 7.55 (d, *J* = 8.4 Hz, 1H), 7.32 (d, *J* = 1.8 Hz, 1H), 7.19 (m, 4H), 6.96 (d, *J* = 9.4 Hz, 1H), 6.39 (dd, *J* = 17.0, 10.0 Hz, 1H), 6.22 (dd, *J* = 17.0, 2.2 Hz, 1H), 5.74 (dd, *J* = 10.0, 2.2 Hz, 1H), 3.03 (s, 3H), 1.91 (s, 3H). HRMS (ESI): *m/z* $[M + H]^+$ calc. for $C_{29}H_{25}N_4O_4S$: 525.1591; found: 525.1587. HPLC Purity: 99.5%.

N-(3-(9-(4-(methylsulfonamido)phenyl)-2-oxobenzo[h][1,6]naphthyridin-1(2H)-yl)phenyl)acrylamide (9d)

Prepared using the procedure described for **9a**. Compound **9d** was obtained as a light-yellow solid (27 mg; 50% yield). ^{1}H NMR (300 MHz, d^6-DMSO): δ 10.50 (s, 1H), 9.91 (s, 1H), 9.12 (s, 1H), 8.31 (d, *J* = 9.4 Hz, 1H), 8.08 (d, *J* = 8.7 Hz, 1H), 8.03 – 7.91 (m, 2H), 7.83 (brs, 1H), 7.63 (t, *J* = 8.1 Hz, 1H), 7.34 (brs, 1H), 7.18 (m, 5H), 6.92 (d, *J* = 9.4 Hz, 1H), 6.42 (dd, *J* = 16.9, 10.0 Hz, 1H), 6.26 (dd, *J* = 16.9, 2.2 Hz, 1H), 5.77 (dd, *J* = 9.7, 1.9 Hz, 1H), 3.03 (s, 3H). HRMS (ESI): *m/z* [M + H]$^+$ calc. for $C_{28}H_{23}N_4O_4S$: 511.1435; found: 511.1433. HPLC Purity: 98.0%.

N-(2-methoxy-5-(9-(4-(methylsulfonamido)phenyl)-2-oxobenzo[h][1,6]naphthyridin-1(2H)-yl)phenyl)acrylamide (9e)

Prepared using the procedure described for **9a**. Compound **9e** was obtained as a light-yellow solid (38 mg; 43% yield). ^{1}H NMR (300 MHz, d^6-DMSO): δ 9.73 (s, 1H), 9.10 (s, 1H), 8.29 (d, *J* = 9.5 Hz, 1H), 8.19 – 8.10 (m, 1H), 8.07 (d, *J* = 8.6 Hz, 1H), 7.97 (d, *J* = 8.7 Hz, 1H), 7.36 – 7.20 (m, 8H), 6.91 (d, *J* = 9.4 Hz, 1H), 6.74 (dd, *J* = 17.0, 10.2 Hz, 1H), 6.13 (dd, *J* = 17.0, 2.1 Hz, 1H), 5.68 (dd, *J* = 10.3, 2.1 Hz, 1H), 4.00 (s, 3H), 3.01 (s, 3H). HRMS (ESI): *m/z* [M + H]$^+$ calc. for $C_{29}H_{25}N_4O_5S$: 541.1540; found 541.1542. HPLC Purity: 97.0%.

N-(2-methyl-5-(9-(4-(methylsulfonamido)phenyl)-2-oxobenzo[h][1,6]naphthyridin-1(2H)-yl)phenyl)but-2-enamide (10)

Prepared using the procedure described for **9a**. Compound **10** was obtained as a pale-yellow solid (30 mg; 41%). ^{1}H NMR (300 MHz, d^6-DMSO): δ 9.86 (s, 1H), 9.55 (s, 1H), 9.10 (s, 1H), 8.29 (d, *J* = 9.5 Hz, 1H), 8.02 (q, *J* = 8.6 Hz 2H), 7.69 (m, 1H), 7.49 (d, *J* = 8.1 Hz, 1H), 7.21 (brs, 6H), 6.91 (d, *J* = 9.4 Hz, 1H), 6.73 (dd, *J* = 15.1, 7.2 Hz, 1H), 6.27 (d, *J* = 15.3 Hz, 1H), 3.02 (s, 3H), 2.41 (s, 3H), 1.83 (s, 3H). HRMS (ESI): *m/z* [M + H]$^+$ calc. for $C_{30}H_{27}N_4O_4S$: 539.1748; found: 539.1746. HPLC Purity: 99.3%.

3-methyl-N-(2-methyl-5-(9-(4-(methylsulfonamido)phenyl)-2-oxobenzo[h][1,6]naphthyridin-1(2H)-yl)phenyl)but-2-enamide (11)

Prepared using the procedure described for **9a**. Compound **11** was obtained as a pale-yellow solid (20 mg; 32%). ^{1}H NMR (300 MHz, d^6-DMSO): δ 9.39 (s, 1H), 9.10 (s, 1H), 8.29 (d, J = 9.5 Hz, 1H), 8.08 – 7.96 (m, 2H), 7.72 (brs, 1H), 7.47 (d, J = 8.1 Hz, 1H), 7.16 (m, 6H), 6.91 (d, J = 9.4 Hz, 1H), 6.03 (s, 1H), 2.98 (s, 3H), 2.40 (s, 3H), 2.04 (s, 3H), 1.84 (s, 3H). HRMS (ESI): *m/z* $[M + H]^+$ calc. for $C_{31}H_{29}N_4O_4S$: 553.1904; found: 553.1909. HPLC Purity: 99.3%.

N-(5-(9-(4-(butylsulfonamido)phenyl)-2-oxobenzo[h][1,6]naphthyridin-1(2H)-yl)-2-methylphenyl)acrylamide (14)

Prepared using the procedure described for **9a**. Compound **14** was obtained as a pale-yellow solid (33 mg; 20%). ^{1}H NMR (300 MHz, d^6-DMSO): δ 9.92 (s, 1H), 9.81 (s, 1H), 9.11 (s, 1H), 8.30 (d, *J* = 9.4 Hz, 1H), 8.07 (d, *J* = 8.6 Hz, 1H), 7.98 (d, *J* = 9.0 Hz, 1H), 7.69 (s, 1H), 7.50 (d, *J* = 8.1 Hz, 1H), 7.19 (brs, 6H), 6.91 (d, *J* = 9.5 Hz, 1H), 6.57 (dd, *J* = 17.1, 9.4 Hz, 1H), 6.19 (d, *J* = 17.0 Hz, 1H), 5.74 (d, *J* = 10.1 Hz, 1H), 3.09 (t, *J* = 7.8 Hz, 2H), 2.40 (s, 3H), 1.74 – 1.54 (m, 2H), 1.35 (q, *J* = 7.4 Hz, 2H), 0.83 (t, *J* = 7.3 Hz, 3H). HRMS (ESI): *m/z* $[M + H]^+$ calc. for $C_{32}H_{31}N_4O_4S$: 567.2061; found 567.2060. HPLC Purity: 95.2%.

N-(2-methyl-5-(9-(3-(methylsulfonamido)phenyl)-2-oxobenzo[h][1,6]naphthyridin-1(2H)-yl)phenyl)acrylamide (15)

Prepared using the procedure described for **9a**. Compound **15** was purified by semi-prep HPLC, with an XBridge BEH C18 OBD column (130 Å, 5 µm, 10 mm x 100 mm) with a gradient 25:75 until 50:50 with a mixture (95:5 ACN:$NaHCO_3$ 10 mM) : ($NaHCO_3$ 10 mM). The title compound was obtained as a white solid (8 mg; 4%). ^{1}H NMR (300 MHz, $CDCl_3$): δ 8.98 (s, 1H), 8.68 (s, 1H), 8.17 (d, *J* = 8.7 Hz, 1H), 8.07 – 7.94 (m, 2H), 7.88 (dd, *J* = 8.7, 1.9 Hz, 1H), 7.54 – 7.32 (m, 5H), 7.25 (m, 1H), 7.09 (dd, *J* = 8.1, 2.2 Hz, 1H), 6.98 – 6.84 (m, 2H), 6.56 (dd, *J* = 16.9, 1.3 Hz, 1H), 6.36 (dd, *J* = 16.9, 10.2 Hz, 1H), 5.85 (dd, *J* = 10.2, 1.3 Hz, 1H), 2.98 (s, 3H), 2.34 (s, 3H). HRMS (ESI): *m/z* $[M + H]^+$ calc. for $C_{29}H_{25}N_4O_4S$: 525.1591; found 525.1594. HPLC Purity: 94.3%.

Methyl4-(1-(3-acrylamido-4-methylphenyl)-2-oxo-1,2-dihydrobenzo[h][1,6]naphthyridin-9-yl)phenylcarbamate (16)

Prepared using the procedure described for **9a**. Compound **16** was obtained as a pale-yellow solid (55 mg; 36%). ^{1}H NMR (300 MHz, d^6-DMSO): δ 9.75 (s, 2H), 9.09 (s, 1H),

8.29 (d, *J* = 9.5 Hz, 1H), 8.15 – 7.90 (m, 2H), 7.69 (d, *J* = 2.0 Hz, 1H), 7.53 - 7.46 (m, 3H), 7.32 – 7.08 (m, 4H), 6.90 (d, *J* = 9.4 Hz, 1H), 6.58 (dd, *J* = 17.0, 10.1 Hz, 1H), 6.19 (dd, *J* = 17.0, 2.0 Hz, 1H), 5.73 (d, *J* = 10.4 Hz, 1H), 3.68 (s, 3H), 2.44 (s, 3H). HRMS (ESI): *m/z* $[M + H]^+$ calc. for $C_{30}H_{25}N_4O_4$: 505.1870; found 505.1869. HPLC Purity: 97.8%.

N-(2-methyl-5-(2-oxo-9-(pyridin-4-yl)benzo[h][1,6]naphthyridin-1(2H)-yl)phenyl) acrylamide (17)

Prepared using the procedure described for **9a**. Compound **17** was obtained as a yellow solid (29 mg; 20%). ^{1}H NMR (300 MHz, d^6-DMSO): δ 9.76 (s, 1H), 9.17 (s, 1H), 8.56 (s, 2H), 8.32 (d, *J* = 9.5 Hz, 1H), 8.16-8.12 (m, 2H), 7.73 (s, 1H), 7.52 (d, *J* = 8.1 Hz, 1H), 7.38 (s, 1H), 7.26-7.20 (m, 3H), 6.94 (d, *J* = 9.6 Hz, 1H), 6.57 (dd, *J* = 16.5, 9.6 Hz, 1H), 6.20 (d, *J* = 16.5 Hz, 1H), 5.74 (d, *J* = 9.3 Hz, 1H), 2.43 (s, 3H). HRMS (ESI): *m/z* $[M + H]^+$ calc. for $C_{27}H_{21}N_4O_2$: 433.1659; found: 433.1656. HPLC Purity: 95.8%.

N-(5-(9-(6-cyanopyridin-3-yl)-2-oxobenzo[h][1,6]naphthyridin-1(2H)-yl)-2-methyl phenyl)acrylamide (18)

Prepared using the procedure described for **9a**. Compound **18** was obtained as a light-yellow solid (14 mg; 17%). ^{1}H NMR (300 MHz, d^6-DMSO): δ 9.75 (s, 1H), 9.19 (s, 1H), 8.61 (dd, *J* = 2.3, 0.8 Hz, 1H), 8.32 (d, *J* = 9.5 Hz, 1H), 8.16 - 8.13 (m, 2H), 8.06 (dd, *J* = 8.2, 0.8 Hz, 1H), 7.85 (dd, *J* = 8.2, 2.3 Hz, 1H), 7.67 (d, *J* = 2.2 Hz, 1H), 7.51 (d, *J* = 8.1 Hz, 1H), 7.25 – 7.22 (m, 2H), 6.94 (d, *J* = 9.4 Hz, 1H), 6.55 (dd, *J* = 17.0, 10.1 Hz, 1H), 6.17 (dd, *J* = 17.0, 2.0 Hz, 1H), 5.73 (dd, *J* = 10.1, 2.0 Hz, 1H), 2.42 (s, 3H). HRMS (ESI): *m/z* $[M + H]^+$ calc. for $C_{28}H_{20}N_5O_2$: 458.1612; found: 458.1610. HPLC Purity: 95.3%.

N-(2-methyl-5-(2-oxo-9-(6-(trifluoromethyl)pyridin-3-yl)benzo[h][1,6]naphthyridin-1(2H)-yl)phenyl)acrylamide (19)

Prepared using the procedure described for **9a**. Compound **19** was obtained as a yellow solid (20 mg; 18%). ^{1}H NMR (300 MHz, d^6-DMSO): δ 9.77 (s, 1H), 9.18 (s, 1H), 8.66 (s, 1H), 8.32 (d, *J* = 9.4 Hz, 1H), 8.17-8.14 (m, 2H), 7.87 (s, 2H), 7.67 (d, *J* = 2.2 Hz, 1H), 7.51 (d, *J* = 8.0 Hz, 1H), 7.25-7.22 (m, 2H), 6.94 (d, *J* = 9.4 Hz, 1H), 6.55 (dd, *J* = 17.1, 10.2 Hz, 1H), 6.17 (dd, *J* = 17.1, 2.2 Hz, 1H), 5.73 (d, *J* = 10.2 Hz, 1H), 2.39 (s, 3H). HRMS (ESI): *m/z* $[M + H]^+$ calc. for $C_{28}H_{20}F_3N_4O_2$: 501.1533; found: 501.1534. HPLC Purity: 98.3%.

N-(2-methyl-5-(2-oxo-9-(piperidin-1-yl)benzo[h][1,6]naphthyridin-1(2H)-yl)phenyl)acrylamide (20)

Prepared using the procedure described for **9a**. Compound **20** was further purified by preparative TLC eluting with DCM:MeOH (96:4) to afford the title compound as a yellow solid (70 mg; 34%). ^{1}H NMR (300 MHz, $CDCl_3$): δ 8.76 (s, 1H), 8.26 (s, 1H), 8.03 – 7.79 (m, 3H), 7.38 – 7.27 (m, 2H), 6.97 - 6.90 (m, 2H), 6.62 (d, *J* = 2.6 Hz, 1H), 6.33 – 6.26 (m, 2H), 5.67 (t, *J* = 5.9 Hz, 1H), 2.74 (m, 4H), 2.29 (s, 3H), 1.48 (m, 6H). HRMS (ESI): *m/z* $[M + H]^+$ calc. for $C_{27}H_{27}N_4O_2$: 439.2129; found: 439.2127. HPLC Purity: 98.2%.

N-(2-methyl-5-(9-morpholino-2-oxobenzo[h][1,6]naphthyridin-1(2H)-yl)phenyl)acrylamide (21)

Prepared using the procedure described for **9a**. Compound **21** was further purified by preparative TLC eluting with DCM:MeOH (95:5) to afford the title compound as a light-yellow solid (36 mg; 29%). ^{1}H NMR (300 MHz, $CDCl_3$): δ 8.80 (s, 1H), 8.17 (s, 1H), 7.97 (t, *J* = 9.4 Hz, 2H), 7.87 (s, 1H), 7.38 – 7.28 (m, 2H), 6.99 - 6.92 (m, 2H), 6.64 (d, *J* = 2.6 Hz, 1H), 6.41 – 6.26 (m, 2H), 5.70 (m, 1H), 3.68 (t, *J* = 4.8 Hz, 4H), 2.88 – 2.62 (m, 4H), 2.28 (s, 3H). HRMS (ESI): *m/z* $[M + H]^+$ calc. for $C_{26}H_{25}N_4O_3$: 441.1921; found: 441.1920. HPLC Purity: 97.0%.

N-(2-methyl-5-(9-(4-(methylsulfonyl)piperazin-1-yl)-2-oxobenzo[h][1,6]naphthyridin-1(2H)-yl)phenyl)acrylamide (22)

Prepared using the procedure described for **9a**. Compound **22** was obtained as a yellow solid (45 mg; 25%). ^{1}H NMR (300 MHz, $CDCl_3$): δ 8.83 (s, 1H), 8.11 – 7.95 (m, 4H), 7.35 – 7.30 (m, 2H), 6.96 (d, *J* = 9.3 Hz, 2H), 6.68 (d, *J* = 2.6 Hz, 1H), 6.34 – 6.30 (m, 2H), 5.71 (m, 1H), 3.29 – 3.02 (m, 4H), 2.97 – 2.93 (m, 4H), 2.76 (s, 3H), 2.29 (s, 3H). HRMS (ESI): *m/z* $[M + H]^+$ calc. for $C_{27}H_{28}N_5O_4S$: 518.1857; found: 518.1859. HPLC Purity: 96.7%.

N-(5-(9-(4-(dimethylamino)piperidin-1-yl)-2-oxobenzo[h][1,6]naphthyridin-1(2H)-yl)-2-methylphenyl)acrylamide (23)

Prepared using the procedure described for **9a**. Compound **23** was obtained as a light-yellow solid (9 mg; 10%). ^{1}H NMR (300 MHz, $CDCl_3$): δ 8.77 (s, 1H), 8.25 (s, 1H), 8.09 – 7.84 (m, 3H), 7.42 – 7.27 (m, 2H), 6.96 – 6.91 (m, 2H), 6.64 (d, *J* = 2.6 Hz, 1H), 6.40 – 6.23 (m, 2H), 5.75 – 5.58 (m, 1H), 3.30 (t, *J* = 12.1 Hz, 2H), 2.43 – 2.29 (m, 3H), 2.29 (s,

3H), 2.26 (s, 6H), 1.70 - 1.66 (m, 2H), 1.44 – 1.38 (m, 2H). HRMS (ESI): *m/z* $[M + H]^+$ calc. for $C_{29}H_{32}N_5O_2$: 482.2551; found: 482.2551. HPLC Purity: 99.5%.

N-(2-methyl-5-(8-(4-(methylsulfonamido)phenyl)-2-oxobenzo[h][1,6]naphthyridin-1(2H)-yl)phenyl)acrylamide (JS24)

Prepared using the procedure described for **9a**. Compound **JS24** was obtained as a yellow solid (35 mg; 43%). ^{1}H NMR (300 MHz, d^6-DMSO): δ 9.98 (s, 1H), 9.68 (s, 1H), 9.13 (s, 1H), 8.37 – 8.23 (m, 2H), 7.83 (d, *J* = 8.6 Hz, 2H), 7.67 (s, 1H), 7.58 – 7.41 (m, 2H), 7.29 (d, *J* = 8.7 Hz, 2H), 7.19 (dd, *J* = 8.0, 2.2 Hz, 1H), 6.98 (d, *J* = 9.3 Hz, 1H), 6.88 (d, *J* = 9.4 Hz, 1H), 6.56 (dd, *J* = 17.1, 10.1 Hz, 1H), 6.19 (dd, *J* = 17.0, 2.1 Hz, 1H), 5.74 (d, *J* = 10.1 Hz, 1H), 3.03 (s, 3H), 2.40 (s, 3H). HRMS (ESI): *m/z* $[M + H]^+$ calc. for $C_{29}H_{25}N_4O_4S$: 525.1591; found 525.1591. HPLC Purity: 95.1%.

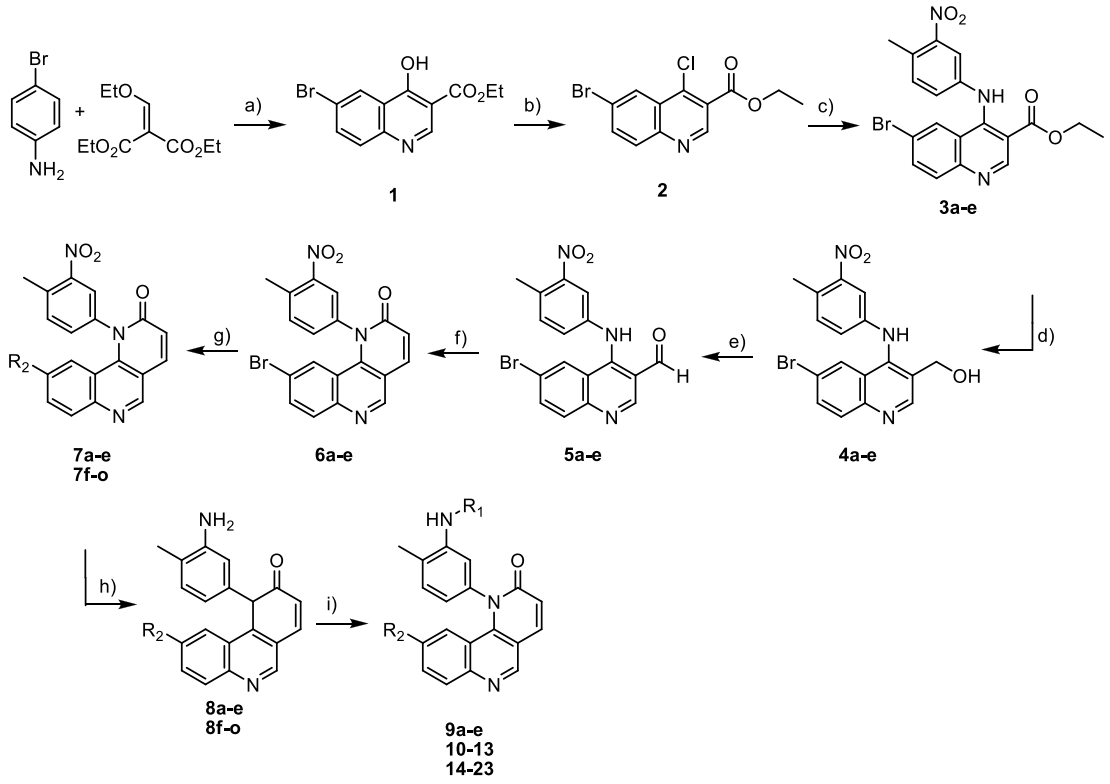

Scheme 5. 1. Synthetic route for the preparation of compounds **JS9**a–e, **JS10–13** and **JS14–23**. a) Reflux (neat), 24h, then Ph_2O, 5h at 240ºC, 40%; b) $SOCl_2$, reflux, 5h, 100%; c) aniline, dioxane, 90ºC, 6h, 90%; d) $NaBH_4$, EtOH, rt, overnight, 100%; e) Dess-Martin Periodinane, DCM, rt, 3h, 75%; f) Triethylphosphonoacetate, K_2CO_3, EtOH, 100ºC, overnight, 60%; g) boronic acid/ester, $PdCl_2(PPh_3)_2$, Na_2CO_3, dioxane, 90ºC, overnight, 50% or amine, $Pd(OAc)_2$, R-BINAP, Cs_2CO_3, dioxane, 85ºC, overnight, 80%; h) Fe,

NH_4Cl, EtOH/H_2O, 80ºC, 2h, 100%; i) acyl chloride, DIPEA, THF, -10ºC to rt 5h, 25% or alkyl halide, K_2CO_3, DMF, rt, overnight, 35%.

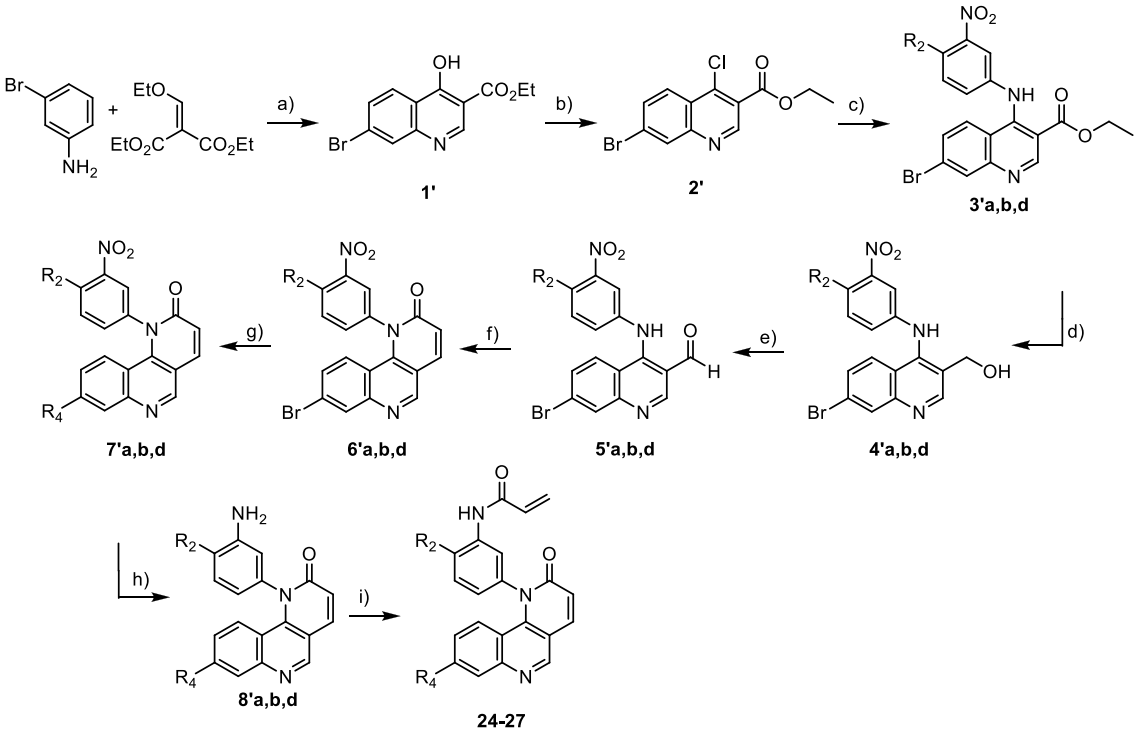

Scheme 5. 2. Synthetic route for the preparation of compounds **JS24–27**. a) Reflux (neat), 24h, then Ph_2O, 5h at 240ºC, 40%; b) $SOCl_2$, reflux, 5h, 100%; c) aniline, dioxane, 90ºC, overnight, 80%; d) $NaBH_4$, EtOH, rt, overnight, 90%; e) Dess-Martin Periodinane, DCM, rt, 3h, 80%; f) Triethylphosphonoacetate, K_2CO_3, EtOH, 100ºC, overnight, 70%; g) boronic acid/ester, $PdCl_2(PPh_3)_2$, Na_2CO_3, dioxane, 90ºC, overnight, 20% or amine, $Pd(OAc)_2$, R-BINAP, Cs_2CO_3, dioxane, 85ºC, overnight, 90%; h) Fe, NH_4Cl, EtOH/H_2O, 80ºC, 2h, 70%; i) acryloyl chloride, DIPEA, THF, -10ºC to rt 5h, 15%

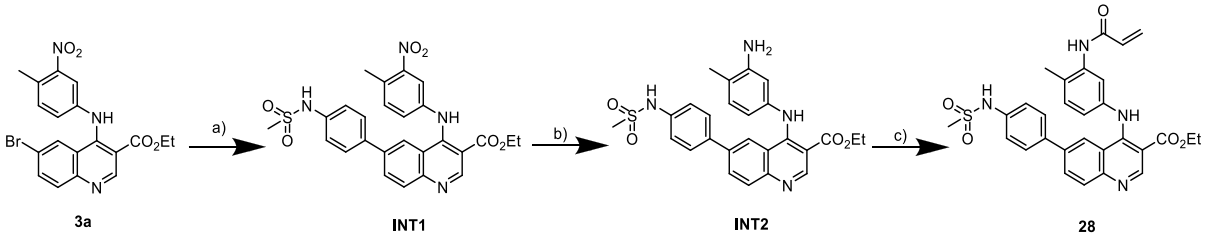

Scheme 5. 3. Synthetic route for the preparation of compound **JS28**. a) 4-(methanesulfonylamino) phenyl boronic acid pinacol ester, $PdCl_2(PPh_3)_2$, Na_2CO_3,

dioxane, 90ºC, o/n, 73%; b) Fe, NH_4Cl, $EtOH/H_2O$, 80ºC, 2h, 88%; c) acryloyl chloride, DIPEA, THF, -10ºC to rt, 5h, 10%.

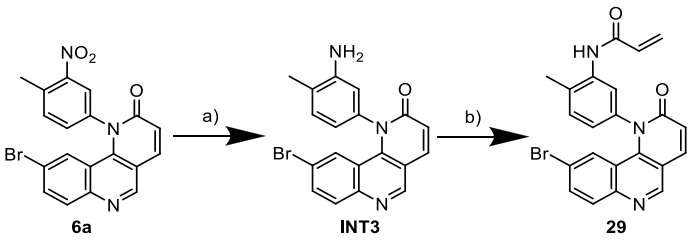

Scheme 5. 4. Synthetic route for the preparation of compound **JS29**. a) $SnCl_2$, EtOAc, 85ºC, 2h, 68%; b) acyl chloride, DIPEA, THF, -10ºC to rt, 5h, 95%.

5.1.2 Biochemical activity assays: BMX and BTK

BMX and BTK kinase activity (IC_{50}) were performed at Eurofins DiscoverX. Briefly, the inhibition of the human recombinant BMX kinase is quantified by measuring the phosphorylation of the substrate biotinyl-βAβAβAEEEPQYEEIPIYLELLP using a human recombinant enzyme expressed in insect cells and the HTRF detection method. The test compound, reference compound or water (control) are preincubated for 5 min at rt with the enzyme (10 ng) in a buffer containing 50 mM HEPES/NaOH (pH 7.4), 10 mM $MnCl_2$, 3.6 mM DTT, 40 µM Na_3VO_4 and 0.005% Tween 20. Thereafter, the reaction is initiated by adding 0.4 µM of the substrate biotinyl-βAβAβAEEEPQYEEIPIYLELLP and 0.7 µM ATP, and the mixture is incubated for 60 min at rt. For control basal measurements, the enzyme is omitted from the reaction mixture. Following incubation, the reaction is stopped by adding 33 mM EDTA. The fluorescence acceptor (XL665-labeled streptavidine) and the fluorescence S65 donor (anti-phospho-tyrosine-66K antibody labeled with europium cryptate) are then added. After 60 min, the fluorescence transfer is measured at λ_{ex}=337 nm, λ_{em}=620 nm and λ_{em}=665 nm using a microplate reader. The enzyme activity is determined by dividing the signal measured at 665 nm by that measured at 620 nm (ratio). The results are expressed as a percent inhibition of the control enzyme activity. BTK kinase activity (IC_{50}) was performed through a radiometric assay with the KinaseProfiler platform. BTK is incubated with 8 mM MOPS pH 7.0, 0.2 mM EDTA, 250 µM KVEKIGEGTYGVVYK (Cdc2 peptide), 10 mM MgAcetate, and [gamma-33P]-ATP (10

μM). The reaction is initiated by the addition of the Mg/ATP mixture. After incubation for 40 min at rt, the reaction is stopped by the addition of phosphoric acid to a concentration of 0.5%. 10 μL of the reaction is then spotted onto a P30 filtermat and washed four times for 4 min in 0.425% phosphoric acid and one in methanol prior to drying and scintillation counting.

5.1.3 Putative 3D structure of JS25 linked to BTK

Structure predictions were performed by Dr Francisco Corzana. **Docking studies with AUTODOCK 4.2.** AUTODOCK 4.2[257] was used to predict the region where **JS25** binds to BTK (PDB: 6TFP). Standard settings for *autogrid* (number of grid points in xyz: 126, 126, 126; spacing (Å) = 0.375) and *autodock* (genetic algorithm, max. number of evaluations = 250000, output=Lamarckian GA(4.2)) were selected with AutoDockTools 1.5.6. **Molecular dynamic (MD) simulations.** Simulations on **JS25** or **Ibrutinib** bound to BTK were performed with AMBER 20 package (University of California) and implemented with GAFF2 force field[258]. For the BTK/**Ibrutinib** complex, the coordinates of the reported X-ray structure were used as starting coordinates (PDB: 5P9J). The setup for the molecular dynamics was performed as previously described[259], with the production step set to 500 ns.

5.1.4 Kinome selectivity of JS25 by competitive assays

Selectivity across human kinome was determined for **JS25** at 1 μM in a KINOMEscan® screen. Screening hits are identified by measuring the amount of tag-kinase captured by the tag-ligand immobilized on a solid support, in experimental *versus* in control samples.

5.1.5 In-cell selectivity of JS25

In-cell target engagement was performed at the Reaction Biology Corporation, using the NanoBRET™ Technology. Very briefly, HEK296T cells were transfected with kinase gene and treated in duplicate with JS25 for 1h of incubation. The compound was diluted 10 times with 3-fold dilution, starting at 1 μM. Curve fits were performed only when % NanoBret signal at the highest concentration of compounds was less than 55%. The IC_{50}

values were determined using the GraphPad Prism 8 (GSL Biotech LLC).

5.1.6 Inhibition kinetics characterisation of JS25

The BTK enzyme system and the ADP-Glo™ kinase assay were purchased from Promega Corporation (V2941). **Ibrutinib** was acquired from BOC Sciences, and **Acalabrutinib** from Advanced ChemBlock. In each kinase reaction, the concentration of BTK was set to 4 ng/µL. The peptide substrate Poly (4:1 Glu, Tyr) and ATP concentrations were set to 0.25 mg/mL and 50 µM, respectively. BTK was pre-incubated with different inhibitor concentrations (8-fold serial dilutions, starting at 100 nM), over different time-periods (2-60 min), before initiating the kinase reactions. Reactions were started by adding 2.5X Poly E4Y1/ATP mixture. The reactions were carried out in a 384-well plate, and quenched simultaneously with the addition of 5 µL of ADP-Glo™ reagent, to consume the remaining ATP within 40 min. Then, 10 µL of kinase detection reagent were added into the wells and incubated for 30 min to produce a luminescence signal. The signal was measured using an Infinite M200 Microplate Reader (Tecan), with an integration time of 0.250 sec. The observed rate constants for inhibition (k_{obs}), at different inhibitor concentrations, were determined from the slope of a semi-logarithmic plot of inhibition *versus* time and re-plotted against inhibitor concentration (nM). The experimental values were fitted into a hyperbolic function using GraphPad Prism 8, to obtain the K_I, k_{inact}, and k_{inact}/K_I, as described previously[260].

5.1.7 Cell culture

All cell lines were purchased from ATCC, except for DoHH-2 cells that were obtained from DSMZ. Cells were cultivated in complete DMEM supplemented with 10% (vol/vol) FBS (Gibco), and 1% of penicillin/streptomycin (Gibco). Cells were grown in a humidified atmosphere of 5% CO_2 at 37ºC, with the medium changed every other day.

5.1.8 Cell viability assay

Cells were inoculated at a density of 5 000 cells/well. Serial diluted compounds (starting at 50 µM) were added 24h later. The assay was performed in triplicates. After 72h of

incubation, cellular viability was assessed by CellTiter-Glo® (Promega) according to the manufacturer's instructions. The values were normalised with the vehicle (DMSO) and the IC_{50} was calculated using GraphPad Prism 8.

5.1.9 In vitro analysis of the blood-brain barrier permeability

Human cerebral microvascular endothelial cells (HBEC-5i) were cultured as a monolayer on attachment factor protein solution (AF)-coated T-flasks (Gibco), using DMEM:F12 medium (Gibco), supplemented with 10% FBS, 1% penicillin/streptomycin, and 40.0 µg/mL of endothelial cell growth supplement (ECGS) (Sigma), according to the manufacturer's instructions. The capacity of the compounds to cross the brain-blood-barrier was evaluated using an *in vitro* HBEC-5i cell model, as previously described[261]. Samples form the apical and basolateral side were collected and fluorescence intensity measured using a Varioskan™ LUX multimode microplate reader. The retention was considered the difference between the initial fluorescence of compounds (100%) and the aggregated apical and basolateral fluorescence.

5.1.10 BTK degradation in Raji cells

Raji cells were inoculated at 0.5×10^6 cells/mL and **JS25** was added at a final concentration of 10 µM. At 0, 4 and 15h of incubation, cells were harvested and the pellets were resuspended in lysis buffer (20 mM Tris-HCl, 150 mM NaCl, pH 8.0, 0.1% Triton X-100), supplemented with EDTA-free Protease Inhibitor Cocktail (Merck) and DNase I (Merck). The protein concentration was determined using the Pierce™ BCA Protein Assay Kit (Thermo Scientific). Western blot was performed with rabbit BTK antibody (1:1000) (3533, Cell Signaling Technology), mouse α-Tubulin antibody (1:5000) (5168, Merck), goat anti-rabbit IgG (H+L) secondary antibody HRP (1:7000) (65-6120, Invitrogen), and goat anti-mouse IgG (H+L) secondary antibody HRP (1:5000) (62-6520, Invitrogen). Signal was revealed with Clarity Western ECL Substrate (Bio-Rad Laboratories), and band intensity was measured using the ImageJ software (National Institutes of Health).

5.1.11 Mice xenograft model of Burkitt's lymphoma

Female adult BALB/c/NSG mice were injected subcutaneously with 1×10^6 Raji cells, in a 1:1 solution of Matrigel® Matrix (Corning) to create solid tumours. When tumours reached 180 mm^3 on average, mice were randomized into four groups (n = 6/group) and dosing began every 2 days. **JS25** and **Ibrutinib** were administered via Intraperitoneal injection, as a mixture of 20% of Kolliphor® (Sigma-Aldrich) in PBS. Three treatment groups were included based on a similar study reported by Li *et al.*, 2014: one dose of **Ibrutinib** (10 mg/Kg), and two doses of **JS25** (10 and 20 mg/Kg). Tumour size and body weight were monitored periodically for 12 days. At the end of the experiment, mice necropsies were performed. Stereological analysis was conducted by the Histopathology Unit at Instituto Gulbenkian de Ciência and by the Comparative Pathology Unit at Instituto de Medicina Molecular João Lobo Antunes. Quantification of metastases and cell necrosis was performed in all groups (n=5/group). Statistical analysis was conducted using one-way ANOVA. Dunnet test was used to analyse the statistical significance between treatment groups and the control.

5.1.12 Ex vivo model of diffuse large B-cell lymphoma

This experiment was performed by our collaborators in Exscientia. **Primary material collection and purification.** Primary lymph node samples were taken from patients, following hospital standard operating procedures. Clinical information including diagnosis was collected by the study centre in a case report form. Target markers were confirmed by flow cytometry at the final laboratory prior to use. **Cell plating, assay, and screening.** Cells were plated at 10 000–20 000 cells per well in 384-well PerkinElmer Cell Carrier Ultra plates, containing pre-spotted small molecules in DMSO distributed by a Labcyte ECHO, in quadruplicate technical replicates in 4-point dose response curves starting at 10 µM and decreasing by 1:3. DMSO volume in each well including controls were kept constant at 0.1% final volume of media. Plates were randomized and contained at least fifteen DMSO vehicle control wells. Incubation took place for 72h at 37ºC in air supplemented with 5% CO_2. At the end of the incubation period, cells were stained with a viability dye (Invitrogen), fixed and permeabilised using low-concentration formaldehyde and Triton X-114 in DPBS, and the resulting monolayers stained with fluorescent antibodies against surface markers (CD19 (eBiosciences, clone HIB19), CD20 (BD, clone

L27), CD79a (BioLegend, clone HM47) along with DAPI (Sigma). Fluorescent antibodies were used in different non-overlapping fluorescent channels. **Imaging and image analysis.** Imaging of the primary cell monolayer was performed using PerkinElmer CLS spinning disk automated confocal microscopes, with non-overlapping, sequential, fluorescent channel imaging. All images were taken with a 20x objective. Five fields were imaged, representing at least 50% of the well bottom, for each well (7 TIFF images in total per field, one for each colour channel plus brightfield, and 405 nm for DAPI, and merged). For analysis, images were subject to image illumination correction. Cell identification in each image works by finding the cell nucleus (relying on DAPI staining) using classical thresholding approaches. Segmentation was performed using proprietary algorithms. Classification (cell antigen expression and viability) of each single cell was achieved using deep convolutional neural networks trained on B-cells and other cells from B-NHL samples stained with the specific markers utilized for these experiments, as well as on fixable live/dead viability dye. The network considers variations in staining of the marker, viability marker intensity (cytoplasm and membrane localized) along with other stain-based characteristics. For this work, the networks had at least a 95% classification accuracy. Information on the calculation of the drug response score (DRS), the relative cell fraction and cell fraction can be found in Snijder *et al*., 2017. All raw Pharmacoscopy data was visualized in R (3.6.1).

5.1.13 Zebrafish xenograft model of chronic lymphocytic leukaemia

This experiment was performed by our collaborators at Champalimaud Foundation. **Peripheral blood mononuclear cells isolation (PBMCs) and cryopreservation.** Whole blood (3-6 mL) from CLL patients was collected and PBMCs were purified by Ficoll-Paque™ PLUS (GE Healthcare) density centrifugation. **PBMCs processing for zebrafish injection.** The collected PBMCs were resuspended with 3 times their volume in RPMI (Biowest) and centrifuged at 1 400 rpm, 4ºC, for 7 min. Cell pellets were resuspended in DPBS 1X (Biowest) supplemented with universal nuclease at 25 U/mL (Thermo Scientific). Concentration was normalised to 5×10^6 cells/µL for zebrafish patient-derived xenograft (zPDX) generation. Prior to drug efficacy analysis in zebrafish, cells were distributed to proceed for flow cytometry, to determine the percentage of CD19+CD5+ cells within CD45+ population, from PBMCs of each CLL patient. The maximum tolerated concentration was also determined for each compound in non-injected zebrafish larvae.

Zebrafish patient-derived xenograft injection and drug administration. Zebrafish larvae were anesthetized with Tricaine 1X and thawed PBMCs were microinjected into the perivitelline space of anesthetized zebrafish larvae, at 48h post fertilisation. After injection, zPDXs were sorted and randomly distributed into the different treatment groups in E2 medium:DMSO (control), **JS25**, **Ibrutinib**, and **Venetoclax**. zPDXs were maintained at 34ºC and all drugs were renewed daily for 2 consecutive days. At the end of the assay, 4 days post-injection, zebrafish xenografts were sacrificed with an overdose of Tricaine 25X and fixed in 4% formaldehyde (Thermo Scientific) overnight, followed by storage in 100% methanol (VWR) at −20°C. **Whole-mount immunofluorescence.** Whole-mount immunofluorescence protocol started by re-hydrating the xenografts through methanol series (75% > 50% > 25% in PBS 1X-Triton 0.1%). Next, xenografts were permeabilised in PBS 1X with 0.1% (v/v) Triton and incubated in a blocking solution (containing 1% BSA and 1.5% goat serum), for 1h at rt. Xenografts were incubated with the primary antibodies (anti-cleaved caspase3, Cell Signaling Technology, clone Asp175, 9661, 1:100; anti-human mitochondria - Merck Millipore, clone 113-1, MAB1273, 1:50) diluted in the blocking solution overnight at 4ºC, followed by an additional overnight incubation with 1:400 of secondary antibodies: Alexa goat anti-rabbit 594 (35560, Thermo Scientific) and Alexa goat anti-mouse 647 (84545, Thermo Scientific), and nuclei counterstaining with DAPI at 50 µg/mL (Sigma-Aldrich). **Imaging and quantification.** All images were obtained using a Zeiss LSM 980 Upright confocal laser scanning microscope. Xenografts were mounted in *in-house* Mowiol mounting media and sequential images along tumour's depth (from cloaca until the end of the tail) with a 5 µm interval were acquired using the z-stack function. Upon image acquisition, analysis was performed using ImageJ software. For tumour burden, the area occupied by the PBMCs in each slice of the z-stack pile was determined by using ImageJ software and summed up to get the tumour burden per xenograft. To express the outcome as fold induction, values obtained for controls and treatment conditions were normalised to the control. Tumour incidence was given by dividing the number of zebrafish xenografts that presented tumour cells, between cloaca and the end of the tail, per the total number of zebrafish xenografts alive at the end of the assay (2 days post-injection). **Statistical analysis of zebrafish patient-derived xenograft data.** Statistical analysis was performed using the GraphPad Prism 8. All data were challenged by two normality tests – the D'Agostino & Pearson and the Shapiro-Wilk normality tests. A Gaussian distribution was only assumed for datasets that pass both normality tests and were analysed by an unpaired t test with Welch's correction. By

opposition, datasets that did not pass one or both normality tests were analysed by Mann-Whitney test, an unpaired and non-parametric U test. Fisher's exact test was used for tumour incidence analysis.

5.2 PROTACs to target APTs

5.2.1 Synthesis

Compound synthesis was performed with the help of Dr Luís Carvalho. Building blocks and solvents were purchased from Sigma Aldrich, Alfa Aesar, Acros, or Fluka and used without further purification. Proton and carbon nuclear magnetic resonance (^{1}H and ^{13}C NMR) spectra were recorded on a Bruker AVANCE 300 or 400 MHz spectrometers. All chemical shifts are quoted on the δ scale in ppm with TMS as an internal reference. Coupling constants (*J*) are reported in Hz with the following splitting abbreviations: s = singlet, d = doublet, t = triplet, m = multiplet. All compounds present ≥ 95% purity.

Tert-butyl 4-(2-(2,6-dioxopiperidin-3-yl)-1,3-dioxoisoindolin-4-yl)piperazine-1-carboxylate (1a)

The 2-(2,6-dioxopiperidin-3-yl)-4-fluoroisoindoline-1,3-dione (1.92 mmol) was dissolved in DMSO. Boc-piperazine (2.3 mmol) and DIPEIA (2.3 mmol) were then added. The reaction was stirred at 90˚C overnight. The product was extracted with 3×10 mL of EtOAc, and the organic layers were evaporated under reduced pressure. The mixture was purified by flash column chromatography (eluent Hexane:EtOAc 50:50 to EtOAc 100%), resulting in the product tert-butyl 4-(2-(2,6-dioxopiperidin-3-yl)-1,3-dioxoisoindolin-4-yl)piperazine-1-carboxylate (84%) **(Scheme 5. 5)**.

^{1}H NMR (300 MHz, Chloroform-d) δ 8.24 (s, 1H), 7.60 (dd, J = 8.4, 7.2 Hz, 1H), 7.42 (dd, J = 7.2, 0.8 Hz, 1H), 7.15 (dd, J = 8.4, 0.9 Hz, 1H), 4.95 (dd, J = 12.1, 5.2 Hz, 1H), 3.64 (t, J = 5.1 Hz, 4H), 3.27 (td, J = 4.6, 2.0 Hz, 4H), 2.18 – 2.07 (m, 1H), 2.06 – 1.94 (m, 4H), 1.48 (s, 9H).

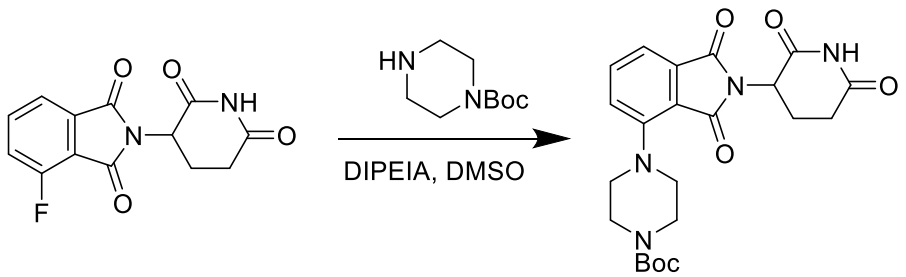

Scheme 5. 5. Synthetic route for the preparation of tert-butyl 4-(2-(2,6-dioxopiperidin-3-yl)-1,3-dioxoisoindolin-4-yl)piperazine-1-carboxylate.

2-(2,6-dioxopiperidin-3-yl)-4-(piperazin-1-yl)isoindoline-1,3-dione (1b)

Prepared using the product from procedure **1a**. Tert-butyl 4-(2-(2,6-dioxopiperidin-3-yl)-1,3-dioxoisoindolin-4-yl)piperazine-1-carboxylate (0.68 mmol) was dissolved in DCM and TFA. The reaction was refluxed at 45˚C for 3h. The mixture was cooled to rt. DCM was added and evaporated 3 times. The resulting solid residue, 2-(2,6-dioxopiperidin-3-yl)-4-(piperazin-1-yl)isoindoline-1,3-dione, was washed with diethyl ether **(Scheme 5. 6)**.

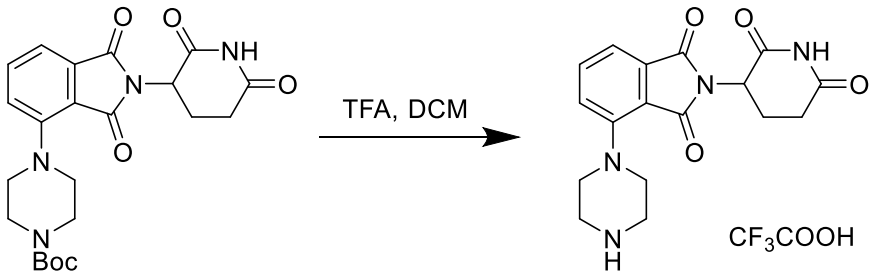

Scheme 5. 6. Synthetic route for the preparation of 2-(2,6-dioxopiperidin-3-yl)-4-(piperazin-1-yl)isoindoline-1,3-dione.

4-(azidomethyl)benzenesulfonyl fluoride (2)

The 4-(bromomethyl)benzenesulfonyl fluoride (0.33 mmol) was dissolved in DMSO. NaN_3 was added. The reaction was stirred at rt for 3h. The product was extracted with 3×1 mL of EtOAc, and the organic layers were evaporated under reduced pressure. The final product, 4-(azidomethyl)benzenesulfonyl fluoride, was stored as a DMSO stock **(Scheme 5. 7)**.

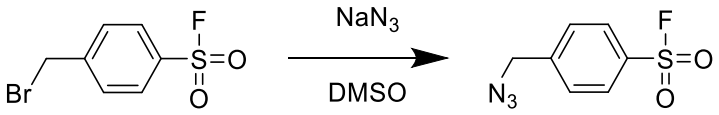

Scheme 5. 7. Synthetic route for the preparation of 4-(azidomethyl)benzenesulfonyl fluoride.

1-(4-(fluorosulfonyl)benzyl)-1H-1,2,3-triazole-4-carboxylic acid (3)

Propiolic acid (0.29 mmol) was dissolved in DMSO. $CuSO_4$ (0.014 mmol), sodium ascorbate (0.028 mmol), and the azide (0.14 mmol) from procedure **2**, were added. The reaction was stirred at rt overnight. The product was extracted with 3×5 mL of EtOAc, and the organic layers were evaporated under reduced pressure. The crude residue was washed with diethyl ether. The compound was purified by flash chromatography (eluent EtOAc 100% to EtOAc:Acetone 1:3), resulting in the product 1-(4-(fluorosulfonyl)benzyl)-1H-1,2,3-triazole-4-carboxylic acid **(Scheme 5. 8)**.

^{1}H NMR (500 MHz, Methanol-d4) δ 8.63 (s, 1H), 8.09 (d, J = 8.5 Hz, 2H), 7.65 (d, J = 8.2 Hz, 2H), 5.86 (s, 2H).

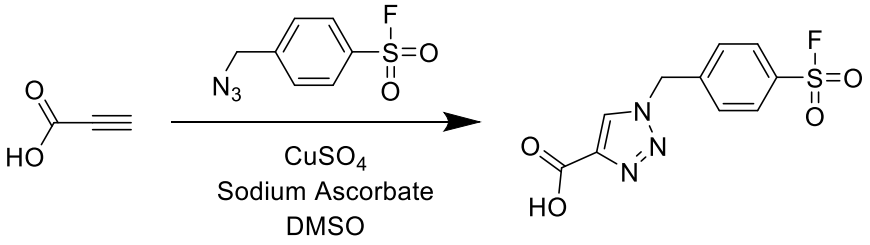

Scheme 5. 8. Synthetic route for the preparation of 1-(4-(fluorosulfonyl)benzyl)-1H-1,2,3-triazole-4-carboxylic acid.

2-(1-(4-(fluorosulfonyl)benzyl)-1H-1,2,3-triazol-4-yl)acetic acid (4)

The but-3-ynoic acid (0.30 mmol) was dissolved in DMSO. $CuSO_4$ (10% mmol), sodium ascorbate (20% mmol), and the azide (1.2 eq.) from procedure **2**, were added. The reaction was stirred at rt overnight. The product was extracted with 3×5 mL of EtOAc and the organic layers were combined and evaporated under reduced pressure. The mixture was washed with diethyl ether, resulting in the pure product 2-(1-(4-(fluorosulfonyl)benzyl)-1H-1,2,3-triazol-4-yl)acetic acid (97%) (**Scheme 5. 9)**.

^{1}H NMR (500 MHz, Methanol-d4) δ 8.07 (d, J = 8.5 Hz, 2H), 8.01 (s, 1H), 7.62 (d, J = 8.1 Hz, 2H), 5.79 (s, 2H), 3.78 (s, 2H).

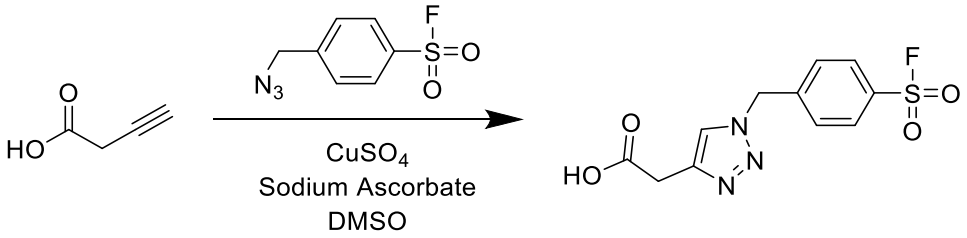

Scheme 5. 9. Synthetic route for the preparation of 2-(1-(4-(fluorosulfonyl)benzyl)-1H-1,2,3-triazol-4-yl)acetic acid.

General preparation of starting material - PROTACs C2 – C8 (5)

Procedure for preparing **PROTAC C2**. Pent-4-ynoic acid (0.49 mmol) was dissolved in DCM and the mixture was cooled to 0˚C. HATU (0.53 mmol) was added, together with DIPEIA (0.65 mmol). The reaction was stirred at 0˚C for 30 min. The pomalidomide-piperazine building block (0.44 mmol) from procedure **1b,** was then added, together with DIPEIA (0.92 mmol). The reaction was allowed to reach rt and stirred overnight. The product was extracted with 6×2 mL of EtOAc, and the organic layers were evaporated under reduced pressure. The mixture was purified by flash column chromatography (eluent Hexane:EtOAc 50:50 to EtOAc 100%), resulting in the product 2-(2,6-dioxopiperidin-3-yl)-4-(4-(pent-4-ynoyl)piperazin-1-yl)isoindoline-1,3-dione (86%) **(Scheme 5. 10)**.

(PROTAC C2) ^{1}HNMR 1H NMR (500 MHz, Chloroform-d) δ 8.25 (s, 1H), 7.62 (dd, J = 8.3, 7.2 Hz, 1H), 7.45 (dd, J = 7.2, 0.7 Hz, 1H), 7.16 (dd, J = 8.4, 0.8 Hz, 1H), 4.96 (dd, J = 12.3, 5.3 Hz, 1H), 3.93 – 3.67 (m, 4H), 3.44 – 3.22 (m, 4H), 2.96 – 2.69 (m, 3H), 2.66 – 2.54 (m, 4H), 2.17 – 2.08 (m, 1H), 1.98 (t, J = 2.6 Hz, 1H).

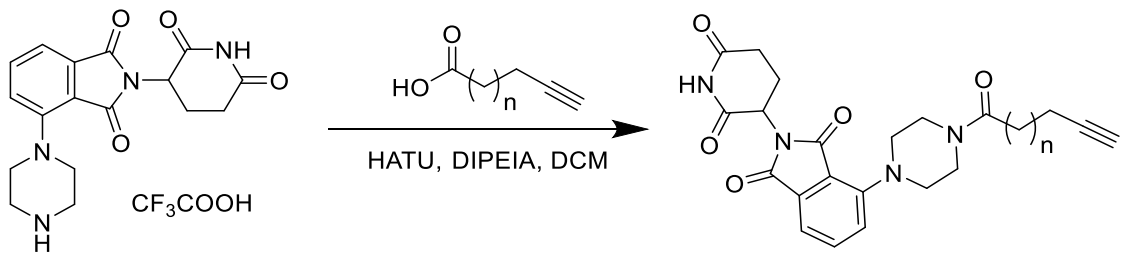

Scheme 5. 10. General synthetic route for the preparation of **PROTACs C2 – C8**.

tert-butyl 4-((4-(2-(2,6-dioxopiperidin-3-yl)-1,3-dioxoisoindolin-4-yl)piperazin-1-yl)methyl)piperidine-1-carboxylate (6a)

The pomalidomide-piperazine building block from procedure **1b**, was dissolved in acetone. Tert-butyl 4-(bromomethyl)piperidine-1-carboxylate (1.2 eq.) was added to the reaction, followed by TEA (1.2 eq.). The reaction was stirred at rt overnight. The product was extracted with 3×10 mL of EtOAc, and the organic layers were evaporated under reduced pressure. The mixture was purified by flash column chromatography (eluent Hexane:EtOAc 50:50 to EtOAc 100%), resulting in the product tert-butyl 4-((4-(2-(2,6-dioxopiperidin-3-yl)-1,3-dioxoisoindolin-4-yl)piperazin-1-yl)methyl)piperidine-1-carboxylate (78%) **(Scheme 5. 11)**.

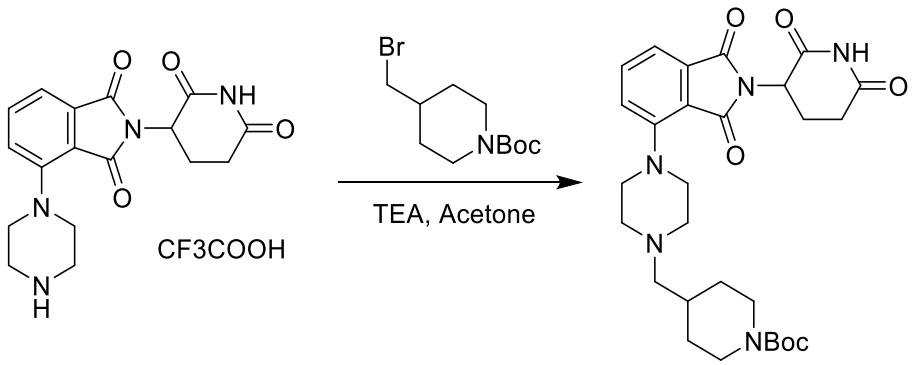

Scheme 5. 11. Synthetic route for the preparation of tert-butyl 4-((4-(2-(2,6-dioxopiperidin-3-yl)-1,3-dioxoisoindolin-4-yl)piperazin-1-yl)methyl)piperidine-1-carboxylate.

2-(2,6-dioxopiperidin-3-yl)-4-(4-(piperidin-4-ylmethyl)piperazin-1-yl)isoindoline-1,3-dione (6b)

Prepared using the product from procedure **6a**. The 2-(2,6-dioxopiperidin-3-yl)-4-(4-(piperidin-4-ylmethyl)piperazin-1-yl)isoindoline-1,3-dione was obtained by suspending tert-butyl 4-((4-(2-(2,6-dioxopiperidin-3-yl)-1,3-dioxoisoindolin-4-yl)piperazin-1-yl)methyl)piperidine-1-carboxylate (0.17 mmol) in DCM. TFA was added. The reaction was refluxed at 50˚C for 3h. The mixture was cooled to rt, and DCM was added and evaporated 3 times. The resulting solid residue was washed with diethyl ether **(Scheme 5. 12)**.

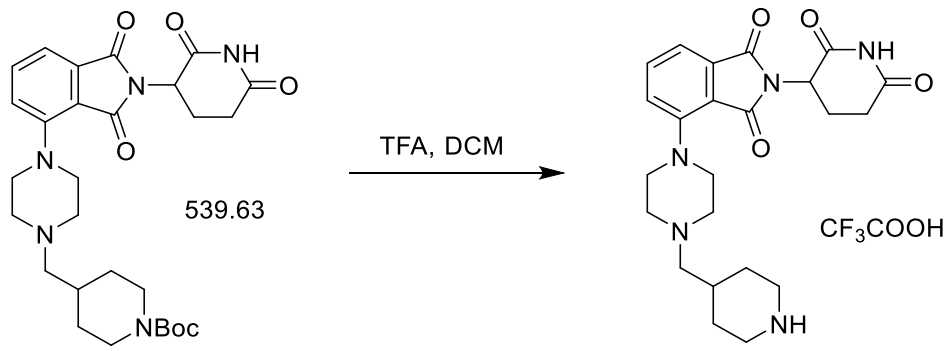

Scheme 5. 12. Synthetic route for the preparation of 2-(2,6-dioxopiperidin-3-yl)-4-(4-(piperidin-4-ylmethyl)piperazin-1-yl)isoindoline-1,3-dione.

4-((4-(2-(2,6-dioxopiperidin-3-yl)-1,3-dioxoisoindolin-4-yl)piperazin-1-yl)methyl)benzenesulfonyl fluoride (PROTAC C-1)

The pomalidomide-piperazine building block from procedure **1b** was dissolved in DMF. TEA (0.222 mmol) was added to the solution, followed by 4-(bromomethyl)benzenesulfonyl fluoride (0.121 mmol). The reaction was heated to 60˚C overnight. The reaction was allowed to reach rt and stirred overnight. The product was extracted with 3×2 mL of EtOAc, and the organic layers were evaporated under reduced pressure. The mixture was purified by flash column chromatography (eluent Hexane:EtOAc 50:50 to EtOAc 100%), resulting in the product 4-((4-(2-(2,6-dioxopiperidin-3-yl)-1,3-dioxoisoindolin-4-yl)piperazin-1-yl)methyl)benzenesulfonyl fluoride (73%) (**Scheme 5. 13)**.

^{1}HNMR 1H NMR (500 MHz, Chloroform-d) δ 7.99 (s, 3H), 7.74 – 7.55 (m, 3H), 7.42 (d, J = 7.2 Hz, 1H), 7.17 (d, J = 8.3 Hz, 1H), 4.95 (dd, J = 12.4, 5.4 Hz, 1H), 3.70 (s, 2H), 3.38 (s, 4H), 2.97 – 2.63 (m, 7H), 2.16 – 2.07 (m, 1H).

^{13}CNMR 13C NMR (101 MHz, CDCl3) δ 171.07, 168.31, 167.40, 166.82, 150.41, 147.37, 135.86, 134.27, 131.96, 131.71, 130.08, 128.67, 123.51, 117.75, 116.09, 62.26, 53.23, 51.16, 49.28, 31.53, 22.81.

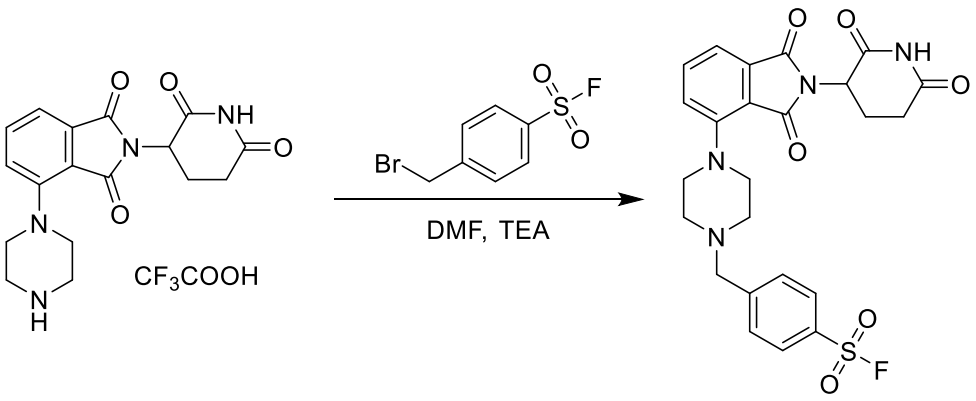

Scheme 5. 13. Synthetic route for the preparation of 4-((4-(2-(2,6-dioxopiperidin-3-yl)-1,3-dioxoisoindolin-4-yl)piperazin-1-yl)methyl)benzenesulfonyl fluoride (**PROTAC C-1**).

4-((4-(4-(2-(2,6-dioxopiperidin-3-yl)-1,3-dioxoisoindolin-4-yl)piperazine-1-carbonyl)-1H-1,2,3-triazol-1-yl)methyl)benzenesulfonyl fluoride (PROTAC C0)

The 1-(4-(fluorosulfonyl)benzyl)-1H-1,2,3-triazole-4-carboxylic acid (0.29 mmol) from procedure **3**, was dissolved in DMF and the mixture was cooled to 0˚C. HATU (0.35 mmol) was added, together with DIPEIA (0.36 mmol). The reaction was stirred at 0˚C for 30 min. The pomalidomide-piperazine building block (0.32 mmol) from procedure **1b**, was added, together with DIPEIA (0.36 mmol). The reaction was allowed to reach rt and stirred overnight. The product was extracted with 3×5 mL of EtOAc, and the organic layers were evaporated under reduced pressure. The mixture was purified by flash column chromatography (eluent Hexane:EtOAC 50:50 to EtOAc 100%), followed by preparative thin layer chromatography (EtOAc:Acetone 2:1), resulting in the product 4-((4-(4-(2-(2,6-dioxopiperidin-3-yl)-1,3-dioxoisoindolin-4-yl)piperazine-1-carbonyl)-1H-1,2,3-triazol-1-yl)methyl)benzenesulfonyl fluoride (15%) **(Scheme 5. 14)**.

^{1}HNMR 1H NMR (500 MHz, Chloroform-d) δ 8.14 (d, J = 1.7 Hz, 1H), 8.10 – 7.95 (m, 3H), 7.63 (t, J = 8.3 Hz, 1H), 7.54 (d, J = 8.0 Hz, 2H), 7.46 (d, J = 7.2 Hz, 1H), 7.18 (d, J = 8.4 Hz, 1H), 5.70 (s, 2H), 4.97 (dd, J = 12.4, 5.2 Hz, 1H), 4.56 (t, J = 4.6 Hz, 2H), 4.01 (q, J = 4.1 Hz, 2H), 3.54 – 3.31 (m, 4H), 2.97 – 2.68 (m, 3H), 2.23 – 2.09 (m, 1H).

^{13}CNMR 13C NMR (101 MHz, CDCl3) δ 170.72, 168.01, 167.16, 166.59, 159.39, 149.93, 145.19, 141.91, 135.86, 134.16, 129.41, 129.06, 128.77, 123.38, 118.12, 116.46, 53.34, 51.68, 51.00, 49.22, 46.66, 42.77, 31.41, 22.66.

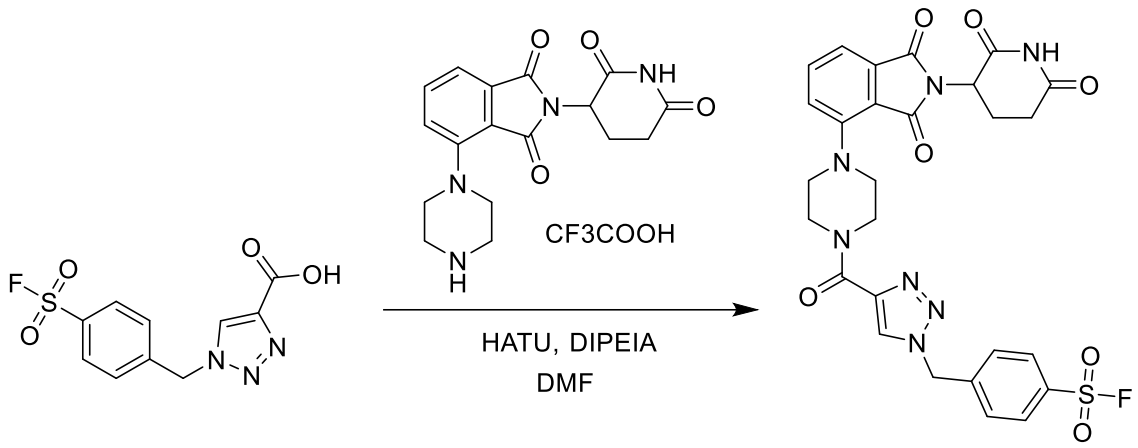

Scheme 5. 14. Synthetic route for the preparation of 4-((4-(4-(2-(2,6-dioxopiperidin-3-yl)-1,3-dioxoisoindolin-4-yl)piperazine-1-carbonyl)-1H-1,2,3-triazol-1-yl)methyl)benzenesulfonyl fluoride (**PROTAC C0**).

4-((4-(2-(4-(2-(2,6-dioxopiperidin-3-yl)-1,3-dioxoisoindolin-4-yl)piperazin-1-yl)-2-oxoethyl)-1H-1,2,3-triazol-1-yl)methyl)benzenesulfonyl fluoride (PROTAC C1)

The 2-(1-(4-(fluorosulfonyl)benzyl)-1H-1,2,3-triazol-4-yl)acetic acid (0.27 mmol) from procedure **4**, was dissolved in DMSO. The mixture was cooled to 0˚C. HATU (0.29 mmol) was added, together with DIPEIA (0.29 mmol). The reaction was stirred at 0˚C for 30 min. The pomalidomide-piperazine building block (0.18 mmol) from procedure **1b**, was added, together with DIPEIA (0.29 mmol). The reaction was allowed to reach rt and stirred overnight. The product was extracted with 3×5 mL of EtOAc, and the organic layers evaporated under reduced pressure. The mixture was purified by flash column chromatography (EtOAc 50:50 to EtOAc:Acetone 50:50), resulting in the product 4-((4-(2-(4-(2-(2,6-dioxopiperidin-3-yl)-1,3-dioxoisoindolin-4-yl)piperazin-1-yl)-2-oxoethyl)-1H-1,2,3-triazol-1-yl)methyl)benzenesulfonyl fluoride (67%) **(Scheme 5. 15)**.

^{1}HNMR 1H NMR (400 MHz, Chloroform-d) δ 8.29 (s, 1H), 8.00 (d, J = 8.5 Hz, 2H), 7.70 (s, 1H), 7.62 (dd, J = 8.4, 7.2 Hz, 1H), 7.48 (d, J = 8.2 Hz, 2H), 7.45 (d, J = 7.2 Hz, 1H), 7.14 (d, J = 8.3 Hz, 1H), 5.64 (s, 2H), 4.97 (dd, J = 12.1, 5.3 Hz, 1H), 3.93 (s, 2H), 3.91 – 3.74 (m, 4H), 3.46 – 3.20 (m, 4H), 2.96 – 2.65 (m, 3H), 2.20 – 2.06 (m, 1H).

^{13}CNMR 13C NMR (101 MHz, CDCl3) δ 170.88, 168.16, 167.85, 167.13, 166.61, 149.74, 142.85, 142.52, 135.88, 134.12, 133.46, 133.21, 129.26, 128.86, 123.35, 123.27, 118.14, 116.56, 53.17, 51.60, 50.39, 49.22, 46.19, 41.86, 31.40, 31.22, 22.64.

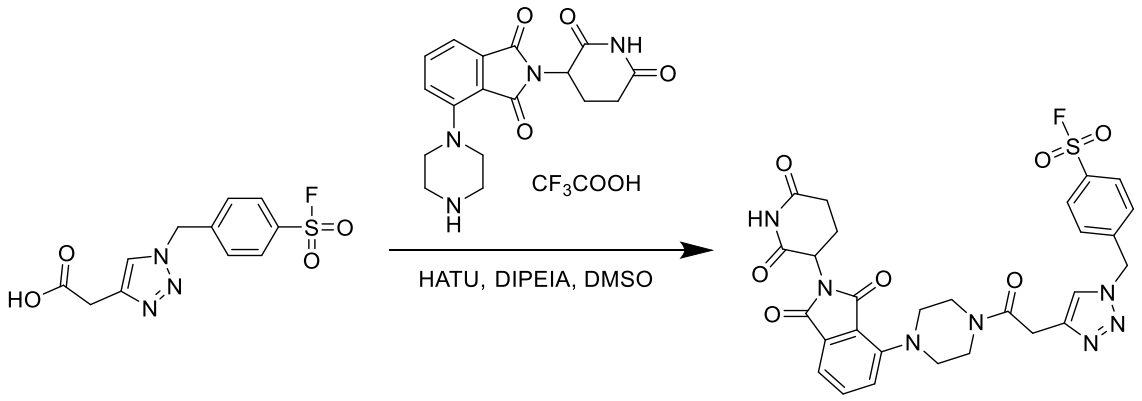

Scheme 5. 15. Synthetic route for the preparation of 4-((4-(2-(4-(2-(2,6-dioxopiperidin-3-yl)-1,3-dioxoisoindolin-4-yl)piperazin-1-yl)-2-oxoethyl)-1H-1,2,3-triazol-1-yl)methyl)benzenesulfonyl fluoride (**PROTAC C1**).

General preparation of PROTACs C2 – C8

Procedure for **PROTAC C2**. The 2-(2,6-dioxopiperidin-3-yl)-4-(4-(pent-4-ynoyl)piperazin-1-yl)isoindoline-1,3-dione (0.095 mmol) from procedure **5**, was dissolved in DMSO. $CuSO_4$ (0.0094 mmol), sodium ascorbate (0.019 mmol), and the azide (0.11 mmol) from procedure **2**, were added. The reaction was stirred at rt overnight. The product was extracted with 6×1 mL of EtOAc, and the organic layers were evaporated under reduced pressure. The mixture was purified by preparative thin layer chromatography (EtOAc:Acetone 2:1), resulting in the product 4-((4-(3-(4-(2-(2,6-dioxopiperidin-3-yl)-1,3-dioxoisoindolin-4-yl)piperazin-1-yl)-3-oxopropyl)-1H-1,2,3-triazol-1-yl)methyl)benzene sulfonyl fluoride (68%) **(Scheme 5. 16)**.

(**PROTAC C2**) ^{1}H NMR (400 MHz, Chloroform-d) δ 8.10 – 7.99 (m, 3H), 7.63 (dd, J = 8.4, 7.2 Hz, 1H), 7.51 – 7.41 (m, 4H), 7.14 (d, J = 8.4 Hz, 1H), 5.61 (s, 1H), 4.97 (dd, J = 12.1, 5.2 Hz, 1H), 3.97 – 3.58 (m, 4H), 3.45 – 3.21 (m, 4H), 3.10 (t, J = 6.9 Hz, 2H), 2.99 – 2.70 (m, 5H), 2.20 – 2.06 (m, 1H).

(**PROTAC C2**) ^{13}CNMR (126 MHz, CDCl3) δ 170.74, 170.36, 168.04, 167.14, 166.60, 149.81, 147.82, 142.99, 135.89, 134.17, 129.27, 128.89, 128.81, 128.31, 123.37, 122.25, 116.56, 53.10, 51.54, 50.57, 49.24, 45.50, 32.21, 31.42, 22.66, 21.00.

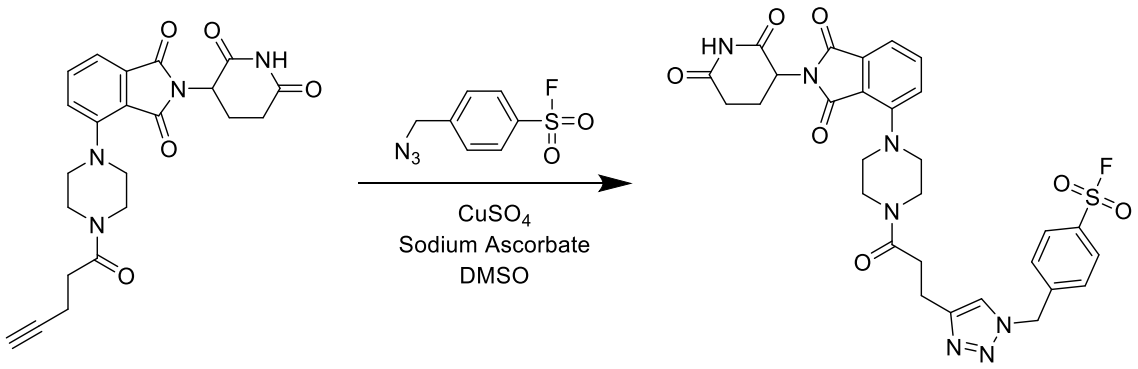

Scheme 5. 16. Synthetic route for the preparation of 4-((4-(3-(4-(2-(2,6-dioxopiperidin-3-yl)-1,3-dioxoisoindolin-4-yl)piperazin-1-yl)-3-oxopropyl)-1H-1,2,3-triazol-1-yl)methyl)benzenesulfonyl fluoride (**PROTAC C2**).

4-((4-((4-(2-(2,6-dioxopiperidin-3-yl)-1,3-dioxoisoindolin-4-yl)piperazin-1-yl)methyl) piperidin-1-yl)methyl)benzenesulfonyl fluoride (PROTAC R1)

The 2-(2,6-dioxopiperidin-3-yl)-4-(4-(piperidin-4-ylmethyl)piperazin-1-yl)isoindoline-1,3-dione (0.18 mmol) from procedure **6b**, was dissolved in DMSO. The 4-(bromomethyl)benzenesulfonyl fluoride (0.2 mmol) was added, followed by TEA (0.38 mmol). The reaction was stirred at rt overnight. The product was extracted with 3×10 mL of EtOAc, and the organic layers were evaporated under reduced pressure. The mixture was purified by flash column chromatography (Hexane:EtOAc 50:50 to EtOAc:Acetone 50:50), resulting in 4-((4-((4-(2-(2,6-dioxopiperidin-3-yl)-1,3-dioxoisoindolin-4-yl)piperazin-1-yl)methyl)piperidin-1-yl)methyl)benzenesulfonyl fluoride (37%) **(Scheme 5. 17)**.

^{1}HNMR 1H NMR (400 MHz, Chloroform-d) δ 8.02 (s, 1H), 7.95 (d, J = 8.0 Hz, 2H), 7.64 – 7.53 (m, 3H), 7.39 (d, J = 7.1 Hz, 1H), 7.16 (d, J = 8.4 Hz, 1H), 4.95 (dd, J = 12.2, 5.3 Hz, 1H), 3.59 (s, 2H), 3.35 (q, J = 5.4 Hz, 4H), 2.94 – 2.69 (m, 5H), 2.63 (d, J = 5.0 Hz, 4H), 2.27 (d, J = 7.0 Hz, 2H), 2.15 – 2.07 (m, 1H), 2.02 (td, J = 11.5, 2.4 Hz, 2H), 1.76 (d, J = 12.4 Hz, 2H), 1.36 – 1.18 (m, 2H).

^{13}C NMR (101 MHz, CDCl3) δ 171.14, 168.38, 167.45, 166.81, 150.51, 135.79, 134.25, 131.63, 131.37, 129.97, 128.54, 123.50, 117.53, 115.87, 69.65, 64.61, 62.66, 53.94, 53.63, 51.06, 49.26, 33.11, 31.87, 31.54, 30.99, 29.40, 22.81.

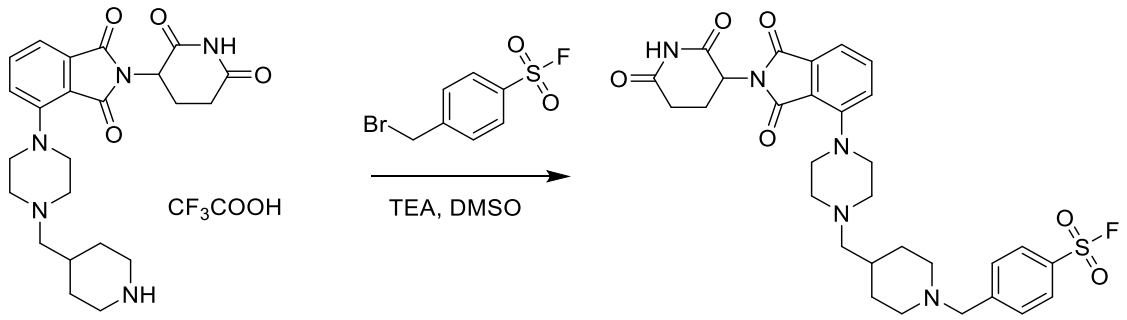

Scheme 5. 17. Synthetic route for the preparation of 4-((4-((4-(2-(2,6-dioxopiperidin-3-yl)-1,3-dioxoisoindolin-4-yl)piperazin-1-yl)methyl)piperidin-1-yl)methyl)benzenesulfonyl fluoride (**PROTAC R1**).

2-(2,6-dioxopiperidin-3-yl)-4-(4-(4-ethynylbenzoyl)piperazin-1-yl)isoindoline-1,3-dion e (7)

The 4-ethynylbenzoic acid (0.684 mmol) was dissolved in DMF and the mixture was cooled to 0˚C. HATU (0.513 mmol) was added, together with DIPEIA (0.821 mmol). The reaction was stirred at 0˚C for 30 min. The pomalidomide-piperazine building block (0.427 mmol) from procedure **1b**, was added, together with DIPEIA (0.821 mmol). The reaction was allowed to reach rt and stirred overnight. The product was extracted with 3×2 mL of EtOAc, and the organic layers were evaporated under reduced pressure. The mixture was purified by flash column chromatography (eluent Hexane:EtOAc 50:50 to EtOAc 100%), resulting in the product 2-(2,6-dioxopiperidin-3-yl)-4-(4-(4-ethynylbenzoyl)piperazin-1-yl)isoindoline-1,3-dione (87%) (**Scheme 5. 18)**.

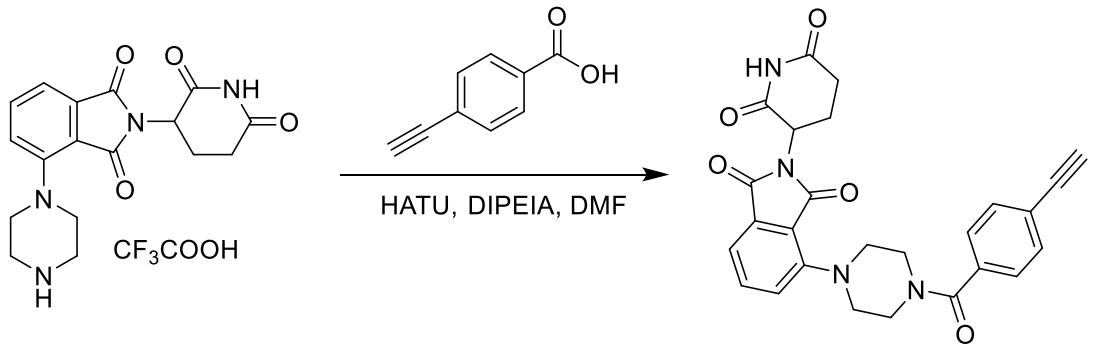

Scheme 5. 18. Synthetic route for the preparation of 2-(2,6-dioxopiperidin-3-yl)-4-(4-(4-ethynylbenzoyl)piperazin-1-yl)isoindoline-1,3-dione.

4-((4-(4-(4-(2-(2,6-dioxopiperidin-3-yl)-1,3-dioxoisoindolin-4-yl)piperazine-1-carbonyl)phenyl)-1H-1,2,3-triazol-1-yl)methyl)benzenesulfonyl fluoride (PROTAC F9)

The 2-(2,6-dioxopiperidin-3-yl)-4-(4-(4-ethynylbenzoyl)piperazin-1-yl)isoindoline-1,3-dione (0.085 mmol) from procedure **7**, was dissolved in DMSO. $CuSO_4$ (0.0087 mmol), sodium ascorbate (0.017 mmol), and the azide (3 eq.) were then added. The reaction was stirred at rt overnight. The product was extracted with 3×2 mL of EtOAc. The organic layers were evaporated under reduced pressure. The mixture was purified by flash column chromatography (EtOAc 50:50 to EtOAc:Acetone 50:50), resulting in the product 4-((4-(4-(4-(2-(2,6-dioxopiperidin-3-yl)-1,3-dioxoisoindolin-4-yl)piperazine-1-carbonyl)phenyl)-1H-1,2,3-triazol-1-yl)methyl)benzenesulfonyl fluoride (77%) **(Scheme 5. 19)**.

^{1}HNMR 1H NMR (400 MHz, Chloroform-d) δ 8.04 (d, J = 8.3 Hz, 2H), 7.88 (d, J = 8.1 Hz, 2H), 7.81 (s, 1H), 7.67 – 7.59 (m, 1H), 7.53 (dd, J = 12.3, 8.3 Hz, 4H), 7.46 (d, J = 7.1 Hz, 1H), 7.17 (d, J = 8.4 Hz, 1H), 5.73 (s, 2H), 4.95 (dd, J = 12.2, 5.3 Hz, 1H), 4.14 – 3.64 (m, 4H), 3.51 – 3.20 (m, 4H), 2.94 – 2.67 (m, 3H), 2.16 – 2.08 (m, 1H).

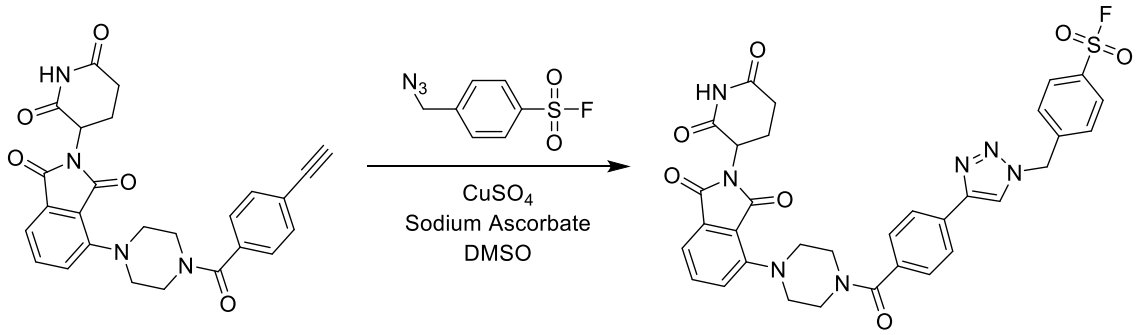

Scheme 5. 19. Synthetic route for the preparation of 4-((4-(4-(4-(2-(2,6-dioxopiperidin-3-yl)-1,3-dioxoisoindolin-4-yl)piperazine-1-carbonyl)phenyl)-1H-1,2,3-triazol-1-yl)methyl)benzenesulfonyl fluoride (**PROTAC F9**).

tert-butyl (3-(4-(2-(2,6-dioxopiperidin-3-yl)-1,3-dioxoisoindolin-4-yl)piperazin-1-yl)-3-oxopropyl)carbamate (8a)

The 3-((tert-butoxycarbonyl)amino)propanoic acid (0.20 mmol) was dissolved in DCM and the mixture was cooled to 0˚C. HATU (0.33 mmol) was added, together with DIPEIA (0.33 mmol). The reaction was stirred at 0˚C for 30 min. The pomalidomide-piperazine building block (0.22 mmol) from procedure **1b**, was added, together with DIPEIA (0.33 mmol). The reaction was allowed to reach rt and stirred overnight. The product was extracted with 3×10 mL of EtOAc, and the organic layers were evaporated under reduced

pressure. The mixture was purified by flash column chromatography (eluent Hexane:EtOAc 50:50 to EtOAc 100%), resulting in the product tert-butyl (3-(4-(2-(2,6-dioxopiperidin-3-yl)-1,3-dioxoisoindolin-4-yl)piperazin-1-yl)-3-oxopropyl)carbamate (76%) **(Scheme 5. 20)**.

^{1}H NMR (500 MHz, Chloroform-d) δ 7.99 (s, 1H), 7.60 (dd, J = 8.2, 7.4 Hz, 1H), 7.43 (d, J = 7.0 Hz, 1H), 7.13 (d, J = 8.4 Hz, 1H), 5.33 (s, 1H), 4.95 (dd, J = 12.2, 5.3 Hz, 1H), 3.90 – 3.74 (m, 2H), 3.66 (t, J = 4.9 Hz, 2H), 3.49 – 3.39 (m, 2H), 3.37 – 3.21 (m, 4H), 2.92 – 2.63 (m, 3H), 2.55 (t, J = 5.4 Hz, 2H), 2.15 – 2.07 (m, 1H), 1.41 (s, 9H).

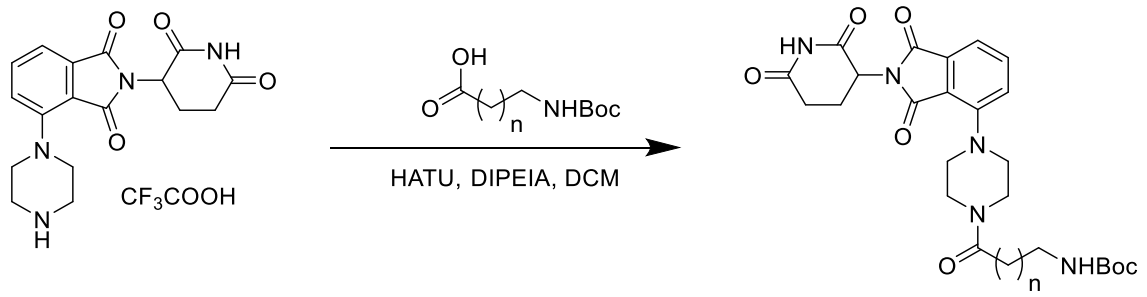

Scheme 5. 20. Synthetic route for the preparation of tert-butyl (3-(4-(2-(2,6-dioxopiperidin-3-yl)-1,3-dioxoisoindolin-4-yl)piperazin-1-yl)-3-oxopropyl)carbamate.

3-(7-(4-(3-aminopropanoyl)piperazin-1-yl)-1-oxoisoindolin-2-yl)piperidine-2,6-dione (8b)

The tert-butyl (3-(4-(2-(2,6-dioxopiperidin-3-yl)-1,3-dioxoisoindolin-4-yl)piperazin-1-yl)-3-oxopropyl)carbamate (0.15 mmol) from procedure **8a**, was suspended in DCM. TFA was added and the reaction was refluxed at 45˚C for 3h. The reaction was cooled to rt and the solvent was evaporated to near completion. Diethyl ether was added, causing the product to precipitate. The product was filtered and washed with diethyl ether 3 times, yielding the TFA salt of 3-(7-(4-(3-aminopropanoyl)piperazin-1-yl)-1-oxoisoindolin-2-yl)piperidine-2,6-dione **(Scheme 5. 21)**.

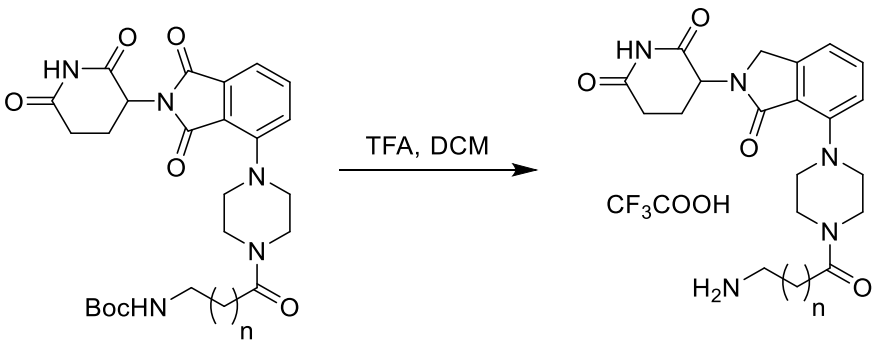

Scheme 5. 21. Synthetic route for the preparation of 3-(7-(4-(3-aminopropanoyl)piperazin-1-yl)-1-oxoisoindolin-2-yl)piperidine-2,6-dione.

N-(3-(4-(2-(2,6-dioxopiperidin-3-yl)-1,3-dioxoisoindolin-4-yl)piperazin-1-yl)-3-oxopropyl)-4-ethynylbenzamide (9)

The 4-ethynylbenzoic acid (0.096 mmol) was dissolved in DMF and the mixture was cooled to 0˚C. HATU (0.092 mmol) was added, together with DIPEIA (0.092 mmol). The reaction was stirred at 0˚C for 30 min. The pomalidomide-piperazine building block (0.076 mmol) from procedure **8b**, was then added, together with DIPEIA (0.092 mmol). The reaction was allowed to reach rt and stirred overnight. The product was extracted with 3×10 mL of EtOAc, and the organic layers were evaporated under reduced pressure. The mixture was purified by flash column chromatography (eluent Hexane:EtOAc 50:50 to EtOAc 100%), resulting in the product N-(3-(4-(2-(2,6-dioxopiperidin-3-yl)-1,3-dioxo isoindolin-4-yl)piperazin-1-yl)-3-oxopropyl)-4-ethynylbenzamide (39%) **(Scheme 5. 22)**.

^{1}H NMR (500 MHz, Chloroform-d) δ 8.45 (s, 1H), 7.74 (d, J = 8.5 Hz, 2H), 7.64 – 7.58 (m, 1H), 7.52 (d, J = 8.4 Hz, 2H), 7.45 (d, J = 7.1 Hz, 1H), 7.27 (d, J = 6.0 Hz, 2H), 7.13 (d, J = 8.4 Hz, 1H), 4.96 (dd, J = 12.4, 5.3 Hz, 1H), 3.91 – 3.74 (m, 4H), 3.67 (t, J = 4.9 Hz, 2H), 3.39 – 3.24 (m, 4H), 3.19 (s, 1H), 2.96 – 2.72 (m, 3H), 2.71 – 2.66 (m, 2H), 2.20 – 2.06 (m, 1H).

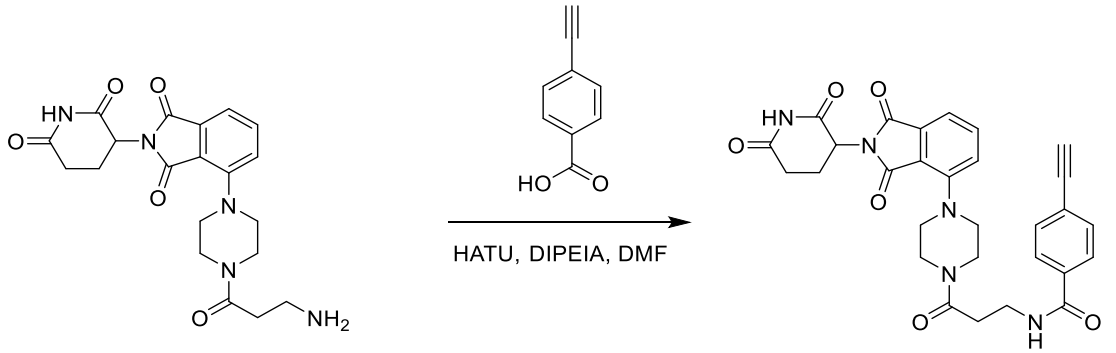

Scheme 5. 22. Synthetic route for the preparation of N-(3-(4-(2-(2,6-dioxopiperidin-3-yl)-1,3-dioxoisoindolin-4-yl)piperazin-1-yl)-3-oxopropyl)-4-ethynylbenzamide.

4-((4-(4-((3-(4-(2-(2,6-dioxopiperidin-3-yl)-1,3-dioxoisoindolin-4-yl)piperazin-1-yl)-3-oxopropyl)carbamoyl)phenyl)-1H-1,2,3-triazol-1-yl)methyl)benzenesulfonyl fluoride (PROTACs F10-F11)

Procedure for **PROTAC F10**. The alkyne N-(3-(4-(2-(2,6-dioxopiperidin-3-yl)-1,3-dioxo isoindolin-4-yl)piperazin-1-yl)-3-oxopropyl)-4-ethynylbenzamide (0.029 mmol) from procedure **9**, was dissolved in DMSO. $CuSO_4$ (0.003 mmol), sodium ascorbate (0.006 mmol), and the azide (0.088 mmol) from procedure **2**, were then added. The reaction was stirred at rt overnight. The product was extracted with 3×5 mL of EtOAc. The organic layers were evaporated under reduced pressure. The product was purified by preparative HPLC (H_2O:ACN 95:5 to 5:95), resulting in the product, 4-((4-(4-((3-(4-(2-(2,6-dioxopiperidin-3-yl)-1,3-dioxoisoindolin-4-yl)piperazin-1-yl)-3-oxopropyl)carbamoyl)phenyl)-1H-1,2,3-triazol-1-yl)methyl)benzenesulfonyl fluoride (52%) **(Scheme 5. 23)**.

(**PROTAC F10**) ^{1}H NMR (400 MHz, Chloroform-d) δ 8.09 (s, 1H), 8.05 (d, J = 8.5 Hz, 2H), 7.91 – 7.81 (m, 4H), 7.62 (dd, J = 8.3, 7.2 Hz, 1H), 7.58 – 7.51 (m, 2H), 7.46 (dd, J = 7.3, 0.7 Hz, 1H), 7.44 – 7.38 (m, 1H), 7.14 (dd, J = 8.4, 0.9 Hz, 1H), 5.74 (s, 2H), 4.96 (dd, J = 12.2, 5.3 Hz, 1H), 3.95 – 3.77 (m, 4H), 3.72 (t, J = 4.9 Hz, 2H), 3.32 (dt, J = 17.5, 5.1 Hz, 4H), 3.02 – 2.70 (m, 5H), 2.16 – 2.09 (m, 1H).

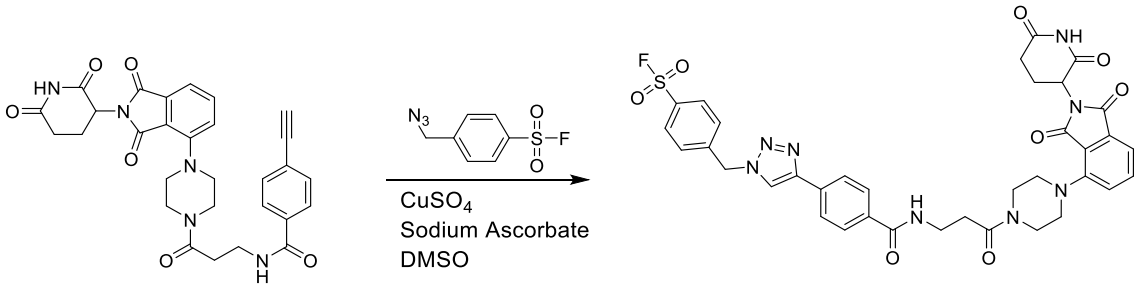

Scheme 5. 23. Synthetic route for the preparation of 4-((4-(4-((3-(4-(2-(2,6-dioxopiperidin-3-yl)-1,3-dioxoisoindolin-4-yl)piperazin-1-yl)-3oxopropyl)carbamoyl)phenyl)-1H-1,2,3-triazol-1-yl)methyl)benzenesulfonyl fluoride (**PROTAC F10**).

tert-butyl (1-((6-(4-(2-(2,6-dioxopiperidin-3-yl)-1,3-dioxoisoindolin-4-yl)piperazin-1-yl)-6-oxohexyl)amino)-1-oxopent-4-yn-2-yl)carbamate (10)

The 2-((tert-butoxycarbonyl)amino)pent-4-ynoic acid (0.075 mmol) was dissolved in DMF and the mixture was cooled to 0˚C. HATU (0.074 mmol) was added, together with DIPEIA (0.075 mmol). The reaction was stirred at 0˚C for 30 min. The pomalidomide-piperazine building block (0.062 mmol) from procedure **8b**, was added, together with DIPEIA (0.075 mmol). The reaction was allowed to reach rt and stirred overnight. The product was extracted with 3×10 mL of EtOAc, and the organic layers were evaporated under reduced pressure. The mixture was purified by flash column chromatography (eluent Hexane:EtOAc 50:50 to EtOAc 100%), resulting in the product tert-butyl (1-((6-(4-(2-(2,6-dioxopiperidin-3-yl)-1,3-dioxoisoindolin-4-yl)piperazin-1-yl)-6-oxohexyl)amino)-1-oxopent-4-yn-2-yl)carbamate (74%) **(Scheme 5. 24)**.

^{1}H NMR (500 MHz, Chloroform-d) δ 8.67 (s, 1H), 7.63 (dd, J = 7.4, 0.8 Hz, 1H), 7.45 (d, J = 7.1 Hz, 1H), 7.17 (d, J = 8.4 Hz, 1H), 6.58 (t, J = 5.7 Hz, 1H), 5.43 (s, 1H), 4.98 (dd, J = 12.2, 5.3 Hz, 1H), 4.27 (s, 1H), 3.99 – 3.59 (m, 4H), 3.42 – 3.24 (m, 6H), 2.93 – 2.71 (m, 4H), 2.65 – 2.56 (m, 1H), 2.38 (t, J = 7.3 Hz, 2H), 2.17 – 2.08 (m, 2H), 1.67 (p, J = 7.3 Hz, 2H), 1.55 (p, J = 7.2 Hz, 2H), 1.46 (s, 9H), 1.41 (p, J = 8.2 Hz, 2H).

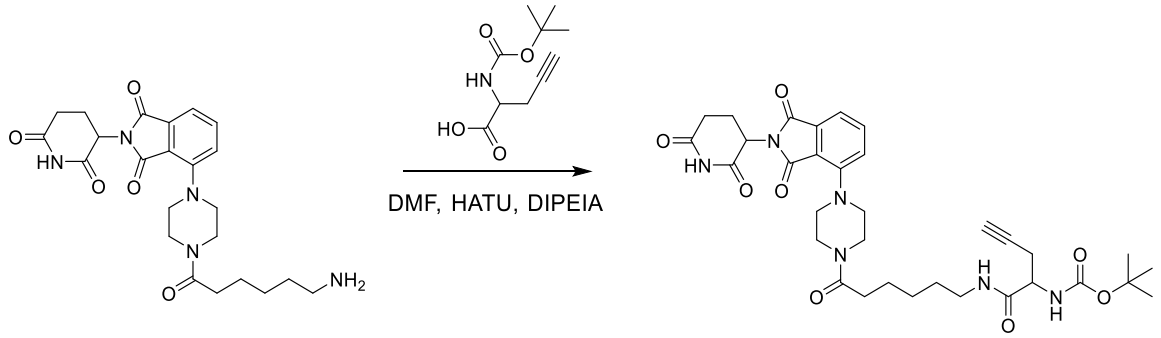

Scheme 5. 24. Synthetic route for the preparation of tert-butyl (1-((6-(4-(2-(2,6-dioxopiperidin-3-yl)-1,3-dioxoisoindolin-4-yl)piperazin-1-yl)-6-oxohexyl)amino)-1-oxopent-4-yn-2-yl)carbamate.

tert-butyl (1-((6-(4-(2-(2,6-dioxopiperidin-3-yl)-1,3-dioxoisoindolin-4-yl)piperazin-1-yl)-6-oxohexyl)amino)-3-(1-(4-(fluorosulfonyl)benzyl)-1H-1,2,3-triazol-4-yl)-1-oxopropan-2-yl)carbamate (11)

The tert-butyl (1-((6-(4-(2-(2,6-dioxopiperidin-3-yl)-1,3-dioxoisoindolin-4-yl)piperazin-1-yl)-6-oxohexyl)amino)-1-oxopent-4-yn-2-yl)carbamate (0.046 mmol), from procedure **10**, was dissolved in DMSO. $CuSO_4$ (0.0048 mmol), sodium ascorbate (0.0096 mmol), and the azide (0.14 mmol) from procedure **2**, were added. The reaction was stirred at rt overnight. The product was extracted with 3×5 mL of EtOAc, and the organic layers were evaporated under reduced pressure. The product was purified by preparative HPLC (H_2O:ACN 95:5 to 5:95), resulting in the product tert-butyl (1-((6-(4-(2-(2,6-dioxopiperidin-3-yl)-1,3-dioxoisoindolin-4-yl)piperazin-1-yl)-6-oxohexyl)amino)-3-(1-(4-(fluorosulfonyl)benzyl)-1H-1,2,3-triazol-4-yl)-1-oxopropan-2-yl)carbamate (68%) **(Scheme 5. 25)**.

^{1}H NMR (500 MHz, Chloroform-d) δ 8.64 (s, 1H), 7.61 (dd, J = 8.4, 7.2 Hz, 1H), 7.43 (d, J = 7.1 Hz, 1H), 7.15 (d, J = 8.4 Hz, 1H), 6.56 (t, J = 5.9 Hz, 1H), 5.41 (s, 1H), 4.96 (dd, J = 12.2, 5.3 Hz, 1H), 4.25 (s, 1H), 3.90 – 3.63 (m, 4H), 3.42 – 3.19 (m, 6H), 2.90 – 2.70 (m, 4H), 2.58 (ddd, J = 16.8, 6.8, 2.6 Hz, 1H), 2.35 (t, J = 7.3 Hz, 2H), 2.14 – 2.06 (m, 2H), 1.65 (p, J = 7.4 Hz, 2H), 1.53 (p, J = 7.1 Hz, 2H), 1.43 (s, 9H), 1.41 – 1.32 (m, 2H).

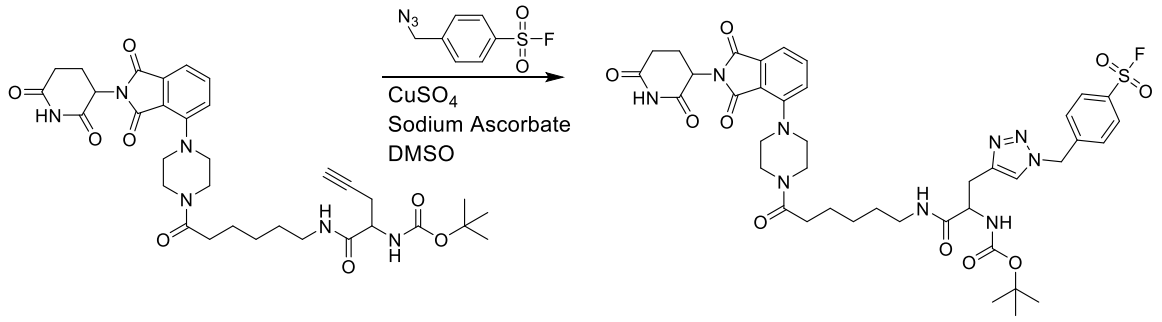

Scheme 5. 25. Synthetic route for the preparation of tert-butyl (1-((6-(4-(2-(2,6-dioxopiperidin-3-yl)-1,3-dioxoisoindolin-4-yl)piperazin-1-yl)-6-oxohexyl)amino)-1-oxopent-4-yn-2-yl)carbamate.

4-((4-(2-amino-3-((6-(4-(2-(2,6-dioxopiperidin-3-yl)-1,3-dioxoisoindolin-4-yl)piperazin-1-yl)-6-oxohexyl)amino)-3-oxopropyl)-1H-1,2,3-triazol-1-yl)methyl)benzenesulfonyl fluoride (PROTAC F12)

The tert-butyl (1-((6-(4-(2-(2,6-dioxopiperidin-3-yl)-1,3-dioxoisoindolin-4-yl)piperazin-1-yl)-6-oxohexyl)amino)-3-(1-(4-(fluorosulfonyl)benzyl)-1H-1,2,3-triazol-4-yl)-1-oxopropan-2-yl)carbamate (0.031 mmol) from procedure **11**, was suspended in DCM. TFA was added and the reaction was refluxed at 45˚C for 3h. The reaction was cooled to rt and the solvent was evaporated to near completion. Diethyl ether was added, causing the product to precipitate. The product was filtered and washed with diethyl ether 3 times. The product was further purified by preparative HPLC (H_2O:ACN 95:5 to 5:95), resulting in the product as the TFA salt of 4-((4-(2-amino-3-((6-(4-(2-(2,6-dioxopiperidin-3-yl)-1,3-dioxoisoindolin-4-yl)piperazin-1-yl)-6-oxohexyl)amino)-3-oxopropyl)-1H-1,2,3-triazol-1-yl)methyl)benzenesulfonyl fluoride **(Scheme 5. 26)**. The solid was purified by preparative HPLC (51%).

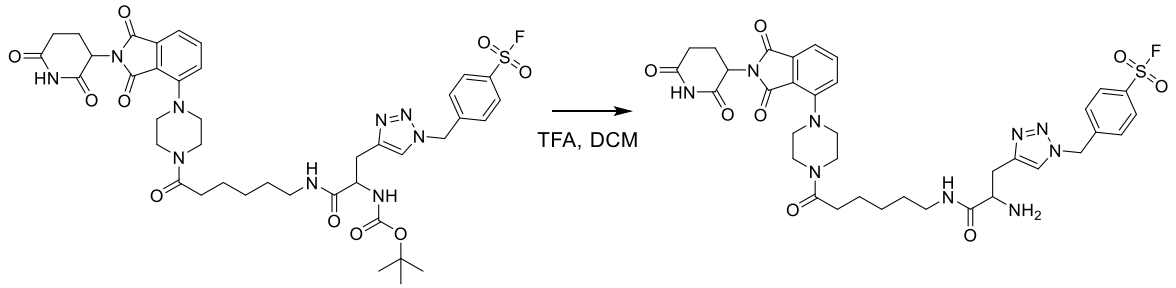

Scheme 5. 26. Synthetic route for the preparation of tert-butyl (1-((6-(4-(2-(2,6-dioxopiperidin-3-yl)-1,3-dioxoisoindolin-4-yl)piperazin-1-yl)-6-oxohexyl)amino)-1-oxopent-4-yn-2-yl)carbamate (**PROTAC F12**).

tert-butyl 4-(2-azidoacetyl)piperazine-1-carboxylate (12a)

The starting compound tert-butyl 4-(2-chloroacetyl)piperazine-1-carboxylate (1.16 mmol) was dissolved in DMSO. NaN_3 (5.8 mmol) and NaI (5.8 mmol) were added. The reaction was stirred at 60˚C for 3h. The product was extracted with 3×10 mL of EtOAc, and the organic layers were evaporated under reduced pressure. The mixture was purified by flash column chromatography (Hexane:EtOAc 50:50), resulting in the product tert-butyl 4-(2-azidoacetyl)piperazine-1-carboxylate (95%) **(Scheme 5. 27)**.

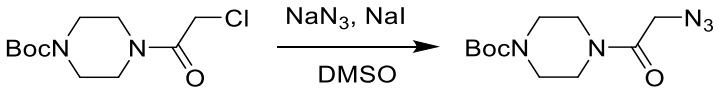

Scheme 5. 27. Synthetic route for the preparation of tert-butyl 4-(2-azidoacetyl)piperazine-1-carboxylate.

2-azido-1-(piperazin-1-yl)ethan-1-one (12b)

The starting compound tert-butyl 4-(2-azidoacetyl)piperazine-1-carboxylate (0.37 mmol) from procedure **12a**, was dissolved in DCM and then TFA was added. The reaction was refluxed at 50˚C for 3h. The solvent was evaporated. DCM was added and then evaporated two times. The compound was obtained as the TFA salt of 2-azido-1-(piperazin-1-yl)ethan-1-one **(Scheme 5. 28)**.

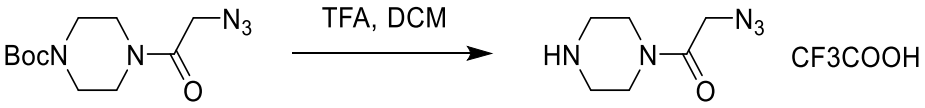

Scheme 5. 28. Synthetic route for the preparation of 2-azido-1-(piperazin-1-yl)ethan-1-one.

2-azido-1-(4-(furan-2-carbonyl)piperazin-1-yl)ethan-1-one (13)

Furan-2-carboxylic acid (0.55 mmol) was dissolved in DMF, and the mixture was cooled to 0˚C. HATU (0.55 mmol) was added, together with DIPEIA (0.57 mmol). The reaction was stirred at 0˚C for 30 min. The TFA salt of 2-azido-1-(piperazin-1-yl)ethan-1-one (0.37 mmol) from procedure **12b**, was added, together with DIPEIA (0.57 mmol). The reaction was allowed to reach rt and stirred overnight. The product was extracted with 3×5 mL of EtOAc, and the organic layers were evaporated under reduced pressure. The mixture was

purified by flash column chromatography (eluent Hexane:EtOAc 50:50 to EtOAc 100%), resulting in the product 2-azido-1-(4-(furan-2-carbonyl)piperazin-1-yl)ethan-1-one (89%) **(Scheme 5. 29)**.

^{1}H NMR (500 MHz, Chloroform-d) δ 7.51 (d, J = 1.8 Hz, 1H), 7.09 (d, J = 3.5 Hz, 1H), 6.52 (dd, J = 3.4, 1.7 Hz, 1H), 3.98 (s, 2H), 3.86 (s, 4H), 3.79 – 3.70 (m, 2H), 3.54 – 3.45 (m, 2H).

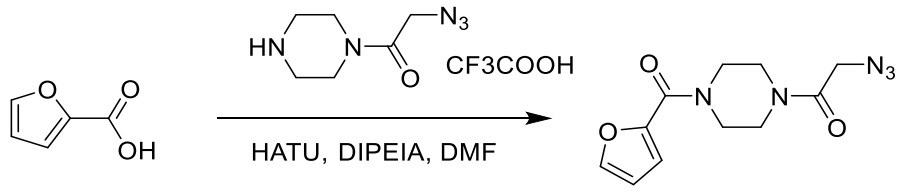

Scheme 5. 29. Synthetic route for the preparation of 2-azido-1-(4-(furan-2-carbonyl)piperazin-1-yl)ethan-1-one.

2-(2,6-dioxopiperidin-3-yl)-4-(4-(5-(1-(2-(4-(furan-2-carbonyl)piperazin-1-yl)-2-oxoeth yl)-1H-1,2,3-triazol-4-yl)pentanoyl)piperazin-1-yl)isoindoline-1,3-dione (R-PROTAC)

The 2-(2,6-dioxopiperidin-3-yl)-4-(4-(hept-6-ynoyl)piperazin-1-yl)isoindoline-1,3-dione (0.12 mmol) from procedure **5**, was dissolved in DMF. $CuSO_4$ (0.014 mmol), sodium ascorbate (0.028 mmol), and the azide 2-azido-1-(4-(furan-2-carbonyl)piperazin-1-yl)ethan-1-one (0.14 eq.) from procedure **13**, were added. The reaction was stirred at rt overnight. The product was extracted with 5×5 mL of EtOAc, and the organic layers were evaporated under reduced pressure. The mixture was purified by flash column chromatography (EtOAc 50:50 to EtOAc:Acetone 50:50), resulting in the product 2-(2,6-dioxopiperidin-3-yl)-4-(4-(5-(1-(2-(4-(furan-2-carbonyl)piperazin-1-yl)-2-oxoethyl)-1H-1, 2,3-triazol-4-yl)pentanoyl)piperazin-1-yl)isoindoline-1,3-dione (77%) **(Scheme 5. 30)**.

^{1}H NMR (500 MHz, Chloroform-d) δ 8.13 (s, 1H), 7.62 (dd, J = 8.4, 7.2 Hz, 1H), 7.55 (s, 1H), 7.50 (dd, J = 1.8, 0.9 Hz, 1H), 7.45 (dd, J = 7.2, 0.8 Hz, 1H), 7.16 (d, J = 8.3 Hz, 1H), 7.09 (dd, J = 3.5, 0.9 Hz, 1H), 6.51 (dd, J = 3.5, 1.8 Hz, 1H), 5.25 (s, 2H), 4.97 (dd, J = 12.3, 5.4 Hz, 1H), 3.94 – 3.76 (m, 6H), 3.74 – 3.61 (m, 6H), 3.41 – 3.24 (m, 4H), 2.94 – 2.69 (m, 5H), 2.41 (t, J = 7.2 Hz, 2H), 2.17 – 2.08 (m, 1H), 1.85 – 1.69 (m, 2H).

^{13}C NMR (126 MHz, Chloroform-d) δ 171.61, 170.96, 168.23, 167.19, 166.63, 163.94,

162.29, 159.17, 149.92, 148.14, 147.43, 144.16, 135.85, 134.14, 123.44, 122.60, 118.03, 117.64, 116.42, 111.66, 51.87, 51.01, 50.38, 49.23, 45.71, 42.35, 41.45, 32.92, 31.42, 28.83, 25.29, 24.61, 22.68.

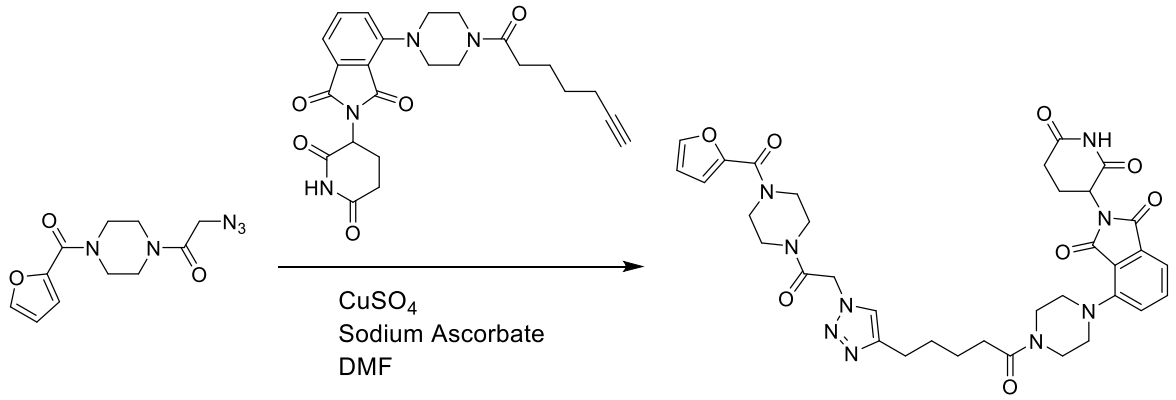

Scheme 5. 30. Synthetic route for the preparation of 2-(2,6-dioxopiperidin-3-yl)-4-(4-(5-(1-(2-(4-(furan-2-carbonyl)piperazin-1-yl)-2-oxoethyl)-1H-1,2,3-triazol-4-yl)pentanoyl)piperazin-1-yl)isoindoline-1,3-dione (**R-PROTAC**).

5.2.2 Ternary structure of the degraders linked to APT1 and CRBN

Structure predictions were performed with the help of Dr Daniel Zaidman. Prediction of the ternary complex was performed by running the PRosettaC software (https://prosettac.weizmann.ac.il/pacb/steps). The program was run on the structures of APT1 (PDB: 6QGS) and CRBN-Pomalidomide (PDB: 4TZ4). The method relies on two main software packages: the chemoinformatics python package RDKit (https://www.rdkit.org/), used to rapidly generate multiple conformations of the PROTAC; and the Rosetta modelling suite (https://www.rosettacommons.org/), used to choose the best conformation of the PROTAC in the context of the two proteins (APT1 and CRBN).

5.2.3 Determination of IC_{50} values for APT1 by competitive ABPP

HEK293T cells were transfected with the vector pcDNA3.1+ (Invitrogen) containing the human APT1 gene, using FuGene transfection reagent (Promega) according to the manufacturer's instructions. Cells were harvested, resuspended in PBS, and lysed by sonication. The proteome was kept at -80ºC until further use. Soluble proteome at 1 mg/ml (50 µL) was treated with varying concentrations of test compound (starting at 30 µL) for

30 min at room temperature. ActivX™ TAMRA-FP Serine Hydrolase Probe (Thermofisher) was added to a final concentration of 4 μM. The reaction was incubated for 1h, quenched with Laemmli sample buffer, followed by SDS-PAGE gel separation. The results were visualized by in-gel fluorescent scanning (Bio-RAD). The percentage activity remaining was determined by measuring the integrated optical density of the APT1 bands relative to a DMSO control. IC_{50} values were determined from dose-response curves using GraphPad Prism 8.

5.2.4 Cell culture

All cell lines were purchased from ATCC. MOLT-4 wild type and MOLT-4-CRBN$^{-/-}$ were kindly provided by Dr Georg Winter from CeMM, Austria. Cells were cultivated in complete DMEM supplemented with 10% (vol/vol) FBS (Gibco), and 1% of penicillin/streptomycin (Gibco). Cells were grown in a humidified atmosphere of 5% CO_2 at 37ºC, with the medium changed every other day.

5.2.5 Cell viability assay

Cells were inoculated at a density of 5 000 cells/well. Serial diluted compounds (starting at 100 μM) were added 24h later. The assay was performed in triplicates. After 72h of incubation, cellular viability was assessed by CellTiter-Glo® (Promega) according to the manufacturer's instructions. The values were normalised with the vehicle (DMSO) and the IC_{50} was calculated using GraphPad Prism 8.

5.2.6 Immunoblotting

Cells were lysed using RIPA buffer supplemented with protease inhibitor cocktail (Roche) and DNase I (Merck), left on ice for 15 min. Protein concentration was determined using BCA assay (Pierce). Western blot was performed with rabbit APT1 antibody (1:500) (ab91606, Abcam), mouse α-GAPDH (1:5000) (ab8245, Abcam), rabbit cereblon (71810, Cell Signaling Technology), goat anti-rabbit IgG secondary antibody HRP (1:7000) (65-6120, Invitrogen), and goat anti-mouse IgG secondary antibody HRP (1:5000) (62-6520, Invitrogen). Signal was revealed with Clarity Western ECL Substrate (Bio-Rad

Laboratories), and band intensity was measured using the ImageJ software (National Institutes of Health).

5.2.7 Cell permeability

Cells were inoculated at a density of 1×10^6 cells/well, and compounds were added at a final concentration of 100 µM. After 30 min of incubation, cells were centrifuged and both soluble and solid fractions were collected for analysis. The pellet was lysed prior to the analysis. Fluorescence signal was measured at the wavelengths (emission/excitation) of 280 and 500 nm, using a MiniMax^{TM} 300 Imaging cytometer (SpectraMax$^{®}$).

5.2.8 Proteomics

Proteome treatment. Raji cells were cultured at 15M per flask, with a working volume of 30 mL. Compounds were added at a final concentration of 5 µM. After a 4h-incubation at 37ºC, cells were harvested by centrifugation. The pellet was lysed, and protein concentration was normalized to 1 mg/mL. Each experiment consisted of two samples (500 µL each), one sample treated with PROTAC and a paired sample treated with DMSO. Both PROTAC- and DMSO-treated samples were labelled with fluorophosphonate desthiobiotin probe (10 µL, 5 µM final concentration) for 1h at rt. The reaction was quenched by adding the samples to to pre-chilled methanol (2 mL). **Preparation of proteomics samples.** The protein content of the samples was precipitated with cold solvents and buffers kept on ice. $CHCl_3$ (0.5 mL) and PBS (1 mL) were added, and the mixture was vortexed. Centrifugation (5 000 × g, 10 min, 4ºC) was used to concentrate the precipitated protein at the interface of the $CHCl_3$ and the methanol/PBS layers. The removed and the protein solid was washed with cold 1:1 methanol:$CHCl_3$ (3 × 1 mL). The protein solid was sonicated into 500 µL of 6 M urea in PBS). TCEP (50 µL, 100 mM in DBPS, basified using K_2CO_3) was added, and the suspension was incubated at 37°C for 30 min, with shaking to redissolve proteins. Proteins were alkylated with 70 µL of 400 mM iodoacetamide in PBS for 30 min at rt. The sample was then diluted with 5 mL of 0.25% SDS in PBS. Probe-labelled proteins were enriched using pre-washed streptavidin-beads (100 µL/sample) while rotating for 2.5h. Streptavidin beads were pelleted by centrifugation (1 000 × g, 1

min) and thoroughly washed with 3×5 mL of 0.25% SDS, 3×1 mL of PBS and 3×1 mL of MilliQ H_2O. Proteins were digested overnight using proteomics grade trypsin (20 µg trypsin in 2 mL 2M urea, with 100 mM TEAB buffer; 200 µL/sample) while shaking at 37°C. Tryptic peptides were labelled with either light or heavy formaldehyde, via reductive dimethylation, using sodium cyanoborohydride. The reaction was carried out at rt for 1h. 32 µL of 1% NH_4OH in water was added, followed by 16 µL of formic acid (5% final). Heavy and light samples were combined, and the beads were filtered using a Bio-Spin column. Samples were lyophilized prior to LC-MS/MS analysis. The analysis was carried out by the Cambridge Center for proteomics (United Kingdom). **Protein identification and quantification.** Proteomics raw data were analysed using MaxQuant software (version 2.3.0.0) with standard settings, unless otherwise specified. A multiplicity of 2 was set with a maximum number of labelled amino acids of 3. Reductive dimethylation technique was used for isotopic labelling. Light label was programmed as dimethyl lysine (lysine 0) and dimethyl n-terminal (n-term 0), and heavy label was programmed as dimethyl lysine (lysine 6) and dimethyl n-terminal (n-term 6). Trypsin/P was set as the digestion enzyme with 2 as the maximum number of missed cleavages. Oxidation of methionine and acetylation of the N-terminal were included as variable modifications and carbamidomethylation of cysteine was included as a fixed modification. The “Re-quantify” option was enabled and advanced ratio estimation was turned on. A Fasta file containing the human proteome and downloaded from uniport was used, together with a concatenated target decoy fasta file, and contaminants were included. Minimum peptide length was set to 7, with a maximum peptide mass of 4 600 Da. “Match between runs” was enabled with the default parameters. An overall false discovery rate (FDR) value of 0.01 was used. After data processing, the results table was filtered for serine hydrolases and the heavy/light ratios were plotted.

6

References

6. References

(1) Hanahan, D. Hallmarks of Cancer: New Dimensions. *Cancer Discov* **2022**, *12* (1), 31–46. https://doi.org/10.1158/2159-8290.CD-21-1059.

(2) Sung, H.; Ferlay, J.; Siegel, R. L.; Laversanne, M.; Soerjomataram, I.; Jemal, A.; Bray, F. Global Cancer Statistics 2020: GLOBOCAN Estimates of Incidence and Mortality Worldwide for 36 Cancers in 185 Countries. *CA Cancer J Clin* **2021**, *71* (3), 209–249. https://doi.org/10.3322/caac.21660.

(3) Mattiuzzi, C.; Lippi, G. Current Cancer Epidemiology. *J Epidemiol Glob Health* **2019**, *9* (4), 217. https://doi.org/10.2991/jegh.k.191008.001.

(4) Janku, F. Tumor Heterogeneity in the Clinic: Is It a Real Problem? *Ther Adv Med Oncol* **2014**, *6* (2), 43–51. https://doi.org/10.1177/1758834013517414.

(5) Debela, D. T.; Muzazu, S. G.; Heraro, K. D.; Ndalama, M. T.; Mesele, B. W.; Haile, D. C.; Kitui, S. K.; Manyazewal, T. New Approaches and Procedures for Cancer Treatment: Current Perspectives. *SAGE Open Med* **2021**, *9*, 205031212110343. https://doi.org/10.1177/20503121211034366.

(6) Arruebo, M.; Vilaboa, N.; Sáez-Gutierrez, B.; Lambea, J.; Tres, A.; Valladares, M.; González-Fernández, Á. Assessment of the Evolution of Cancer Treatment Therapies. *Cancers (Basel)* **2011**, *3* (3), 3279–3330. https://doi.org/10.3390/cancers3033279.

(7) Sekhoacha, M.; Riet, K.; Motloung, P.; Gumenku, L.; Adegoke, A.; Mashele, S. Prostate Cancer Review: Genetics, Diagnosis, Treatment Options, and Alternative Approaches. *Molecules* **2022**, *27* (17), 5730. https://doi.org/10.3390/molecules27175730.

(8) Rebello, R. J.; Oing, C.; Knudsen, K. E.; Loeb, S.; Johnson, D. C.; Reiter, R. E.; Gillessen, S.; van der Kwast, T.; Bristow, R. G. Prostate Cancer. *Nat Rev Dis Primers* **2021**, *7* (1), 9. https://doi.org/10.1038/s41572-020-00243-0.

(9) Dozzo, M.; Carobolante, F.; Donisi, P. M.; Scattolin, A.; Maino, E.; Sancetta, R.; Viero, P.; Bassan, R. Burkitt Lymphoma in Adolescents and Young Adults: Management Challenges. *Adolesc Health Med Ther* **2016**, *Volume 8*, 11–29. https://doi.org/10.2147/AHMT.S94170.

(10) Weledji, E. P.; Enow Orock, G. Surgery for Non-Hodgkin's Lymphoma. *Oncol Rev* **2015**. https://doi.org/10.4081/oncol.2015.274.

(11) Chen, H. H. W.; Kuo, M. T. Improving Radiotherapy in Cancer Treatment: Promises and Challenges. *Oncotarget* **2017**, *8* (37), 62742–62758. https://doi.org/10.18632/oncotarget.18409.

(12) Sgouros, G.; Bodei, L.; McDevitt, M. R.; Nedrow, J. R. Radiopharmaceutical Therapy in Cancer: Clinical Advances and Challenges. *Nat Rev Drug Discov* **2020**, *19* (9), 589–608. https://doi.org/10.1038/s41573-020-0073-9.

(13) Anand, U.; Dey, A.; Chandel, A. K. S.; Sanyal, R.; Mishra, A.; Pandey, D. K.; de Falco, V.; Upadhyay, A.; Kandimalla, R.; Chaudhary, A.; Dhanjal, J. K.; Dewanjee, S.; Vallamkondu, J.; Pérez de la Lastra, J. M. Cancer Chemotherapy and beyond: Current Status, Drug Candidates, Associated Risks and Progress in Targeted Therapeutics. *Genes Dis* **2022**. https://doi.org/10.1016/j.gendis.2022.02.007.

(14) Corrie, P. G. Cytotoxic Chemotherapy: Clinical Aspects. *Medicine* **2008**, *36* (1), 24–28. https://doi.org/10.1016/j.mpmed.2007.10.012.

(15) Houillier, C.; Chabrot, C. M.; Moles-Moreau, M.-P.; Willems, L.; Ahle, G.; Waultier-Rascalou, A.; Fornecker, L.-M.; Hoang-Xuan, K.; Soussain, C. Rituximab-Lenalidomide-Ibrutinib Combination for Relapsed/Refractory Primary CNS Lymphoma. *Neurology* **2021**, *97* (13), 628–631. https://doi.org/10.1212/WNL.0000000000012515.

(16) Padma, V. V. An Overview of Targeted Cancer Therapy. *Biomedicine (Taipei)* **2015**, *5* (4), 19. https://doi.org/10.7603/s40681-015-0019-4.

(17) An, S.; Fu, L. Small-Molecule PROTACs: An Emerging and Promising Approach for the Development of Targeted Therapy Drugs. *EBioMedicine* **2018**, *36*, 553–562. https://doi.org/10.1016/j.ebiom.2018.09.005.

(18) Singh, J.; Petter, R. C.; Baillie, T. A.; Whitty, A. The Resurgence of Covalent Drugs. *Nat Rev Drug Discov* **2011**, *10* (4), 307–317. https://doi.org/10.1038/nrd3410.

(19) Pillaiyar, T.; Manickam, M.; Namasivayam, V.; Hayashi, Y.; Jung, S.-H. An Overview of Severe Acute Respiratory Syndrome–Coronavirus (SARS-CoV) 3CL Protease Inhibitors: Peptidomimetics and Small Molecule Chemotherapy. *J Med Chem* **2016**, *59* (14), 6595–6628. https://doi.org/10.1021/acs.jmedchem.5b01461.

(20) VANE, J. R. Inhibition of Prostaglandin Synthesis as a Mechanism of Action for Aspirin-like Drugs. *Nat New Biol* **1971**, *231* (25), 232–235. https://doi.org/10.1038/newbio231232a0.

(21) Boike, L.; Henning, N. J.; Nomura, D. K. Advances in Covalent Drug Discovery.

Nat Rev Drug Discov **2022**, *21* (12), 881–898. https://doi.org/10.1038/s41573-022-00542-z.

(22) Bhana, N.; Ormrod, D.; Perry, C. M.; Figgitt, D. P. Zidovudine. *Pediatric Drugs* **2002**, *4* (8), 515–553. https://doi.org/10.2165/00128072-200204080-00004.

(23) Kiely-Collins, H.; Winter, G. E.; Bernardes, G. J. L. The Role of Reversible and Irreversible Covalent Chemistry in Targeted Protein Degradation. *Cell Chem Biol* **2021**, *28* (7), 952–968. https://doi.org/10.1016/j.chembiol.2021.03.005.

(24) Reker, D.; Rodrigues, T.; Schneider, P.; Schneider, G. Identifying the Macromolecular Targets of de Novo-Designed Chemical Entities through Self-Organizing Map Consensus. *PNAS* **2014**, *111* (11), 4067–4072. https://doi.org/10.1073/pnas.1320001111.

(25) Strelow, J. M. A Perspective on the Kinetics of Covalent and Irreversible Inhibition. *SLAS DISCOVERY: Advancing the Science of Drug Discovery* **2017**, *22* (1), 3–20. https://doi.org/10.1177/1087057116671509.

(26) Johnson, D. S.; Weerapana, E.; Cravatt, B. F. Strategies for Discovering and Derisking Covalent, Irreversible Enzyme Inhibitors. *Future Med Chem* **2010**, *2* (6), 949–964. https://doi.org/10.4155/fmc.10.21.

(27) Martin, J. S.; MacKenzie, C. J.; Fletcher, D.; Gilbert, I. H. Characterising Covalent Warhead Reactivity. *Bioorg Med Chem* **2019**, *27* (10), 2066–2074. https://doi.org/10.1016/j.bmc.2019.04.002.

(28) Huang, L.; Guo, Z.; Wang, F.; Fu, L. KRAS Mutation: From Undruggable to Druggable in Cancer. *Signal Transduct Target Ther* **2021**, *6* (1), 386. https://doi.org/10.1038/s41392-021-00780-4.

(29) Wang, J.; Martin-Romano, P.; Cassier, P.; Johnson, M.; Haura, E.; Lenox, L.; Guo, Y.; Bandyopadhyay, N.; Russell, M.; Shearin, E.; Lauring, J.; Dahan, L. Phase I Study of JNJ-74699157 in Patients with Advanced Solid Tumors Harboring the *KRAS G12C* Mutation. *Oncologist* **2022**, *27* (7), 536-e553. https://doi.org/10.1093/oncolo/oyab080.

(30) Sakamoto, K. M.; Kim, K. B.; Kumagai, A.; Mercurio, F.; Crews, C. M.; Deshaies, R. J. Protacs: Chimeric Molecules That Target Proteins to the Skp1–Cullin–F Box Complex for Ubiquitination and Degradation. *PNAS* **2001**, *98* (15), 8554–8559. https://doi.org/10.1073/pnas.141230798.

(31) Békés, M.; Langley, D. R.; Crews, C. M. PROTAC Targeted Protein Degraders: The Past Is Prologue. *Nat Rev Drug Discov* **2022**, *21* (3), 181–200.

https://doi.org/10.1038/s41573-021-00371-6.

(32) Belcher, B. P.; Ward, C. C.; Nomura, D. K. Ligandability of E3 Ligases for Targeted Protein Degradation Applications. *Biochem* **2023**, *62* (3), 588–600. https://doi.org/10.1021/acs.biochem.1c00464.

(33) Kostic, M.; Jones, L. H. Critical Assessment of Targeted Protein Degradation as a Research Tool and Pharmacological Modality. *Trends Pharmacol Sci* **2020**, *41* (5), 305–317. https://doi.org/10.1016/j.tips.2020.02.006.

(34) Alabi, S. B.; Crews, C. M. Major Advances in Targeted Protein Degradation: PROTACs, LYTACs, and MADTACs. *JBC* **2021**, *296*, 100647. https://doi.org/10.1016/j.jbc.2021.100647.

(35) Troup, R. I.; Fallan, C.; Baud, M. G. J. Current Strategies for the Design of PROTAC Linkers: A Critical Review. *Explor Target Antitumor Ther* **2020**, *1* (5). https://doi.org/10.37349/etat.2020.00018.

(36) Nunes, J.; McGonagle, G. A.; Eden, J.; Kiritharan, G.; Touzet, M.; Lewell, X.; Emery, J.; Eidam, H.; Harling, J. D.; Anderson, N. A. Targeting IRAK4 for Degradation with PROTACs. *ACS Med Chem Lett* **2019**, *10* (7), 1081–1085. https://doi.org/10.1021/acsmedchemlett.9b00219.

(37) de Wispelaere, M.; Du, G.; Donovan, K. A.; Zhang, T.; Eleuteri, N. A.; Yuan, J. C.; Kalabathula, J.; Nowak, R. P.; Fischer, E. S.; Gray, N. S.; Yang, P. L. Small Molecule Degraders of the Hepatitis C Virus Protease Reduce Susceptibility to Resistance Mutations. *Nat Commun* **2019**, *10* (1), 3468. https://doi.org/10.1038/s41467-019-11429-w.

(38) Silva, M. C.; Ferguson, F. M.; Cai, Q.; Donovan, K. A.; Nandi, G.; Patnaik, D.; Zhang, T.; Huang, H.-T.; Lucente, D. E.; Dickerson, B. C.; Mitchison, T. J.; Fischer, E. S.; Gray, N. S.; Haggarty, S. J. Targeted Degradation of Aberrant Tau in Frontotemporal Dementia Patient-Derived Neuronal Cell Models. *Elife* **2019**, *8*. https://doi.org/10.7554/eLife.45457.

(39) Paiva, S.-L.; Crews, C. M. Targeted Protein Degradation: Elements of PROTAC Design. *Curr Opin Chem Biol* **2019**, *50*, 111–119. https://doi.org/10.1016/j.cbpa.2019.02.022.

(40) Gechijian, L. N.; Buckley, D. L.; Lawlor, M. A.; Reyes, J. M.; Paulk, J.; Ott, C. J.; Winter, G. E.; Erb, M. A.; Scott, T. G.; Xu, M.; Seo, H.-S.; Dhe-Paganon, S.; Kwiatkowski, N. P.; Perry, J. A.; Qi, J.; Gray, N. S.; Bradner, J. E. Functional TRIM24 Degrader via Conjugation of Ineffectual Bromodomain and VHL Ligands.

Nat Chem Biol **2018**, *14* (4), 405–412. https://doi.org/10.1038/s41589-018-0010-y.

(41) Gabizon, R.; Shraga, A.; Gehrtz, P.; Livnah, E.; Shorer, Y.; Gurwicz, N.; Avram, L.; Unger, T.; Aharoni, H.; Albeck, S.; Brandis, A.; Shulman, Z.; Katz, B.-Z.; Herishanu, Y.; London, N. Efficient Targeted Degradation via Reversible and Irreversible Covalent PROTACs. *J Am Chem Soc* **2020**, *142* (27), 11734–11742. https://doi.org/10.1021/jacs.9b13907.

(42) Dobrovolsky, D.; Wang, E. S.; Morrow, S.; Leahy, C.; Faust, T.; Nowak, R. P.; Donovan, K. A.; Yang, G.; Li, Z.; Fischer, E. S.; Treon, S. P.; Weinstock, D. M.; Gray, N. S. Bruton Tyrosine Kinase Degradation as a Therapeutic Strategy for Cancer. *Blood* **2019**, *133* (9), 952–961. https://doi.org/10.1182/blood-2018-07-862953.

(43) Buhimschi, A. D.; Armstrong, H. A.; Toure, M.; Jaime-Figueroa, S.; Chen, T. L.; Lehman, A. M.; Woyach, J. A.; Johnson, A. J.; Byrd, J. C.; Crews, C. M. Targeting the C481S Ibrutinib-Resistance Mutation in Bruton's Tyrosine Kinase Using PROTAC-Mediated Degradation. *Biochem* **2018**, *57* (26), 3564–3575. https://doi.org/10.1021/acs.biochem.8b00391.

(44) Bond, M. J.; Chu, L.; Nalawansha, D. A.; Li, K.; Crews, C. M. Targeted Degradation of Oncogenic KRAS ^{G12C} by VHL-Recruiting PROTACs. *ACS Cent Sci* **2020**, *6* (8), 1367–1375. https://doi.org/10.1021/acscentsci.0c00411.

(45) Fell, J. B.; Fischer, J. P.; Baer, B. R.; Blake, J. F.; Bouhana, K.; Briere, D. M.; Brown, K. D.; Burgess, L. E.; Burns, A. C.; Burkard, M. R.; Chiang, H.; Chicarelli, M. J.; Cook, A. W.; Gaudino, J. J.; Hallin, J.; Hanson, L.; Hartley, D. P.; Hicken, E. J.; Hingorani, G. P.; Hinklin, R. J.; Mejia, M. J.; Olson, P.; Otten, J. N.; Rhodes, S. P.; Rodriguez, M. E.; Savechenkov, P.; Smith, D. J.; Sudhakar, N.; Sullivan, F. X.; Tang, T. P.; Vigers, G. P.; Wollenberg, L.; Christensen, J. G.; Marx, M. A. Identification of the Clinical Development Candidate **MRTX849** , a Covalent KRAS ^{G12C} Inhibitor for the Treatment of Cancer. *J Med Chem* **2020**, *63* (13), 6679–6693. https://doi.org/10.1021/acs.jmedchem.9b02052.

(46) Bemis, T. A.; la Clair, J. J.; Burkart, M. D. Unraveling the Role of Linker Design in Proteolysis Targeting Chimeras. *J Med Chem* **2021**, *64* (12), 8042–8052. https://doi.org/10.1021/acs.jmedchem.1c00482.

(47) Zaidman, D.; Prilusky, J.; London, N. PRosettaC: Rosetta Based Modeling of PROTAC Mediated Ternary Complexes. *J Chem Inf Model* **2020**, *60* (10), 4894–4903. https://doi.org/10.1021/acs.jcim.0c00589.

(48) Zorba, A.; Nguyen, C.; Xu, Y.; Starr, J.; Borzilleri, K.; Smith, J.; Zhu, H.; Farley, K. A.; Ding, W.; Schiemer, J.; Feng, X.; Chang, J. S.; Uccello, D. P.; Young, J. A.; Garcia-Irrizary, C. N.; Czabaniuk, L.; Schuff, B.; Oliver, R.; Montgomery, J.; Hayward, M. M.; Coe, J.; Chen, J.; Niosi, M.; Luthra, S.; Shah, J. C.; El-Kattan, A.; Qiu, X.; West, G. M.; Noe, M. C.; Shanmugasundaram, V.; Gilbert, A. M.; Brown, M. F.; Calabrese, M. F. Delineating the Role of Cooperativity in the Design of Potent PROTACs for BTK. *PNAS* **2018**, *115* (31). https://doi.org/10.1073/pnas.1803662115.

(49) Hughes, S. J.; Ciulli, A. Molecular Recognition of Ternary Complexes: A New Dimension in the Structure-Guided Design of Chemical Degraders. *Essays Biochem* **2017**, *61* (5), 505–516. https://doi.org/10.1042/EBC20170041.

(50) Testa, A.; Hughes, S. J.; Lucas, X.; Wright, J. E.; Ciulli, A. Structure-Based Design of a Macrocyclic PROTAC. *Angew Chem* **2020**, *132* (4), 1744–1751. https://doi.org/10.1002/ange.201914396.

(51) Gadd, M. S.; Testa, A.; Lucas, X.; Chan, K.-H.; Chen, W.; Lamont, D. J.; Zengerle, M.; Ciulli, A. Structural Basis of PROTAC Cooperative Recognition for Selective Protein Degradation. *Nat Chem Biol* **2017**, *13* (5), 514–521. https://doi.org/10.1038/nchembio.2329.

(52) Roy, M. J.; Winkler, S.; Hughes, S. J.; Whitworth, C.; Galant, M.; Farnaby, W.; Rumpel, K.; Ciulli, A. SPR-Measured Dissociation Kinetics of PROTAC Ternary Complexes Influence Target Degradation Rate. *ACS Chem Biol* **2019**, *14* (3), 361–368. https://doi.org/10.1021/acschembio.9b00092.

(53) Chung, C.; Dai, H.; Fernandez, E.; Tinworth, C. P.; Churcher, I.; Cryan, J.; Denyer, J.; Harling, J. D.; Konopacka, A.; Queisser, M. A.; Tame, C. J.; Watt, G.; Jiang, F.; Qian, D.; Benowitz, A. B. Structural Insights into PROTAC-Mediated Degradation of Bcl-XL. *ACS Chem Biol* **2020**, *15* (9), 2316–2323. https://doi.org/10.1021/acschembio.0c00266.

(54) Crew, A. P.; Raina, K.; Dong, H.; Qian, Y.; Wang, J.; Vigil, D.; Serebrenik, Y. v.; Hamman, B. D.; Morgan, A.; Ferraro, C.; Siu, K.; Neklesa, T. K.; Winkler, J. D.; Coleman, K. G.; Crews, C. M. Identification and Characterization of Von Hippel-Lindau-Recruiting Proteolysis Targeting Chimeras (PROTACs) of TANK-Binding Kinase 1. *J Med Chem* **2018**, *61* (2), 583–598. https://doi.org/10.1021/acs.jmedchem.7b00635.

(55) Mayor-Ruiz, C.; Jaeger, M. G.; Bauer, S.; Brand, M.; Sin, C.; Hanzl, A.; Mueller, A.

C.; Menche, J.; Winter, G. E. Plasticity of the Cullin-RING Ligase Repertoire Shapes Sensitivity to Ligand-Induced Protein Degradation. *Mol Cell* **2019**, *75* (4), 849-858.e8. https://doi.org/10.1016/j.molcel.2019.07.013.

(56) Zheng, S.; Tao, W. Targeting Cullin-RING E3 Ligases for Radiosensitization: From NEDDylation Inhibition to PROTACs. *Front Oncol* **2020**, *10*. https://doi.org/10.3389/fonc.2020.01517.

(57) Ottis, P.; Toure, M.; Cromm, P. M.; Ko, E.; Gustafson, J. L.; Crews, C. M. Assessing Different E3 Ligases for Small Molecule Induced Protein Ubiquitination and Degradation. *ACS Chem Biol* **2017**, *12* (10), 2570–2578. https://doi.org/10.1021/acschembio.7b00485.

(58) Bond, M. J.; Crews, C. M. Proteolysis Targeting Chimeras (PROTACs) Come of Age: Entering the Third Decade of Targeted Protein Degradation. *RSC Chem Biol* **2021**, *2* (3), 725–742. https://doi.org/10.1039/D1CB00011J.

(59) Schapira, M.; Calabrese, M. F.; Bullock, A. N.; Crews, C. M. Targeted Protein Degradation: Expanding the Toolbox. *Nat Rev Drug Discov* **2019**, *18* (12), 949–963. https://doi.org/10.1038/s41573-019-0047-y.

(60) He, Y.; Zhang, X.; Chang, J.; Kim, H.-N.; Zhang, P.; Wang, Y.; Khan, S.; Liu, X.; Zhang, X.; Lv, D.; Song, L.; Li, W.; Thummuri, D.; Yuan, Y.; Wiegand, J. S.; Ortiz, Y. T.; Budamagunta, V.; Elisseeff, J. H.; Campisi, J.; Almeida, M.; Zheng, G.; Zhou, D. Using Proteolysis-Targeting Chimera Technology to Reduce Navitoclax Platelet Toxicity and Improve Its Senolytic Activity. *Nat Commun* **2020**, *11* (1), 1996. https://doi.org/10.1038/s41467-020-15838-0.

(61) Matyskiela, M. E.; Couto, S.; Zheng, X.; Lu, G.; Hui, J.; Stamp, K.; Drew, C.; Ren, Y.; Wang, M.; Carpenter, A.; Lee, C.-W.; Clayton, T.; Fang, W.; Lu, C.-C.; Riley, M.; Abdubek, P.; Blease, K.; Hartke, J.; Kumar, G.; Vessey, R.; Rolfe, M.; Hamann, L. G.; Chamberlain, P. P. SALL4 Mediates Teratogenicity as a Thalidomide-Dependent Cereblon Substrate. *Nat Chem Biol* **2018**, *14* (10), 981–987. https://doi.org/10.1038/s41589-018-0129-x.

(62) Zhang, L.; Riley-Gillis, B.; Vijay, P.; Shen, Y. Acquired Resistance to BET-PROTACs (Proteolysis-Targeting Chimeras) Caused by Genomic Alterations in Core Components of E3 Ligase Complexes. *Mol Cancer Ther* **2019**, *18* (7), 1302–1311. https://doi.org/10.1158/1535-7163.MCT-18-1129.

(63) Ito, T.; Yamaguchi, Y.; Handa, H. Exploiting Ubiquitin Ligase Cereblon as a Target for Small-Molecule Compounds in Medicine and Chemical Biology. *Cell Chem Biol*

2021, *28* (7), 987–999. https://doi.org/10.1016/j.chembiol.2021.04.012.

(64) Yamamoto, J.; Ito, T.; Yamaguchi, Y.; Handa, H. Discovery of CRBN as a Target of Thalidomide: A Breakthrough for Progress in the Development of Protein Degraders. *Chem Soc Rev* **2022**, *51* (15), 6234–6250. https://doi.org/10.1039/D2CS00116K.

(65) Mori, T.; Ito, T.; Liu, S.; Ando, H.; Sakamoto, S.; Yamaguchi, Y.; Tokunaga, E.; Shibata, N.; Handa, H.; Hakoshima, T. Structural Basis of Thalidomide Enantiomer Binding to Cereblon. *Sci Rep* **2018**, *8* (1), 1294. https://doi.org/10.1038/s41598-018-19202-7.

(66) Winter, G. E.; Buckley, D. L.; Paulk, J.; Roberts, J. M.; Souza, A.; Dhe-Paganon, S.; Bradner, J. E. Phthalimide Conjugation as a Strategy for in Vivo Target Protein Degradation. *Science (1979)* **2015**. https://doi.org/10.1126/science.aab1433.

(67) Lu, J.; Qian, Y.; Altieri, M.; Dong, H.; Wang, J.; Raina, K.; Hines, J.; Winkler, J. D.; Crew, A. P.; Coleman, K.; Crews, C. M. Hijacking the E3 Ubiquitin Ligase Cereblon to Efficiently Target BRD4. *Chem Biol* **2015**, *22* (6), 755–763. https://doi.org/10.1016/j.chembiol.2015.05.009.

(68) Graves, L. M.; Duncan, J. S.; Whittle, M. C.; Johnson, G. L. The Dynamic Nature of the Kinome. *Biochem* **2013**, *450* (1), 1–8. https://doi.org/10.1042/BJ20121456.

(69) Petrylak, D. P.; Gao, X.; Vogelzang, N. J.; Garfield, M. H.; Taylor, I.; Dougan Moore, M.; Peck, R. A.; Burris, H. A. First-in-Human Phase I Study of ARV-110, an Androgen Receptor (AR) PROTAC Degrader in Patients (Pts) with Metastatic Castrate-Resistant Prostate Cancer (MCRPC) Following Enzalutamide (ENZ) and/or Abiraterone (ABI). *J Clin Oncol* **2020**, *38* (15_suppl), 3500–3500. https://doi.org/10.1200/JCO.2020.38.15_suppl.3500.

(70) Liu, F.; Zhang, X.; Weisberg, E.; Chen, S.; Hur, W.; Wu, H.; Zhao, Z.; Wang, W.; Mao, M.; Cai, C.; Simon, N. I.; Sanda, T.; Wang, J.; Look, A. T.; Griffin, J. D.; Balk, S. P.; Liu, Q.; Gray, N. S. Discovery of a Selective Irreversible BMX Inhibitor for Prostate Cancer. *ACS Chem Biol* **2013**, *8* (7), 1423–1428. https://doi.org/10.1021/cb4000629.

(71) Smith, C. I. E.; Islam, T. C.; Mattsson, P. T.; Mohamed, A. J.; Nore, B. F.; Vihinen, M. The Tec Family of Cytoplasmic Tyrosine Kinases: Mammalian Btk, Bmx, Itk, Tec, Txk and Homologs in Other Species: Review Articles. *BioEssays*. 2001. https://doi.org/10.1002/bies.1062.

(72) Siveen, K. S.; Prabhu, K. S.; Achkar, I. W.; Kuttikrishnan, S.; Shyam, S.; Khan, A.

Q.; Merhi, M.; Dermime, S.; Uddin, S. Role of Non Receptor Tyrosine Kinases in Hematological Malignances and Its Targeting by Natural Products. *Mol Cancer*. 2018. https://doi.org/10.1186/s12943-018-0788-y.

(73) Muckelbauer, J.; Sack, J. S.; Ahmed, N.; Burke, J.; Chang, C. Y.; Gao, M.; Tino, J.; Xie, D.; Tebben, A. J. X-Ray Crystal Structure of Bone Marrow Kinase in the X Chromosome: A Tec Family Kinase. *Chem Biol Drug Des* **2011**, *78* (5), 739–748. https://doi.org/10.1111/j.1747-0285.2011.01230.x.

(74) Schwartzberg, P. L.; Finkelstein, L. D.; Readinger, J. A. TEC-Family Kinases: Regulators of T-Helper-Cell Differentiation. *Nat Rev Immunol* **2005**, *5* (4), 284–295. https://doi.org/10.1038/nri1591.

(75) Jarboe, J. S.; Dutta, S.; Velu, S. E.; Willey, C. D. Mini-Review: Bmx Kinase Inhibitors for Cancer Therapy. *Recent Pat Anticancer Drug Discov* **2013**. https://doi.org/10.2174/15748928113089990043.

(76) Horwood, N. J.; Urbaniak, A. M.; Danks, L. Tec Family Kinases in Inflammation and Disease. *Int Rev of Immunol*. 2012. https://doi.org/10.3109/08830185.2012.670334.

(77) Schmidt, U.; Boucheron, N.; Unger, B.; Ellmeier, W. The Role of Tec Family Kinases in Myeloid Cells. *Int Arch Allergy Immunol*. 2004. https://doi.org/10.1159/000078339.

(78) Schaeffer, E. M.; Debnath, J.; Yap, G.; McVicar, D.; Liao, X. C.; Littman, D. R.; Sher, A.; Varmus, H. E.; Lenardo, M. J.; Schwartzberg, P. L. Requirement for Tec Kinases Rlk and Ltk in T Cell Receptor Signaling and Immunity. *Science (1979)* **1999**. https://doi.org/10.1126/science.284.5414.638.

(79) Felices, M.; Berg, L. J. The Tec Kinases Itk and Rlk Regulate NKT Cell Maturation, Cytokine Production, and Survival. *J Immun***2008**. https://doi.org/10.4049/jimmunol.180.5.3007.

(80) Alu, A.; Lei, H.; Han, X.; Wei, Y.; Wei, X. BTK Inhibitors in the Treatment of Hematological Malignancies and Inflammatory Diseases: Mechanisms and Clinical Studies. *J Hematol Oncol* **2022**, *15* (1), 138. https://doi.org/10.1186/s13045-022-01353-w.

(81) Pal Singh, S.; Dammeijer, F.; Hendriks, R. W. Role of Bruton's Tyrosine Kinase in B Cells and Malignancies. *Mol Cancer* **2018**, *17* (1), 57. https://doi.org/10.1186/s12943-018-0779-z.

(82) Dai, B.; Chen, H.; Guo, S.; Yang, X.; Linn, D. E.; Sun, F.; Li, W.; Guo, Z.; Xu, K.;

Kim, O.; Kong, X.; Melamed, J.; Qiu, S.; Chen, H.; Qiu, Y. Compensatory Upregulation of Tyrosine Kinase Etk/BMX in Response to Androgen Deprivation Promotes Castration-Resistant Growth of Prostate Cancer Cells. *Cancer Res* **2010**, *70* (13), 5587–5596. https://doi.org/10.1158/0008-5472.CAN-09-4610.

(83) Li, Y.; Cui, N.; Zheng, P.-S.; Yang, W.-T.; Li, Y.; Cui, N.; Zheng, P.-S.; Yang, W.-T. BMX/Etk Promotes Cell Proliferation and Tumorigenicity of Cervical Cancer Cells through PI3K/AKT/MTOR and STAT3 Pathways. *Oncotarget* **2017**. https://doi.org/10.18632/oncotarget.17493.

(84) Li, K.; Pan, W.; Ma, Y.; Xu, X.; Gao, Y.; He, Y.; Wei, L.; Zhang, J. BMX Activates Wnt/β-Catenin Signaling Pathway to Promote Cell Proliferation and Migration in Breast Cancer. *Breast Cancer* **2020**, *27* (3), 363–371. https://doi.org/10.1007/s12282-019-01024-8.

(85) Shinohara, M.; Koga, T.; Okamoto, K.; Sakaguchi, S.; Arai, K.; Yasuda, H.; Takai, T.; Kodama, T.; Morio, T.; Geha, R. S.; Kitamura, D.; Kurosaki, T.; Ellmeier, W.; Takayanagi, H. Tyrosine Kinases Btk and Tec Regulate Osteoclast Differentiation by Linking RANK and ITAM Signals. *Cell* **2008**. https://doi.org/10.1016/j.cell.2007.12.037.

(86) Forster, M.; Liang, X. J.; Schröder, M.; Gerstenecker, S.; Chaikuad, A.; Knapp, S.; Laufer, S.; Gehringer, M. Discovery of a Novel Class of Covalent Dual Inhibitors Targeting the Protein Kinases BMX and BTK. *Int J Mol Sci* **2020**, *21* (23), 9269. https://doi.org/10.3390/ijms21239269.

(87) Kohs, T. C. L.; Olson, S. R.; Pang, J.; Jordan, K. R.; Zheng, T. J.; Xie, A.; Hodovan, J.; Muller, M.; McArthur, C.; Johnson, J.; Sousa, B. B.; Wallisch, M.; Kievit, P.; Aslan, J. E.; Seixas, J. D.; Bernardes, G. J. L.; Hinds, M. T.; Lindner, J. R.; McCarty, O. J. T.; Puy, C.; Shatzel, J. J. Ibrutinib Inhibits BMX-Dependent Endothelial VCAM-1 Expression In Vitro and Pro-Atherosclerotic Endothelial Activation and Platelet Adhesion In Vivo. *Cell Mol Bioeng* **2022**, *15* (3), 231–243. https://doi.org/10.1007/s12195-022-00723-1.

(88) Lechner, K. S.; Neurath, M. F.; Weigmann, B. Role of the IL-2 Inducible Tyrosine Kinase ITK and Its Inhibitors in Disease Pathogenesis. *J Mol Med* **2020**, *98* (10), 1385–1395. https://doi.org/10.1007/s00109-020-01958-z.

(89) Zhong, Y.; Johnson, A. J.; Byrd, J. C.; Dubovsky, J. A. Targeting Interleukin-2 Inducible T-Cell Kinase (ITK) in T-Cell Related Diseases. *Postdoc Journal* **2014**, *2* (6). https://doi.org/10.14304/SURYA.JPR.V2N6.1.

(90) Dubovsky, J. A.; Beckwith, K. A.; Natarajan, G.; Woyach, J. A.; Jaglowski, S.; Zhong, Y.; Hessler, J. D.; Liu, T.-M.; Chang, B. Y.; Larkin, K. M.; Stefanovski, M. R.; Chappell, D. L.; Frissora, F. W.; Smith, L. L.; Smucker, K. A.; Flynn, J. M.; Jones, J. A.; Andritsos, L. A.; Maddocks, K.; Lehman, A. M.; Furman, R.; Sharman, J.; Mishra, A.; Caligiuri, M. A.; Satoskar, A. R.; Buggy, J. J.; Muthusamy, N.; Johnson, A. J.; Byrd, J. C. Ibrutinib Is an Irreversible Molecular Inhibitor of ITK Driving a Th1-Selective Pressure in T Lymphocytes. *Blood* **2013**, *122* (15), 2539–2549. https://doi.org/10.1182/blood-2013-06-507947.

(91) Vargas, L.; Hamasy, A.; Nore, B. F.; E. Smith, C. I. Inhibitors of BTK and ITK: State of the New Drugs for Cancer, Autoimmunity and Inflammatory Diseases. *Scand J Immunol* **2013**, *78* (2), 130–139. https://doi.org/10.1111/sji.12069.

(92) Vanova, T.; Konecna, Z.; Zbonakova, Z.; la Venuta, G.; Zoufalova, K.; Jelinkova, S.; Varecha, M.; Rotrekl, V.; Krejci, P.; Nickel, W.; Dvorak, P.; Kunova Bosakova, M. Tyrosine Kinase Expressed in Hepatocellular Carcinoma, TEC, Controls Pluripotency and Early Cell Fate Decisions of Human Pluripotent Stem Cells via Regulation of Fibroblast Growth Factor-2 Secretion. *Stem Cells* **2017**, *35* (9), 2050–2059. https://doi.org/10.1002/stem.2660.

(93) Bachovchin, D. A.; Cravatt, B. F. The Pharmacological Landscape and Therapeutic Potential of Serine Hydrolases. *Nat Rev Drug Discov* **2012**, *11* (1), 52–68. https://doi.org/10.1038/nrd3620.

(94) Simon, G. M.; Cravatt, B. F. Activity-Based Proteomics of Enzyme Superfamilies: Serine Hydrolases as a Case Study. *JBC* **2010**, *285* (15), 11051–11055. https://doi.org/10.1074/jbc.R109.097600.

(95) Bracey, M. H.; Hanson, M. A.; Masuda, K. R.; Stevens, R. C.; Cravatt, B. F. Structural Adaptations in a Membrane Enzyme That Terminates Endocannabinoid Signaling. *Science (1979)* **2002**, *298* (5599), 1793–1796. https://doi.org/10.1126/science.1076535.

(96) Shin, S. Structure of Malonamidase E2 Reveals a Novel Ser-CisSer-Lys Catalytic Triad in a New Serine Hydrolase Fold That Is Prevalent in Nature. *EMBO J* **2002**, *21* (11), 2509–2516. https://doi.org/10.1093/emboj/21.11.2509.

(97) Kienesberger, P. C.; Oberer, M.; Lass, A.; Zechner, R. Mammalian Patatin Domain Containing Proteins: A Family with Diverse Lipolytic Activities Involved in Multiple Biological Functions. *J Lipid Res* **2009**, *50*, S63–S68. https://doi.org/10.1194/jlr.R800082-JLR200.

(98) Yousef, G. M.; Kopolovic, A. D.; Elliott, M. B.; Diamandis, E. P. Genomic Overview of Serine Proteases. *Biochem Biophys Res Commun* **2003**, *305* (1), 28–36. https://doi.org/10.1016/S0006-291X(03)00638-7.

(99) Perona, J. J.; Craik, C. S. Structural Basis of Substrate Specificity in the Serine Proteases. *Protein Science* **2008**, *4* (3), 337–360. https://doi.org/10.1002/pro.5560040301.

(100) He, L.-W.; Dai, W.-C.; Li, N.-G. Development of Orally Active Thrombin Inhibitors for the Treatment of Thrombotic Disorder Diseases. *Molecules* **2015**, *20* (6), 11046–11062. https://doi.org/10.3390/molecules200611046.

(101) Tissot, G.; Canard, H.; Nadai, M.; Martone, A.; Botterman, J.; Dubald, M. Translocation of Aprotinin, a Therapeutic Protease Inhibitor, into the Thylakoid Lumen of Genetically Engineered Tobacco Chloroplasts. *Plant Biotechnol J* **2008**, *6* (3), 309–320. https://doi.org/10.1111/j.1467-7652.2008.00321.x.

(102) Weber, A. N. R.; Bittner, Z.; Liu, X.; Dang, T.-M.; Radsak, M. P.; Brunner, C. Bruton's Tyrosine Kinase: An Emerging Key Player in Innate Immunity. *Front Immunol* **2017**, *8*. https://doi.org/10.3389/fimmu.2017.01454.

(103) Corneth, O. B. J.; Klein Wolterink, R. G. J.; Hendriks, R. W. BTK Signaling in B Cell Differentiation and Autoimmunity; Springer, Cham, 2015; Vol. 393, pp 67–105. https://doi.org/10.1007/82_2015_478.

(104) Vassilev, A.; Ozer, Z.; Navara, C.; Mahajan, S.; Uckun, F. M. Bruton's Tyrosine Kinase as an Inhibitor of the Fas/CD95 Death-Inducing Signaling Complex. *JBC* **1999**, *274* (3), 1646–1656. https://doi.org/10.1074/jbc.274.3.1646.

(105) Xia, S.; Liu, X.; Cao, X.; Xu, S. T-Cell Expression of Bruton's Tyrosine Kinase Promotes Autoreactive T-Cell Activation and Exacerbates Aplastic Anemia. *Cell Mol Immunol* **2020**, *17* (10), 1042–1052. https://doi.org/10.1038/s41423-019-0270-9.

(106) Torke, S.; Weber, M. S. Inhibition of Bruton´s Tyrosine Kinase as a Novel Therapeutic Approach in Multiple Sclerosis. *Expert Opin Investig Drugs* **2020**, *29* (10), 1143–1150. https://doi.org/10.1080/13543784.2020.1807934.

(107) Haselmayer, P.; Camps, M.; Liu-Bujalski, L.; Nguyen, N.; Morandi, F.; Head, J.; O'Mahony, A.; Zimmerli, S. C.; Bruns, L.; Bender, A. T.; Schroeder, P.; Grenningloh, R. Efficacy and Pharmacodynamic Modeling of the BTK Inhibitor Evobrutinib in Autoimmune Disease Models. *J Immunol* **2019**, *202* (10), 2888–2906. https://doi.org/10.4049/jimmunol.1800583.

(108) Kim, E.; Hurtz, C.; Koehrer, S.; Wang, Z.; Balasubramanian, S.; Chang, B. Y.; Müschen, M.; Davis, R. E.; Burger, J. A. Ibrutinib Inhibits Pre-BCR+ B-Cell Acute Lymphoblastic Leukemia Progression by Targeting BTK and BLK. *Blood* **2017**, *129* (9), 1155–1165. https://doi.org/10.1182/blood-2016-06-722900.

(109) Pillinger, G.; Abdul-Aziz, A.; Zaitseva, L.; Lawes, M.; MacEwan, D. J.; Bowles, K. M.; Rushworth, S. A. Targeting BTK for the Treatment of FLT3-ITD Mutated Acute Myeloid Leukemia. *Sci Rep* **2015**, *5* (1), 12949. https://doi.org/10.1038/srep12949.

(110) Humphries, L. A.; Dangelmaier, C.; Sommer, K.; Kipp, K.; Kato, R. M.; Griffith, N.; Bakman, I.; Turk, C. W.; Daniel, J. L.; Rawlings, D. J. Tec Kinases Mediate Sustained Calcium Influx via Site-Specific Tyrosine Phosphorylation of the Phospholipase Cγ Src Homology 2-Src Homology 3 Linker. *JBC* **2004**, *279* (36), 37651–37661. https://doi.org/10.1074/jbc.M311985200.

(111) Ahn, I. E.; Brown, J. R. Targeting Bruton's Tyrosine Kinase in CLL. *Front Immunol* **2021**, *12*. https://doi.org/10.3389/fimmu.2021.687458.

(112) Davis, R. E.; Ngo, V. N.; Lenz, G.; Tolar, P.; Young, R. M.; Romesser, P. B.; Kohlhammer, H.; Lamy, L.; Zhao, H.; Yang, Y.; Xu, W.; Shaffer, A. L.; Wright, G.; Xiao, W.; Powell, J.; Jiang, J.; Thomas, C. J.; Rosenwald, A.; Ott, G.; Muller-Hermelink, H. K.; Gascoyne, R. D.; Connors, J. M.; Johnson, N. A.; Rimsza, L. M.; Campo, E.; Jaffe, E. S.; Wilson, W. H.; Delabie, J.; Smeland, E. B.; Fisher, R. I.; Braziel, R. M.; Tubbs, R. R.; Cook, J. R.; Weisenburger, D. D.; Chan, W. C.; Pierce, S. K.; Staudt, L. M. Chronic Active B-Cell-Receptor Signalling in Diffuse Large B-Cell Lymphoma. *Nature* **2010**, *463* (7277), 88–92. https://doi.org/10.1038/nature08638.

(113) Srinivasan, L.; Sasaki, Y.; Calado, D. P.; Zhang, B.; Paik, J. H.; DePinho, R. A.; Kutok, J. L.; Kearney, J. F.; Otipoby, K. L.; Rajewsky, K. PI3 Kinase Signals BCR-Dependent Mature B Cell Survival. *Cell* **2009**, *139* (3), 573–586. https://doi.org/10.1016/j.cell.2009.08.041.

(114) Lam, K.-P.; Kühn, R.; Rajewsky, K. In Vivo Ablation of Surface Immunoglobulin on Mature B Cells by Inducible Gene Targeting Results in Rapid Cell Death. *Cell* **1997**, *90* (6), 1073–1083. https://doi.org/10.1016/S0092-8674(00)80373-6.

(115) Spaargaren, M.; Beuling, E. A.; Rurup, M. L.; Meijer, H. P.; Klok, M. D.; Middendorp, S.; Hendriks, R. W.; Pals, S. T. The B Cell Antigen Receptor Controls Integrin Activity through Btk and PLCγ2. *J Exp Med***2003**, *198* (10), 1539–1550.

https://doi.org/10.1084/jem.20011866.

(116) Halcomb, K. E.; Contreras, C. M.; Hinman, R. M.; Coursey, T. G.; Wright, H. L.; Satterthwaite, A. B. Btk and Phospholipase Cγ2 Can Function Independently during B Cell Development. *Eur J Immunol* **2007**, *37* (4), 1033–1042. https://doi.org/10.1002/eji.200636451.

(117) de Gorter, D. J. J.; Beuling, E. A.; Kersseboom, R.; Middendorp, S.; van Gils, J. M.; Hendriks, R. W.; Pals, S. T.; Spaargaren, M. Bruton's Tyrosine Kinase and Phospholipase Cγ2 Mediate Chemokine-Controlled B Cell Migration and Homing. *Immunity* **2007**, *26* (1), 93–104. https://doi.org/10.1016/j.immuni.2006.11.012.

(118) Mahajan, S.; Ghosh, S.; Sudbeck, E. A.; Zheng, Y.; Downs, S.; Hupke, M.; Uckun, F. M. Rational Design and Synthesis of a Novel Anti-Leukemic Agent Targeting Bruton′s Tyrosine Kinase (BTK), LFM-A13 [α-Cyano-β-Hydroxy-β-Methyl-N-(2,5-Dibromophenyl)Propenamide]. *JBC* **1999**, *274* (14), 9587–9599. https://doi.org/10.1074/jbc.274.14.9587.

(119) Wen, T.; Wang, J.; Shi, Y.; Qian, H.; Liu, P. Inhibitors Targeting Bruton's Tyrosine Kinase in Cancers: Drug Development Advances. *Leukemia* **2021**, *35* (2), 312–332. https://doi.org/10.1038/s41375-020-01072-6.

(120) Brullo, C.; Villa, C.; Tasso, B.; Russo, E.; Spallarossa, A. Btk Inhibitors: A Medicinal Chemistry and Drug Delivery Perspective. *Int J Mol Sci* **2021**, *22* (14), 7641. https://doi.org/10.3390/ijms22147641.

(121) Honigberg, L. A.; Smith, A. M.; Sirisawad, M.; Verner, E.; Loury, D.; Chang, B.; Li, S.; Pan, Z.; Thamm, D. H.; Miller, R. A.; Buggy, J. J. The Bruton Tyrosine Kinase Inhibitor PCI-32765 Blocks B-Cell Activation and Is Efficacious in Models of Autoimmune Disease and B-Cell Malignancy. *PNAS* **2010**, *107* (29), 13075–13080. https://doi.org/10.1073/pnas.1004594107.

(122) Pan, Z.; Scheerens, H.; Li, S.-J.; Schultz, B. E.; Sprengeler, P. A.; Burrill, L. C.; Mendonca, R. V.; Sweeney, M. D.; Scott, K. C. K.; Grothaus, P. G.; Jeffery, D. A.; Spoerke, J. M.; Honigberg, L. A.; Young, P. R.; Dalrymple, S. A.; Palmer, J. T. Discovery of Selective Irreversible Inhibitors for Bruton's Tyrosine Kinase. *ChemMedChem* **2007**, *2* (1), 58–61. https://doi.org/10.1002/cmdc.200600221.

(123) Estupiñán, H. Y.; Berglöf, A.; Zain, R.; Smith, C. I. E. Comparative Analysis of BTK Inhibitors and Mechanisms Underlying Adverse Effects. *Front Cell Dev Biol* **2021**, *9*. https://doi.org/10.3389/fcell.2021.630942.

(124) Rajasekaran, N.; Sadaram, M.; Hebb, J.; Sagiv-Barfi, I.; Ambulkar, S.; Rajapaksa,

A.; Chang, S.; Chester, C.; Waller, E.; Wang, L.; Lannutti, B.; Johnson, D.; Levy, R.; Kohrt, H. E. Three BTK-Specific Inhibitors, in Contrast to Ibrutinib, Do Not Antagonize Rituximab-Dependent NK-Cell Mediated Cytotoxicity. *Blood* **2014**, *124* (21), 3118–3118. https://doi.org/10.1182/blood.V124.21.3118.3118.

(125) Barf, T.; Covey, T.; Izumi, R.; van de Kar, B.; Gulrajani, M.; van Lith, B.; van Hoek, M.; de Zwart, E.; Mittag, D.; Demont, D.; Verkaik, S.; Krantz, F.; Pearson, P. G.; Ulrich, R.; Kaptein, A. Acalabrutinib (ACP-196): A Covalent Bruton Tyrosine Kinase Inhibitor with a Differentiated Selectivity and In Vivo Potency Profile. *J Pharmacol Exp Ther* **2017**, *363* (2), 240–252. https://doi.org/10.1124/jpet.117.242909.

(126) Flinsenberg, T. W. H.; Tromedjo, C. C.; Hu, N.; Liu, Y.; Guo, Y.; Thia, K. Y. T.; Noori, T.; Song, X.; Aw Yeang, H. X.; Tantalo, D. G.; Handunnetti, S.; Seymour, J. F.; Roberts, A. W.; Ritchie, D.; Koldej, R.; Neeson, P. J.; Wang, L.; Trapani, J. A.; Tam, C. S.; Voskoboinik, I. Differential Effects of BTK Inhibitors Ibrutinib and Zanubrutinib on NK-Cell Effector Function in Patients with Mantle Cell Lymphoma. *Haematologica* **2020**, *105* (2), e76–e79. https://doi.org/10.3324/haematol.2019.220590.

(127) Dhillon, S. Tirabrutinib: First Approval. *Drugs* **2020**, *80* (8), 835–840. https://doi.org/10.1007/s40265-020-01318-8.

(128) Narita, Y.; Nagane, M.; Mishima, K.; Terui, Y.; Arakawa, Y.; Yonezawa, H.; Asai, K.; Fukuhara, N.; Sugiyama, K.; Shinojima, N.; Kitagawa, J.; Aoi, A.; Nishikawa, R. Phase I/II Study of Tirabrutinib, a Second-Generation Bruton's Tyrosine Kinase Inhibitor, in Relapsed/Refractory Primary Central Nervous System Lymphoma. *Neuro Oncol* **2021**, *23* (1), 122–133. https://doi.org/10.1093/neuonc/noaa145.

(129) Ariza, Y.; Murata, M.; Ueda, Y.; Yoshizawa, T. Bruton's Tyrosine Kinase (Btk) Inhibitor Tirabrutinib Suppresses Osteoclastic Bone Resorption. *Bone Rep* **2019**, *10*, 100201. https://doi.org/10.1016/j.bonr.2019.100201.

(130) Dhillon, S. Orelabrutinib: First Approval. *Drugs* **2021**, *81* (4), 503–507. https://doi.org/10.1007/s40265-021-01482-5.

(131) Xu, W.; Song, Y.; Li, Z.; Yang, S.; Liu, L.; Hu, Y.; Zhang, W.; Zhou, J.; Gao, S.; Ding, K.; Zhang, H.; Zhu, Z.; Wang, S.; Xu, B.; Hu, J.; Liu, T.; Ji, C.; Xia, Z.; Li, Y.; Wang, X.; Xu, Z.; Zhao, R.; Zhang, B.; Zhu, A.; Li, J. Safety, Tolerability and Efficacy of Orelabrutinib, Once a Day, to Treat Chinese Patients with Relapsed or Refractory Chronic Lymphocytic Leukemia/Small Cell Leukemia. *Blood* **2019**, *134*

(Supplement_1), 4319–4319. https://doi.org/10.1182/blood-2019-123331.

(132) Xu, W.; Song, Y.; Wang, T.; Yang, S.; Liu, L.; Hu, Y.; Zhang, W.; Zhou, J.; Gao, S.; Ding, K.; Zhang, H.; Zhu, Z.; Wang, S.-Q.; Xu, B.; Hu, J.; Liu, T.; Ji, C.; Xia, Z.; Li, Y.; Wang, X.; Zhu, H.; Zhao, R.; Zhang, B.; Xu, Z.; Li, J. Updated Results from the Phase II Study of Orelabrutinib Monotherapy in Chinese Patients with Relapsed or Refractory Chronic Lymphocytic Leukemia/Small Cell Leukemia. *Blood* **2020**, *136* (Supplement 1), 26–27. https://doi.org/10.1182/blood-2020-134531.

(133) Gomez, E. B.; Ebata, K.; Randeria, H. S.; Rosendahl, M. S.; Cedervall, E. P.; Morales, T. H.; Hanson, L. M.; Brown, N. E.; Gong, X.; Stephens, J. R.; Wu, W.; Lippincott, I.; Ku, K. S.; Walgren, R. A.; Abada, P. B.; Ballard, J. A.; Allerston, C. K.; Brandhuber, B. J. Pirtobrutinib Preclinical Characterization: A Highly Selective, Non-Covalent (Reversible) BTK Inhibitor. *Blood* **2023**. https://doi.org/10.1182/blood.2022018674.

(134) Mato, A. R.; Shah, N. N.; Jurczak, W.; Cheah, C. Y.; Pagel, J. M.; Woyach, J. A.; Fakhri, B.; Eyre, T. A.; Lamanna, N.; Patel, M. R.; Alencar, A.; Lech-Maranda, E.; Wierda, W. G.; Coombs, C. C.; Gerson, J. N.; Ghia, P.; le Gouill, S.; Lewis, D. J.; Sundaram, S.; Cohen, J. B.; Flinn, I. W.; Tam, C. S.; Barve, M. A.; Kuss, B.; Taylor, J.; Abdel-Wahab, O.; Schuster, S. J.; Palomba, M. L.; Lewis, K. L.; Roeker, L. E.; Davids, M. S.; Tan, X. N.; Fenske, T. S.; Wallin, J.; Tsai, D. E.; Ku, N. C.; Zhu, E.; Chen, J.; Yin, M.; Nair, B.; Ebata, K.; Marella, N.; Brown, J. R.; Wang, M. Pirtobrutinib in Relapsed or Refractory B-Cell Malignancies (BRUIN): A Phase 1/2 Study. *The Lancet* **2021**, *397* (10277), 892–901. https://doi.org/10.1016/S0140-6736(21)00224-5.

(135) Kaptein, A.; de Bruin, G.; Emmelot-van Hoek, M.; van de Kar, B.; de Jong, A.; Gulrajani, M.; Demont, D.; Covey, T.; Mittag, D.; Barf, T. Potency and Selectivity of BTK Inhibitors in Clinical Development for B-Cell Malignancies. *Blood* **2018**, *132* (Supplement 1), 1871–1871. https://doi.org/10.1182/blood-2018-99-109973.

(136) Brandhuber, B.; Gomez, E.; Smith, S.; Eary, T.; Spencer, S.; Rothenberg, S. M.; Andrews, S. LOXO-305, A Next Generation Reversible BTK Inhibitor, for Overcoming Acquired Resistance to Irreversible BTK Inhibitors. *Clin Lymphoma Myeloma Leuk* **2018**, *18*, S216. https://doi.org/10.1016/j.clml.2018.07.081.

(137) God, J. M.; Haque, A. Burkitt Lymphoma: Pathogenesis and Immune Evasion. *J Oncol* **2010**, *2010*, 1–14. https://doi.org/10.1155/2010/516047.

(138) Bouska, A.; Bi, C.; Lone, W.; Zhang, W.; Kedwaii, A.; Heavican, T.; Lachel, C. M.;

Yu, J.; Ferro, R.; Eldorghamy, N.; Greiner, T. C.; Vose, J.; Weisenburger, D. D.; Gascoyne, R. D.; Rosenwald, A.; Ott, G.; Campo, E.; Rimsza, L. M.; Jaffe, E. S.; Braziel, R. M.; Siebert, R.; Miles, R. R.; Dave, S.; Reddy, A.; Delabie, J.; Staudt, L. M.; Song, J. Y.; McKeithan, T. W.; Fu, K.; Green, M.; Chan, W. C.; Iqbal, J. Adult High-Grade B-Cell Lymphoma with Burkitt Lymphoma Signature: Genomic Features and Potential Therapeutic Targets. *Blood* **2017**, *130* (16), 1819–1831. https://doi.org/10.1182/blood-2017-02-767335.

(139) Tomska, K.; Kurilov, R.; Lee, K. S.; Hüllein, J.; Lukas, M.; Sellner, L.; Walther, T.; Wagner, L.; Oleś, M.; Brors, B.; Huber, W.; Zenz, T. Drug-Based Perturbation Screen Uncovers Synergistic Drug Combinations in Burkitt Lymphoma. *Sci Rep* **2018**, *8* (1), 12046. https://doi.org/10.1038/s41598-018-30509-3.

(140) Szklener, K.; Michalski, A.; Żak, K.; Piwoński, M.; Mańdziuk, S. Ibrutinib in the Treatment of Solid Tumors: Current State of Knowledge and Future Directions. *Cells* **2022**, *11* (8), 1338. https://doi.org/10.3390/cells11081338.

(141) Burke, A.; Vinti, L.; Kabickova, E.; Beishuizen, A.; Tacyildiz, N.; Uyttebroeck, A.; Kang, H. J.; Luisi, F.; Minard-Colin, V.; Burkhardt, B.; Tamegnon, M.; Sun, S.; Curtis, M.; Deshpande, S.; Nottage, K.; Howes, A. J.; Srinivasan, S.; Bhojwani, D.; Norris, R. E.; Cairo, M. S. Ibrutinib plus RICE/RVICI for R/R Mature B-NHL in Children/Young Adults: SPARKLE Trial. *Blood Adv* **2022**. https://doi.org/10.1182/bloodadvances.2022008802.

(142) Tichenor, M. S.; Wiener, J. J. M.; Rao, N. L.; Bacani, G. M.; Wei, J.; Pooley Deckhut, C.; Barbay, J. K.; Kreutter, K. D.; Chang, L.; Clancy, K. W.; Murrey, H. E.; Wang, W.; Ahn, K.; Huber, M.; Rex, E.; Coe, K. J.; Wu, J.; Rui, H.; Sepassi, K.; Gaudiano, M.; Bekkers, M.; Cornelissen, I.; Packman, K.; Seierstad, M.; Xiouras, C.; Bembenek, S. D.; Alexander, R.; Milligan, C.; Balasubramanian, S.; Lebsack, A. D.; Venable, J. D.; Philippar, U.; Edwards, J. P.; Hirst, G. Discovery of JNJ-64264681: A Potent and Selective Covalent Inhibitor of Bruton's Tyrosine Kinase. *J Med Chem* **2022**, *65* (21), 14326–14336. https://doi.org/10.1021/acs.jmedchem.2c01026.

(143) Lenz, G.; Wright, G.; Dave, S. S.; Xiao, W.; Powell, J.; Zhao, H.; Xu, W.; Tan, B.; Goldschmidt, N.; Iqbal, J.; Vose, J.; Bast, M.; Fu, K.; Weisenburger, D. D.; Greiner, T. C.; Armitage, J. O.; Kyle, A.; May, L.; Gascoyne, R. D.; Connors, J. M.; Troen, G.; Holte, H.; Kvaloy, S.; Dierickx, D.; Verhoef, G.; Delabie, J.; Smeland, E. B.; Jares, P.; Martinez, A.; Lopez-Guillermo, A.; Montserrat, E.; Campo, E.; Braziel, R.

M.; Miller, T. P.; Rimsza, L. M.; Cook, J. R.; Pohlman, B.; Sweetenham, J.; Tubbs, R. R.; Fisher, R. I.; Hartmann, E.; Rosenwald, A.; Ott, G.; Muller-Hermelink, H.-K.; Wrench, D.; Lister, T. A.; Jaffe, E. S.; Wilson, W. H.; Chan, W. C.; Staudt, L. M. Stromal Gene Signatures in Large-B-Cell Lymphomas. *N Engl J Med* **2008**, *359* (22), 2313–2323. https://doi.org/10.1056/NEJMoa0802885.

(144) Wilson, W. H.; Young, R. M.; Schmitz, R.; Yang, Y.; Pittaluga, S.; Wright, G.; Lih, C.-J.; Williams, P. M.; Shaffer, A. L.; Gerecitano, J.; de Vos, S.; Goy, A.; Kenkre, V. P.; Barr, P. M.; Blum, K. A.; Shustov, A.; Advani, R.; Fowler, N. H.; Vose, J. M.; Elstrom, R. L.; Habermann, T. M.; Barrientos, J. C.; McGreivy, J.; Fardis, M.; Chang, B. Y.; Clow, F.; Munneke, B.; Moussa, D.; Beaupre, D. M.; Staudt, L. M. Targeting B Cell Receptor Signaling with Ibrutinib in Diffuse Large B Cell Lymphoma. *Nat Med* **2015**, *21* (8), 922–926. https://doi.org/10.1038/nm.3884.

(145) Feldman, T.; Mato, A. R.; Chow, K. F.; Protomastro, E. A.; Yannotti, K. M. L.; Bhattacharyya, P.; Yang, X.; Donato, M. L.; Rowley, S. D.; Carini, C.; Valentinetti, M.; Smith, J.; Gadaleta, G.; Bejot, C.; Stives, S.; Timberg, M.; Kdiry, S.; Pecora, A. L.; Beaven, A. W.; Goy, A. Addition of Lenalidomide to Rituximab, Ifosfamide, Carboplatin, Etoposide (<scp>RICER</Scp>) in First-relapse/Primary Refractory Diffuse Large B-cell Lymphoma. *Br J Haematol* **2014**, *166* (1), 77–83. https://doi.org/10.1111/bjh.12846.

(146) Younes, A.; Sehn, L. H.; Johnson, P.; Zinzani, P. L.; Hong, X.; Zhu, J.; Patti, C.; Belada, D.; Samoilova, O.; Suh, C.; Leppä, S.; Rai, S.; Turgut, M.; Jurczak, W.; Cheung, M. C.; Gurion, R.; Yeh, S.-P.; Lopez-Hernandez, A.; Dührsen, U.; Thieblemont, C.; Chiattone, C. S.; Balasubramanian, S.; Carey, J.; Liu, G.; Shreeve, S. M.; Sun, S.; Zhuang, S. H.; Vermeulen, J.; Staudt, L. M.; Wilson, W. Randomized Phase III Trial of Ibrutinib and Rituximab Plus Cyclophosphamide, Doxorubicin, Vincristine, and Prednisone in Non–Germinal Center B-Cell Diffuse Large B-Cell Lymphoma. *J Clin Oncol* **2019**, *37* (15), 1285–1295. https://doi.org/10.1200/JCO.18.02403.

(147) Strati, P.; de Vos, S.; Ruan, J.; Maddocks, K. J.; Flowers, C. R.; Rule, S.; Patel, P.; Xu, Y.; Wei, H.; Frigault, M. M.; Calvo, R.; Dyer, M. J. S. Acalabrutinib for Treatment of Diffuse Large B-Cell Lymphoma: Results from a Phase Ib Study. *Haematologica* **2021**, *106* (10), 2774–2778. https://doi.org/10.3324/haematol.2021.278654.

(148) Yang, H.; Xiang, B.; Song, Y.; Zhang, H.; Zhao, W.; Zou, D.; Lv, F.; Guo, W.; Liu,

A.; Li, C.; Tan, Z.; Liu, Y.; Fu, L.; Guo, H.; Novotny, W.; Huang, J.; Li, Y. Zanubrutinib Monotherapy for Relapsed or Refractory Non-Germinal Center Diffuse Large B-Cell Lymphoma. *Blood Adv* **2022**, *6* (6), 1629–1636. https://doi.org/10.1182/bloodadvances.2020003698.

(149) Hallek, M.; Cheson, B. D.; Catovsky, D.; Caligaris-Cappio, F.; Dighiero, G.; Döhner, H.; Hillmen, P.; Keating, M.; Montserrat, E.; Chiorazzi, N.; Stilgenbauer, S.; Rai, K. R.; Byrd, J. C.; Eichhorst, B.; O'Brien, S.; Robak, T.; Seymour, J. F.; Kipps, T. J. IwCLL Guidelines for Diagnosis, Indications for Treatment, Response Assessment, and Supportive Management of CLL. *Blood* **2018**, *131* (25), 2745–2760. https://doi.org/10.1182/blood-2017-09-806398.

(150) Strati, P.; Schlette, E. J.; Solis Soto, L. M.; Duenas, D. E.; Sivina, M.; Kim, E.; Keating, M. J.; Wierda, W. G.; Ferrajoli, A.; Kantarjian, H.; Estrov, Z.; Jain, N.; Thompson, P. A.; Wistuba, I. I.; Burger, J. A. Achieving Complete Remission in CLL Patients Treated with Ibrutinib: Clinical Significance and Predictive Factors. *Blood* **2020**, *135* (7), 510–513. https://doi.org/10.1182/blood.2019003570.

(151) O'Brien, S.; Furman, R. R.; Coutre, S.; Flinn, I. W.; Burger, J. A.; Blum, K.; Sharman, J.; Wierda, W.; Jones, J.; Zhao, W.; Heerema, N. A.; Johnson, A. J.; Luan, Y.; James, D. F.; Chu, A. D.; Byrd, J. C. Single-Agent Ibrutinib in Treatment-Naïve and Relapsed/Refractory Chronic Lymphocytic Leukemia: A 5-Year Experience. *Blood* **2018**, *131* (17), 1910–1919. https://doi.org/10.1182/blood-2017-10-810044.

(152) Sharman, J. P.; Farber, C. M.; Mahadevan, D.; Schreeder, M. T.; Brooks, H. D.; Kolibaba, K. S.; Fanning, S.; Klein, L.; Greenwald, D. R.; Sportelli, P.; Miskin, H. P.; Weiss, M. S.; Burke, J. M. Ublituximab (TG-1101), a Novel Glycoengineered Anti-CD20 Antibody, in Combination with Ibrutinib Is Safe and Highly Active in Patients with Relapsed and/or Refractory Chronic Lymphocytic Leukaemia: Results of a Phase 2 Trial. *Br J Haematol* **2017**, *176* (3), 412–420. https://doi.org/10.1111/bjh.14447.

(153) Jaglowski, S. M.; Jones, J. A.; Nagar, V.; Flynn, J. M.; Andritsos, L. A.; Maddocks, K. J.; Woyach, J. A.; Blum, K. A.; Grever, M. R.; Smucker, K.; Ruppert, A. S.; Heerema, N. A.; Lozanski, G.; Stefanos, M.; Munneke, B.; West, J.-S.; Neuenburg, J. K.; James, D. F.; Hall, N.; Johnson, A. J.; Byrd, J. C. Safety and Activity of BTK Inhibitor Ibrutinib Combined with Ofatumumab in Chronic Lymphocytic Leukemia: A Phase 1b/2 Study. *Blood* **2015**, *126* (7), 842–850. https://doi.org/10.1182/blood-2014-12-617522.

(154) Moreno, C.; Greil, R.; Demirkan, F.; Tedeschi, A.; Anz, B.; Larratt, L.; Simkovic, M.; Samoilova, O.; Novak, J.; Ben-Yehuda, D.; Strugov, V.; Gill, D.; Gribben, J. G.; Hsu, E.; Lih, C.-J.; Zhou, C.; Clow, F.; James, D. F.; Styles, L.; Flinn, I. W. Ibrutinib plus Obinutuzumab versus Chlorambucil plus Obinutuzumab in First-Line Treatment of Chronic Lymphocytic Leukaemia (ILLUMINATE): A Multicentre, Randomised, Open-Label, Phase 3 Trial. *Lancet Oncol* **2019**, *20* (1), 43–56. https://doi.org/10.1016/S1470-2045(18)30788-5.

(155) Shanafelt, T. D.; Wang, X. V.; Hanson, C. A.; Paietta, E. M.; O'Brien, S.; Barrientos, J.; Jelinek, D. F.; Braggio, E.; Leis, J. F.; Zhang, C. C.; Coutre, S. E.; Barr, P. M.; Cashen, A. F.; Mato, A. R.; Singh, A. K.; Mullane, M. P.; Little, R. F.; Erba, H.; Stone, R. M.; Litzow, M.; Tallman, M.; Kay, N. E. Long-Term Outcomes for Ibrutinib–Rituximab and Chemoimmunotherapy in CLL: Updated Results of the E1912 Trial. *Blood* **2022**, *140* (2), 112–120. https://doi.org/10.1182/blood.2021014960.

(156) Robak, T.; Burger, J. A.; Tedeschi, A.; Barr, P. M.; Owen, C.; Bairey, O.; Hillmen, P.; Simpson, D.; Grosicki, S.; Devereux, S.; McCarthy, H.; Coutre, S. E.; Quach, H.; Gaidano, G.; Maslyak, Z.; Stevens, D. A.; Moreno, C.; Gill, D. S.; Flinn, I. W.; Gribben, J. G.; Mokatrin, A.; Cheng, M.; Styles, L.; James, D. F.; Kipps, T. J.; Ghia, P. Single-Agent Ibrutinib versus Chemoimmunotherapy Regimens for Treatment-Naïve Patients with Chronic Lymphocytic Leukemia: A Cross-Trial Comparison of Phase 3 Studies. *Am J Hematol* **2018**, *93* (11), 1402–1410. https://doi.org/10.1002/ajh.25259.

(157) Wierda, W. G.; Allan, J. N.; Siddiqi, T.; Kipps, T. J.; Opat, S.; Tedeschi, A.; Badoux, X. C.; Kuss, B. J.; Jackson, S.; Moreno, C.; Jacobs, R.; Pagel, J. M.; Flinn, I.; Pak, Y.; Zhou, C.; Szafer-Glusman, E.; Ninomoto, J.; Dean, J. P.; James, D. F.; Ghia, P.; Tam, C. S. Ibrutinib Plus Venetoclax for First-Line Treatment of Chronic Lymphocytic Leukemia: Primary Analysis Results From the Minimal Residual Disease Cohort of the Randomized Phase II CAPTIVATE Study. *J Clin Oncol* **2021**, *39* (34), 3853–3865. https://doi.org/10.1200/JCO.21.00807.

(158) Fraietta, J. A.; Beckwith, K. A.; Patel, P. R.; Ruella, M.; Zheng, Z.; Barrett, D. M.; Lacey, S. F.; Melenhorst, J. J.; McGettigan, S. E.; Cook, D. R.; Zhang, C.; Xu, J.; Do, P.; Hulitt, J.; Kudchodkar, S. B.; Cogdill, A. P.; Gill, S.; Porter, D. L.; Woyach, J. A.; Long, M.; Johnson, A. J.; Maddocks, K.; Muthusamy, N.; Levine, B. L.; June, C. H.; Byrd, J. C.; Maus, M. v. Ibrutinib Enhances Chimeric Antigen Receptor T-

Cell Engraftment and Efficacy in Leukemia. *Blood* **2016**, *127* (9), 1117–1127. https://doi.org/10.1182/blood-2015-11-679134.

(159) Sun, C.; Nierman, P.; Kendall, E. K.; Cheung, J.; Gulrajani, M.; Herman, S. E. M.; Pleyer, C.; Ahn, I. E.; Stetler-Stevenson, M.; Yuan, C. M.; Maric, I.; Gaglione, E. M.; Harris, H. M.; Pittaluga, S.; Wang, M. H.; Patel, P.; Farooqui, M. Z. H.; Izumi, R.; Hamdy, A.; Covey, T.; Wiestner, A. Clinical and Biological Implications of Target Occupancy in CLL Treated with the BTK Inhibitor Acalabrutinib. *Blood* **2020**, *136* (1), 93–105. https://doi.org/10.1182/blood.2019003715.

(160) Byrd, J. C.; Hillmen, P.; Ghia, P.; Kater, A. P.; Chanan-Khan, A.; Furman, R. R.; O'Brien, S.; Yenerel, M. N.; Illés, A.; Kay, N.; Garcia-Marco, J. A.; Mato, A.; Pinilla-Ibarz, J.; Seymour, J. F.; Lepretre, S.; Stilgenbauer, S.; Robak, T.; Rothbaum, W.; Izumi, R.; Hamdy, A.; Patel, P.; Higgins, K.; Sohoni, S.; Jurczak, W. Acalabrutinib Versus Ibrutinib in Previously Treated Chronic Lymphocytic Leukemia: Results of the First Randomized Phase III Trial. *J Clin Oncol* **2021**, *39* (31), 3441–3452. https://doi.org/10.1200/JCO.21.01210.

(161) Rogers, K. A.; Thompson, P. A.; Allan, J. N.; Coleman, M.; Sharman, J. P.; Cheson, B. D.; Jones, D.; Izumi, R.; Frigault, M. M.; Quah, C.; Raman, R. K.; Patel, P.; Wang, M. H.; Kipps, T. J. Phase II Study of Acalabrutinib in Ibrutinib-Intolerant Patients with Relapsed/Refractory Chronic Lymphocytic Leukemia. *Haematologica* **2021**, *106* (9), 2364–2373. https://doi.org/10.3324/haematol.2020.272500.

(162) Awan, F. T.; Schuh, A.; Brown, J. R.; Furman, R. R.; Pagel, J. M.; Hillmen, P.; Stephens, D. M.; Woyach, J.; Bibikova, E.; Charuworn, P.; Frigault, M. M.; Hamdy, A.; Izumi, R.; Linghu, B.; Patel, P.; Wang, M. H.; Byrd, J. C. Acalabrutinib Monotherapy in Patients with Chronic Lymphocytic Leukemia Who Are Intolerant to Ibrutinib. *Blood Adv* **2019**, *3* (9), 1553–1562. https://doi.org/10.1182/bloodadvances.2018030007.

(163) Woyach, J. A.; Blachly, J. S.; Rogers, K. A.; Bhat, S. A.; Jianfar, M.; Lozanski, G.; Weiss, D. M.; Andersen, B. L.; Gulrajani, M.; Frigault, M. M.; Hamdy, A.; Izumi, R.; Munugalavadla, V.; Quah, C.; Wang, M.-H.; Byrd, J. C. Acalabrutinib plus Obinutuzumab in Treatment-Naïve and Relapsed/Refractory Chronic Lymphocytic Leukemia. *Cancer Discov* **2020**, *10* (3), 394–405. https://doi.org/10.1158/2159-8290.CD-19-1130.

(164) Sharman, J. P.; Egyed, M.; Jurczak, W.; Skarbnik, A.; Pagel, J. M.; Flinn, I. W.; Kamdar, M.; Munir, T.; Walewska, R.; Corbett, G.; Fogliatto, L. M.; Herishanu, Y.;

Banerji, V.; Coutre, S.; Follows, G.; Walker, P.; Karlsson, K.; Ghia, P.; Janssens, A.; Cymbalista, F.; Woyach, J. A.; Salles, G.; Wierda, W. G.; Izumi, R.; Munugalavadla, V.; Patel, P.; Wang, M. H.; Wong, S.; Byrd, J. C. Acalabrutinib with or without Obinutuzumab versus Chlorambucil and Obinutuzumab for Treatment-Naive Chronic Lymphocytic Leukaemia (ELEVATE-TN): A Randomised, Controlled, Phase 3 Trial. *The Lancet* **2020**, *395* (10232), 1278–1291. https://doi.org/10.1016/S0140-6736(20)30262-2.

(165) Davids, M. S.; Lampson, B. L.; Tyekucheva, S.; Wang, Z.; Lowney, J. C.; Pazienza, S.; Montegaard, J.; Patterson, V.; Weinstock, M.; Crombie, J. L.; Ng, S. Y.; Kim, A. I.; Jacobson, C. A.; LaCasce, A. S.; Armand, P.; Arnason, J. E.; Fisher, D. C.; Brown, J. R. Acalabrutinib, Venetoclax, and Obinutuzumab as Frontline Treatment for Chronic Lymphocytic Leukaemia: A Single-Arm, Open-Label, Phase 2 Study. *Lancet Oncol* **2021**, *22* (10), 1391–1402. https://doi.org/10.1016/S1470-2045(21)00455-1.

(166) Cull, G.; Burger, J. A.; Opat, S.; Gottlieb, D.; Verner, E.; Trotman, J.; Marlton, P.; Munoz, J.; Johnston, P.; Simpson, D.; Stern, J. C.; Prathikanti, R.; Wu, K.; Novotny, W.; Huang, J.; Tam, C. S. Zanubrutinib for Treatment-naïve and Relapsed/Refractory Chronic Lymphocytic Leukaemia: Long-term Follow-up of the Phase I/II AU-003 Study. *Br J Haematol* **2022**, *196* (5), 1209–1218. https://doi.org/10.1111/bjh.17994.

(167) Tam, C. S.; Trotman, J.; Opat, S.; Burger, J. A.; Cull, G.; Gottlieb, D.; Harrup, R.; Johnston, P. B.; Marlton, P.; Munoz, J.; Seymour, J. F.; Simpson, D.; Tedeschi, A.; Elstrom, R.; Yu, Y.; Tang, Z.; Han, L.; Huang, J.; Novotny, W.; Wang, L.; Roberts, A. W. Phase 1 Study of the Selective BTK Inhibitor Zanubrutinib in B-Cell Malignancies and Safety and Efficacy Evaluation in CLL. *Blood* **2019**, *134* (11), 851–859. https://doi.org/10.1182/blood.2019001160.

(168) Soumerai, J. D.; Mato, A. R.; Dogan, A.; Seshan, V. E.; Joffe, E.; Flaherty, K.; Carter, J.; Hochberg, E.; Barnes, J. A.; Hamilton, A. M.; Abramson, J. S.; Batlevi, C. L.; Matasar, M. J.; Noy, A.; Owens, C. N.; Palomba, M. L.; Kumar, A.; Takvorian, T.; Ni, A.; Choma, M.; Friedman, C.; Chadha, P.; Simkins, E.; Ruiters, J.; Sechio, S.; Portman, D.; Ramos, L.; Nolet, N.; Mahajan, N.; Martignetti, R.; Mi, J.; Scorsune, K.; Lynch, J.; McGree, B.; Hughes, S.; Grieve, C.; Roeker, L. E.; Thompson, M.; Johnson, P. C.; Roshal, M.; Huang, J.; Biondo, J.; Wu, Q.; Jacob, A.; Abdel-Wahab, O.; Zelenetz, A. D. Zanubrutinib, Obinutuzumab, and Venetoclax

with Minimal Residual Disease-Driven Discontinuation in Previously Untreated Patients with Chronic Lymphocytic Leukaemia or Small Lymphocytic Lymphoma: A Multicentre, Single-Arm, Phase 2 Trial. *Lancet Haematol* **2021**, *8* (12), e879–e890. https://doi.org/10.1016/S2352-3026(21)00307-0.

(169) Mato, A. R.; Shah, N. N.; Jurczak, W.; Cheah, C. Y.; Pagel, J. M.; Woyach, J. A.; Fakhri, B.; Eyre, T. A.; Lamanna, N.; Patel, M. R.; Alencar, A.; Lech-Maranda, E.; Wierda, W. G.; Coombs, C. C.; Gerson, J. N.; Ghia, P.; le Gouill, S.; Lewis, D. J.; Sundaram, S.; Cohen, J. B.; Flinn, I. W.; Tam, C. S.; Barve, M. A.; Kuss, B.; Taylor, J.; Abdel-Wahab, O.; Schuster, S. J.; Palomba, M. L.; Lewis, K. L.; Roeker, L. E.; Davids, M. S.; Tan, X. N.; Fenske, T. S.; Wallin, J.; Tsai, D. E.; Ku, N. C.; Zhu, E.; Chen, J.; Yin, M.; Nair, B.; Ebata, K.; Marella, N.; Brown, J. R.; Wang, M. Pirtobrutinib in Relapsed or Refractory B-Cell Malignancies (BRUIN): A Phase 1/2 Study. *The Lancet* **2021**, *397* (10277), 892–901. https://doi.org/10.1016/S0140-6736(21)00224-5.

(170) Walter, H. S.; Rule, S. A.; Dyer, M. J. S.; Karlin, L.; Jones, C.; Cazin, B.; Quittet, P.; Shah, N.; Hutchinson, C. v.; Honda, H.; Duffy, K.; Birkett, J.; Jamieson, V.; Courtenay-Luck, N.; Yoshizawa, T.; Sharpe, J.; Ohno, T.; Abe, S.; Nishimura, A.; Cartron, G.; Morschhauser, F.; Fegan, C.; Salles, G. A Phase 1 Clinical Trial of the Selective BTK Inhibitor ONO/GS-4059 in Relapsed and Refractory Mature B-Cell Malignancies. *Blood* **2016**, *127* (4), 411–419. https://doi.org/10.1182/blood-2015-08-664086.

(171) Danilov, A. v.; Herbaux, C.; Walter, H. S.; Hillmen, P.; Rule, S. A.; Kio, E. A.; Karlin, L.; Dyer, M. J. S.; Mitra, S. S.; Yi, P. C.; Humeniuk, R.; Huang, X.; Zhou, Z.; Bhargava, P.; Jürgensmeier, J. M.; Fegan, C. D. Phase Ib Study of Tirabrutinib in Combination with Idelalisib or Entospletinib in Previously Treated Chronic Lymphocytic Leukemia. *Clin Cancer Res* **2020**, *26* (12), 2810–2818. https://doi.org/10.1158/1078-0432.CCR-19-3504.

(172) Kutsch, N.; Pallasch, C.; Tausch, E.; Böhme, V.; Ritgen, M.; Liersch, R.; Wacker, A.; Jacobs, G.; Trappe, R. U.; Dreger, P.; Fischer, K.; Fink, A.-M.; Stilgenbauer, S.; Zhai, S.; Li, B.; Jürgensmeier, J. M.; Rajakumaraswamy, N.; Bhargava, P.; Hallek, M.; Eichhorst, B. F. Efficacy and Safety of the Combination of Tirabrutinib and Entospletinib With or Without Obinutuzumab in Relapsed Chronic Lymphocytic Leukemia. *Hemasphere* **2022**, *6* (4), e692. https://doi.org/10.1097/HS9.0000000000000692.

(173) Malikova, H.; Burghardtova, M.; Koubska, E.; Mandys, V.; Kozak, T.; Weichet, J. Secondary Central Nervous System Lymphoma: Spectrum of Morphological MRI Appearances. *Neuropsychiatr Dis Treat* **2018**, *14*, 733–740. https://doi.org/10.2147/NDT.S157959.

(174) Batchelor, T. T. Primary Central Nervous System Lymphoma. *Hematology* **2016**, *2016* (1), 379–385. https://doi.org/10.1182/asheducation-2016.1.379.

(175) Rusconi, C.; Cheah, C. Y.; Eyre, T. A.; Tucker, D.; Klener, P.; Giné, E.; Crucitti, L.; Muzi, C.; Iadecola, S.; Infante, G.; Bernard, S.; Auer, R. L.; Pagani, C.; Duglosz-Danecka, M.; Mocikova, H.; van Meerten, T.; Cencini, E.; Marin-Niebla, A.; Williams, M. E.; Angelillo, P.; Nicoli, P.; Arcari, A.; Morello, L.; Mannina, D.; Vitagliano, O.; Sartori, R.; Chiappella, A.; Sciarra, R.; Stefani, P. M.; Dreyling, M.; Seymour, J. F.; Visco, C. Ibrutinib Improves Survival Compared with Chemotherapy in Mantle Cell Lymphoma with Central Nervous System Relapse. *Blood* **2022**, *140* (17), 1907–1916. https://doi.org/10.1182/blood.2022015560.

(176) Rios, A.; Rekoff, G.; Dinh, B.; Chen, L.; Wahed, A.; Nguyen, N. MCL-247: Durable Response of a Patient with a Mantle Cell Lymphoma Central Nervous System (CNS) Relapse to Treatment with a Bruton Tyrosine Kinase Inhibitor (BTKi) Monotherapy. *Clin Lymphoma Myeloma Leuk* **2020**, *20*, S259–S260. https://doi.org/10.1016/S2152-2650(20)30862-4.

(177) Soussain, C.; Choquet, S.; Blonski, M.; Leclercq, D.; Houillier, C.; Rezai, K.; Bijou, F.; Houot, R.; Boyle, E.; Gressin, R.; Nicolas-Virelizier, E.; Barrie, M.; Moluçon-Chabrot, C.; Lelez, M. L.; Clavert, A.; Coisy, S.; Leruez, S.; Touitou, V.; Cassoux, N.; Daniau, M.; Ertault de la Bretonnière, M.; el Yamani, A.; Ghesquières, H.; Hoang-Xuan, K. Ibrutinib Monotherapy for Relapse or Refractory Primary CNS Lymphoma and Primary Vitreoretinal Lymphoma: Final Analysis of the Phase II 'Proof-of-Concept' ILOC Study by the Lymphoma Study Association (LYSA) and the French Oculo-Cerebral Lymphoma (LOC) Network. *Eur J Cancer* **2019**, *117*, 121–130. https://doi.org/10.1016/j.ejca.2019.05.024.

(178) Lionakis, M. S.; Dunleavy, K.; Roschewski, M.; Widemann, B. C.; Butman, J. A.; Schmitz, R.; Yang, Y.; Cole, D. E.; Melani, C.; Higham, C. S.; Desai, J. v.; Ceribelli, M.; Chen, L.; Thomas, C. J.; Little, R. F.; Gea-Banacloche, J.; Bhaumik, S.; Stetler-Stevenson, M.; Pittaluga, S.; Jaffe, E. S.; Heiss, J.; Lucas, N.; Steinberg, S. M.; Staudt, L. M.; Wilson, W. H. Inhibition of B Cell Receptor Signaling by Ibrutinib in Primary CNS Lymphoma. *Cancer Cell* **2017**, *31* (6), 833-843.e5.

https://doi.org/10.1016/j.ccell.2017.04.012.

(179) Chen, F.; Pang, D.; Guo, H.; Ou, Q.; Wu, X.; Jiang, X.; Wei, X.; Liu, S.; Huang, L.; Liang, Z.; Zhou, D.; Li, W. Clinical Outcomes of Newly Diagnosed Primary CNS Lymphoma Treated with Ibrutinib-based Combination Therapy: A Real-world Experience of Off-label Ibrutinib Use. *Cancer Med* **2020**, *9* (22), 8676–8684. https://doi.org/10.1002/cam4.3499.

(180) Grommes, C.; Tang, S. S.; Wolfe, J.; Kaley, T. J.; Daras, M.; Pentsova, E. I.; Piotrowski, A. F.; Stone, J.; Lin, A.; Nolan, C. P.; Manne, M.; Codega, P.; Campos, C.; Viale, A.; Thomas, A. A.; Berger, M. F.; Hatzoglou, V.; Reiner, A. S.; Panageas, K. S.; DeAngelis, L. M.; Mellinghoff, I. K. Phase 1b Trial of an Ibrutinib-Based Combination Therapy in Recurrent/Refractory CNS Lymphoma. *Blood* **2019**, *133* (5), 436–445. https://doi.org/10.1182/blood-2018-09-875732.

(181) McLaughlin, N.; Wang, Y.; Inwards, D. J.; Villasboas, J. C.; Micallef, I. N. M.; Habermann, T. M.; Nowakowski, G. S.; Witzig, T. E.; Thanarajasingam, G.; Porrata, L. F.; Lin, Y.; Thompson, C. A.; Bennani, N. N.; Johnston, P. B.; Ansell, S. M.; Paludo, J. Outcomes in Mantle Cell Lymphoma with Central Nervous System Involvement. *J Clin Oncol* **2021**, *39* (15_suppl), e19527–e19527. https://doi.org/10.1200/JCO.2021.39.15_suppl.e19527.

(182) Yao, Y.; Li, F.; Huang, J.; Jin, J.; Wang, H. Leukemia Stem Cell-Bone Marrow Microenvironment Interplay in Acute Myeloid Leukemia Development. *Exp Hematol Oncol* **2021**, *10* (1), 39. https://doi.org/10.1186/s40164-021-00233-2.

(183) Rushworth, S. A.; Murray, M. Y.; Zaitseva, L.; Bowles, K. M.; MacEwan, D. J. Identification of Bruton's Tyrosine Kinase as a Therapeutic Target in Acute Myeloid Leukemia. *Blood* **2014**, *123* (8), 1229–1238. https://doi.org/10.1182/blood-2013-06-511154.

(184) Zhu, S.; Jung, J.; Victor, E.; Arceo, J.; Gokhale, S.; Xie, P. Clinical Trials of the BTK Inhibitors Ibrutinib and Acalabrutinib in Human Diseases Beyond B Cell Malignancies. *Front Oncol* **2021**, *11*. https://doi.org/10.3389/fonc.2021.737943.

(185) Rushworth, S. A.; Pillinger, G.; Abdul-Aziz, A.; Piddock, R.; Shafat, M. S.; Murray, M. Y.; Zaitseva, L.; Lawes, M. J.; MacEwan, D. J.; Bowles, K. M. Activity of Bruton's Tyrosine-Kinase Inhibitor Ibrutinib in Patients with CD117-Positive Acute Myeloid Leukaemia: A Mechanistic Study Using Patient-Derived Blast Cells. *Lancet Haematol* **2015**, *2* (5), e204–e211. https://doi.org/10.1016/S2352-3026(15)00046-0.

(186) Dwivedi, P.; Muench, D. E.; Wagner, M.; Azam, M.; Grimes, H. L.; Greis, K. D. Time Resolved Quantitative Phospho-Tyrosine Analysis Reveals Bruton's Tyrosine Kinase Mediated Signaling Downstream of the Mutated Granulocyte-Colony Stimulating Factor Receptors. *Leukemia* **2019**, *33* (1), 75–87. https://doi.org/10.1038/s41375-018-0188-8.

(187) Dombret, H.; Gardin, C. An Update of Current Treatments for Adult Acute Myeloid Leukemia. *Blood* **2016**, *127* (1), 53–61. https://doi.org/10.1182/blood-2015-08-604520.

(188) Woyach, J. A.; Flinn, I. W.; Awan, F. T.; Eradat, H.; Brander, D.; Tees, M.; Parikh, S. A.; Phillips, T. J.; Ghori, R.; Reddy, N. M.; Farooqui, M. Z. H.; Byrd, J. C.; Stephens, D. M. Efficacy and Safety of Nemtabrutinib, a Wild-Type and C481S-Mutated Bruton Tyrosine Kinase Inhibitor for B-Cell Malignancies: Updated Analysis of the Open-Label Phase 1/2 Dose-Expansion Bellwave-001 Study. *Blood* **2022**, *140* (Supplement 1), 7004–7006. https://doi.org/10.1182/blood-2022-163596.

(189) Huang, S.; Pan, J.; Jin, J.; Li, C.; Li, X.; Huang, J.; Huang, X.; Yan, X.; Li, F.; Yu, M.; Hu, C.; Jin, J.; Xu, Y.; Ling, Q.; Ye, W.; Wang, Y.; Jin, J. Abivertinib, a Novel BTK Inhibitor: Anti-Leukemia Effects and Synergistic Efficacy with Homoharringtonine in Acute Myeloid Leukemia. *Cancer Lett* **2019**, *461*, 132–143. https://doi.org/10.1016/j.canlet.2019.07.008.

(190) Burger, J. A. Bruton Tyrosine Kinase Inhibitors. *The Cancer Journal* **2019**, *25* (6), 386–393. https://doi.org/10.1097/PPO.0000000000000412.

(191) Coutre, S. E.; Byrd, J. C.; Hillmen, P.; Barrientos, J. C.; Barr, P. M.; Devereux, S.; Robak, T.; Kipps, T. J.; Schuh, A.; Moreno, C.; Furman, R. R.; Burger, J. A.; O'Dwyer, M.; Ghia, P.; Valentino, R.; Chang, S.; Dean, J. P.; James, D. F.; O'Brien, S. M. Long-Term Safety of Single-Agent Ibrutinib in Patients with Chronic Lymphocytic Leukemia in 3 Pivotal Studies. *Blood Adv* **2019**, *3* (12), 1799–1807. https://doi.org/10.1182/bloodadvances.2018028761.

(192) Tam, C. S.; Robak, T.; Ghia, P.; Kahl, B. S.; Walker, P.; Janowski, W.; Simpson, D.; Shadman, M.; Ganly, P. S.; Laurenti, L.; Opat, S.; Tani, M.; Ciepluch, H.; Verner, E.; Šimkovič, M.; Österborg, A.; Trněný, M.; Tedeschi, A.; Paik, J. C.; Kuwahara, S. B.; Feng, S.; Ramakrishnan, V.; Cohen, A.; Huang, J.; Hillmen, P.; Brown, J. R. Zanubrutinib Monotherapy for Patients with Treatment-Naïve Chronic Lymphocytic Leukemia and 17p Deletion. *Haematologica* **2020**, *106* (9), 2354–2363. https://doi.org/10.3324/haematol.2020.259432.

(193) He, M. Y.; Kridel, R. Treatment Resistance in Diffuse Large B-Cell Lymphoma. *Leukemia* **2021**, *35* (8), 2151–2165. https://doi.org/10.1038/s41375-021-01285-3.

(194) Jones, J. A.; Mato, A. R.; Wierda, W. G.; Davids, M. S.; Choi, M.; Cheson, B. D.; Furman, R. R.; Lamanna, N.; Barr, P. M.; Zhou, L.; Chyla, B.; Salem, A. H.; Verdugo, M.; Humerickhouse, R. A.; Potluri, J.; Coutre, S.; Woyach, J.; Byrd, J. C. Venetoclax for Chronic Lymphocytic Leukaemia Progressing after Ibrutinib: An Interim Analysis of a Multicentre, Open-Label, Phase 2 Trial. *Lancet Oncol* **2018**, *19* (1), 65–75. https://doi.org/10.1016/S1470-2045(17)30909-9.

(195) Liu, Q.; Sabnis, Y.; Zhao, Z.; Zhang, T.; Buhrlage, S. J.; Jones, L. H.; Gray, N. S. Developing Irreversible Inhibitors of the Protein Kinase Cysteinome. *Chem Biol* **2013**, *20* (2), 146–159. https://doi.org/10.1016/j.chembiol.2012.12.006.

(196) Zhang, J.; Yang, P. L.; Gray, N. S. Targeting Cancer with Small Molecule Kinase Inhibitors. *Nat Rev Cancer* **2009**, *9* (1), 28–39. https://doi.org/10.1038/nrc2559.

(197) Zhao, Z.; Liu, Q.; Bliven, S.; Xie, L.; Bourne, P. E. Determining Cysteines Available for Covalent Inhibition Across the Human Kinome. *J Med Chem* **2017**, *60* (7), 2879–2889. https://doi.org/10.1021/acs.jmedchem.6b01815.

(198) Bosc, N.; Meyer, C.; Bonnet, P. The Use of Novel Selectivity Metrics in Kinase Research. *BMC Bioinformatics* **2017**, *18* (1), 17. https://doi.org/10.1186/s12859-016-1413-y.

(199) Liclican, A.; Serafini, L.; Xing, W.; Czerwieniec, G.; Steiner, B.; Wang, T.; Brendza, K. M.; Lutz, J. D.; Keegan, K. S.; Ray, A. S.; Schultz, B. E.; Sakowicz, R.; Feng, J. Y. Biochemical Characterization of Tirabrutinib and Other Irreversible Inhibitors of Bruton's Tyrosine Kinase Reveals Differences in on - and off - Target Inhibition. *Biochim Biophys Acta Gen Subj* **2020**, *1864* (4), 129531. https://doi.org/10.1016/j.bbagen.2020.129531.

(200) Wang, B.; Deng, Y.; Chen, Y.; Yu, K.; Wang, A.; Liang, Q.; Wang, W.; Chen, C.; Wu, H.; Hu, C.; Miao, W.; Hur, W.; Wang, W.; Hu, Z.; Weisberg, E. L.; Wang, J.; Ren, T.; Wang, Y.; Gray, N. S.; Liu, Q.; Liu, J. Structure-Activity Relationship Investigation for Benzonaphthyridinone Derivatives as Novel Potent Bruton's Tyrosine Kinase (BTK) Irreversible Inhibitors. *Eur J Med Chem* **2017**, *137*, 545–557. https://doi.org/10.1016/j.ejmech.2017.06.016.

(201) Snijder, B.; Vladimer, G. I.; Krall, N.; Miura, K.; Schmolke, A.-S.; Kornauth, C.; Lopez de la Fuente, O.; Choi, H.-S.; van der Kouwe, E.; Gültekin, S.; Kazianka, L.; Bigenzahn, J. W.; Hoermann, G.; Prutsch, N.; Merkel, O.; Ringler, A.; Sabler, M.;

Jeryczynski, G.; Mayerhoefer, M. E.; Simonitsch-Klupp, I.; Ocko, K.; Felberbauer, F.; Müllauer, L.; Prager, G. W.; Korkmaz, B.; Kenner, L.; Sperr, W. R.; Kralovics, R.; Gisslinger, H.; Valent, P.; Kubicek, S.; Jäger, U.; Staber, P. B.; Superti-Furga, G. Image-Based Ex-Vivo Drug Screening for Patients with Aggressive Haematological Malignancies: Interim Results from a Single-Arm, Open-Label, Pilot Study. *Lancet Haematol* **2017**, *4* (12), e595–e606. https://doi.org/10.1016/S2352-3026(17)30208-9.

(202) Leverson, J. D.; Sampath, D.; Souers, A. J.; Rosenberg, S. H.; Fairbrother, W. J.; Amiot, M.; Konopleva, M.; Letai, A. Found in Translation: How Preclinical Research Is Guiding the Clinical Development of the BCL2-Selective Inhibitor Venetoclax. *Cancer Discov* **2017**, *7* (12), 1376–1393. https://doi.org/10.1158/2159-8290.CD-17-0797.

(203) Roberts, A. W.; Huang, D. Targeting BCL2 With BH3 Mimetics: Basic Science and Clinical Application of Venetoclax in Chronic Lymphocytic Leukemia and Related B Cell Malignancies. *Clin Pharmacol Ther* **2017**, *101* (1), 89–98. https://doi.org/10.1002/cpt.553.

(204) Byrd, J. C.; Furman, R. R.; Coutre, S. E.; Flinn, I. W.; Burger, J. A.; Blum, K. A.; Grant, B.; Sharman, J. P.; Coleman, M.; Wierda, W. G.; Jones, J. A.; Zhao, W.; Heerema, N. A.; Johnson, A. J.; Sukbuntherng, J.; Chang, B. Y.; Clow, F.; Hedrick, E.; Buggy, J. J.; James, D. F.; O'Brien, S. Targeting BTK with Ibrutinib in Relapsed Chronic Lymphocytic Leukemia. *N Engl J Med* **2013**, *369* (1), 32–42. https://doi.org/10.1056/NEJMoa1215637.

(205) Gleeson, M. P.; Hersey, A.; Montanari, D.; Overington, J. Probing the Links between in Vitro Potency, ADMET and Physicochemical Parameters. *Nat Rev Drug Discov* **2011**, *10* (3), 197–208. https://doi.org/10.1038/nrd3367.

(206) Estupiñán, H. Y.; Wang, Q.; Berglöf, A.; Schaafsma, G. C. P.; Shi, Y.; Zhou, L.; Mohammad, D. K.; Yu, L.; Vihinen, M.; Zain, R.; Smith, C. I. E. BTK Gatekeeper Residue Variation Combined with Cysteine 481 Substitution Causes Super-Resistance to Irreversible Inhibitors Acalabrutinib, Ibrutinib and Zanubrutinib. *Leukemia* **2021**, *35* (5), 1317–1329. https://doi.org/10.1038/s41375-021-01123-6.

(207) Lynch, T. J.; Kim, E. S.; Eaby, B.; Garey, J.; West, D. P.; Lacouture, M. E. Epidermal Growth Factor Receptor Inhibitor–Associated Cutaneous Toxicities: An Evolving Paradigm in Clinical Management. *Oncologist* **2007**, *12* (5), 610–621. https://doi.org/10.1634/theoncologist.12-5-610.

(208) von Hundelshausen, P.; Siess, W. Bleeding by Bruton Tyrosine Kinase-Inhibitors: Dependency on Drug Type and Disease. *Cancers (Basel)* **2021**, *13* (5), 1103. https://doi.org/10.3390/cancers13051103.

(209) Eichhorst, B.; Robak, T.; Montserrat, E.; Ghia, P.; Niemann, C. U.; Kater, A. P.; Gregor, M.; Cymbalista, F.; Buske, C.; Hillmen, P.; Hallek, M.; Mey, U. Chronic Lymphocytic Leukaemia: ESMO Clinical Practice Guidelines for Diagnosis, Treatment and Follow-Up. *Annals of Oncology* **2021**, *32* (1), 23–33. https://doi.org/10.1016/j.annonc.2020.09.019.

(210) Xu, W.; Yang, S.; Zhou, K.; Pan, L.; Li, Z.; Zhou, J.; Gao, S.; Zhou, D.; Hu, J.; Feng, R.; Huang, H.; Ji, M.; Guo, H.; Huang, J.; Novotny, W.; Feng, S.; Li, J. Treatment of Relapsed/Refractory Chronic Lymphocytic Leukemia/Small Lymphocytic Lymphoma with the BTK Inhibitor Zanubrutinib: Phase 2, Single-Arm, Multicenter Study. *J Hematol Oncol* **2020**, *13* (1), 48. https://doi.org/10.1186/s13045-020-00884-4.

(211) Burger, J. A.; Tedeschi, A.; Barr, P. M.; Robak, T.; Owen, C.; Ghia, P.; Bairey, O.; Hillmen, P.; Bartlett, N. L.; Li, J.; Simpson, D.; Grosicki, S.; Devereux, S.; McCarthy, H.; Coutre, S.; Quach, H.; Gaidano, G.; Maslyak, Z.; Stevens, D. A.; Janssens, A.; Offner, F.; Mayer, J.; O'Dwyer, M.; Hellmann, A.; Schuh, A.; Siddiqi, T.; Polliack, A.; Tam, C. S.; Suri, D.; Cheng, M.; Clow, F.; Styles, L.; James, D. F.; Kipps, T. J. Ibrutinib as Initial Therapy for Patients with Chronic Lymphocytic Leukemia. *N Engl J Med* **2015**, *373* (25), 2425–2437. https://doi.org/10.1056/NEJMoa1509388.

(212) Chavda, B.; Arnott, J. A.; Planey, S. L. Targeting Protein Palmitoylation: Selective Inhibitors and Implications in Disease. *Expert Opin Drug Discov* **2014**, *9* (9), 1005–1019. https://doi.org/10.1517/17460441.2014.933802.

(213) Virlogeux, A.; Scaramuzzino, C.; Lenoir, S.; Carpentier, R.; Louessard, M.; Genoux, A.; Lino, P.; Hinckelmann, M.-V.; Perrier, A. L.; Humbert, S.; Saudou, F. Increasing Brain Palmitoylation Rescues Behavior and Neuropathology in Huntington Disease Mice. *Sci Adv* **2021**, *7* (14). https://doi.org/10.1126/sciadv.abb0799.

(214) Yao, T.; Xiao, H.; Wang, H.; Xu, X. Recent Advances in PROTACs for Drug Targeted Protein Research. *Int J Mol Sci* **2022**, *23* (18), 10328. https://doi.org/10.3390/ijms231810328.

(215) Won, S. J.; Davda, D.; Labby, K. J.; Hwang, S. Y.; Pricer, R.; Majmudar, J. D.;

Armacost, K. A.; Rodriguez, L. A.; Rodriguez, C. L.; Chong, F. S.; Torossian, K. A.; Palakurthi, J.; Hur, E. S.; Meagher, J. L.; Brooks, C. L.; Stuckey, J. A.; Martin, B. R. Molecular Mechanism for Isoform-Selective Inhibition of Acyl Protein Thioesterases 1 and 2 (APT1 and APT2). *ACS Chem Biol* **2016**, *11* (12), 3374–3382. https://doi.org/10.1021/acschembio.6b00720.

(216) Tomatis, V. M.; Trenchi, A.; Gomez, G. A.; Daniotti, J. L. Acyl-Protein Thioesterase 2 Catalizes the Deacylation of Peripheral Membrane-Associated GAP-43. *PLoS One* **2010**, *5* (11), e15045. https://doi.org/10.1371/journal.pone.0015045.

(217) Duncan, J. A.; Gilman, A. G. A Cytoplasmic Acyl-Protein Thioesterase That Removes Palmitate from G Protein α Subunits and P21RAS. *JBC* **1998**, *273* (25), 15830–15837. https://doi.org/10.1074/jbc.273.25.15830.

(218) Abrami, L.; Audagnotto, M.; Ho, S.; Marcaida, M. J.; Mesquita, F. S.; Anwar, M. U.; Sandoz, P. A.; Fonti, G.; Pojer, F.; Dal Peraro, M.; van der Goot, F. G. Palmitoylated Acyl Protein Thioesterase APT2 Deforms Membranes to Extract Substrate Acyl Chains. *Nat Chem Biol* **2021**, *17* (4), 438–447. https://doi.org/10.1038/s41589-021-00753-2.

(219) Cho, E.; Park, M. Palmitoylation in Alzheimer□s Disease and Other Neurodegenerative Diseases. *Pharmacol Res* **2016**, *111*, 133–151. https://doi.org/10.1016/j.phrs.2016.06.008.

(220) Long, J. Z.; Cravatt, B. F. The Metabolic Serine Hydrolases and Their Functions in Mammalian Physiology and Disease. *Chem Rev* **2011**, *111* (10), 6022–6063. https://doi.org/10.1021/cr200075y.

(221) Wang, A.; Deems, R. A.; Dennis, E. A. Cloning, Expression, and Catalytic Mechanism of Murine Lysophospholipase I. *JBC* **1997**, *272* (19), 12723–12729. https://doi.org/10.1074/jbc.272.19.12723.

(222) Duncan, J. A.; Gilman, A. G. Characterization of Saccharomyces CerevisiaeAcyl-Protein Thioesterase 1, the Enzyme Responsible for G Protein α Subunit Deacylation in Vivo. *JBC* **2002**, *277* (35), 31740–31752. https://doi.org/10.1074/jbc.M202505200.

(223) Yeh, D. C.; Duncan, J. A.; Yamashita, S.; Michel, T. Depalmitoylation of Endothelial Nitric-Oxide Synthase by Acyl-Protein Thioesterase 1 Is Potentiated by Ca2+-Calmodulin. *JBC* **1999**, *274* (46), 33148–33154. https://doi.org/10.1074/jbc.274.46.33148.

(224) Flaumenhaft, R.; Rozenvayn, N.; Feng, D.; Dvorak, A. M. SNAP-23 and Syntaxin-2

Localize to the Extracellular Surface of the Platelet Plasma Membrane. *Blood* **2007**, *110* (5), 1492–1501. https://doi.org/10.1182/blood-2006-11-055772.

(225) Veit, M.; Schmidt, M. F. G. Enzymatic Depalmitoylation of Viral Glycoproteins with Acyl-Protein Thioesterase 1 in Vitro. *Virology* **2001**, *288* (1), 89–95. https://doi.org/10.1006/viro.2001.1063.

(226) Carrel, D.; Firestein, B. L. MicroRNA-Mediated Regulation of Synaptic Palmitoylation: Shrinking Fat Spines. *Nat Cell Biol* **2009**, *11* (6), 681–682. https://doi.org/10.1038/ncb0609-681.

(227) Siegel, G.; Obernosterer, G.; Fiore, R.; Oehmen, M.; Bicker, S.; Christensen, M.; Khudayberdiev, S.; Leuschner, P. F.; Busch, C. J. L.; Kane, C.; Hübel, K.; Dekker, F.; Hedberg, C.; Rengarajan, B.; Drepper, C.; Waldmann, H.; Kauppinen, S.; Greenberg, M. E.; Draguhn, A.; Rehmsmeier, M.; Martinez, J.; Schratt, G. M. A Functional Screen Implicates MicroRNA-138-Dependent Regulation of the Depalmitoylation Enzyme APT1 in Dendritic Spine Morphogenesis. *Nat Cell Biol* **2009**, *11* (6), 705–716. https://doi.org/10.1038/ncb1876.

(228) Toyoda, T.; Sugimoto, H.; Yamashita, S. Sequence, Expression in Escherichia Coli, and Characterization of Lysophospholipase II. *Biochim Biophys Acta Mol Cell Biol Lipids* **1999**, *1437* (2), 182–193. https://doi.org/10.1016/S1388-1981(99)00007-4.

(229) Field, S. D.; Lee, W.; Dutra, J. K.; Serneo, F. S. F.; Oyer, J.; Xu, H.; Johnson, D. S.; am Ende, C. W.; Seneviratne, U. Fluorophosphonate-Based Degrader Identifies Degradable Serine Hydrolases by Quantitative Proteomics. *ChemBioChem* **2020**, *21* (20), 2916–2920. https://doi.org/10.1002/cbic.202000253.

(230) Rocks, O.; Peyker, A.; Kahms, M.; Verveer, P. J.; Koerner, C.; Lumbierres, M.; Kuhlmann, J.; Waldmann, H.; Wittinghofer, A.; Bastiaens, P. I. H. An Acylation Cycle Regulates Localization and Activity of Palmitoylated Ras Isoforms. *Science (1979)* **2005**, *307* (5716), 1746–1752. https://doi.org/10.1126/science.1105654.

(231) Dekker, F. J.; Rocks, O.; Vartak, N.; Menninger, S.; Hedberg, C.; Balamurugan, R.; Wetzel, S.; Renner, S.; Gerauer, M.; Schölermann, B.; Rusch, M.; Kramer, J. W.; Rauh, D.; Coates, G. W.; Brunsveld, L.; Bastiaens, P. I. H.; Waldmann, H. Small-Molecule Inhibition of APT1 Affects Ras Localization and Signaling. *Nat Chem Biol* **2010**, *6* (6), 449–456. https://doi.org/10.1038/nchembio.362.

(232) Lin, D. T. S.; Conibear, E. ABHD17 Proteins Are Novel Protein Depalmitoylases That Regulate N-Ras Palmitate Turnover and Subcellular Localization. *Elife* **2015**, *4*. https://doi.org/10.7554/eLife.11306.

(233) Sadeghi, R. S.; Kulej, K.; Kathayat, R. S.; Garcia, B. A.; Dickinson, B. C.; Brady, D. C.; Witze, E. S. Wnt5a Signaling Induced Phosphorylation Increases APT1 Activity and Promotes Melanoma Metastatic Behavior. *Elife* **2018**, *7*. https://doi.org/10.7554/eLife.34362.

(234) Mohammed, A.; Zhang, C.; Zhang, S.; Shen, Q.; Li, J.; Tang, Z.; Liu, H. Inhibition of Cell Proliferation and Migration in Non-small Cell Lung Cancer Cells through the Suppression of LYPLA1. *Oncol Rep* **2018**. https://doi.org/10.3892/or.2018.6857.

(235) Berg, V.; Rusch, M.; Vartak, N.; Jüngst, C.; Schauss, A.; Waldmann, H.; Hedberg, C.; Pallasch, C. P.; Bastiaens, P. I. H.; Hallek, M.; Wendtner, C.-M.; Frenzel, L. P. MiRs-138 and -424 Control Palmitoylation-Dependent CD95-Mediated Cell Death by Targeting Acyl Protein Thioesterases 1 and 2 in CLL. *Blood* **2015**, *125* (19), 2948–2957. https://doi.org/10.1182/blood-2014-07-586511.

(236) Yeste-Velasco, M.; Linder, M. E.; Lu, Y.-J. Protein S-Palmitoylation and Cancer. *Biochim Biophys Acta Rev Cancer* **2015**, *1856* (1), 107–120. https://doi.org/10.1016/j.bbcan.2015.06.004.

(237) Rusch, M.; Zimmermann, T. J.; Bürger, M.; Dekker, F. J.; Görmer, K.; Triola, G.; Brockmeyer, A.; Janning, P.; Böttcher, T.; Sieber, S. A.; Vetter, I. R.; Hedberg, C.; Waldmann, H. Identification of Acyl Protein Thioesterases 1 and 2 as the Cellular Targets of the Ras-Signaling Modulators Palmostatin B and M. *Angew Chem Int Ed* **2011**, *50* (42), 9838–9842. https://doi.org/10.1002/anie.201102967.

(238) Vujic, I.; Sanlorenzo, M.; Esteve-Puig, R.; Vujic, M.; Kwong, A.; Tsumura, A.; Murphy, R.; Moy, A.; Posch, C.; Monshi, B.; Rappersberger, K.; Ortiz-Urda, S. Acyl Protein Thioesterase 1 and 2 (APT-1, APT-2) Inhibitors Palmostatin B, ML348 and ML349 Have Different Effects on NRAS Mutant Melanoma Cells. *Oncotarget* **2016**, *7* (6), 7297–7306. https://doi.org/10.18632/oncotarget.6907.

(239) Speers, A. E.; Cravatt, B. F. Activity-Based Protein Profiling (ABPP) and Click Chemistry (CC)–ABPP by MudPIT Mass Spectrometry. *Curr Protoc Chem Biol* **2009**, *1* (1), 29–41. https://doi.org/10.1002/9780470559277.ch090138.

(240) Jessani, N.; Liu, Y.; Humphrey, M.; Cravatt, B. F. Enzyme Activity Profiles of the Secreted and Membrane Proteome That Depict Cancer Cell Invasiveness. *PNAS* **2002**, *99* (16), 10335–10340. https://doi.org/10.1073/pnas.162187599.

(241) Jessani, N.; Cravatt, B. F. The Development and Application of Methods for Activity-Based Protein Profiling. *Curr Opin Chem Biol* **2004**, *8* (1), 54–59. https://doi.org/10.1016/j.cbpa.2003.11.004.

(242) Leung, D.; Hardouin, C.; Boger, D. L.; Cravatt, B. F. Discovering Potent and Selective Reversible Inhibitors of Enzymes in Complex Proteomes. *Nat Biotechnol* **2003**, *21* (6), 687–691. https://doi.org/10.1038/nbt826.

(243) Li, W.; Blankman, J. L.; Cravatt, B. F. A Functional Proteomic Strategy to Discover Inhibitors for Uncharacterized Hydrolases. *J Am Chem Soc* **2007**, *129* (31), 9594–9595. https://doi.org/10.1021/ja073650c.

(244) Roberts, A. M.; Ward, C. C.; Nomura, D. K. Activity-Based Protein Profiling for Mapping and Pharmacologically Interrogating Proteome-Wide Ligandable Hotspots. *Curr Opin Biotechnol* **2017**, *43*, 25–33. https://doi.org/10.1016/j.copbio.2016.08.003.

(245) Zalewski, A.; Macphee, C.; Nelson, J. Lipoprotein-Associated Phospholipase A2: A Potential Therapeutic Target for Atherosclerosis. *Current Drug Target - Cardiovascular & Hematological Disorders* **2005**, *5* (6), 527–532. https://doi.org/10.2174/156800605774962103.

(246) Packard, C. J.; O'Reilly, D. S. J.; Caslake, M. J.; McMahon, A. D.; Ford, I.; Cooney, J.; Macphee, C. H.; Suckling, K. E.; Krishna, M.; Wilkinson, F. E.; Rumley, A.; Docherty, G.; Burczak, J. D.; Lowe, G. D. O. Lipoprotein-Associated Phospholipase A $_2$ as an Independent Predictor of Coronary Heart Disease. *N Engl J Med* **2000**, *343* (16), 1148–1155. https://doi.org/10.1056/NEJM200010193431603.

(247) Bai, N.; Miller, S. A.; Andrianov, G. v.; Yates, M.; Kirubakaran, P.; Karanicolas, J. Rationalizing PROTAC-Mediated Ternary Complex Formation Using Rosetta. *J Chem Inf Model* **2021**, *61* (3), 1368–1382. https://doi.org/10.1021/acs.jcim.0c01451.

(248) Lv, D.; Pal, P.; Liu, X.; Jia, Y.; Thummuri, D.; Zhang, P.; Hu, W.; Pei, J.; Zhang, Q.; Zhou, S.; Khan, S.; Zhang, X.; Hua, N.; Yang, Q.; Arango, S.; Zhang, W.; Nayak, D.; Olsen, S. K.; Weintraub, S. T.; Hromas, R.; Konopleva, M.; Yuan, Y.; Zheng, G.; Zhou, D. Development of a BCL-XL and BCL-2 Dual Degrader with Improved Anti-Leukemic Activity,. *Nat Commun* **2021**, *12* (1), 6896. https://doi.org/10.1038/s41467-021-27210-x.

(249) Soucy, T. A.; Smith, P. G.; Milhollen, M. A.; Berger, A. J.; Gavin, J. M.; Adhikari, S.; Brownell, J. E.; Burke, K. E.; Cardin, D. P.; Critchley, S.; Cullis, C. A.; Doucette, A.; Garnsey, J. J.; Gaulin, J. L.; Gershman, R. E.; Lublinsky, A. R.; McDonald, A.; Mizutani, H.; Narayanan, U.; Olhava, E. J.; Peluso, S.; Rezaei, M.; Sintchak, M. D.; Talreja, T.; Thomas, M. P.; Traore, T.; Vyskocil, S.; Weatherhead, G. S.; Yu, J.; Zhang, J.; Dick, L. R.; Claiborne, C. F.; Rolfe, M.; Bolen, J. B.;

Langston, S. P. An Inhibitor of NEDD8-Activating Enzyme as a New Approach to Treat Cancer. *Nature* **2009**, *458* (7239), 732–736. https://doi.org/10.1038/nature07884.

(250) Lu, G.; Middleton, R. E.; Sun, H.; Naniong, M.; Ott, C. J.; Mitsiades, C. S.; Wong, K.-K.; Bradner, J. E.; Kaelin, W. G. The Myeloma Drug Lenalidomide Promotes the Cereblon-Dependent Destruction of Ikaros Proteins. *Science (1979)* **2014**, *343* (6168), 305–309. https://doi.org/10.1126/science.1244917.

(251) Sufan, R. I.; Ohh, M. Role of the NEDD8 Modification of Cul2 in the Sequential Activation of ECV Complex. *Neoplasia* **2006**, *8* (11), 956–963. https://doi.org/10.1593/neo.06520.

(252) Tuan M. Nguyen; Vedagopuram Sreekanth; Arghya Deb; Praveen Kokkonda; Praveen K. Tiwari; Katherine A. Donovan; Veronika Shoba; Santosh K. Chaudhary; Jaron A. M. Mercer; Sophia Lai; Ananthan Sadagopan; Max Jan; Eric S. Fischer; David R. Liu; Benjamin L. Ebert; Amit Choudhary. Proteolysis Targeting Chimeras With Reduced Off-Targets. *bioRxiv preprint* **2023**.

(253) Bashore, F. M.; Foley, C. A.; Ong, H. W.; Rectenwald, J. M.; Hanley, R. P.; Norris-Drouin, J. L.; Cholensky, S. H.; Mills, C. A.; Pearce, K. H.; Herring, L. E.; Kireev, D.; Frye, S. V.; James, L. I. PROTAC Linkerology Leads to an Optimized Bivalent Chemical Degrader of Polycomb Repressive Complex 2 (PRC2) Components. *ACS Chem Biol* **2023**. https://doi.org/10.1021/acschembio.2c00804.

(254) Kakugawa, S.; Langton, P. F.; Zebisch, M.; Howell, S. A.; Chang, T.-H.; Liu, Y.; Feizi, T.; Bineva, G.; O'Reilly, N.; Snijders, A. P.; Jones, E. Y.; Vincent, J.-P. Notum Deacylates Wnt Proteins to Suppress Signalling Activity. *Nature* **2015**, *519* (7542), 187–192. https://doi.org/10.1038/nature14259.

(255) Narayanan, A.; Jones, L. H. Sulfonyl Fluorides as Privileged Warheads in Chemical Biology. *Chem Sci* **2015**, *6* (5), 2650–2659. https://doi.org/10.1039/C5SC00408J.

(256) Remsberg, J. R.; Suciu, R. M.; Zambetti, N. A.; Hanigan, T. W.; Firestone, A. J.; Inguva, A.; Long, A.; Ngo, N.; Lum, K. M.; Henry, C. L.; Richardson, S. K.; Predovic, M.; Huang, B.; Dix, M. M.; Howell, A. R.; Niphakis, M. J.; Shannon, K.; Cravatt, B. F. ABHD17 Regulation of Plasma Membrane Palmitoylation and N-Ras-Dependent Cancer Growth. *Nat Chem Biol* **2021**, *17* (8), 856–864. https://doi.org/10.1038/s41589-021-00785-8.

(257) Morris, G. M.; Huey, R.; Lindstrom, W.; Sanner, M. F.; Belew, R. K.; Goodsell, D. S.; Olson, A. J. AutoDock4 and AutoDockTools4: Automated Docking with

Selective Receptor Flexibility. *J Comput Chem* **2009**, *30* (16), 2785–2791. https://doi.org/10.1002/jcc.21256.

(258) Wang, J.; Wolf, R. M.; Caldwell, J. W.; Kollman, P. A.; Case, D. A. Development and Testing of a General Amber Force Field. *J Comput Chem* **2004**, *25* (9), 1157–1174. https://doi.org/10.1002/jcc.20035.

(259) Somovilla, V. J.; Bermejo, I. A.; Albuquerque, I. S.; Martínez-Sáez, N.; Castro-López, J.; García-Martín, F.; Compañón, I.; Hinou, H.; Nishimura, S.-I.; Jiménez-Barbero, J.; Asensio, J. L.; Avenoza, A.; Busto, J. H.; Hurtado-Guerrero, R.; Peregrina, J. M.; Bernardes, G. J. L.; Corzana, F. The Use of Fluoroproline in MUC1 Antigen Enables Efficient Detection of Antibodies in Patients with Prostate Cancer. *J Am Chem Soc* **2017**, *139* (50), 18255–18261. https://doi.org/10.1021/jacs.7b09447.

(260) Krippendorff, B.-F.; Neuhaus, R.; Lienau, P.; Reichel, A.; Huisinga, W. Mechanism-Based Inhibition: Deriving K_I and k_{inact} Directly from Time-Dependent IC_{50} Values. *J Biomol Screen* **2009**, *14* (8), 913–923. https://doi.org/10.1177/1087057109336751.

(261) Cavaco, M.; Pérez-Peinado, C.; Valle, J.; Silva, R. D. M.; Correia, J. D. G.; Andreu, D.; Castanho, M. A. R. B.; Neves, V. To What Extent Do Fluorophores Bias the Biological Activity of Peptides? A Practical Approach Using Membrane-Active Peptides as Models. *Front Bioeng Biotechnol* **2020**, *8*. https://doi.org/10.3389/fbioe.2020.552035.

7

Annexes

7. Annex

7.1 Annex 1 - Full list of serine hydrolases detected by chemical proteomics

Protein names	Abbreviation	Average H/L ratio		
		F10	R-PROTAC	C8
Abhydrolase domain-containing protein 16A	ABHD16A	0.91	0.87	0.81
Acylamino-acid-releasing enzyme	APEH	0.93	0.71	0.83
Acyl-protein thioesterase 1	LYPLA1	1.04	0.84	30.26
Acyl-protein thioesterase 2	LYPLA2	1.40	0.82	10.68
Alpha/beta hydrolase domain-containing protein 11	ABHD11	1.09	0.92	6.80
Alpha/beta hydrolase domain-containing protein 17A	ABHD17A	0.91		
Alpha/beta hydrolase domain-containing protein 17B	ABHD17B	0.86	0.72	1.48
Alpha-enolase	ENO1		0.02	
Cathepsin G	CTSG	0.85	0.92	1.08
Dipeptidyl peptidase 2	DPP2	0.89	0.70	1.13
Dipeptidyl peptidase 3	DPP3			
Dipeptidyl peptidase 8	DPP8	0.80	0.83	1.10
Dipeptidyl peptidase 9	DPP9	0.81	0.75	0.98
Fatty acid synthase	FASN	0.97	0.83	1.21
Isoamyl acetate-hydrolyzing esterase 1 homolog	IAH1			
Lysophospholipase-like protein 1	LYPLAL1	0.79	0.29	5.82
Lysosomal protective protein	CTSA	1.25	0.85	1.13
Lysosomal Pro-X carboxypeptidase	PRCP	0.73		
Lysosomal thioesterase PPT2	PPT2	0.72	0.81	1.00
Monoacylglycerol lipase ABHD12	ABHD12	0.89	0.95	0.89
Monoacylglycerol lipase ABHD6	ABHD6		0.94	16.37
Neutral cholesterol ester hydrolase 1	NCEH1	0.85	0.87	1.01
Phospholipase ABHD3	ABHD3			
Platelet-activating factor acetylhydrolase 2, cytoplasmic	PAFAH2	1.04	0.74	4.52
Platelet-activating factor acetylhydrolase IB subunit gamma	PAFAH1B3	0.93	0.93	0.83
Prolyl endopeptidase	PREP	0.91	0.82	1.04
Prolyl endopeptidase-like	PREPL	0.58	0.79	0.94
Protein phosphatase methylesterase 1	PPME1	0.95		0.81
Serine protease HTRA2, mitochondrial	HTRA2			
S-formylglutathione hydrolase	ESD	0.73	1.01	0.93
Testis-expressed sequence 30 protein	TEX30	0.84	1.11	1.05
Tripeptidyl-peptidase 2	TPP2	0.61	0.71	1.02

7.2 Annex 2 - Thesis papers

RSC Chemical Biology

ROYAL SOCIETY OF CHEMISTRY

PAPER

View Article Online
View Journal | View Issue

Cite this: *RSC Chem. Biol.*, 2020, **1**, 251

Structural and biophysical insights into the mode of covalent binding of rationally designed potent BMX inhibitors†

João D. Seixas,‡*[a] Bárbara B. Sousa,‡[ab] Marta C. Marques,[a] Ana Guerreiro,[a] Rui Traquete,[a] Tiago Rodrigues,[a] Inês S. Albuquerque,[a] Marcos F. Q. Sousa,[bc] Ana R. Lemos,[bc] Pedro M. F. Sousa,[bc] Tiago M. Bandeiras,[bc] Di Wu,[d] Shelby K. Doyle,[e] Carol V. Robinson,[d] Angela N. Koehler,[e] Francisco Corzana,[f] Pedro M. Matias[bc] and Gonçalo J. L. Bernardes*[ag]

Received 26th March 2020,
Accepted 21st August 2020

DOI: 10.1039/d0cb00033g

rsc.li/rsc-chembio

The bone marrow tyrosine kinase in chromosome X (BMX) is pursued as a drug target because of its role in various pathophysiological processes. We designed BMX covalent inhibitors with single-digit nanomolar potency with unexploited topological pharmacophore patterns. Importantly, we reveal the first X-ray crystal structure of covalently inhibited BMX at Cys496, which displays key interactions with Lys445, responsible for hampering ATP catalysis and the DFG-out-like motif, typical of an inactive conformation. Molecular dynamic simulations also showed this interaction for two ligand/BMX complexes. Kinome selectivity profiling showed that the most potent compound is the strongest binder, displays intracellular target engagement in BMX-transfected cells with two-digit nanomolar inhibitory potency, and leads to BMX degradation PC3 in cells. The new inhibitors displayed anti-proliferative effects in androgen-receptor positive prostate cancer cells that where further increased when combined with known inhibitors of related signaling pathways, such as PI3K, AKT and Androgen Receptor. We expect these findings to guide development of new selective BMX therapeutic approaches.

Introduction

Over recent years, the development of covalent kinase inhibitors has gained more traction both in academia and pharmaceutical industry.[1–3] Historically, irreversible covalent inhibitors were considered unsafe because of their lack of selectivity and concomitant undesired engagement of off-targets. However, these potential liabilities can be overcome and the development of covalent small molecule kinase inhibitors has recently seen renewed interest. Irreversible covalent inhibitors can display higher efficacy, since they achieve high target occupancy and a prolonged pharmacodynamic effect, depending on the *de novo* re-synthesis rate of the target protein.[4,5] Supporting the value and "renaissance" of covalent inhibitors, since October 2018 six kinase-targeting small molecule covalent inhibitors[6] were approved by the FDA for clinical use: the EGFR inhibitors Afatinib®, Neratinib®, Osimertinib® and Dacomitinib® and the BTK inhibitors Ibrutinib® and Acalabrutinib®.[7–11] However, not all kinases are accessible for covalent binding since the covalent bond formation depends on the nature and positioning of the target amino acid.[12–15] One such kinase of interest is the epithelial and endothelial tyrosine kinase, commonly known as bone marrow tyrosine kinase in chromosome X (BMX). BMX is a major member of the TEC family of non-receptor tyrosine kinases, together with ITK, TEC, BTK and TXK [reviewed in ref. 16 and 17]. TEC kinases are activated by many cell-surface receptor-associated signaling complexes and are recruited to the plasma membrane or specific micro-environments by a variety

[a] *Instituto de Medicina Molecular João Lobo Antunes, Faculdade de Medicina, Universidade de Lisboa, Avenida Professor Egas Moniz, 1649-028 Lisboa, Portugal. E-mail: gbernardes@medicina.ulisboa.pt, joaoseixas@medicina.ulisboa.pt*
[b] *Instituto de Tecnologia Química e Biológica António Xavier, Universidade Nova de Lisboa, Av. da República, EAN, 2780-157 Oeiras, Portugal*
[c] *IBET - Instituto de Biologia Experimental e Tecnológica, Av. da República, EAN, 2780-157 Oeiras, Portugal*
[d] *Department of Chemistry, University of Oxford, South Parks Road, Oxford, OX1 3QZ, UK*
[e] *David H. Koch Institute for Integrative Cancer Research, Massachusetts Institute of Technology, Cambridge, MA 02142, USA*
[f] *Departamento de Química, Universidad de La Rioja, Centro de Investigación en Síntesis Química, 26006 Logroño, Spain*
[g] *Department of Chemistry, University of Cambridge, Lensfield Road, Cambridge, CB2 1EW, UK. E-mail: gb453@cam.ac.uk*

† Electronic supplementary information (ESI) available: Methods and materials, supporting figures and tables, synthesis and characterisation including NMR spectra, and references. Two supporting videos are also available. See DOI: 10.1039/d0cb00033g

‡ These authors contributed equally.

of lipids and proteins. Through this mechanism, they are involved in signal transduction in response to a myriad of extracellular stimuli, including those mediated by growth-factor receptors, cytokine receptors, G-protein coupled receptors, antigen-receptors, integrins and death receptors. Moreover, TEC kinases regulate many of the major signaling pathways, such as those of PI3K, PKC, PLCγ, AKT, STAT3 and p21-activated kinase 1 (PAK1)[18,19] and are responsible for a variety of cell processes, including regulation of gene expression, calcium mobilization, actin reorganization/motility and survival/apoptosis.[16,17]

BMX is widely expressed in granulocytes, monocytes, cells of epithelial and endothelial lineages, as well as brain, prostate, lung and heart.[19–22] It is specifically involved in tumorigenicity, adhesion, motility, angiogenesis, proliferation and differentiation. Moreover, it has been found to be overexpressed in numerous cancer types, such as breast,[23–25] prostate,[26,27] colon[28] and cervical carcinoma,[29] which suggests that elevated levels of BMX increase cancer-cell survival. BMX is also required for stem-cell maintenance and survival[22] and its up-regulation provides a survival benefit to both primary tumors and cancer stem cells that are highly resistant to apoptosis and many chemotherapeutic agents.

Homozygous BMX knockout mice have a normal life span without any obvious altered phenotype, which suggests that therapies based on BMX inhibition might have few side effects[30] and although BMX is a key regulator it might not represent a fundamental effector. Therefore, by considering the existence of multiple downstream target proteins, the integration in multiple and diverse signaling pathways, and the fact that it regulates proliferation, migration and has an anti-apoptotic effect, BMX emerges as a potential target for multiple aspects of cancer therapy. Recent studies also highlighted that modulation of BMX activity sensitizes cells to therapeutic agents to improve response to chemotherapy DNA damaging agents or radiation. These studies show strong evidence that both direct inhibition of BMX and modulation of related pathways result in increased therapeutic efficacy.[28,31,32]

BMX-IN-1 is one of the most potent BMX inhibitors (IC_{50}: 8.0 nM) reported in the literature, which also binds to BTK with very high affinity (IC_{50}: 10.4 nM).[33] Like other BMX covalent inhibitors, it reacts with a cysteine residue (Cys496) in the ATP binding site. This residue is a unique occurrence found in the ATP binding pocket and is present in all five members of the TEC family kinase members. Therefore, by virtue of structural homology these compounds could also be covalent inhibitors of the other kinases in the TEC family.

In this study, we describe the discovery of **JS24–JS27**, which are among the most potent covalent inhibitors of BMX reported to date and possess topological pharmacophoric features not exploited in the BMX inhibitors' chemical space. We asserted the selectivity against a panel of 36 kinases that possess an equally placed cysteine or up- and downstream regulators of the BMX signaling pathway. We further demonstrated that the lead compounds have the potential to inhibit proliferation of androgen-receptor-positive prostate-cancer cells (LNCaP) and their inhibitory potential is enhanced in a co-treatment regimen with known PI3K, AKT and androgen receptor inhibitors (LY294002, AKT1/2 and Flutamide, respectively). As part of our efforts to explore this scaffold to identify regions of the molecule amenable to conjugation we also report the first X-ray structure of BMX with a covalent inhibitor as well as MD simulations on two complexes with this receptor, which provide insight into the mode of binding and will contribute towards the future development of inhibitors with improved efficacy and selectivity.

Results and discussion

Discovery of a single-digit nanomolar BMX inhibitor

To evaluate substituent tolerability at each position and to establish an optimal vector through positioning of different functionalities, a structure–activity relationship (SAR) study was used to establish the limitations of the tool chemotype **BMX-IN-1**. A total of 24 analogues were synthesized in an attempt to both enhance potency and optimize physicochemical properties within the allowable SAR study (Fig. S1, ESI†). Upon systematic evaluation, we found that analogues with substituents in position R^3 (Fig. 1a) of the quinoline moiety had only marginal effects on BMX inhibition Furthermore, any change of the electrophilic warhead (position R^1, Fig. 1a) for cysteine covalent ligation resulted in loss of potency as illustrated for instance by

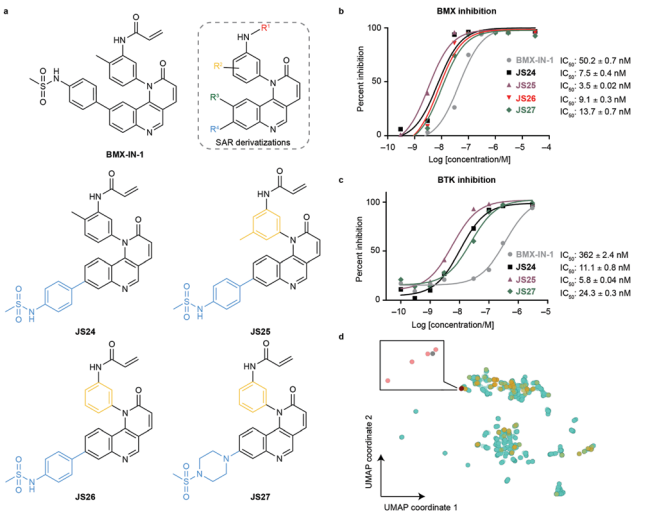

Fig. 1 Compound structures and biochemical characterization of their inhibitory effects on BMX and BTK. (a) The structures of **BMX-IN-1**, the SAR explored (shown in Fig. S1, ESI†) and **JS24–JS27** leads generated in this study. (b) Eurofins DiscoverX *in vitro* BMX activity evaluation by measuring the phosphorylation of a biotinylated peptide with human recombinant enzyme expressed in insect cells and HTRF detection method, tested in duplicate, showing mean ± S.D. Cells were treated for 1 h and IC_{50} values were calculated and plotted by using GraphPad Prism 8 based on a sigmoidal dose response curve. (c) Eurofins DiscoverX *in vitro* BTK activity evaluation by measuring scintillation count with a radiometric assay tested in duplicate, showing mean ± S.D. Cells were treated for 1 h and IC_{50} values were calculated and plotted by using GraphPad Prism 8 based on a sigmoidal dose response curve. (d) Projection of BMX and BTK inhibitor space with a multidimensional scaling algorithm. Green: BTK inhibitors; orange: BMX inhibitors; grey: **BMX-IN-1**; red: **JS24–J27**.

the introduction of the enamide substituents in **JS10** and **JS11** (Fig. S1, ESI†). The substituents in the aromatic ring bearing the amide functionality play an unexpected relevant role for the activity, affording different reactivity patterns arising from non-covalent interactions. Introducing a strong electron-donating group such as a methoxy group (OMe) (**JS9E**) in R^2 decreases potency by 4-fold. In contrast, the use of a weak electron-donating group, such as a methyl substituent, has different effects depending on the positioning. Thus, moving the methyl group to the ortho position abolishes target inhibition (**JS9C**), while a methyl positioning in the meta position slightly improved inhibition by 2-fold. Even more striking is the effect of no substituent in the ring (**JS9D**), which increased inhibition by 6-fold. Since the electronic influence of the methyl substituents in the different positions is not expected to account for these differences, we consider that a conformational effect may play an important role. The ortho substitution may increase the constraints for fitting into the pocket, while the removal of the methyl groups affords less spatial restriction.

Interestingly, substituents in position R^4 (Fig. 1a and Fig. S2, ESI†) were found to significantly enhance BMX inhibition relative to **BMX-IN-1** (Fig. 1a and Fig. S2, ESI†). With this SAR information in hand, we decided to prepare **JS24–JS27** that were designed to include substituents at position R^4 of the quinoline and incorporated features from previous analogues that afforded a preferred overall profile, varying methyl positioning in R^2 and retaining the acrylamide electrophilic warhead for cysteine covalent binding. Details for the synthesis of **JS24–JS27** can be found in the ESI† (Schemes S1–S4). Compound **JS24**, which features a methyl sulfonamide at position 7, showed considerable gain of inhibition potency from IC_{50} 50 to 7.5 nM relative to the parent molecule **BMX-IN-1** (Fig. 1a and b). Further derivatives that presented changes in the aniline core (R^2) with a methyl in the *meta* position (**JS25**) and without any substituent in this position (**JS26**), but that features the same methyl sulfonamide at R^4, were designed and prepared. Both compounds showed significantly improved activity (IC_{50} of 3.5 and 9.1 nM, respectively; Fig. 1a and 1b).

Similarly, in **JS27** we installed a substituted piperazine in the R^4 position that affords less restraint relative to the aromatic phenyl-sulfonamide ring, but which renders it the least active analogue of the series (13.7 nM) albeit considerably more potent ($\approx$4-fold) relative to **BMX-IN-1** (Fig. 1a and b).

Modulation of physicochemical profile, BTK inhibition and pharmacophore diversity

Taking into account that **BMX-IN-1** does not exhibit an optimal physicochemical profile, we aimed at lowering the lipophilicity and increasing water solubility within the established SAR. Initial investigations showed an improved profile when the sulfonamide aromatic ring was replaced by cyclic aliphatic amines (Table S1, ESI†). These observations prompted us to use 1-(methylsulfonyl)-piperazine in compound **JS27**. Consequently, we were able to obtain the analogue with the best *in silico* lipophilicity and water solubility profile ($c\log P = 2.32$ and $\log S = -4.36$; Table S1, ESI†). Interestingly, compound **JS26** shows a slightly improved reduction of $c\log P$. The presence of a methyl group (compounds **JS24** and **JS25**) increases hydrophobicity and, consequently, removal of this group (**JS26–JS27**) decreases the hydrophobicity and the partition coefficient.

We anticipated that some analogues could have limited membrane permeability, which is of utmost importance for any drug, in particular if a molecule is targeting cytoplasmic proteins. For assessment of drug permeability, we relied on parallel artificial membrane permeability assay (PAMPA) performed at Pion Inc. with the PAMPA Evolution™ instrument (Table S1, ESI†). We observed that compounds **JS24** (6.8×10^{-6} cm s^{-1}) and **JS25** (3.8×10^{-6} cm s^{-1}) show a lower PAMPA permeability relative to **BMX-IN-1** (8.9×10^{-6} cm s^{-1}), whereas compounds with the unsubstituted backbone aniline (**JS26** and **JS27**) show increased permeability (19×10^{-6} cm s^{-1} and 12×10^{-6} cm s^{-1}, respectively). As shown in Fig. 1a, the four leads share a similar scaffold and only compound **JS27** displays a distinct structural feature. Because other analogues display similar $c\log P$ values with improved PAMPA permeability (up to 45×10^{-6} cm s^{-1}; Table S1, ESI†), the observed increased permeability may be mostly a result of intramolecular interactions, such as hydrogen bonding, more than the lipophilic contribution, because the algorithm for $c\log P$ calculation does not consider 3D conformations. In addition, we measured particle sizes by using dynamic light scattering (DLS). Up to 95% of false positive readouts in high-throughput screens originate from colloidal aggregation.[34] This phenomenon is driven by the physicochemical properties of the small molecule and buffer conditions. Generally, aggregates bind non-specifically to proteins, sequestering and denaturating them. Our data shows that, regardless of their limited solubility, compounds **JS24–JS27** do not form aggregates at the relevant inhibitory concentrations, which rules out unspecific binding to BMX (Table S1, ESI†).

To date, all the reported BMX inhibitors also display the ability to inhibit Bruton's tyrosine kinase (BTK). To determine if our leads were selective binders of BMX, we evaluated inhibitory capacity of our compounds against BTK. For the BTK IC_{50} assay (KinaseProfiler by Eurofins DiscoverX), we selected **BMX-IN-1**, the two analogues with higher BMX inhibitory capacity (**JS24** and **JS25**) and **JS27**, which presents the best *in silico* physicochemical profile, and also offers the possibility of derivatization. The results showed that all the leads are also potent BTK inhibitors, in the low nanomolar range (Fig. 1c). The same inhibitory trend is observed with an increase of 62-, 33- and 15-fold potency gain with **JS25**, **JS24** and **JS27**, respectively, relative to **BMX-IN-1**. Interestingly, in this assay **BMX-IN-1** displays 7-fold higher IC_{50} against BTK than BMX.

We aimed to modulate the physicochemical properties of the molecules to enhance the overall "drug-likeness" profile of the ligands. Ligand efficiency (LE) and lipophilic efficiency (LipE) are two important metrics that are associated with improved prospects for good drug properties (*e.g.* bioavailability) and are used as criteria for progression of the most promising candidates across drug discovery pipelines.[35] LE is used to compare binding efficacy of inhibitors/ligands relative to their size, and LipE is used to compare binding efficacy by taking into

Table 1 Ligand efficiency and lipophilic efficiency of **BMX-IN-1** and **JS24–JS27** against BMX and BTK

Compound	LE (BMX)	LipE (BMX)	LE (BTK)	LipE (BTK)
BMX-IN-1	0.26	3.36	0.23	2.50
JS24	0.29	4.17	0.29	4.00
JS25	0.30	4.43	0.30	4.22
JS26	0.30	4.45	Nd	Nd
JS27	0.30	5.54	0.29	5.29

LE – ligand efficiency; LipE – lipophilic efficiency; Nd – not defined.

consideration the lipophilicity of the molecules. With regards to BMX inhibition, compound **JS27** displayed a major LipE improvement relative to **BMX-IN-1** (5.54 *versus* 3.36) empowered by the drastic reduction in $c\log P$ as a result of the introduction of the aliphatic sulfonamide. Analogues **JS24–JS26** displayed mild LipE improvement (4.17, 4.43 and 4.45), which is mainly due to their structural similarity with **BMX-IN-1**. However, the LE improvement is mostly driven by the increased potency of all analogues rather than a decrease in the molecules' size (Table 1). Similarly, the designed ligands offer a greater improvement of LE and LipE metrics with respect to BTK binding, relative to **BMX-IN-1**, driven also by a drastic potency gain.

Finally, we analyzed the pharmacophore diversity of the designed ligands against that of known BMX and BTK inhibitors. Ligand data was collected from ChEMBL v24, pre-processed as previously described[36] and projected to the plane by means of a learning algorithm (Fig. 1d). It is apparent that BTK has been more often interrogated with small molecules (green) and that the studied chemotypes are more diverse in regard to topological pharmacophore arrangements relative to previously described BMX modulators (blue). Compounds **JS24–JS27** (yellow) focus on unexplored regions in BMX inhibitor space but overlaps with previously studied BTK chemotypes. Indeed, our compounds have shown potent activities against BTK, which is fully in line with the output of the learning algorithm. Altogether, our data shows that compounds **JS24–JS27** explore a new chemical space and provides a rationale to re-investigate and potentially repurpose BTK inhibitors as leads for future development of BMX ligands and *vice versa*.

JS24–JS27 show strong binding interactions with BMX

We further characterized the binding interaction between **JS24–JS27** and BMX by using differential scanning fluorimetry (DSF) and surface plasmon resonance (SPR). Purified recombinant human BMX protein (hBMX) was first subjected to thermal scanning in the absence and presence of **JS24–JS27**, and the respective protein melting temperature (T_m) calculated. As shown in Table 2, **BMX-IN-1** increases the T_m value by 8.04 °C. Among the lead inhibitors, **JS24** displayed the highest stabilization, with an increase in Tm of 11.34 °C. Compounds **JS27** (10.81 °C), **JS26** (9.34 °C) and **JS25** (9.30 °C) showed high stabilization of the protein, which also suggests direct binding to BMX with a higher affinity relative to parent scaffold **BMX-IN-1** (Table 2 and Table S2, ESI†). The binding of **JS24–JS27** to BMX immobilized surfaces was then monitored in real-time by SPR assays (Table 2 and Fig. S3, Table S3, ESI†). **BMX-IN-1** was shown to bind to BMX with an affinity of K_D = 69 nM. It is important to note that it was not possible to accurately fit the dissociation rate constant of **BMX-IN-1** interaction with BMX because of the initial non-covalent binding event. In contrast, **JS24–JS27** K_D values could not be determined due to the even higher prolonged off-rates, which were outside the range of the instrument specifications. The results suggest that compounds **JS24–JS27** have higher affinity interactions with BMX, showing comparable association rates (k_{on} from 5.4×10^4–1.4×10^5 $M^{-1}s^{-1}$) but, most importantly, very slow dissociation rates ($k_{off} < 1 \times 10^{-4}$ s^{-1}), which is in agreement with the covalent nature of the interaction (Table 2).

JS24–JS27 displays greater irreversible binding efficacy relative to BMX-IN-1

The inactivation of BMX occurs in a two-step process that is governed by two parameters: the affinity of the initial non-covalent binding, K_I, and the rate of the subsequent covalent bond-forming reaction with the thiol of the cysteine residue, k_{inact}. The rate of inactivation (k_{inact}/K_I) is a second-order event, which describes the efficiency of covalent bond formation,.[37] Therefore, we evaluated the irreversible binding efficiency of our rationally designed compounds, as previously described.[38] The kinetic analysis presented in Table 3, reveals that compound **JS25** exhibits the best binding fit with the target, with an inhibition rate constant of 323 pM. This represents an increase in excess of 10-fold relative to **BMX-IN-1** (K_I: 4.07 nM). The other leads display a similar binding affinity among themselves (1.93–2.52 nM), lower than **JS25** and approximately 2-fold higher than **BMX-IN-1**. However, the rate of covalent bond formation of the bound inhibitor (determined by k_{inact}) shows that compounds **JS24**, **JS25**, and **JS26** showed slightly improved efficiency (0.335, 0.378 and 0.443 min^{-1}, respectively) in comparison to **BMX-IN-1** (0.217 min^{-1}) and **JS27** (0.166 min^{-1}). Consequently, the irreversible binding efficiency of **JS25**

Table 2 Melting temperature (T_m) shift calculated with a DSF assay and kinetic constants calculated from SPR

Compound	Aveg. T_m (°C)	apo-BMX T_m (°C)	ΔT_m (°C)	k_{on}/M^{-1} s^{-1}	k_{off}/s^{-1}	K_D/M
BMX-IN-1	60.17 ± 0.32	52.13 ± 0.11	8.04 ± 0.32	7.4×10^3	5.10×10^{-4}	6.9×10^{-8}
JS24	63.57 ± 0.01	52.23 ± 0.06	11.34 ± 0.01	1.4×10^5	$<1 \times 10^{-4}$	Nd[a]
JS25	61.43 ± 0.48	52.13 ± 0.11	9.30 ± 0.48	5.4×10^4	$<1 \times 10^{-4}$	Nd[a]
JS26	61.47 ± 0.21	52.13 ± 0.11	9.34 ± 0.21	7.2×10^4	$<1 \times 10^{-4}$	Nd[a]
JS27	62.94 ± 0.06	52.13 ± 0.11	10.81 ± 0.06	9.9×10^4	$<1 \times 10^{-4}$	Nd[a]

Nd – not determined. [a] K_D not measured due to very prolonged off-rates (outside instrument specifications).

Table 3 Determination of the kinetic parameters K_I, k_{inact}, k_{inact}/K_I[a]

Compound	K_I [nM]	k_{inact} [min^{-1}]	k_{inact}/K_I [μM^{-1} s^{-1}]
JS25	0.32 ± 0.05	0.378 ± 0.034	19.4 ± 1.55
JS26	1.93 ± 0.18	0.443 ± 0.003	3.86 ± 0.34
JS24	2.52 ± 0.01	0.335 ± 0.001	2.22 ± 0.01
JS27	2.15 ± 0.13	0.166 ± 0.003	1.29 ± 0.10
BMX-IN-1	4.07 ± 0.06	0.217 ± 0.005	0.89 ± 0.20[b]

[a] Results tested in duplicate, showing mean ± S.D. [b] Value with a 0.06 μM^{-1} s^{-1} deviation from published results.[38]

(19.4 μM^{-1} s^{-1}) is the highest of the series, whereas **BMX-IN-1** shows the lowest result (0.89 μM^{-1} s^{-1}) relative to the remaining inhibitors. Overall, these results provide quantitative evidence that the improved activity is mostly driven by changes in the binding complementarity between the compound and target rather than faster rate of covalent binding. Thus, taking into account that all the analogues have the same Michael acceptor moiety, the enhanced activity must be a result of the structural modifications introduced in the scaffold.

JS24 covalently modifies cysteine 496 in BMX

Mass spectrometry (MS) studies confirmed the covalent binding of **JS24** at cysteine 496 of BMX. The truncated hBMX was analyzed by native MS and the protein mass found was 30899 Da (Fig. 2a). The protein was then treated with 2.5 mM of **JS24** at room temperature for 30 min in PBS pH 7.4 and directly analyzed by denaturing MS. The protein was fully denatured and cleaned on a reverse phase column, discarding any non-specific binding, to retain only any covalently linked compound. The mass found upon incubation with **JS24** is 31 424 Da, which is 525 Da larger than the apo-form of hBMX (Fig. 2b). This result suggests covalent conjugation of a single molecule of **JS24** to hBMX. Furthermore, MS/MS analysis after digestion of the drug conjugated hBMX indicates the covalent modification at cysteine residue 496 (Fig. 2c).

The first X-ray structure of BMX with covalent inhibitor

To characterize the inhibition mechanism and binding mode of **JS24** to BMX at the atomic level, we tested a variety of commercial crystallization screens to obtain a protein crystal suitable for X-ray diffraction. Crystals were grown through co-crystallization of BMX protein at a final concentration of 10 mg mL^{-1}, with a 2-fold molar excess concentration of inhibitor **JS24**, in a lead condition that consists of 0.2 M imidazole-malate buffer, pH 5.5, and 42% v/v PEG 600. The X-ray crystal structure of BMX in complex with inhibitor **JS24** was determined at 2.0 Å resolution (PDB ID: 6I99) with a well-defined electron density map around the BMX ATP binding pocket in which the inhibitor is bound (Fig. 3a). The values of the equivalent isotropic atomic displacement parameters for the ligand atoms within the pocket are comparable to those of the protein atoms they are interacting with, an indication of full ligand occupancy of the binding site. Not surprisingly, an increase is observed in the sulfonamide aromatic ring because this group is more exposed to the solvent and hence more mobile.

The crystal structure shows the expected covalent binding between the acrylamide warhead and Cys496. Other major interactions of the inhibitor with the enzyme active site are mediated through hydrogen bonds between the nitrogen in the quinoline ring and Ile492, and between the Lys445 and the oxygen located in the fused pyridinone ring (Fig. 3b). The hydrogen bond between **JS24** and Lys445 is actually one of the key points to regulate BMX activity. The conserved β3 Lys interacts with αC-helix Glu residue to form a salt bridge required for ATP catalysis. The binding of **JS24** to Lys445 alters this interaction between the β3 Lys and the αC-helix Glu and consequently inactivates BMX. The aromatic rings of **JS24** are engaged in CH/π interactions with the side chains of Tyr491, Ala443, Val431, and Leu543 (Fig. S4, ESI†). Compound **JS24** is further stabilized by a hydrogen bond between a water molecule (W1) and the carbonyl oxygen of the acrylamide group. A second water molecule (W2) stabilizes the first (W1) through a hydrogen bond, and forms hydrogen bonds with the peptide nitrogen of Cys496 and the terminal amide group of Asn499 (Fig. 3b).

The crystal structure also shows that the DFG-motif adopts an out-like conformation (Fig. 3c) in which the Asp554 side chain is positioned in the back cleft, away from the ATP binding pocket, and the Phe555 aromatic ring points up into the gatekeeper region blocking the β3 Lys445-αC Glu460 ion pair formation. Both the activation loop and the DFG-out-like conformation are similar to what is observed in the only reported BMX crystal structure with non-covalent inhibitors Dasatinib and PP2.[39] The positioning of the BMX DFG-motif is reminiscent of an inactive conformation or DFG-out, typically found in BTK and other kinases inactive structures,[40] and it is also commonly observed in type II inhibitor complexes.[41] In the apo-BTK (PDB: 3P08), the DFG-in Asp539 rotates towards the ATP binding pocket to chelate magnesium and the DFG-in Phe540 is positioned in the back cleft to allow the formation of the β Lys430-αC Glu445 ion pair, which is important for catalysis. In BMX/**JS24** complex the DFG-out-like Asp554 points down and away from the ATP binding pocket and the Phe555 swings up to block the ion pair formation (Fig. 3d). However, relative to the DFG-out-like structure in BMX/**JS24** complex with a BTK DFG-out structure (PDB: 3PIY), both structures display complete rotation of the DFG-aspartate residue away from the

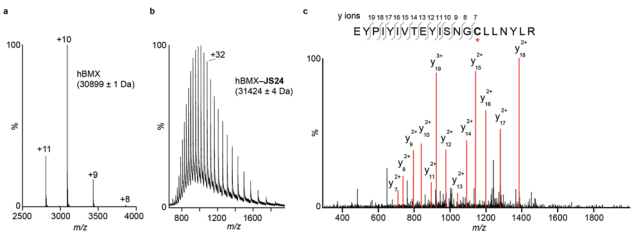

Fig. 2 Mass spectrometric analysis of BMX and **JS24** conjugated to BMX. (a) Native MS analysis of hBMX. The measured molecular weight is indicated. (b) Denaturing MS analysis of drug-conjugated hBMX. The measured molecular weight is indicated. (c) Tandem MS analysis of the drug conjugated tryptic peptide of hBMX labelled on the sequence (top) and MS/MS mass spectrum (bottom). The red asterisk indicates the Cys site to which **JS24** is covalently linked.

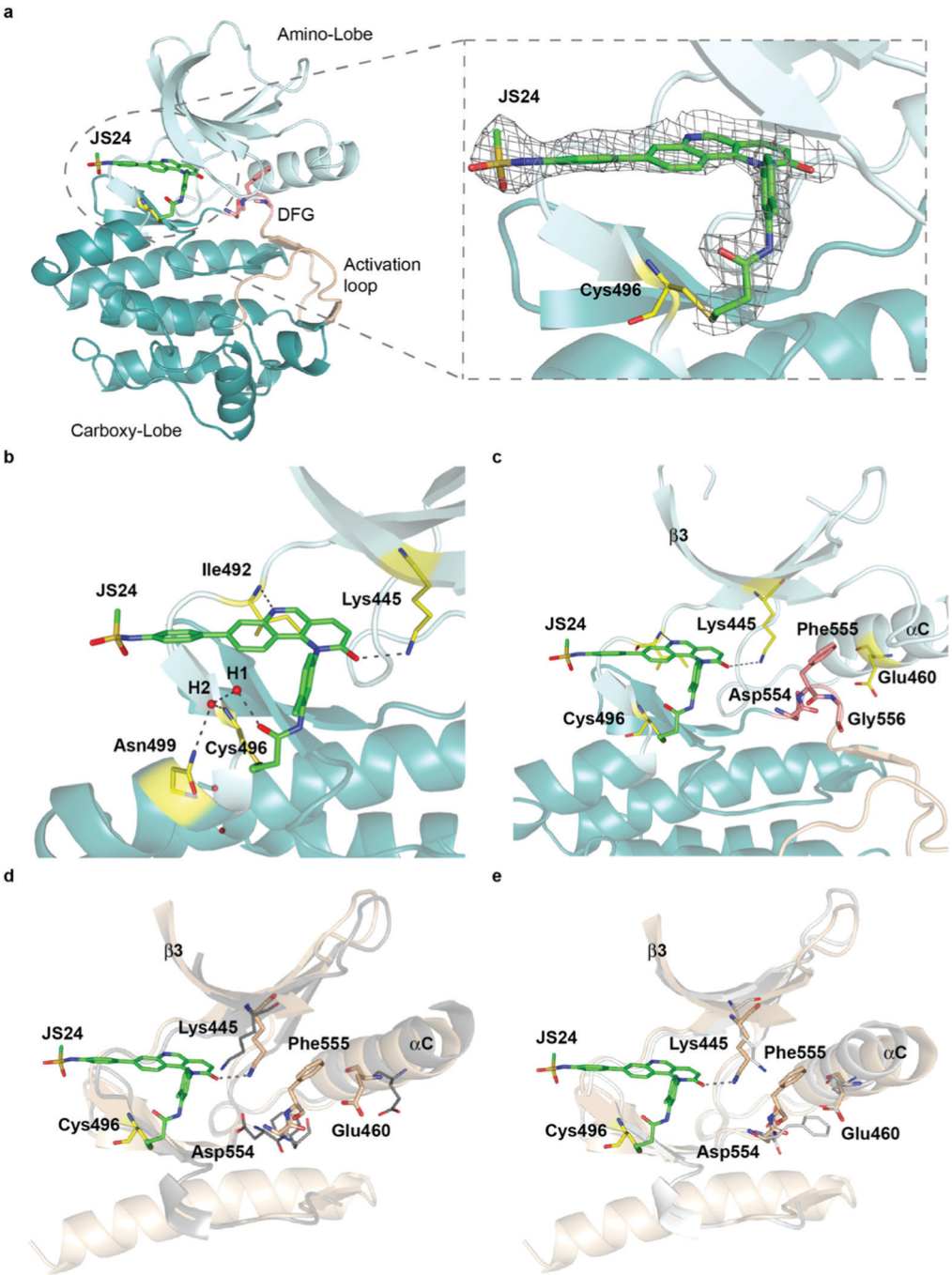

Fig. 3 Crystal structure of the BMX-**JS24** complex (a). Representation of the co-crystal structure of BMX catalytic domain in complex with **JS24** (PDB code 6I99). The panel shows the well-defined electron density around the inhibitor, which is bound to BMX ATP binding pocket through a covalent bond with a cysteine residue (Cys496). (b) Non-bonding interactions of **JS24** in the ATP binding pocket. (c) BMX DFG-motif adopting the out-like conformation. (d) Analysis of the BMX-DFG$^{out\text{-}like}$ motif conformation and BTK DFG^{in}. (e) Analysis of the BMX DFG$^{out\text{-}like}$ conformation with BTK DFG^{out}.

ATP binding pocket. Only the BTK DFG-out Phe540 residue rotates away from the core of the protein and towards the ATP binding pocket to create a back pocket capable of accepting an aromatic moiety (Fig. 3e).

Finally, the positioning of the sulfonamide aromatic ring is also of utmost importance. This group does not interact with any important residue and it is in fact pointing out of the ATP pocket (Fig. S4, ESI†). Interestingly, this feature would allow for the installation of a linker or chemical handle in this region of the molecule without altering significantly the inhibitor binding capacity of the lead compound.

Molecular dynamics (MD) simulations on BMX covalently linked to JS24 and JS27

We performed then 0.5 μs MD simulations on BMX covalently linked to **JS24** (Fig. 4a and b). Computational details can be

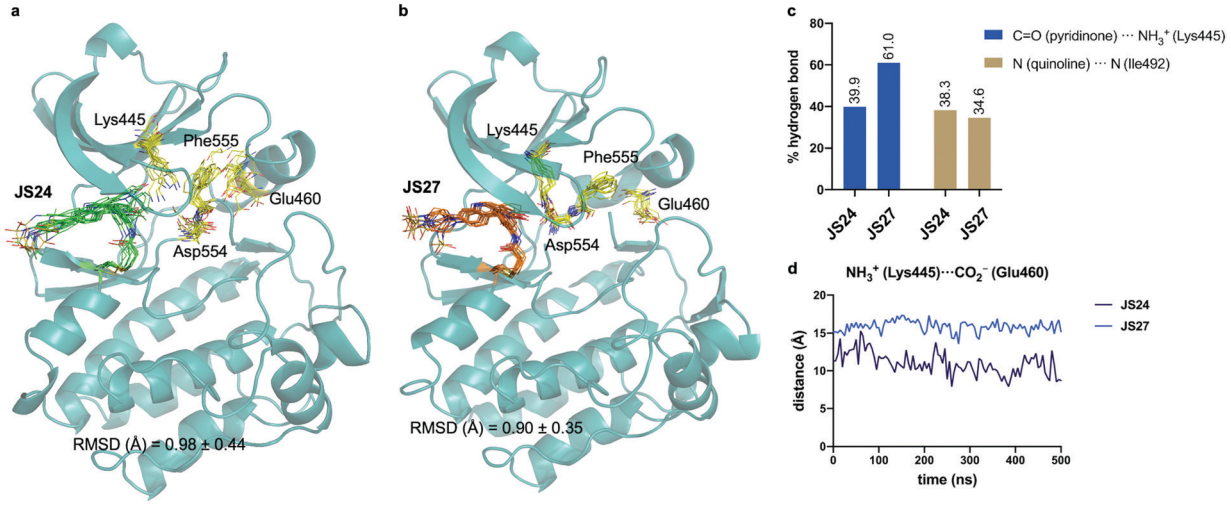

Fig. 4 (a and b) Structural ensembles derived from 0.5 μs MD simulations on BMX covalently linked to **JS24** and **JS27**. (c) Population of the most relevant hydrogen bonds between the ligands and BMX derived from the MD simulations. (d) Evolution of the Lys445–Glu460 distance along the MD simulations of both complexes. See also Videos 1 and 2 (ESI†). **JS24**, **JS27**, Lys445, Glu460, Asp554 and Phe555 are shown as sticks. The protein is shown as ribbons and only the first conformer (time = 0 ns) is shown for clarity.

found in the ESI.† According to these calculations, the binding mode found in the X-ray structure is retained in solution. Both hydrogen bonds releveled by the crystallographic studies, one between the backbone of Ile492 and the nitrogen atom of the quinoline and the other one between the side chain of Lys445 and the carbonyl oxygen of the quinoline ring, are populated in the complex (Fig. 4c). Also, as it occurs in the X-ray structure, **JS24** is engaged in CH/π interactions with the side chains of Val431, Ala443, Tyr491 and Leu543 (Fig. S5, ESI†). The MD calculations show that the DFG-motif also adopts an out-like conformation in solution (Fig. 4a). Thus, Phe555 precludes the ion pair formation between Lys445 and Glu460, which is supported by the distance between the side chains of Lys455 and Glu460 (Fig. 4d). Asp554 side chain is located away from the ATP binding pocket (Fig. 4a). The good agreement between the X-ray and the structure proposed by the simulations prompted us to propose a 3D-model for BMX linked to ligand **JS27**. To this purpose, **JS27** covalently linked to Cys496 was superimpose on the X-ray structure of the BMX/**JS24** complex. and used as starting structure in the simulations. The simulations show that **JS27** adopts a similar pose in the binding site than **JS24** (Fig. 4b). Thus, **JS27** is engaged in the same hydrogen bonds with the receptor as in BMX/**JS24** complex, with populations close to 61.0% and 34.6% for the interactions involving Lys445 and Ile492, respectively. The aromatic system of the ligand interacts with the hydrophobic residues Val431, Ala443, Tyr491 and Leu543 through hydrophobic interactions (Fig. S5, ESI†). As in BMX/**JS24** complex, the binding of **JS27** impedes the ion pair Lys445-Gl460 formation (Fig. 4d). Significantly, in both complexes, the sulfonamide group of the ligands does not stablish any contact with the receptor and is exposed to the solvent.

JS25 is a selective TEC family inhibitor

Most of BMX inhibitors reported to date offer poor selectivity because they are both BMX and BTK inhibitors. Their cellular effect is often attributed to off-target activity either upstream or downstream of BMX signaling pathways. To investigate in which targets the new inhibitors could have an effect we tested potent inhibitor **JS25** against a panel of 36 BMX-related kinases in the Eurofins DiscoverX's KINOMEscan™ platform at a concentration of 1 μM.

It is important to note that from the extensive number of accessible cysteine residues distributed across the whole kinome not all are available for covalent modification.[12–14] BMX belongs to a restricted group that includes 10 other kinases that share an equivalently placed cysteine in the ATP binding pocket. This group comprises members from the TEC family (BTK, ITK, TXK and TEC), the EGFR family (EGFR, Her2, Her4), JAK3, BLK and dual specificity mitogen-activated protein kinase 7 (MAP2K7). Therefore, we included the whole TEC, EGFR and JAK family in our screening, and the Src family and Lkb1, which also have a cysteine within the same sequence alignment. We also included kinases involved in upstream (Src, FAK, PI3K, mTOR, PDK1) and downstream (Akt, PAK1, TAM) regulation of BMX signaling pathway and non-receptor tyrosine protein kinase Abl. The KinomeScan platform is a binding assay and the screening showed that **JS25** displays a strong binding affinity against all the members of TEC family that share an equivalently placed cysteine and within these, higher affinity is observed towards BMX, BTK and TEC (Table 4).

As stated above, the TEC family has high sequence similarity and in particular residues in the ATP binding kinase domain share 40–65% identity and 60–80% similarity. The ATP binding sites are also highly conserved between the TEC and Src families with 14 identical residues out of 18 that comprise the ATP binding pocket. More specifically, BMX shares a 57% similarity to Src and most importantly, one of the key determinants of kinase selectivity – the gatekeeper residue – is a Thr in both the Src family and the TEC family members except ITK.[39] It is therefore not surprising that **JS25** also binds Blk (and JAK3) whereas no affinity was observed with other potential targets.

Table 4 Kinase selectivity of **JS25** over 36 BMX-related kinases in the KINOMEscan™ platform. The results for primary screen binding interactions at 1 μM concentration are reported as % DMSO control

Family	Target	% Ctrl	Family	Target	% Ctrl
TEC	BMX	1.3	Src	FYN	99
	BTK	0		SRC	92
	ITK	4.7		YES1	85
	TEC	0.4		BLK	16
	TXK	3.4		FGR	93
EGFR	EGFR	87		LCK	80
	ERBB2	89		HCK	95
	ERBB3	91		LYN	100
	ERBB4	66	mTOR	MTOR	100
JAK	JAK1(JH1domain-catalytic)	93	Liver Kinase B1	STK11	52
	JAK2(JH1domain-catalytic)	81	Pkb	AKT1	100
	JAK3(JH1domain-catalytic)	21		AKT2	94
	TYK2(JH1domain-catalytic)	100		AKT3	99
FAK	PTK2	93	PAK1	PAK1	100
PI3K	PIK3CA	79	TAM	AXL	93
	PIK3CB	89		MERTK	89
	PIK3CG	64	Abl	ABL1-phosphorylated	100
	PIK3CD	100	PDPK1	PDPK1	92

These results reveal **JS25** as a selective probe for TEC kinases and suggest that any cellular activity mediated by **JS25** is probably a result of inhibition of any of the TEC kinases rather than any off-target inhibition of upstream and downstream BMX regulators.

Intracellular BMX inhibition and degradation by JS25

To validate target affinity and identification for **JS25**, we performed an intracellular target engagement kinase assay with HEK293 cells expressing NanoLuc®-BMX fusion vector with Promega's NanoBRET™ TE Intracellular Kinase Assay. The cell proliferation depends on BMX kinase activity that was used to monitor the cellular activity of the compounds (IC_{50}). As shown in Fig. 5a, the IC_{50} determination showed the inhibitory capacity of **JS25** (IC_{50}: 44.8 nM) is 10 times greater than **BMX-IN-1** (IC_{50}: 495 nM), which aligns with the previous observations of an increased biochemical potency with similar activity difference. We next investigated whether the treatment of wild-type PC3 cells with **JS25**, as well as **BMX-IN-1** (as a control), would induce degradation of BMX. After 24 and 72 h, it was possible to verify that the level of expressed BMX protein in PC3 cells decreased upon treatment with **JS25** as well as with the control molecule (Fig. 5b and Fig. S11, ESI†). This data indicates that **JS25** is able both inhibit catalytic activity and degrade BMX it in cells.

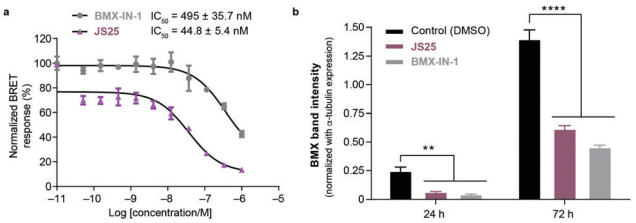

Fig. 5 (a) Intracellular target engagement in HEK293 cells transiently transfected with BMX expressing NanoLuc®-BMX fusion vector with Promega's NanoBRET™ TE Intracellular Kinase Assay. Assay performed at Reaction Biology Corporation (USA), with concentrations tested in duplicate, showing mean ± S.D. Cells were treated for 1 h and IC_{50} values were calculated and plotted by using GraphPad Prism 8 based on a sigmoidal dose response curve. (b) **JS25** (10 μM) and **BMX-IN-1** (10 μM) induce degradation of wild-type BMX in PC3 cells. Sampling was taken after 24 h and 72 h of incubation with **JS25** and **BMX-IN-1**. Band intensity was measured using ImageJ and normalized with α-Tubulin band intensity. Differences between groups were revealed through 2way-ANOVA. Data are mean ± standard deviation obtained from at least three independent measurements (n = 3). See ESI† for additional data and analysis.

Cancer cell growth inhibition by BMX inhibitors

The role of BMX in different pathologies is not yet fully validated. Nevertheless, it has been implicated in many regulatory mechanisms and despite the absence of a BMX dependent disease model, prostate cancer cell lines have been used to evaluate anti-proliferative effects of the inhibitors in a cellular context. In a previous experiment (unpublished results) we screened several inhibitors from Table S1 (ESI†) in a collection of cell lines representing prostate, brain, blood, breast, ovary, lung, bone marrow and lymphoid tumour tissues. Compounds were incubated with cells for 72 h in a 386 well-plate format to monitor dose-dependent impact on viable cell growth by using the CellTiter-Glo® luminescent assay, which quantifies ATP and the presence of metabolically active cells. The study included **JS24**, **BMX-IN-1** and the structurally similar compounds **JS10** and **JS11** which do not bind to BMX (Fig. S1 and Table S1, ESI†).

The results presented in Table 5 show that **JS10** and **JS11** (non-binders) have little or no effect on viable cell growth of the majority of the tested cell lines. **BMX-IN-1** demonstrated more potent inhibitory effects relative to **JS24** in the four prostate cancer cell lines that were included in the panel, 22RV1, PC3, LNCaP and DU145, particularly in those dependent on androgen receptor signaling (LNCaP and 22RV1). In contrast, androgen receptor negative cells (DU145 and PC3) were overall more resistant to treatment. In addition, **JS24** showed potent inhibitory effects against LNCaP and 22RV1 but also against PC3, which are androgen receptor negative cells. Furthermore, both compounds were also potent inhibitors of viable cell growth for

Table 5 Viable cell growth inhibition of compounds **BMX-IN-1**, **JS10**, **JS11** and **JS24** in a panel of prostate, brain, blood, breast, ovary, lung and lymphoid cancer cells[a]

Tissue	Cell line	BMX-IN-1	JS24	JS10	JS11
Prostate	LNCaP	1.81 ± 0.05	4.4 ± NC	9.7 ± NC	10.41 ± NC
	22 RV1	2.07 ± 0.06	6.66 ± 0.09	4.86 ± 0.11	7.3 ± NC
	PC3	10.98 ± 1.13	4.8 ± NC	ND	20.12 ± NC
	DU145	17.7 ± NC	ND	ND	ND
Brain	U-87MG	5.33 ± 0.19	5.04 ± 0.01	ND	ND
	SK-N-MC	2.36 ± NC	8.53 ± 0.44	11.19 ± NC	8.24 ± NC
Blood	Jurkat	5.99 ± NC	5.48 ± ND	9.71 ± 1.48	6.36 ± 0.17
	Kasumi	3.13 ± 0.06	5.12 ± 0.12	4.37 ± 0.04	10.14 ± 0.07
Breast	MDA-MB-231	23.61 ± 0.48	ND	ND	ND
Ovary	CAOV3	7.68 ± 0.13	8.56 ± NC	17.30 ± NC	19.31 ± NC
	OVCAR3	ND	ND	ND	ND
Bone marrow	H1299	ND	7.28 ± 0.37	19.42 ± NC	ND
Lung	RS4(11)	1.176 ± 0.06	2.09 ± NC	5.06 ± NC	6.66 ± NC
Lymphoid	DAUDI	1.68 ± 0.07	1.27 ± 0.05	2.57 ± 0.09	4.57 ± 0.12

[a] Viable cell growth was measured after 72 h incubation in 386 well-plate format. GI_{50} values were tested in triplicate and are reported as the mean ± SD in μM. ND, non-determined, no growth inhibition observed within the concentrations tested. NC, non-calculated. When ambiguous fit was observed curves were top (100%) and bottom (0%) constrained and GI_{50} was determined with 4-P least squares fit. In these cases, SD is not calculated by GraphPad Prism 8.

RS4 (11) (lymphoblast) and DAUDI (T-lymphoblast) cells, in which BTK is highly overexpressed. Altogether, these results demonstrate BMX inhibition impacts viable cell growth of prostate cancer cells and prompted us to investigate further the importance of the androgen receptor and related BMX pathways in these cell lines.

Androgen-receptor positive prostate-cancer cells are sensitive to JS24–JS27

Based on the results showed in the previous section, we tested the ability of compounds **JS24–JS27** to inhibit the proliferation of LNCaP and PC3 prostate cancer cell lines by using CellTiter-Glow®. The androgen-receptor negative PC3 cells are resistant to the treatment, with no significant anti-proliferative effect at the maximum concentration tested (10 μM). With androgen-receptor positive cells LNCaP a different profile was observed. **BMX-IN-1** and **JS24** showed a GI_{50} of 1.7 and 1.5 μM, respectively. Compound **JS27** was the least active (GI_{50} 9.3 μM), and **JS25** and **JS26** inhibited proliferation with a GI_{50} of 6.6 and 7.7 μM, respectively, as shown in Fig. 6.

To determine whether the growth inhibition was due to apoptosis, we carried out fluorescence-assisted cell sorting analysis with propidium iodide staining. LNCaP cells were incubated with **BMX-IN-1** and **JS24–JS27** for 64h, at 10 μM and results showed that no marked differences in the percentage of necrotic events relative to the vehicle control, which suggests that in these conditions these molecules do not enhance cell death (Fig. S6, ESI†). It is not surprising that all these compounds show only moderate proliferation inhibitory potential in prostate-cancer cell lines and it remains questionable whether modulation of BMX *per se* is relevant or not, towards anti-proliferative effects.[33] In fact, a large body of evidence in the literature shows that selective or dual BMX/BTK inhibitors have poor anti-proliferative effects in BMX-dependent models, most probably from dynamic compensation of signaling mechanisms. Focus has been placed on the modulation of BMX activity to

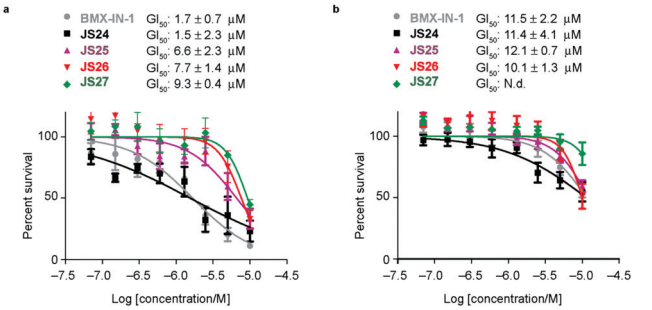

Fig. 6 Anti-proliferative activity of compounds **BMX-IN-1** and **JS24–JS27** against LNCaP (a) and PC3 (b) prostate-cancer cell lines. Briefly, proliferation in LNCaP and PC3 cells was measured after 96 h incubation, in 96-well plates with **BMX-IN-1** and **JS24–JS27**. GI_{50} values are reported in μM and are the mean of three individual experiments performed in triplicate. N.d., non-determined, no growth inhibition observed within the concentrations tested.

sensitize prostate-cancer cells to other therapeutic agents because anti-proliferative effects are only observed in combination with inhibitors of related pathways.[42] **BMX-IN-1** growth inhibition of RV-1 cells could only be potentiated with the Akt inhibitor MK2206;[33] ABT-737, a non-covalent inhibitor only induces apoptosis upon co-treatment with PI3K inhibitors;[28] the dual BMX/BTK inhibitor CTN06 requires co-treatment with autophagy inhibitor chloroquine (CQ) or docetaxel to inhibit PC3 cells growth[43] and a similar profile is observed with the dual BMX/Src inhibitor CTA095 to synergize with CQ and paclitaxel.[44]

The activation of BMX in response to PI3K signaling is just one of the mechanisms through which the levels of BMX become increased in prostate cancer.[43,45] A very recent study[46] showed that BMX expression in prostate cancer is suppressed directly through androgen receptor as a result of binding to BMX. Consequently, BMX expression rapidly increases in response to androgen deprivation therapy which enhances tyrosine kinase signaling and the subsequent emergence of castration-resistant

prostate cancer. This study further highlights the potential use of BMX inhibitors in combination therapy, in this case in combination with AR targeting. To further validate this hypothesis and assess the effect of our inhibitors with other drugs, we performed a co-treatment regimen with known inhibitors of related upstream and downstream pathways.

Co-treatment of LNCaP cells with JS24–JS26 and androgen receptor antagonist, PI3K and AKT inhibitors

As shown above, BMX inhibition alone induces limited cell death in BMX-expressed cell lines owing to the existence of compensatory mechanisms in signaling pathways. To evaluate whether our BMX inhibitors could potentially be used in combination treatment regimens, we sought to look at the synergistic anti-proliferative effects of BMX inhibitors when combined with other therapeutic agents, which pre-sensitize prostate cancer cells. For this purpose, LNCaP cells were co-treated in a combinatorial fashion with compounds **JS24–26**, **AKT1/2** (AKT inhibitor), **Flutamide** (androgen receptor antagonist) and **LY294002** (PI3K inhibitor). Cell viability was evaluated after 5 days with CellTiter-Glo® and compared with the overall anti-proliferative effects of the compounds alone. An optimization study was performed by screening several concentrations (Fig. S7, ESI†) to determine the ideal conditions to obtain initial viability above 80% with the individual inhibitors alone (Fig. S8, ESI†). Based on these results, we tested **JS24** (at 3 μM), **JS25** (5 μM) and **JS26** (6 μM) with **AKT1/2** (1 μM), **Flutamide** (50 μM) and **LY294002** (3 μM). Results are shown in Fig. 7.

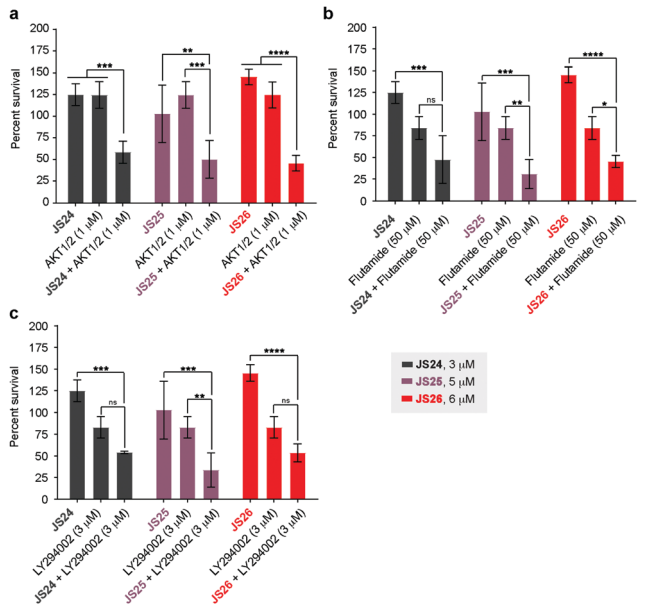

Fig. 7 Anti-proliferative activity in LNCaP cells of compounds **JS24–JS26** in combination with **AKT1/2** (AKT inhibitor), **Flutamide** (androgen receptor antagonist) and **LY293002** (PI3K inhibitor). (a) Cells co-treated with **JS24** (3 μM), **JS25** (5 μM) and **JS26** (6 μM) with **AKT1/2** (1 μM); (b) **JS24** (3 μM), **JS25** (5 μM) and **JS26** (6 μM) with **Flutamide** (50 μM); (c) **JS24** (3 μM), **JS25** (5 μM) and **JS26** (6 μM) with **LY294002** (3 μM). Values are reported in % cell viability normalized to DMSO controls and are the mean of three individual experiments performed in triplicate. Determined *P*-values are illustrated as ns ($P > 0.05$), * ($P \leq 0.05$), ** ($P \leq 0.01$), *** ($P \leq 0.001$) and **** ($P \leq 0.0001$).

Although the control concentrations of **JS24–26** and the inhibitors did not have an effect on reducing cell viability upon co-treatment, a marked viability decrease was observed in all tested conditions. With **AKT1/2** a decrease in cell viability ranging from 48% (with **JS24**) to 63% (with **JS26**) was observed, relative to control **AKT1/2**. With **Flutamide**, the most effective combination was with compound **JS25** (63% cell viability reduction) and the least effective with **JS24** (44% reduction). Finally, co-treatment with **LY294002** decreased cell viability by 35% (with **JS24** and **JS26**) and 59% (with **JS25**). Overall, these results demonstrate a synergistic effect between **JS24-26** and **AKT1/2**, **Flutamide** and **LY294002** in cancer cell proliferation capable of overcoming the compensatory mechanisms of BMX inhibition, and open the possibility of becoming useful molecules for drug combination approaches.

Conclusions

We explored a chemical scaffold that contains an archetypal tricyclic core of a quinoline with a fused pyridinone, which is present in BMX covalent inhibitor **BMX-IN-1**. We sought to introduce a chemical handle that may be used for further derivatization whilst simultaneously tuning the physicochemical properties. We found that rational modification introduced at the position 7 of the quinoline moiety leads to potent, single-digit nanomolar inhibition of BMX and BTK. Topological pharmacophoric features are outside the chemical space previously explored in BMX inhibition, and afford molecules with more favorable physicochemical profiles with a reduced *c* log *P* and increased permeability (**JS26** and **JS27**). We also unveiled the X-ray crystal structure of BMX with a covalent inhibitor (**JS24**), which shows the protein with the "DFG-out like" motif typical of an inactive conformation. The crystal structure also shows that the "tail substituent", opposite to the acrylamide warhead points outside the ATP pocket, which suggests an exit vector for further derivatizations. A comparable pose for ligands **JS24** and **JS27** were proposed by extensive MD simulations performed on the complexes with BMX.

We determined the rate of covalent modification and, to our knowledge, this is the highest value reported in the literature. The kinetic analysis showed that this is mostly driven from the potency of the first reversible binding event (K_I = 323 pM) and shows that our rational design afforded a preferred fit for the BMX binding pocket. In a cellular context, most potent compound **JS25** also showed low nanomolar potency in a target engagement assay (45 nM) in BMX-dependent cells (transfected HEK293) which is 10-fold superior to the reference ligand. Treatment of PC3 cells with **JS25** also led to degradation BMX. Furthermore, all lead compounds displayed anti-proliferative effects in androgen-receptor positive prostate cancer cells that where further increased when combined with known inhibitors of related signaling pathways, further highlighting the potential of combinatorial effects with BMX-related pathways.

As stated above, selectivity among members of the TEC family is hard to achieve. Interestingly, available data shows that therapeutically active drugs are not selective molecules.

Ibrutinib, developed as a covalent BTK inhibitor, has been approved by the FDA for the treatment of chronic lymphocytic leukemia, mantle cell leukemia (MCL) and Waldenström macroglobulinemia and is currently in multiple clinical trials because it has proved efficacy in different indications, such as non-small cell lung cancer and autoimmune diseases.[7,47,48] With a broad selectivity profile, Ibrutinib inhibits the whole TEC family, EGFR, JAK3, Her2, Blk and Itk kinases. Acalabrutinib, a second generation BTK inhibitor that was also granted FDA approval for MCL is more selective, and only inhibits BTK, TEC, BMX and TXK.[49] Other BTK inhibitors in clinical development (Spebrutinib, Zanubrutinib and Tirabrutinib) also display a broad selectivity for kinases with a cysteine as the Cys496 residue in BMX,[50] consequently, it is reasonable to extrapolate that the compounds developed here can become therapeutically useful as BMX inhibitors and find application in other TEC-related B-cell malignancies. The most potent compound **JS25** also has a multi-target profile and is active against all five TEC kinases, JAK3 and BLK. As such, we are currently evaluating the utility of these new molecules in B-cell related lymphocytic diseases where TEC-kinases play a prominent role.[17,51]

Conflicts of interest

J. D. S. and G. J. L. B. are inventors in a patent application related to the findings reported in this manuscript. Other authors declare no competing interests.

Acknowledgements

Funded under the Royal Society (URF to G. J. L. B., URF\R\180019), FCT Portugal (iFCT to G. J. L. B., IF/00624/2015, Postdoctoral Fellowship SFRH/BPD/95253/2013 to J. D. S., project PTDC/MED-QUI/28764/2017 to J. D. S., 02/SAICT/2017 grant 28333 to T. R., doctoral studentship SFRH/BD/143583/2019 to B. B. S., and DL 57/2016/CP1451/CT0025 to J. D. S.). This project has received funding from the European Union's Horizon 2020 research and innovation programme under grant agreements No. 807281 and 702428. The authors acknowledge the Wellcome Trust (104633/Z/14/Z, to D. W. and C. V. R.), Ministerio de Economía y Competitividad (project RTI2018-099592-B-C21 to F. C.), the Royal G. and Mae H. Westaway Family Memorial Fund (A. N. K.), National Science Foundation Graduate Research Fellowship (Grant No 1122374 to S. K. D.) and Ludwig Center at MIT's Koch Institute (S. K. D.). We also thank the High-Throughput Science Core at MIT supported by the Koch Institute Cancer Center Support Core Grant (P30-CA14051 to A. N. K.). The NMR spectrometers are part of the National NMR Facility, supported by Fundação para a Ciência e Technologic (RECI/BBB-BQB/0230/2012). The authors also thank ESRF and the ID30A-3 beamline staff for support with the X-ray data collection. iNOVA4Health – UID/Multi/04462/2013, a program financially supported by Fundação para a Ciência e Technologic/Ministério da Educação e Ciência, through national funds and co-funded by FEDER under the PT2020 Partnership Agreement, and MOSTMICRO (project LISBOA-01-0145-FEDER-007660) co-funded by FCT/MCTES and FEDER funds through COMPETE2020—Programa Operacional Competitividade e Internacionalização (POCI) are also acknowledged. The authors thank Dr Vikki Cantrill for her help with the preparation and editing of this manuscript.

Notes and references

1 J. Singh, R. C. Petter, T. A. Baillie and A. Whitty, *Nat. Rev. Drug Discovery*, 2011, **10**, 307–317.
2 Z. Zhao and P. E. Bourne, *Drug Discovery Today*, 2018, **23**, 727–735.
3 A. Chaikuad, P. Koch, S. A. Laufer and S. Knapp, *Angew. Chem., Int. Ed.*, 2018, **57**, 4372–4385.
4 T. Barf and A. Kaptein, *J. Med. Chem.*, 2012, **55**, 6243–6262.
5 R. Lagoutte, R. Patouret and N. Winssinger, *Curr. Opin. Chem. Biol.*, 2017, **39**, 54–63.
6 A. Abdeldayem, Y. S. Raouf, S. N. Constantinescu, R. Moriggl and P. T. Gunning, *Chem. Soc. Rev.*, 2020, **49**, 2617–2687.
7 L. A. Honigberg, A. M. Smith, M. Sirisawad, E. Verner, D. Loury, B. Chang, S. Li, Z. Pan, D. H. Thamm, R. A. Miller and J. J. Buggy, *Proc. Natl. Acad. Sci. U. S. A.*, 2010, **107**, 13075–13080.
8 J. C. Byrd, B. Harrington, S. O'Brien, J. A. Jones, A. Schuh, S. Devereux, J. Chaves, W. G. Wierda, F. T. Awan, J. R. Brown, P. Hillmen, D. M. Stephens, P. Ghia, J. C. Barrientos, J. M. Pagel, J. Woyach, D. Johnson, J. Huang, X. Wang, A. Kaptein, B. J. Lannutti, T. Covey, M. Fardis, J. McGreivy, A. Hamdy, W. Rothbaum, R. Izumi, T. G. Diacovo, A. J. Johnson and R. R. Furman, *N. Engl. J. Med.*, 2015, **374**, 323–332.
9 V. A. Miller, V. Hirsh, J. Cadranel, Y. M. Chen, K. Park, S. W. Kim, C. Zhou, W. C. Su, M. Wang, Y. Sun, D. S. Heo, L. Crino, E. H. Tan, T. Y. Chao, M. Shahidi, X. J. Cong, R. M. Lorence and J. C. Yang, *Lancet Oncol.*, 2012, **13**, 528–538.
10 J.-C. Soria, Y. Ohe, J. Vansteenkiste, T. Reungwetwattana, B. Chewaskulyong, K. H. Lee, A. Dechaphunkul, F. Imamura, N. Nogami, T. Kurata, I. Okamoto, C. Zhou, B. C. Cho, Y. Cheng, E. K. Cho, P. J. Voon, D. Planchard, W.-C. Su, J. E. Gray, S.-M. Lee, R. Hodge, M. Marotti, Y. Rukazenkov and S. S. Ramalingam, *N. Engl. J. Med.*, 2017, **378**, 113–125.
11 S. K. Rabindran, C. M. Discafani, E. C. Rosfjord, M. Baxter, M. B. Floyd, J. Golas, W. A. Hallett, B. D. Johnson, R. Nilakantan, E. Overbeek, M. F. Reich, R. Shen, X. Shi, H.-R. Tsou, Y.-F. Wang and A. Wissner, *Cancer Res.*, 2004, **64**, 3958–3965.
12 J. Zhang, P. L. Yang and N. S. Gray, *Nat. Rev. Cancer*, 2009, **9**, 28–39.
13 Q. Liu, Y. Sabnis, Z. Zhao, T. Zhang, S. J. Buhrlage, L. H. Jones and N. S. Gray, *Chem. Biol.*, 2013, **20**, 146–159.
14 Z. Zhao, Q. Liu, S. Bliven, L. Xie and P. E. Bourne, *J. Med. Chem.*, 2017, **60**, 2879–2889.
15 B. R. Lanning, L. R. Whitby, M. M. Dix, J. Douhan, A. M. Gilbert, E. C. Hett, T. O. Johnson, C. Joslyn,

J. C. Kath, S. Niessen, L. R. Roberts, M. E. Schnute, C. Wang, J. J. Hulce, B. Wei, L. O. Whiteley, M. M. Hayward and B. F. Cravatt, *Nat. Chem. Biol.*, 2014, **10**, 760–767.

16 C. I. Smith, T. C. Islam, P. T. Mattsson, A. J. Mohamed, B. F. Nore and M. Vihinen, *BioEssays*, 2001, **23**, 436–446.

17 N. J. Horwood, A. M. Urbaniak and L. Danks, *Int. Rev. Immunol.*, 2012, **31**, 87–103.

18 J. S. Jarboe, S. Dutta, S. E. Velu and C. D. Willey, *Recent Pat. Anticancer Drug Discovery*, 2013, **8**, 228–238.

19 Y. Qiu and H. J. Kung, *Oncogene*, 2000, **19**, 5651–5661.

20 X. Wen, H. H. Lin, H. M. Shih, H. J. Kung and D. K. Ann, *J. Biol. Chem.*, 1999, **274**, 38204–38210.

21 O. A. Guryanova, Q. Wu, L. Cheng, J. D. Lathia, Z. Huang, J. Yang, J. MacSwords, C. E. Eyler, R. E. McLendon, J. M. Heddleston, W. Shou, D. Hambardzumyan, J. Lee, A. B. Hjelmeland, A. E. Sloan, M. Bredel, G. R. Stark, J. N. Rich and S. Bao, *Cancer Cell*, 2011, **19**, 498–511.

22 J. Kaukonen, I. Lahtinen, S. Laine, K. Alitalo and A. Palotie, *Br. J. Haematol.*, 1996, **94**, 455–460.

23 R. Bagheri-Yarmand, M. Mandal, A. H. Taludker, R. A. Wang, R. K. Vadlamudi, H. J. Kung and R. Kumar, *J. Biol. Chem.*, 2001, **276**, 29403–29409.

24 K. Y. Chen, L. M. Huang, H. J. Kung, D. K. Ann and H. M. Shih, *Oncogene*, 2004, **23**, 1854–1862.

25 I. Cohen, M. Maoz, H. Turm, S. Grisaru-Granovsky, B. Maly, B. Uziely, E. Weiss, R. Abramovitch, E. Gross, O. Barzilay, Y. Qiu and R. Bar-Shavit, *PLoS One*, 2010, **5**, e11135.

26 B. Dai, H. Chen, S. Guo, X. Yang, D. E. Linn, F. Sun, W. Li, Z. Guo, K. Xu, O. Kim, X. Kong, J. Melamed, S. Qiu and Y. Qiu, *Cancer Res.*, 2010, **70**, 5587–5596.

27 B. Dai, O. Kim, Y. Xie, Z. Guo, K. Xu, B. Wang, X. Kong, J. Melamed, H. Chen, C. J. Bieberich, A. D. Borowsky, H. J. Kung, G. Wei, M. C. Ostrowski, A. Brodie and Y. Qiu, *Cancer Res.*, 2006, **66**, 8058–8064.

28 D. S. Potter, P. Kelly, O. Denneny, V. Juvin, L. R. Stephens, C. Dive and C. J. Morrow, *Neoplasia*, 2014, **16**, 147–157.

29 Y. Li, N. Cui, P. S. Zheng and W. T. Yang, *Oncotarget*, 2017, **8**, 49238–49252.

30 I. Rajantie, N. Ekman, K. Iljin, E. Arighi, Y. Gunji, J. Kaukonen, A. Palotie, M. Dewerchin, P. Carmeliet and K. Alitalo, *Mol. Cell. Biol.*, 2001, **21**, 4647–4655.

31 D. S. Potter, M. Galvin, S. Brown, A. Lallo, C. L. Hodgkinson, F. Blackhall, C. J. Morrow and C. Dive, *Mol. Cancer Ther.*, 2016, **15**, 1248–1260.

32 J. L. Fox and A. Storey, *Cancer Res.*, 2015, **75**, 1345–1355.

33 F. Liu, X. Zhang, E. Weisberg, S. Chen, W. Hur, H. Wu, Z. Zhao, W. Wang, M. Mao, C. Cai, N. I. Simon, T. Sanda, J. Wang, A. T. Look, J. D. Griffin, S. P. Balk, Q. Liu and N. S. Gray, *ACS Chem. Biol.*, 2013, **8**, 1423–1428.

34 D. Reker, G. J. L. Bernardes and T. Rodrigues, *Nat. Chem.*, 2019, **11**, 402–418.

35 M. M. Hann and G. M. Keserü, *Nat. Rev. Drug Discovery*, 2012, **11**, 355–365.

36 T. Rodrigues, M. Werner, J. Roth, E. H. G. da Cruz, M. C. Marques, P. Akkapeddi, S. A. Lobo, A. Koeberle, F. Corzana, E. N. da Silva Júnior, O. Werz and G. J. L. Bernardes, *Chem. Sci.*, 2018, **9**, 6899–6903.

37 J. M. Strelow, *SLAS Discovery*, 2016, **22**, 3–20.

38 B. Wang, Y. Deng, Y. Chen, K. Yu, A. Wang, Q. Liang, W. Wang, C. Chen, H. Wu, C. Hu, W. Miao, W. Hur, W. Wang, Z. Hu, E. L. Weisberg, J. Wang, T. Ren, Y. Wang, N. S. Gray, Q. Liu and J. Liu, *Eur. J. Med. Chem.*, 2017, **137**, 545–557.

39 J. Muckelbauer, J. S. Sack, N. Ahmed, J. Burke, C. Y. Chang, M. Gao, J. Tino, D. Xie and A. J. Tebben, *Chem. Biol. Drug Des.*, 2011, **78**, 739–748.

40 M. M. Sultan, R. A. Denny, R. Unwalla, F. Lovering and V. S. Pande, *Sci. Rep.*, 2017, **7**, 15604.

41 Z. Zhao, H. Wu, L. Wang, Y. Liu, S. Knapp, Q. Liu and N. S. Gray, *ACS Chem. Biol.*, 2014, **9**, 1230–1241.

42 J. L. Fox, F. Ismail, A. Azad, N. Ternette, S. Leverrier, M. J. Edelmann, B. M. Kessler, I. M. Leigh, S. Jackson and A. Storey, *EMBO J.*, 2010, **29**, 3853–3868.

43 W. Guo, R. Liu, G. Bhardwaj, J. C. Yang, C. Changou, A. H. Ma, A. Mazloom, S. Chintapalli, K. Xiao, W. Xiao, P. Kumaresan, E. Sanchez, C. T. Yeh, C. P. Evans, R. Patterson, K. S. Lam and H. J. Kung, *Cell Death Dis.*, 2014, **5**, e1409.

44 W. Guo, R. Liu, G. Bhardwaj, A. H. Ma, C. Changou, J. C. Yang, Y. Li, C. Feng, Y. Luo, A. Mazloom, E. Sanchez, Y. Wang, W. Huang, R. Patterson, C. P. Evans, K. S. Lam and H. J. Kung, *PLoS One*, 2013, **8**, e70910.

45 C. H. Chau, K. Y. Chen, H. T. Deng, K. J. Kim, K. Hosoya, T. Terasaki, H. M. Shih and D. K. Ann, *Oncogene*, 2002, **21**, 8817–8829.

46 S. Chen, C. Cai, A. G. Sowalsky, H. Ye, F. Ma, X. Yuan, N. I. Simon, N. S. Gray and S. P. Balk, *Cancer Res.*, 2018, **78**, 5203–5215.

47 C. S. Lee, M. A. Rattu and S. S. Kim, *J. Oncol. Pharm. Pract.*, 2016, **22**, 92–104.

48 B. Xia, F. Qu, T. Yuan and Y. Zhang, *Oncol. Lett.*, 2015, **10**, 3339–3344.

49 T. Barf, T. Covey, R. Izumi, B. van de Kar, M. Gulrajani, B. van Lith, M. van Hoek, E. de Zwart, D. Mittag, D. Demont, S. Verkaik, F. Krantz, P. G. Pearson, R. Ulrich and A. Kaptein, *J. Pharmacol. Exp. Ther.*, 2017, **363**, 240–252.

50 A. Kaptein, G. de Bruin, M. Emmelot-van Hoek, B. van de Kar, A. de Jong, M. Gulrajani, D. Demont, T. Covey, D. Mittag and T. Barf, *Blood*, 2018, **132**, 1871.

51 M. J. de Bruijn, J. Rip, E. K. van der Ploeg, L. W. van Greuningen, V. T. Ta, L. P. Kil, A. W. Langerak, G. F. Rimmelzwaan, W. Ellmeier, R. W. Hendriks and O. B. Corneth, *J. Immunol.*, 2017, **198**, 3058–3068.

ACS Pharmacology & Translational Science

pubs.acs.org/ptsci

Article

Selective Inhibition of Bruton's Tyrosine Kinase by a Designed Covalent Ligand Leads to Potent Therapeutic Efficacy in Blood Cancers Relative to Clinically Used Inhibitors

Bárbara B. Sousa, Cátia Rebelo de Almeida, Ana F. Barahona, Raquel Lopes, Ana Martins-Lograd, Marco Cavaco, Vera Neves, Luís A. R. Carvalho, Carlos Labão-Almeida, Ana R. Coelho, Marta Leal Bento, Ricardo M. R. M. Lopes, Bruno L. Oliveira, Miguel A. R. B. Castanho, Peter Neumeister, Alexander Deutsch, Gregory I. Vladimer, Nikolaus Krall, Cristina João, Francisco Corzana, João D. Seixas, Rita Fior, and Gonçalo J. L. Bernardes*

Cite This: https://doi.org/10.1021/acsptsci.2c00163

Read Online

ACCESS | Metrics & More | Article Recommendations | Supporting Information

ABSTRACT: Bruton's tyrosine kinase (BTK) is a member of the TEC-family kinases and crucial for the proliferation and differentiation of B-cells. We evaluated the therapeutic potential of a covalent inhibitor (JS25) with nanomolar potency against BTK and with a more desirable selectivity and inhibitory profile compared to the FDA-approved BTK inhibitors ibrutinib and acalabrutinib. Structural prediction of the BTK/JS25 complex revealed sequestration of Tyr551 that leads to BTK's inactivation. JS25 also inhibited the proliferation of myeloid and lymphoid B-cell cancer cell lines. Its therapeutic potential was further tested against ibrutinib in preclinical models of B-cell cancers. JS25 treatment induced a more pronounced cell death in a murine xenograft model of Burkitt's lymphoma, causing a 30−40% reduction of the subcutaneous tumor and an overall reduction in the percentage of metastasis and secondary tumor formation. In a patient model of diffuse large B-cell lymphoma, the drug response of JS25 was higher than that of ibrutinib, leading to a 64% "on-target" efficacy. Finally, in zebrafish patient-derived xenografts of chronic lymphocytic leukemia, JS25 was faster and more effective in decreasing tumor burden, producing superior therapeutic effects compared to ibrutinib. We expect JS25 to become therapeutically relevant as a BTK inhibitor and to find applications in the treatment of hematological cancers and other pathologies with unmet clinical treatment.

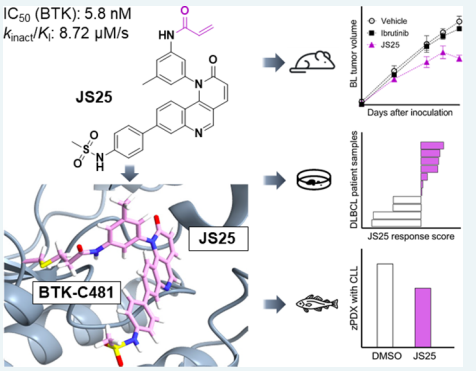

KEYWORDS: *covalent inhibitor, BTK, antitumor activity, preclinical studies, hematological cancers*

Bruton's tyrosine kinase (BTK) belongs to the TEC family of cytoplasmatic kinases and presents a functional cysteine in the 481 position prone to covalent binding.[1] BTK is expressed in many cells of the hematopoietic lineage, including B- and T-cells, monocytes, neutrophils, and mast cells.[1,2] Expression of this protein is essential for the development and function of mature B-cells, and inactivating mutations in the BTK gene cause primary immunodeficiency disease X-linked agammaglobulinemia in humans and X-linked immunodeficiency in mice.[3] Moreover, constitutive activation of BTK in systemic lupus erythematosus results in an accumulation of antibody-secreting plasma cells.[4] BTK is also a proximal component of the B-cell receptor, and it is activated by upstream Src-family kinases through intermediate signaling generated by PI3 kinase.[5,6] Once activated, BTK phosphorylates phospholipase-Cγ (PLCγ), leading to Ca^{2+} mobilization and activation of NF-κB and MAP kinase pathways, promoting proliferation and survival of B-cells.[7] BTK also induces the dependent proinflammatory production of cytokines IL-6 and IL-10[8,9] and controls integrin-mediated adhesion of B-cells[10] and their responses to chemokines, such as SDF-1.[11,12] Deregulation of BTK is observed in some autoimmune diseases[13,14] and in hematological cancers, including myeloid and B-lymphocytic leukemias (acute myeloid leukemia (AML), acute lymphocytic leukemia (ALL), chronic lymphocytic leukemia (CLL)), Waldenström's macroglobulinemia (WM), mantle cell lymphoma (MCL), Burkitt's lymphoma (BL), and diffuse large B-cell lymphoma (DLBCL), further indicating that BTK is an effective target for numerous pathologies.[1,15,16]

Received: August 16, 2022

Since its first description, multiple BTK inhibitors (BTKi) have been developed. The irreversible BTK inhibitor ibrutinib was the first FDA-approved BTKi and is associated with high response rates in relapsed/refractory CLL, WM, and MCL and in chronic graft *versus* host disease.[17,18] However, with a broad selectivity profile, ibrutinib inhibits the whole TEC family, EGFR, JAK3, Her2, Blk, and ITK kinases. Ibrutinib's "off-target" binding is usually associated with adverse effects such as rash, diarrhea, bleedings, infections, and atrial fibrillation, leading to treatment withdrawal in 9−23% of patients.[19] Ibrutinib can also antagonize rituximab-induced antibody-dependent cellular cytotoxicity due to inhibition of its family member ITK, further limiting its use in combination regimens.[20] Despite the clinical success of ibrutinib, further refinement was required in terms of adverse effects, fueling the development of highly selective BTKi. Acalabrutinib and zanubrutinib are the most recently FDA-approved inhibitors and show clinical potential with improved selectivity and with fewer adverse effects relative to ibrutinib. Acalabrutinib was approved in 2017 for MCL and in 2019 for CLL. With higher selectivity than ibrutinib, acalabrutinib inhibits only BTK, TEC, BMX, and TXK.[19,21] Zanubrutinib was approved in 2019 to treat MCL in adults who previously received therapy.[19,22] Zanubrutinib is similar to acalabrutinib with less activity on TEC and ITK and also displays higher potency and selectivity for BTK than ibrutinib, with fewer "off-target" effects. In this study, we investigate the therapeutic potential of a small covalent molecule (JS25) with nanomolar potency against BTK (5.8 nM). JS25 was obtained from the scaffold of BMX-IN-1, a recently discovered molecule that has been shown to also inhibit BTK, as part of our efforts to identify regions of the molecule that could be modulated for improved efficacy and selectivity.[23,24] Initially, we had explored the JS25 potential for treating prostate cancer, but later experiments revealed that JS25 was highly selective for BTK, and therefore, it could have therapeutic importance in blood malignancies that derive from BTK's abnormal expression. Following the preliminary data, we sought to characterize the binding mode of JS25 to BTK and asserted its selectivity against a panel of eight kinases related to BTK's signaling pathway or with an equally placed cysteine as to the Cys481 of BTK. We further demonstrate that the lead compound has potential to inhibit the proliferation of several hematological cancers and to induce the degradation of BTK. Validation of its therapeutic effect was conducted in xenograft murine models of Burkitt's lymphoma, and in patient-derived models of diffuse large B-cell lymphoma and chronic lymphocytic leukemia. Finally, we explore the capability of JS25 to cross the brain−blood barrier and treat infiltration of tumor cells in the brain.

EXPERIMENTAL SECTION

Putative 3D Structure of JS25 Linked to BTK. *Docking Studies with AutoDock 4.2.* AutoDock 4.2[25] was used to predict the region where JS25 binds to BTK (PDB: 6TFP). Standard settings for *autogrid* (number of grid points in *xyz*: 126, 126, 126; spacing (Å) = 0.375) and *autodock* (genetic algorithm, max. number of evaluations = 250,000, output = Lamarckian GA(4.2)) were selected with AutoDockTools 1.5.6.

Molecular Dynamics (MD) Simulations. Simulations on JS25 or ibrutinib bound to BTK were performed with the AMBER 20 package (University of California) and implemented with the GAFF2 force field.[26] For the BTK/ibrutinib complex, the coordinates of the reported X-ray structure were used as starting coordinates (PDB: 5P9J). The setup for the molecular dynamics was performed as previously described,[27] with the production step set to 500 ns.

Selectivity Determination against BTK. In-cell target engagement was performed at Reaction Biology Corporation, using NanoBRET technology. Very briefly, HEK296T cells were transfected and treated in duplicate with JS25 for 1 h of incubation. The compound was diluted 10 times with 3-fold dilution, starting at 1 μM. Curve fits were performed only when the % NanoBret signal at the highest concentration of compounds was less than 55%. The IC_{50} values were determined using GraphPad Prism 8 (GSL Biotech LLC).

Inhibition Kinetics Characterization. The BTK enzyme system and the ADP-Glo kinase assay were purchased from Promega Corporation (V2941). Ibrutinib was acquired from BOC Sciences, and acalabrutinib from Advanced ChemBlock. In each kinase reaction, the concentration of BTK was set to 4 ng/μL. The peptide substrate Poly (4:1 Glu, Tyr) and ATP concentrations were set to 0.25 mg/mL and 50 μM, respectively. BTK was preincubated with different inhibitor concentrations (8-fold serial dilutions, starting at 100 nM) over different time periods (2−60 min), before initiating the kinase reactions. Reactions were started by adding a 2.5× Poly E4Y1/ATP mixture. The reactions were carried out in a 384-well plate and quenched simultaneously with the addition of 5 μL of the ADP-Glo reagent to consume the remaining ATP within 40 min. Then, 10 μL of the kinase detection reagent was added into the wells and incubated for 30 min to produce a luminescence signal. The signal was measured using an Infinite M200 Microplate Reader (Tecan) with an integration time of 0.250 s. The observed rate constants for inhibition (k_{obs}) at different inhibitor concentrations were determined from the slope of a semilogarithmic plot of inhibition *versus* time and replotted against inhibitor concentration (nM). The experimental values were fitted into a hyperbolic function using GraphPad Prism 8 to obtain K_I, k_{inact}, and k_{inact}/K_I, as described previously.[28]

Cell Culture. All cell lines were purchased from ATCC, except for DoHH-2 cells that were obtained from DSMZ. Cells were cultivated in complete DMEM supplemented with 10% (vol/vol) FBS (Gibco) and 1% of penicillin/streptomycin (Gibco). The cells were grown in a humidified atmosphere of 5% CO_2 at 37°C, with the medium changed every other day.

Cell Viability Assay. Cells were inoculated at a density of 5000 cells/well. Serially diluted compounds (starting at 50 μM) were added 24 h later. The assay was performed in triplicates. After 72 h of incubation, cellular viability was assessed by CellTiter-Glo (Promega) according to the manufacturer's instructions. The values were normalized with the vehicle (DMSO), and the IC_{50} was calculated using GraphPad Prism 8.

***In Vitro* Analysis of the Blood−Brain Barrier Permeability.** Human cerebral microvascular endothelial cells (HBEC-5i) were cultured as a monolayer on attachment factor protein solution (AF)-coated T-flasks (Gibco), using DMEM/F12 medium (Gibco), supplemented with 10% FBS, 1% penicillin/streptomycin, and 40.0 μg/mL endothelial cell growth supplement (ECGS, Sigma), according to the manufacturer's instructions. The capacity of the compounds to cross the brain−blood barrier (BBB) was evaluated using an *in vitro* HBEC-5i cell model, as previously described.[29] Samples from the apical and basolateral sides were collected, and

https://doi.org/10.1021/acsptsci.2c00163
ACS Pharmacol. Transl. Sci. XXXX, XXX, XXX−XXX

fluorescence intensity was measured using a Varioskan LUX multimode microplate reader. The retention was considered the difference between the initial fluorescence of compounds (100%) and the aggregated apical and basolateral fluorescence.

BTK Degradation in Raji Cells (Burkitt's Lymphoma). Raji cells were inoculated at 0.5×10^6 cells/mL, and JS25 was added at a final concentration of 10 μM. At 0, 4, and 15 h of incubation, the cells were harvested, and the pellets were resuspended in lysis buffer (20 mM Tris−HCl, 150 mM NaCl, pH 8.0, 0.1% Triton X-100), supplemented with EDTA-free Protease Inhibitor Cocktail (Merck) and DNase I (Merck). The protein concentration was determined using the Pierce BCA Protein Assay Kit (Thermo Scientific). Western blot was performed with rabbit BTK antibody (1:1000; 3533, Cell Signaling Technology), mouse α-Tubulin antibody (1:5000; 5168, Merck), goat anti-rabbit IgG (H + L) secondary antibody HRP (1:7000; 65-6120, Invitrogen), and goat anti-mouse IgG (H + L) secondary antibody HRP (1:5000; 2-6520, Invitrogen). The Signal was revealed with the Clarity Western ECL Substrate (Bio-Rad Laboratories), and band intensity was measured using ImageJ software (National Institutes of Health).

Mice Xenograft Model of Burkitt's Lymphoma. Female adult BALB/c/NSG mice were injected subcutaneously with 1×10^6 Raji cells, in a 1:1 solution of Matrigel Matrix (Corning) to create solid tumors. When tumors reached 180 mm^3 on average, mice were randomized into four groups (n = 6/group), and dosing began every 2 days. JS25 and ibrutinib were administered *via* i.p. injection, as a mixture of 20% of Kolliphor (Sigma-Aldrich) in PBS. Three treatment groups were included based on a similar study reported by Li et al.: one dose of ibrutinib (10 mg/kg), and two doses of JS25 (10 and 20 mg/kg). Tumor size and body weight were monitored periodically for 12 days. At the end of the experiment, mice necropsies were performed. Stereological analysis was conducted by the Histopathology Unit at Instituto Gulbenkian de Ciência and by the Comparative Pathology Unit at Instituto de Medicina Molecular João Lobo Antunes. Quantification of metastases and cell necrosis was performed in all groups (n = 5/group). Statistical analysis was conducted using one-way ANOVA. The Dunnet test was used to analyze the statistical significance between the treatment groups and the control.

***Ex Vivo* Model of Diffuse Large B-Cell Lymphoma.** *Primary Material Collection and Purification.* Primary lymph node samples were taken from patients, following hospital standard operating procedures. Clinical information including diagnosis was collected by the study center in a case report form. Target markers were confirmed by flow cytometry at the final laboratory prior to use.

Cell Plating, Assay, and Screening. Cells were plated at 10,000−20,000 cells per well in 384-well PerkinElmer Cell Carrier Ultra plates, containing prespotted small molecules in DMSO distributed by a Labcyte ECHO, in quadruplicate technical replicates in 4-point dose−response curves starting at 10 μM and decreasing by 1:3. DMSO volume in each well including controls were kept constant at 0.1% final volume of media. Plates were randomized and contained at least 15 DMSO vehicle control wells. Incubation took place for 72 h at 37 °C in air supplemented with 5% CO_2. At the end of the incubation period, the cells were stained with a viability dye (Invitrogen), fixed, and permeabilized using low-concentration formaldehyde and Triton X-114 in DPBS, and the resulting monolayers were stained with fluorescent antibodies against surface markers (CD19 (eBiosciences, clone HIB19), CD20 (BD, clone L27), and CD79a (BioLegend, clone HM47) along with DAPI (Sigma)). Fluorescent antibodies are used in different nonoverlapping fluorescent channels.

Imaging and Image Analysis. Imaging of the primary cell monolayer was performed using PerkinElmer CLS spinning disk automated confocal microscopes, with nonoverlapping, sequential, fluorescent channel imaging. All images were taken with a 20× objective. Five fields were imaged, representing at least 50% of the well bottom, for each well (seven TIFF images in total per field, one for each color channel plus brightfield, and 405 nm for DAPI, and merged). For analysis, the images were subject to image illumination correction. Cell identification in each image works by finding the cell nucleus (relying on DAPI staining) using classical thresholding approaches. Segmentation was performed using proprietary algorithms. Classification (cell antigen expression and viability) of every single cell was achieved using deep convolutional neural networks trained on B-cells and other cells from B-NHL samples stained with the specific markers utilized for these experiments, as well as on the fixable live/dead viability dye. The network considers variations in staining of the marker and viability marker intensity (cytoplasm and membrane localized) along with other stain-based characteristics. For this work, the networks had at least 95% classification accuracy. Information on the calculation of the drug response score (DRS), the relative cell fraction, and cell fraction can be found in Snijder et al. All raw Pharmacoscopy data were visualized in R (3.6.1).

Zebrafish Xenograft Model of Chronic Lymphocytic Leukemia. *Peripheral Blood Mononuclear Cell (PBMC) Isolation and Cryopreservation.* Whole blood (3−6 mL) from CLL patients (Supporting Table S1) was collected, and PBMCs were purified by Ficoll-Paque PLUS (GE Healthcare) density centrifugation.

PBMC Processing for Zebrafish Injection. The collected PBMCs were resuspended in RPMI (Biowest) with 3 times their volume and centrifuged at 1400 rpm, 4 °C, for 7 min. Cell pellets were resuspended in DPBS 1× (Biowest) supplemented with universal nuclease at 25 U/mL (Thermo Scientific). Concentration was normalized to 5×10^6 cells/μL for zebrafish patient-derived xenograft (zPDX) generation. Prior to drug efficacy analysis in zebrafish, the cells were distributed to proceed for flow cytometry, to determine the percentage of CD19+CD5+ cells within the CD45+ population, from PBMCs of each CLL patient. The maximum tolerated concentration was also determined for each compound in noninjected zebrafish larvae (Supporting Figure S1).

Zebrafish Patient-Derived Xenograft Injection and Drug Administration. Zebrafish larvae were anesthetized with Tricaine 1×, and thawed PBMCs were microinjected into the perivitelline space of anesthetized zebrafish larvae at 48 h post fertilization. After injection, zPDXs were sorted and randomly distributed into the different treatment groups in E2 medium/DMSO (control), JS25, ibrutinib, and venetoclax. zPDXs were maintained at 34 °C, and all drugs were renewed daily for 2 consecutive days. At the end of the assay, 4 days post injection, zebrafish xenografts were sacrificed with an overdose of Tricaine 25× and fixed in 4% formaldehyde (Thermo Scientific) overnight, followed by storage in 100% methanol (VWR) at −20 °C.

Whole Mount Immunofluorescence. The whole mount immunofluorescence protocol was started by rehydrating the xenografts through methanol series (75% > 50% > 25% in PBS

https://doi.org/10.1021/acsptsci.2c00163
ACS Pharmacol. Transl. Sci. XXXX, XXX, XXX−XXX

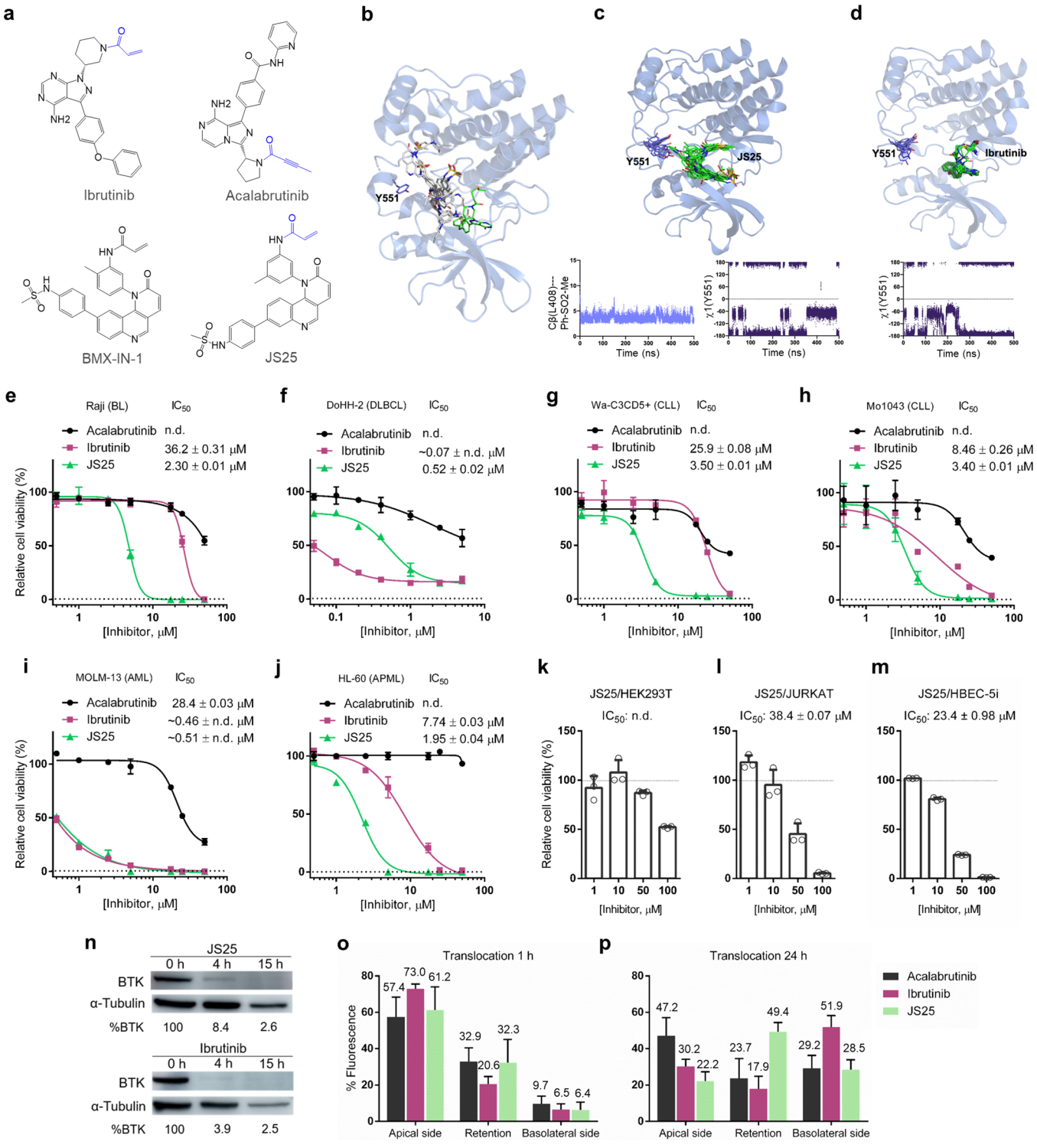

Figure 1. Putative structure of BTK covalently inhibited and cell viability assays. (a) Chemical structure of JS25 and other BTK inhibitors used. (b) The energetically best poses for BTK as determined by docking calculations. (c) Overlay of 10 frames of BTK/JS25 complex sampled from 0.5 μs MD simulations, together with the distance between the sidechain of Leu408 and the aromatic ring (Ph-SO_2Me) of JS25, and the geometry of the sidechain (χ^1 dihedral angle) of Tyr551 throughout MD simulations. (d) Overlay of 10 frames of BTK/Ibrutinib complex sampled from 0.5 μs MD simulations, together with the geometry of the sidechain (χ1 dihedral angle) of Tyr551 through MD simulations. BTK is shown as blue ribbons, and carbon atoms of the ligand and Tyr551 are shown in green and purple, respectively. (e) Cell viability of Raji, (f) DoHH-2, (g) WA-C3CD5+, (h) Mo1034, (i) MOLM-13, (j) HL-60, (k) HEK293T, (l) JURKAT, and (m) HBEC-5i. Cells were treated with serial doses of acalabrutinib, ibrutinib, and JS25 for 72 h. Error bars correspond to the standard deviation of the mean, n = 3 technical replicates. (n) Degradation analysis of BTK after treating Raji cells with JS25. (o) Translocation profile of different compounds (15 μM) at 1 h and (p) 24 h. Experiments were performed in triplicates on at least three different days using independently grown cell cultures. Error bars correspond to the standard deviation of the mean.

https://doi.org/10.1021/acsptsci.2c00163
ACS Pharmacol. Transl. Sci. XXXX, XXX, XXX−XXX

1×-Triton 0.1%). Next, the xenografts were permeabilized in PBS 1× with 0.1% (v/v) Triton and incubated in a blocking solution (containing 1% BSA and 1.5% goat serum) for 1 h at room temperature. The xenografts were incubated with the primary antibodies (anti-cleaved caspase 3—Cell Signaling Technology, clone Asp175, 9661, 1:100; anti-human mitochondria—Merck Millipore, clone 113-1, MAB1273, 1:50) diluted in the blocking solution overnight at 4 °C, followed by additional overnight incubation with 1:400 of secondary antibodies: Alexa goat anti-rabbit 594 (35560, Thermo Scientific) and Alexa goat anti-mouse 647 (84545, Thermo Scientific), and nuclei counterstaining with DAPI at 50 μg/mL (Sigma-Aldrich).

Imaging and Quantification. All images were obtained using a Zeiss LSM 980 Upright confocal laser scanning microscope. Xenografts were mounted in in-house Mowiol mounting media, and sequential images along tumor's depth (from cloaca until the end of the tail) with a 5 μm interval were acquired using the z-stack function. Upon image acquisition, analysis was performed using ImageJ software. For tumor burden, the area occupied by the PBMCs in each slice of the z-stack pile was determined by ImageJ software and summed up to obtain the tumor burden per xenograft. To express the outcome as fold induction, values obtained for controls and treatment conditions were normalized to the control. Tumor incidence was given by dividing the number of zebrafish xenografts that presented tumor cells between cloaca and the end of the tail, per the total number of zebrafish xenografts alive at the end of the assay (2 days post injection).

Statistical Analysis of Zebrafish Patient-Derived Xenograft Data. Statistical analysis was performed using GraphPad Prism 8. All data were challenged by two normality tests—the D'Agostino−Pearson and Shapiro−Wilk normality tests. A Gaussian distribution was only assumed for data sets that pass both normality tests and were analyzed by an unpaired *t*-test with Welch's correction. By opposition, data sets that did not pass one or both normality tests were analyzed by the Mann−Whitney test, an unpaired and nonparametric U test. Fisher's exact test was used for tumor incidence analysis.

RESULTS

JS25 Exhibits Higher Potency in Inhibiting BTK Compared to Ibrutinib, Acalabrutinib, and BMX-IN-1. Covalent modification of BTK is a two-step process that covers the affinity of the initial noncovalent binding, K_I, and the rate of covalent bond formation, k_{inact}.[30] The rate of inactivation (k_{inact}/K_I) is a second-order event, which describes the efficacy of the covalent bond binding event. To characterize the covalent interactions of JS25 with BTK, evaluation of the irreversible binding efficacy was performed as previously described.[23] Additionally, we included ibrutinib, acalabrutinib, and BMX-IN-1 (Figure 1a). The calculated kinetic parameters K_I, k_{inact}, and k_{inact}/K_I are shown in Table 1. The data demonstrated similar binding affinity between JS25, ibrutinib, and BMX-IN-1 for BTK, as indicated by their respective K_I values: 0.77, 0.59, and 1.29 nM. Out of the four compounds, acalabrutinib presented the weakest binding affinity for BTK (K_I = 15.07 nM). Most importantly, the rate of covalent bond formation, k_{inact}, of JS25 is 10-fold faster (0.401 min^{-1}) compared with ibrutinib (0.041 min^{-1}), acalabrutinib (0.038 min^{-1}), and BMX-IN-1 (0.038 min^{-1}); consequently, JS25 efficiently inactivated BTK with a k_{inact}/K_I of 8.72 μM^{-1} s^{-1}, displaying an increased rate of inactivation of approximately 8-fold relative to ibrutinib (1.17 μM^{-1} s^{-1}), 200-fold relative to acalabrutinib (0.04 μM^{-1} s^{-1}), and 18-fold relative to BMX-IN-1 (0.49 μM^{-1} s^{-1}). The differences in kinetic properties between the tested compounds highlight the variances in their specific binding modes and suggest an improved complementarity of JS25 with the target protein.

Table 1. Comparison of the Kinetic Parameters

compound	K_I [nM]	k_{inact} [min^{-1}]	k_{inact}/K_I [μM^{-1} s^{-1}]
JS25	0.77 ± 0.06	0.401 ± 0.064	8.72 ± 1.02
ibrutinib	0.59 ± 0.03	0.041 ± 0.004	1.17 ± 0.13[a]
acalabrutinib	15.07 ± 0.51	0.038 ± 0.005	0.04 ± 0.01[b]
BMX-IN-1	1.29 ± 0.50	0.038 ± 0.008	0.49 ± 0.15[c]

[a]Value with a 0.17 deviation from published results (Liclican et al., 2020).[48] [b]Value with a 0.002 deviation from published results (Liclican et al., 2020).[48] [c]Value with a 0.29 deviation from published results (Wang et al. 2017).[49]

Selectivity and Inhibition for BTK are Induced by Hijacking of Me477, Leu408, and Tyr551. The putative 3D structure of JS25 covalently bound to BTK was generated. AutoDock 4.2 software was used to predict the region where JS25 binds to BTK (noncovalent docking). The crystal structure of this protein, reported together with an inhibitor (PDB: 6TFP), was used for the docking studies. Interestingly, the best 10 docking poses in terms of binding affinity interact with BTK in the same region as other reported inhibitors[21] (Figure 1b). A detailed analysis of the different poses shows that pose #10 localizes the Michael acceptor moiety near Cys481. Therefore, we covalently bound JS25 with this 3D orientation to this cysteine residue of BTK and performed 0.5 μs MD simulations in explicit water (Figure 1c). The simulations show that the complex is stable due to the occurrence of hydrogen bonds and hydrophobic contacts between the ligand and the receptor. Hydrogen bonds are established between the oxygen atoms of the sulfonamide and the main chain of Me477 (which occupies about 30% of the total trajectory time). Equally, the aromatic ring containing the sulfonamide group is engaged in a CH/π interaction with the sidechain of Leu408, which is maintained throughout the simulation time (Figure 1c). We also analyzed the dynamics of Tyr551, as BTK inhibitors can be classified according to their ability to trigger the "sequestration" of this Tyr residue. In cells, sequestration of Tyr551 was shown to render it inaccessible for phosphorylation.[21] According to our calculations, Tyr551 is sequestrated around 60% of the whole trajectory (χ^1 torsional angle close to 180°). To validate our simulation protocol, we performed MD simulations for the complex of BTK with ibrutinib (Figure 1d), using the X-ray structure as the initial coordinates (PDB: 5P9J). As in the X-ray structure, the MD simulations show a hydrogen bond between the $-NH_2$ group of the ligand and the main chain of Glu475 (with a population of about 32%) and a hydrophobic contact between the phenyl group of ibrutinib and (population about 83%). As for the dynamics of Tyr551, our calculations showed that this residue is inaccessible about 72% of the time, which is consistent with the X-ray structure and experimental data.

JS25 Presents a More Favorable Selectivity Profile than Ibrutinib and Acalabrutinib. Compound selectivity is a crucial factor to take into consideration in drug discovery, as in many cases, a lack of selectivity can translate into increased toxicity in clinical trials.[31] It is also important to note that

https://doi.org/10.1021/acsptsci.2c00163
ACS Pharmacol. Transl. Sci. XXXX, XXX, XXX−XXX

selectivity toward specific TEC kinases and other pathway-related proteins is particularly difficult, as these share a high sequence and structural similarity, including a reactive cysteine in the catalytic pocket.[32] To determine whether JS25 is a selective binder, we evaluated its inhibitory capability against BTK, BMX, ITK, TXK, and TEC and against other BTK pathway-related proteins (BLK, EGFR, ERBB2, and JAK3). The selectivity of JS25 is shown in Table 2, and it is defined as IC_{50} kinase/IC_{50} BTK. JS25 showed an IC_{50} value of 28.5 nM against BTK, and the value for BMX was 49.0 nM, representing an ∼2-fold increase in the selectivity toward BTK. Within the TEC-family kinases, JS25 presented ∼7-fold, ∼8-fold, 15-fold, and 100-fold higher selectivity for BTK, relative to TXK, TEC, ITK, and BLK, respectively. Importantly, the values of IC_{50} for EGFR, ERBB2, and JAK3 were all higher than 3 μM. Overall, our data reveal that JS25 is very selective for both BMX and BTK, but with lower reactivity for other proteins within the TEC family, as well as for other proteins in BTK's signaling pathways, possibly mitigating the chances for "off-target" effects in the clinical stages.

Table 2. Kinome Selectivity of JS25

kinase	IC_{50} (M)[ab]	selectivity (kinase/BTK)
BTK	$2.85 \times 10^{-8} \pm 0.55$	1
BMX	$4.90 \times 10^{-8} \pm 0.40$	1.7
TXK	$1.90 \times 10^{-7} \pm 0.50$	6.7
TEC	$2.20 \times 10^{-7} \pm 0.30$	7.7
ITK	$4.40 \times 10^{-7} \pm 0.10$	15.4
BLK	2.60×10^{-6} ± n.d.	104
EGFR	$>3 \times 10^{-6}$	n.d.
ERBB2	$>3 \times 10^{-6}$	n.d.
JAK3	$>3 \times 10^{-6}$	n.d.

[a]Average of duplicates, showing mean ± S.D. [b]n.d.: not determined.

JS25 Has a Wide Spectrum of Activity in Blood Cancer Cell Lines. Having demonstrated JS25 as a potent inhibitor of BTK in biochemical assays, we turned to its characterization in standard cell lines of hematological cancers, related to an abnormal expression of BTK, including BL, DLBCL, CLL, AML, and acute promyelocytic leukemia (APML). Acalabrutinib and ibrutinib were also included to validate the therapeutic relevance of JS25 in these cell lines. The results presented in Figure 1e–m show that JS25 has a significant effect on viable cell growth in all of the tested cells, and it has the capability to inhibit the proliferation with similar

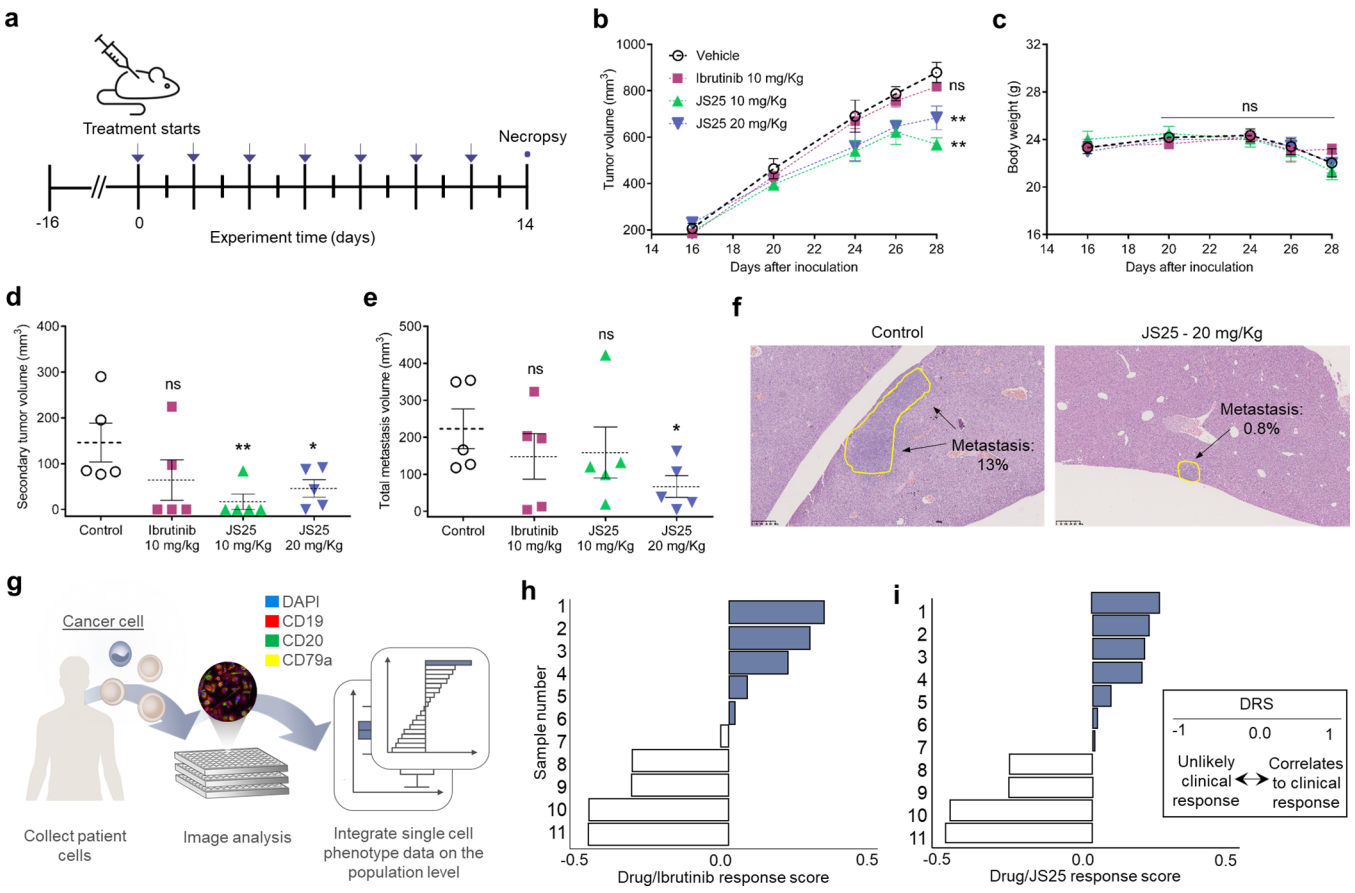

Figure 2. JS25 treatment inhibits the tumor growth of Burkitt's lymphoma and induces selective *ex vivo* cytotoxicity in primary DLBCL samples. (a) Schematic representation of the *in vivo* assay. Blue arrows indicate days of treatment. (b) Tumor size and (c) body weight were monitored periodically. (d, e) Quantification and analysis of the metastases and tumor formation observed (n = 5/group), ((b) $^{**}p$ = 0.0018 and 0.0090, (d) $^{**}p$ = 0.0086, $^{*}p$ = 0.0418, (e) $^{*}p$ = 0.0386). Statistical analysis was conducted by one-way ANOVA, followed by Dunnett's test for significance: not significant (ns) $p > 0.05$; $^{*}p < 0.05$ (*); $^{**}p < 0.01$. (f) Example of neoplastic cells observed in the liver of the control and JS25-treated groups. (g) Schematic representation of the *ex vivo* experiment. (h) JS25 and (i) ibrutinib/drug response score (DRS) calculated as 1-mean of the RCF. Each concentration point for each sample was performed in four replicates at 72 h incubation time point. Blue indicates DRS > 0, and white indicates DRS < 0. DRS scores > 0 indicate "on-target" cytotoxic response, and <0 indicates general cytotoxicity or "off-target" cytotoxic response.

https://doi.org/10.1021/acsptsci.2c00163
ACS Pharmacol. Transl. Sci. XXXX, XXX, XXX−XXX

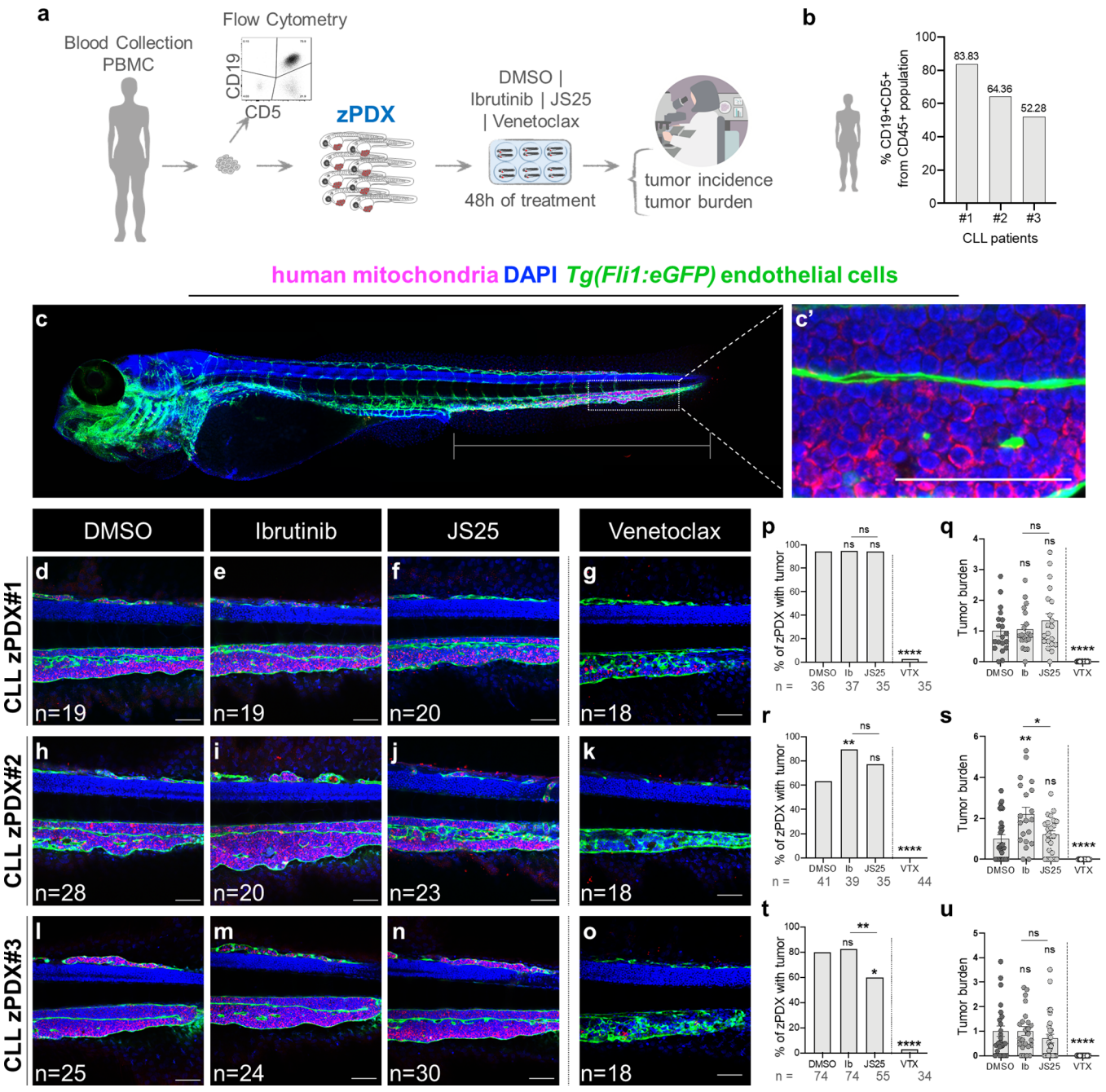

Figure 3. Comparison of the therapeutic effects of BTK inhibitors in zebrafish patient-derived xenografts of CLL disease. (a) Representative scheme of the zPDX assay. (b) Percentage of CD19+CD5+ cells within the CD45+ population from PBMCs of each CLL patient. (c–c′) Representative zPDX confocal image on where the therapeutic effects of the different compounds were analyzed (white rectangle). (d–o) Representative confocal images for each zPDX. Percentage of zPDXs with tumor ((p) ****p < 0.0001, (r) **p = 0.0080, ****p <0.0001, (t) *p = 0.0183, **p = 0.0054, ****p < 0.0001) and tumor burden ((q) ****p <0.0001, (s) *p = 0.0188, **p = 0.0045, ****p <0.0001, (u) ****p < 0.0001). The outcomes are expressed as AVG (b, p, r, t) and AVG ± SEM (fold induction-normalized values to controls) (q, s, u). Data are from one independent experiment, and the number of xenografts analyzed for tumor burden is indicated in the representative images. The number of total zPDXs analyzed at the end of the assay to generate the tumor incidence is indicated below the respective charts. Each dot represents one zebrafish xenograft. Statistical analysis was performed using Fisher's exact test (tumor incidence) and an unpaired test (tumor burden). Statistical results: ns > 0.05, *$p \leq 0.05$, **$p \leq 0.01$, ***$p \leq 0.001$, and ****$p \leq 0.0001$. Scale bar represents 50 μm.

or greater potency than the FDA-approved BTKi, acalabrutinib, and ibrutinib. JS25 presented 15-fold greater efficacy than Ibrutinib to inhibit the proliferation of Raji cells (BL), with an IC_{50} value of 2.3 μM (Figure 1e). In DoHH-2 (DLBCL), Mo1043 (CLL), and MOLM-13 (AML) cell lines, there were no major improvements (Figure 1f,h,i); however, in WA-C3CD5+ cells (CLL), the antiproliferative potency of JS25 (3.5 μM) was approximately 7-fold greater than Ibrutinib (25.9 μM; Figure 1g). In addition, JS25 also presented better efficacy than ibrutinib in HL-60 cells (APML) with an IC_{50} value of 1.95 μM (Figure 1j). Importantly, other non-B-cell lines (JURKAT, HEK293T, and HBEC-5i) were not as sensitive to the treatment (Figure 1k–m). Degradation of BTK was also investigated by treating wild-type Raji cells with a 10 μM

https://doi.org/10.1021/acsptsci.2c00163
ACS Pharmacol. Transl. Sci. XXXX, XXX, XXX−XXX

concentration of JS25 and ibrutinib. Western blot analysis showed that BTK degradation was evident at 4 h of treatment, and it was almost completed at 15 h (Figure 1n). These results validate JS25 as a potential therapeutic candidate with applicability against hematological cancers and demonstrate its ability to inhibit both the catalytic activity and the expression of BTK in tumor cells.

JS25 Effectively Crosses the Blood−Brain Barrier. In several types of blood cancers, infiltration of malignant white blood cells occurs in the central nervous system (CNSi) and is only detected in 3−5% of patients at initial diagnosis, and 30−40% of patients at relapse.[33] In relapsed and refractory MCL CNSi, monotherapy with BTKi has been proven to be effective, with an objective response rate of 68%. This efficacy is attributed to the ability of these drugs to cross the BBB and reach the tumor site.[34] The permeability of JS25 on the BBB was evaluated using an *in vitro* HBEC-5i cell model. Ibrutinib and acalabrutinib were included as controls. As shown in Figure 1o,p, JS25 and acalabrutinib showed similar permeability to the BBB at 24 h (28.5 and 29.2%, respectively). However, these were comparatively lower than the permeability of ibrutinib (51.9%), due to higher retention rates of JS25 and acalabrutinib in the cells. Depending on the intracellular mechanism involved, higher retention of the compound in the BBB could result in its degradation or in greater durability of the treatment. These results open a possibility for JS25 to become useful for the treatment of more aggressive forms of hematological cancers.

JS25 Has a Superior Therapeutic Effect Relative to Ibrutinib in a Xenograft Model of BL. To further validate its therapeutic potency, JS25 was examined in a mouse xenograft model inoculated subcutaneously with human lymphoma Raji cells (BL). This study comprised a vehicle control group and three treatment groups, including one dose of ibrutinib (10 mg/kg) and two doses of JS25 (10 and 20 mg/kg). The compounds were administered through intraperitoneal injection once every two days for 14 days, and tumor sizes were measured periodically (Figure 2a). As shown in Figure 2b, JS25 caused a significant reduction in the solid tumor sizes (around 30−40%), while ibrutinib−treated groups did not show significant changes relative to the control. Additionally, no weight fluctuations were observed by the end of the treatment (Figure 2c). Considering that drug dosing strongly influences the existing number of metastases, we sought to determine the overall percentage in each experimental group (Figure 2d−f and Supporting Table S2). Our quantitative analysis revealed that mice treated with JS25 had a significant reduction in their secondary tumor formation (71−88%; Figure 2d); however, only mice treated with the highest dose of JS25 (20 mg/kg) presented a significantly lower percentage of metastases (70% reduction; Figure 2e−f and Supporting Table S2). For both ibrutinib and JS25 (10 mg/kg doses), the reduction was similar and around 30% (Figure 2e). Infiltration of tumor cells was not observed in the heart and kidneys, and drug-induced necrosis of normal cells was also not observed. Our data show that JS25 has a potential therapeutic effect in this mouse xenograft model of BL, supported by the generalized reduction in the size of the primary tumors, and in the presence of secondary tumors and metastasis.

JS25 Demonstrates Selective "On-Target" Activity in the Primary Samples of DLBCL Patients. On the basis of its kinetic and cytotoxic efficiency, we tested the ability of JS25 to induce targeted cell cytotoxicity on viable DLBCL tumor tissues, by collecting lymph node samples from patients with the pathology (Figure 2g). Solid tissues were dissociated; cells were treated with JS25 and ibrutinib, then fixed, and permeabilized; and the resulting monolayers were stained with fluorescent antibodies against surface markers: CD19 (clone HIB19), CD20 (clone L27), and CD79a (clone HM47), along with DAPI. Imaging of the primary cell monolayer was carried out, and the viability and identity (cancer *versus* non-cancer) of individual cells were evaluated using deep learning-driven image analysis. The "on-target" cytotoxicity was identified by calculation of the DRS, which has been shown to correlate with the clinical response for late-stage hematological cancer patients. This score is measured by dividing the fraction of live cancer cells under treatment[35] by the fraction of live cancer cells of total cells under controls, averaging across multiple concentrations. As shown in Figure 2h and Supporting Figure S2a, JS25 had an "on-target" effect in 7 out of 11 patients (∼64%), and in 4 patients, the "killing" was off-target or nonspecific (∼36%). Ibrutinib presented "on-target" toxicity in 5 out of 10 patients (50%) (Figure 2i and Supporting Figure S2b). Overall, JS25 presented a greater pharmacologic effect at the target of interest than ibrutinib, supported by the number of samples that were more sensitive to the treatment with JS25.

JS25 is More Effective than Ibrutinib in Zebrafish Patient-Derived Xenografts of CLL. To evaluate the efficacy of JS25 in CLL patient samples, PBMCs were collected and used to generate zebrafish patient-derived xenografts. Here, we compared JS25's efficacy with ibrutinib's, and venetoclax was also included as a positive control. Venetoclax is a BH3-mimetic Bcl2 inhibitor that induces significant cell death,[36] and it is highly efficient for treating CLL; however, the rapid onset of apoptosis often leads to tumor lysis syndrome complications.[37] In contrast, ibrutinib has different dynamics and therefore is less prone to induce tumor lysis syndrome.[38]

CLL zPDXs with tumor cells in circulation were randomly distributed into four conditions immediately following injection: DMSO (control), ibrutinib (Ib), JS25, and venetoclax. After 48 h of treatment, all zPDXs were fixed and analyzed by confocal microscopy to evaluate tumor burden and incidence (Figure 3a). Tumor incidence is the percentage of zPDXs with tumors by the end of the assay, while tumor burden is the area occupied by PBMCs from the cloaca region until the end of the tail (Figure 3c−c′). In 2 out of the 3 CLL-zPDX, JS25 was more efficient than ibrutinib in reducing the CLL disease burden (Figure 3d−u). In CLL-zPDX#2 (del17p+), JS25 treatment led to a reduction of the tumor burden by ∼45% when compared to ibrutinib (Figure 3h−k,r,s), whereas in CLL-zPDX#3, JS25 reduces the incidence of zPDXs with tumors to 27% relative to ibrutinib and 25% in relation to DMSO controls (Figure 3l−o,t,u) and a tendency to reduce tumor burden (Figure 3l−o,t,u). In all of the zPDXs, venetoclax has a major impact on tumor incidence and burden, being able to induce massive cell death of all CLL cells within 48 h (Figure 3d−u), which is in accordance with the fast CLL cell killing effect observed in patients. Altogether, our results suggest that JS25 has a higher therapeutic impact in CLL, being faster and more effective than its counterpart ibrutinib.

https://doi.org/10.1021/acsptsci.2c00163
ACS Pharmacol. Transl. Sci. XXXX, XXX, XXX−XXX

DISCUSSION

Selective BTK inhibition is well viewed as a promising therapy for multiple hematological cancers and autoimmune diseases. Ibrutinib was the first-in-class BTKi, and although it is well tolerated with a durable response, its clinical use has been limited, prompting the development of second-generation BTKi. Here, we report a new inhibitor, JS25, a covalent small molecule with high potency and selectivity for BTK.

We first characterized the covalent modification of BTK by JS25 using kinetic analysis. An improvement in the covalent binding efficiency of JS25 to BTK was observed when compared to ibrutinib, acalabrutinib, and BMX-IN-1, with an increase of ∼8−200-fold in the rate of protein inactivation ($8.72 \pm 1.02\ \mu M^{-1}\ s^{-1}$). The mechanism of target-specific covalent inhibition is governed by an initial noncovalently binding event that places the reactive electrophile close to the specific nucleophile on the target protein.[30] The success of this initial fitting dictates the rate of covalent bond formation. Therefore, inhibitors' structural variations can affect covalent bond formation and consequent target inhibition, as observed in this study. Moreover, the combined effect of higher potency and a faster rate of covalent bond formation seen with JS25 directly translates into less compound required to achieve the same pharmacologic effect, thereby reducing the probability of side effects.[39]

Our MD simulation studies of BTK covalently linked to JS25 demonstrated that Tyr551 was sequestrated around 60% of the whole trajectory, possibly rendering BTK inaccessible for phosphorylation and causing its inactivation. Consistently, inactivation of BTK is usually achieved through blocking of Tyr551 phosphorylation within the Src homology type 1 (SH1) domain by Src kinases, consequently hindering autophosphorylation of Tyr223.[40] Many BTKi, both covalent and noncovalent, act directly within the SH1 domain, thereby interfering with cell survival and proliferation.

JS25 is also a dual inhibitor of BMX and BTK and presents lower reactivity for TEC, ITK, and TXK and nonreactivity toward EGFR, BLK, JAK3, and Her2. Additionally, we had previously shown that JS25 did not react with other Scr kinases.[23] On comparing the JS25 selectivity profile with other BTKi (Supporting Table S3), we find that JS25 is less reactive than ibrutinib for TEC, TXK, ITK, EGFR, JAK3, BLK, and Her2; less reactive for TEC and TXK than acalabrutinib; less reactive toward EGFR, JAK3, and Her2 than zanubrutinib; and less reactive toward TEC, TXK, and BLK than tirabrutinib, although slightly more reactive against ITK. The BTKi acalabrutinib, zanubrutinib, and tirabrutinib are second-generation inhibitors, and relative to ibrutinib, these molecules presented fewer "off-target" effects in early clinical trials. Dermatitis is a known adverse side effect attributed to ibrutinib's "off-targeting" of EGFR;[41] and bleeding is attributed to the "off-targeting" of the TEC protein, although a recent study suggested it may be caused by inhibition of Scr (*e.g.*, BLK).[42] In clinical studies, patients treated with BTKi that have no "off-target" effect for TEC kinase (*e.g.*, branebrutinib, evobrutinib, and fenebrutinib) reported less or no bleeding events.[43] For this reason, it is desirable that newly developed BTKi, such as JS25, have higher selectivity for BTK and lower reactivity toward this particular group of kinases, as shown in this study. The JS25 "off-target" profile suggests a more favorable therapeutic index in comparison to other BTKi. However, some clarification within the clinical context is required to understand whether the JS25 selectivity profile will translate into higher efficacy and safety, particularly in combinatorial regimens with other drugs.

In the cellular context, JS25 presented a wide spectrum of activity against several myeloid/lymphoid B-cell cancers dependent on BTK expression. In addition to inducing degradation of BTK, JS25 effectively crosses the BBB, but with higher retention rates than ibrutinib. However, this does not devaluate the therapeutic potential of JS25 in brain cancers, since higher retention rates can result in longer pharmacological effects, depending on the intracellular metabolism involved. Besides, clinical treatment with acalabrutinib (which showed a similar retention rate to JS25) did not affect the quality of the response to MCL-cell infiltration in the brain.[34]

As a proof of concept of the therapeutic potential, mice with BL were treated with JS25 and presented a reduction of 30−40% in the size of their solid tumors, and an overall reduction in metastasis and secondary tumor formation, relative to ibrutinib. The percentage of metastatic cells present in the liver, lungs, brain/meninges, and spinal cord/bone marrow was similar between treated groups (30% reduction), although lower with a higher JS25 dosage (70% reduction). Naturally, a variety of factors can impact JS25's distribution throughout the body and even decrease its availability in specific organs.[39] Thus, within these conditions, a higher drug dosage was more impactful in impairing tumor spread and growth in the mice. Nevertheless, in consistency with the *in vitro* experiments performed here, treatment-induced cell death was significantly more pronounced with JS25. Additionally, no weight fluctuations were observed by the end of the treatment, even at the highest dose (20 mg/kg), suggesting a safe and tolerable profile for JS25 in animal models, within the doses tested.

The drug response score of JS25, in a DLBCL patient model, was slightly higher than that of ibrutinib, proven by the overall increased cell death, leading to 64% "on-target" efficacy. Several genetic variations are on the basis of cellular resistance to ibrutinib in B-cell cancers such as DLBCL,[44] including the missense cysteine-to-serine mutation at position 481 in BTK, and the compensatory upregulation of the PI3K/AKT signaling pathway. Mutations that lead to acquired resistance to JS25 are still unknown and will be important when evaluating its effectiveness and safety in the clinical stages. Nonetheless, comprehensive drug-responsive profiles such as those generated here directly translate the clinical outcome of JS25 efficacy, thus being a useful route to understand its potential relevance in the clinic.

In the zebrafish patient model of CLL, in 2 out of 3 zPDXs, JS25 was more effective and/or faster than ibrutinib, reducing tumor incidence and tumor burden, thus suggesting a competitive potential of JS25 over ibrutinib as a promising anticancer therapy. CLL is a heterogeneous oncological disease of mature B-cells, in which BTKi are largely prescribed both as first-line and relapse therapy.[45] The responses to the current FDA- and EMA-approved therapies are diverse and commonly lead to a pathological partial response with incomplete management of the symptoms.[46,47] Therefore, there is an unmet need to develop more effective and faster BTKi that produce higher antitumoural responses.

CONCLUSIONS

Small-molecule covalent inhibitors combine prolonged inhibition with high selectivity to the target protein. We showed that

https://doi.org/10.1021/acsptsci.2c00163
ACS Pharmacol. Transl. Sci. XXXX, XXX, XXX−XXX

JS25 binds covalently to BTK at Cys481, and this binding is more efficient than other BTKi in the market. The measurement of selectivity IC_{50} values shows an improved selectivity pattern against EGFR and TEC kinases compared to ibrutinib and the second-generation inhibitors, acalabrutinib, tirabrutinib, and zanubrutinib. JS25 also presented a broad spectrum of activity in myeloid and lymphoid B-cell cancers and demonstrated improved therapeutic efficacy against ibrutinib in patient-derived DLBCL models, as well as in xenograft models of BL and CLL. JS25 also possesses the potential to treat metastatic forms of blood cancers in the brain, as proved by its ability to cross the blood−brain barrier. Taken together, our results establish JS25 as a therapeutically relevant BTKi, with demonstrated antiproliferative effects and improved selectivity profile, and we envisage its clinical use against hematological cancers and autoimmune diseases.

■ ASSOCIATED CONTENT

Supporting Information

The Supporting Information is available free of charge at https://pubs.acs.org/doi/10.1021/acsptsci.2c00163.

(1) Maximum tolerated concentration assay performed in zebrafish models; (2) JS25 and ibrutinib's cytotoxicity in primary DLBCL samples; (3) clinicopathological characterization of CLL patients; (4) stereological analysis of the mice treated with ibrutinib and JS25; (5) heat map with selectivity screening values of several BTK inhibitors (PDF)

■ AUTHOR INFORMATION

Corresponding Author

Gonçalo J. L. Bernardes − *Instituto de Medicina Molecular João Lobo Antunes, Faculdade de Medicina, Universidade de Lisboa, 1649-028 Lisbon, Portugal; Yusuf Hamied Department of Chemistry, University of Cambridge, Cambridge CB2 1EW, U.K.;* orcid.org/0000-0001-6594-8917; Email: gb453@cam.ac.uk

Authors

Bárbara B. Sousa − *Instituto de Medicina Molecular João Lobo Antunes, Faculdade de Medicina, Universidade de Lisboa, 1649-028 Lisbon, Portugal*

Cátia Rebelo de Almeida − *Champalimaud Foundation, 1400-038 Lisbon, Portugal*

Ana F. Barahona − *Champalimaud Foundation, 1400-038 Lisbon, Portugal*

Raquel Lopes − *Champalimaud Foundation, 1400-038 Lisbon, Portugal*

Ana Martins-Logrado − *Champalimaud Foundation, 1400-038 Lisbon, Portugal*

Marco Cavaco − *Instituto de Medicina Molecular João Lobo Antunes, Faculdade de Medicina, Universidade de Lisboa, 1649-028 Lisbon, Portugal;* orcid.org/0000-0002-0938-9038

Vera Neves − *Instituto de Medicina Molecular João Lobo Antunes, Faculdade de Medicina, Universidade de Lisboa, 1649-028 Lisbon, Portugal;* orcid.org/0000-0002-2989-7208

Luís A. R. Carvalho − *Yusuf Hamied Department of Chemistry, University of Cambridge, Cambridge CB2 1EW, U.K.*

Carlos Labão-Almeida − *Instituto de Medicina Molecular João Lobo Antunes, Faculdade de Medicina, Universidade de Lisboa, 1649-028 Lisbon, Portugal*

Ana R. Coelho − *Instituto de Medicina Molecular João Lobo Antunes, Faculdade de Medicina, Universidade de Lisboa, 1649-028 Lisbon, Portugal*

Marta Leal Bento − *Instituto de Medicina Molecular João Lobo Antunes, Faculdade de Medicina, Universidade de Lisboa, 1649-028 Lisbon, Portugal; Centro Hospitalar Lisboa Norte, Department of Hematology and Bone Marrow Transplantation, 1649-035 Lisbon, Portugal*

Ricardo M. R. M. Lopes − *Research Institute for Medicines (iMed.ULisboa), Faculdade de Farmácia, Universidade de Lisboa, 1600-277 Lisbon, Portugal*

Bruno L. Oliveira − *Instituto de Medicina Molecular João Lobo Antunes, Faculdade de Medicina, Universidade de Lisboa, 1649-028 Lisbon, Portugal*

Miguel A. R. B. Castanho − *Instituto de Medicina Molecular João Lobo Antunes, Faculdade de Medicina, Universidade de Lisboa, 1649-028 Lisbon, Portugal;* orcid.org/0000-0001-7891-7562

Peter Neumeister − *Division of Hematology, Medical University of Graz, 8036 Graz, Austria*

Alexander Deutsch − *Division of Hematology, Medical University of Graz, 8036 Graz, Austria*

Gregory I. Vladimer − *Exscientia, Oxford OX4 4GE, U.K.;* orcid.org/0000-0003-4205-7585

Nikolaus Krall − *Exscientia, Oxford OX4 4GE, U.K.*

Cristina João − *Champalimaud Foundation, 1400-038 Lisbon, Portugal*

Francisco Corzana − *Centro de Investigación en Síntesis Química, Departamento de Química, Universidad de La Rioja, 26006 Logroño, Spain;* orcid.org/0000-0001-5597-8127

João D. Seixas − *Instituto de Medicina Molecular João Lobo Antunes, Faculdade de Medicina, Universidade de Lisboa, 1649-028 Lisbon, Portugal; TARGTEX S.A., 2560-275 Torres Vedras, Portugal*

Rita Fior − *Champalimaud Foundation, 1400-038 Lisbon, Portugal*

Complete contact information is available at: https://pubs.acs.org/10.1021/acsptsci.2c00163

Author Contributions

The authors critically reviewed the manuscript and their contribution are as follows: B.B.S.: conceptualization, methodology, investigation, and writing−original draft; C.R.A.: investigation, formal analysis, and writing—review; A.F.B.: investigation and formal analysis; R.L.: investigation and formal analysis; A.L.: investigation and formal analysis; M.C.: investigation and formal analysis; V.N.: conceptualization and validation; L.A.R.C.: investigation and writing—review and editing; C.L.A.: methodology and investigation; A.R.C.: investigation; M.L.B.: conceptualization and formal analysis; R.M.R.M.L.: investigation; B.L.O.: investigation; M.A.R.B.C.: conceptualization and validation; P.N.: methodology and investigation; A.D.: methodology and investigation; G.I.V.: conceptualization and investigation; N.K.: conceptualization and investigation; C.J.: conceptualization, resources, and formal analysis; F.C.: conceptualization, investigation, and formal analysis; J.D.S.: conceptualization, funding acquisition, formal analysis, and writing—review and editing; R.F.:

https://doi.org/10.1021/acsptsci.2c00163
ACS Pharmacol. Transl. Sci. XXXX, XXX, XXX−XXX

conceptualization, formal analysis, and writing—review and editing; G.J.L.B.: conceptualization, resources, supervision, funding acquisition, writing—review and editing, and project administration.

Funding

Funded under FCT Portugal (Stimulus CEECIND/00453/2018 to G.J.L.B., Postdoctoral Fellowship SFRH/BPD/95253/2013 to J.D.S., project PTDC/MED-QUI/28764/2017 to J.D.S., 57/2016/CP1451/CT0025 to J.D.S., doctoral studentships SFRH/BD/143583/2019 to B.B.S., FCT2020.05466.BD to M.L.B., PD/BD/128281/2017 to M.C., FCT2021.08619.BD to C.R.A., FCT2020.4875.BD to R.L., and FCT2021.04906.BD to A.F.B). The authors also thank Champalimaud Foundation, Congento (LISBOA-01-0145-FEDER-022170, co-financed by FCT/Lisboa2020) and Agencia Estatal Investigación of Spain (AEI; Grant RTI2018-099592-B-C21 to F.C.) for funding. This project has received funding from the European Union's Horizon 2020 research and innovation programme under grant agreements Nos. 852985 and 702428.

Notes

The authors declare the following competing financial interest(s): J. D. S. and G. J. L. B. are inventors in a patent (WO2020245430A1) related to the findings reported in this manuscript.

J.D.S. and G.J.L.B. are inventors in a patent (WO2020245430A1) related to the findings reported in this manuscript. Other authors declare no competing interests.

All animal studies were conducted under the approval of Direção Geral da Alimentação e Veterinária (DGAV), following the European Animal Welfare Legislation (Directive 2010/63/EU). Human tissue collection for DLBCL patient models was conducted in accordance with the Declaration of Helsinki, and the protocol was approved by the Ethics Committee of the Medical University of Graz (Ethical application 30-528 ex 17/18). For human tissue collection in zebrafish xenograft model studies, informed consent was obtained from all of the participants, and the experiments were conducted according to the Ethics Committee at Champalimaud Foundation and following hospital standard operating procedures.

■ ACKNOWLEDGMENTS

The authors thank the team of Dr. Pedro Faísca from the Histopathology Unit of Instituto Gulbenkian de Ciência and the Comparative Pathology Unit from Instituto de Medicina Molecular João Lobo Antunes for their efforts in the histological analysis, Dr. Pedro Góis from Research Institute for Medicines, and Dr. Daniel Zaidman from the University of Cambridge for their constructive ideas.

■ ABBREVIATIONS

BTK, Bruton's tyrosine kinase; AML, acute myeloid leukemia; ALL, acute lymphocytic leukemia; CLL, chronic lymphocytic leukemia; WM, Waldenström's macroglobulinaemia; MCL, mantle cell lymphoma; BL, Burkitt's lymphoma; DLBCL, diffuse large B-cell lymphoma; BTKi, BTK inhibitors; MD, Molecular dynamics; HBEC-5i, human cerebral microvascular endothelial cells; DRS, drug response score; PBMCs, peripheral blood mononuclear cells isolation; zPDX, zebrafish patient-derived xenograft; K_I, initial noncovalent binding; k_{inact}, rate of covalent bond formation; k_{inact}/K_I, rate of inactivation; APML, acute promyelocytic leukemia; CNSi, central nervous system; Ib, ibrutinib

■ REFERENCES

(1) Pal Singh, S.; Dammeijer, F.; Hendriks, R. W. Role of Bruton's Tyrosine Kinase in B Cells and Malignancies. *Mol. Cancer* **2018**, *17*, No. 57.

(2) Xia, S.; Liu, X.; Cao, X.; Xu, S. T-Cell Expression of Bruton's Tyrosine Kinase Promotes Autoreactive T-Cell Activation and Exacerbates Aplastic Anemia. *Cell Mol. Immunol.* **2020**, *17*, 1042−1052.

(3) Smith, C. I.; Baskin, B.; Humire-Greiff, P.; Zhou, J. N.; Olsson, P. G.; Maniar, H. S.; Kjellén, P.; Lambris, J. D.; Christensson, B.; Hammarström, L. Expression of Bruton's Agammaglobulinemia Tyrosine Kinase Gene, BTK, Is Selectively down-Regulated in T Lymphocytes and Plasma Cells. *J. Immunol.* **1994**, *152*, 557−565.

(4) Satterthwaite, A. B. Bruton's Tyrosine Kinase, a Component of B Cell Signaling Pathways, Has Multiple Roles in the Pathogenesis of Lupus. *Front. Immunol.* **2018**, *8*, No. 1986.

(5) Li, Z.; Wahl, M. I.; Eguinoa, A.; Stephens, L. R.; Hawkins, P. T.; Witte, O. N. Phosphatidylinositol 3-Kinase-Gamma Activates Bruton's Tyrosine Kinase in Concert with Src Family Kinases. *Proc. Natl. Acad. Sci. U.S.A.* **1997**, *94*, 13820−13825.

(6) Saito, K.; Scharenberg, A. M.; Kinet, J.-P. Interaction between the Btk PH Domain and Phosphatidylinositol-3,4,5-Trisphosphate Directly Regulates Btk. *J. Biol. Chem.* **2001**, *276*, 16201−16206.

(7) Humphries, L. A.; Dangelmaier, C.; Sommer, K.; Kipp, K.; Kato, R. M.; Griffith, N.; Bakman, I.; Turk, C. W.; Daniel, J. L.; Rawlings, D. J. Tec Kinases Mediate Sustained Calcium Influx via Site-Specific Tyrosine Phosphorylation of the Phospholipase Cγ Src Homology 2-Src Homology 3 Linker. *J. Biol. Chem.* **2004**, *279*, 37651−37661.

(8) Halcomb, K. E.; Musuka, S.; Gutierrez, T.; Wright, H. L.; Satterthwaite, A. B. Btk Regulates Localization, in Vivo Activation, and Class Switching of Anti-DNA B Cells. *Mol. Immunol.* **2008**, *46*, 233−241.

(9) Kenny, E. F.; Quinn, S. R.; Doyle, S. L.; Vink, P. M.; van Eenennaam, H.; O'Neill, L. A. J. Bruton's Tyrosine Kinase Mediates the Synergistic Signalling between TLR9 and the B Cell Receptor by Regulating Calcium and Calmodulin. *PLoS One* **2013**, *8*, No. e74103.

(10) Spaargaren, M.; Beuling, E. A.; Rurup, M. L.; Meijer, H. P.; Klok, M. D.; Middendorp, S.; Hendriks, R. W.; Pals, S. T. The B Cell Antigen Receptor Controls Integrin Activity through Btk and PLCγ2. *J. Exp. Med.* **2003**, *198*, 1539−1550.

(11) Halcomb, K. E.; Contreras, C. M.; Hinman, R. M.; Coursey, T. G.; Wright, H. L.; Satterthwaite, A. B. Btk and Phospholipase Cγ2 Can Function Independently during B Cell Development. *Eur. J. Immunol.* **2007**, *37*, 1033−1042.

(12) de Gorter, D. J. J.; Beuling, E. A.; Kersseboom, R.; Middendorp, S.; van Gils, J. M.; Hendriks, R. W.; Pals, S. T.; Spaargaren, M. Bruton's Tyrosine Kinase and Phospholipase Cγ2 Mediate Chemokine-Controlled B Cell Migration and Homing. *Immunity* **2007**, *26*, 93−104.

(13) Torke, S.; Weber, M. S. Inhibition of Bruton's Tyrosine Kinase as a Novel Therapeutic Approach in Multiple Sclerosis. *Expert Opin. Investig. Drugs* **2020**, *29*, 1143−1150.

(14) Haselmayer, P.; Camps, M.; Liu-Bujalski, L.; Nguyen, N.; Morandi, F.; Head, J.; O'Mahony, A.; Zimmerli, S. C.; Bruns, L.; Bender, A. T.; Schroeder, P.; Grenningloh, R. Efficacy and Pharmacodynamic Modeling of the BTK Inhibitor Evobrutinib in Autoimmune Disease Models. *J. Immunol.* **2019**, *202*, 2888−2906.

(15) Pillinger, G.; Abdul-Aziz, A.; Zaitseva, L.; Lawes, M.; MacEwan, D. J.; Bowles, K. M.; Rushworth, S. A. Targeting BTK for the Treatment of FLT3-ITD Mutated Acute Myeloid Leukemia. *Sci. Rep.* **2015**, *5*, No. 12949.

(16) Kim, E.; Hurtz, C.; Koehrer, S.; Wang, Z.; Balasubramanian, S.; Chang, B. Y.; Müschen, M.; Davis, R. E.; Burger, J. A. Ibrutinib Inhibits Pre-BCR+ B-Cell Acute Lymphoblastic Leukemia Progression by Targeting BTK and BLK. *Blood* **2017**, *129*, 1155−1165.

https://doi.org/10.1021/acsptsci.2c00163
ACS Pharmacol. Transl. Sci. XXXX, XXX, XXX−XXX

(17) Honigberg, L. A.; Smith, A. M.; Sirisawad, M.; Verner, E.; Loury, D.; Chang, B.; Li, S.; Pan, Z.; Thamm, D. H.; Miller, R. A.; Buggy, J. J. The Bruton Tyrosine Kinase Inhibitor PCI-32765 Blocks B-Cell Activation and Is Efficacious in Models of Autoimmune Disease and B-Cell Malignancy. *Proc. Natl. Acad. Sci. U.S.A.* **2010**, *107*, 13075−13080.
(18) Pan, Z.; Scheerens, H.; Li, S. J.; Schultz, B. E.; Sprengeler, P. A.; Burrill, L. C.; Mendonca, R. V.; Sweeney, M. D.; Scott, K. C. K.; Grothaus, P. G.; Jeffery, D. A.; Spoerke, J. M.; Honigberg, L. A.; Young, P. R.; Dalrymple, S. A.; Palmer, J. T. Discovery of Selective Irreversible Inhibitors for Bruton's Tyrosine Kinase. *ChemMedChem* **2007**, *2*, 58−61.
(19) Estupiñán, H. Y.; Berglöf, A.; Zain, R.; Smith, C. I. E. Comparative Analysis of BTK Inhibitors and Mechanisms Underlying Adverse Effects. *Front. Cell Dev. Biol.* **2021**, *9*, No. 630942.
(20) Rajasekaran, N.; Sadaram, M.; Hebb, J.; Sagiv-Barfi, I.; Ambulkar, S.; Rajapaksa, A.; Chang, S.; Chester, C.; Waller, E.; Wang, L.; Lannutti, B.; Johnson, D.; Levy, R.; Kohrt, H. E. Three BTK-Specific Inhibitors, in Contrast to Ibrutinib, Do Not Antagonize Rituximab-Dependent NK-Cell Mediated Cytotoxicity. *Blood* **2014**, *124*, 3118.
(21) Barf, T.; Covey, T.; Izumi, R.; van de Kar, B.; Gulrajani, M.; van Lith, B.; van Hoek, M.; de Zwart, E.; Mittag, D.; Demont, D.; Verkaik, S.; Krantz, F.; Pearson, P. G.; Ulrich, R.; Kaptein, A. Acalabrutinib (ACP-196): A Covalent Bruton Tyrosine Kinase Inhibitor with a Differentiated Selectivity and In Vivo Potency Profile. *J. Pharmacol. Exp. Ther.* **2017**, *363*, 240−252.
(22) Flinsenberg, T. W. H.; Tromedjo, C. C.; Hu, N.; Liu, Y.; Guo, Y.; Thia, K. Y. T.; Noori, T.; Song, X.; Aw Yeang, H. X.; Tantalo, D. G.; Handunnetti, S.; Seymour, J. F.; Roberts, A. W.; Ritchie, D.; Koldej, R.; Neeson, P. J.; Wang, L.; Trapani, J. A.; Tam, C. S.; Voskoboinik, I. Differential Effects of BTK Inhibitors Ibrutinib and Zanubrutinib on NK-Cell Effector Function in Patients with Mantle Cell Lymphoma. *Haematologica* **2020**, *105*, e76−e79.
(23) Seixas, J. D.; Sousa, B. B.; Marques, M. C.; Guerreiro, A.; Traquete, R.; Rodrigues, T.; Albuquerque, I. S.; Sousa, M. F. Q.; Lemos, A. R.; Sousa, P. M. F.; Bandeiras, T. M.; Wu, D.; Doyle, S. K.; Robinson, C. V.; Koehler, A. N.; Corzana, F.; Matias, P. M.; Bernardes, G. J. L. Structural and Biophysical Insights into the Mode of Covalent Binding of Rationally Designed Potent BMX Inhibitors. *RSC Chem. Biol.* **2020**, *1*, 251−262.
(24) Liu, F.; Zhang, X.; Weisberg, E.; Chen, S.; Hur, W.; Wu, H.; Zhao, Z.; Wang, W.; Mao, M.; Cai, C.; Simon, N. I.; Sanda, T.; Wang, J.; Look, A. T.; Griffin, J. D.; Balk, S. P.; Liu, Q.; Gray, N. S. Discovery of a Selective Irreversible BMX Inhibitor for Prostate Cancer. *ACS Chem. Biol.* **2013**, *8*, 1423−1428.
(25) Morris, G. M.; Huey, R.; Lindstrom, W.; Sanner, M. F.; Belew, R. K.; Goodsell, D. S.; Olson, A. J. AutoDock4 and AutoDockTools4: Automated Docking with Selective Receptor Flexibility. *J. Comput. Chem.* **2009**, *30*, 2785−2791.
(26) Wang, J.; Wolf, R. M.; Caldwell, J. W.; Kollman, P. A.; Case, D. A. Development and Testing of a General Amber Force Field. *J. Comput. Chem.* **2004**, *25*, 1157−1174.
(27) Somovilla, V. J.; Bermejo, I. A.; Albuquerque, I. S.; Martínez-Sáez, N.; Castro-López, J.; García-Martín, F.; Compañón, I.; Hinou, H.; Nishimura, S.-I.; Jiménez-Barbero, J.; Asensio, J. L.; Avenoza, A.; Busto, J. H.; Hurtado-Guerrero, R.; Peregrina, J. M.; Bernardes, G. J. L.; Corzana, F. The Use of Fluoroproline in MUC1 Antigen Enables Efficient Detection of Antibodies in Patients with Prostate Cancer. *J. Am. Chem. Soc.* **2017**, *139*, 18255−18261.
(28) Krippendorff, B.-F.; Neuhaus, R.; Lienau, P.; Reichel, A.; Huisinga, W. Mechanism-Based Inhibition: Deriving K_I and k_{inact} Directly from Time-Dependent IC_{50} Values. *SLAS Discovery* **2009**, *14*, 913−923.
(29) Cavaco, M.; Pérez-Peinado, C.; Valle, J.; Silva, R. D. M.; Correia, J. D. G.; Andreu, D.; Castanho, M. A. R. B.; Neves, V. To What Extent Do Fluorophores Bias the Biological Activity of Peptides? A Practical Approach Using Membrane-Active Peptides as Models. *Front. Bioeng. Biotechnol.* **2020**, *8*, No. 552035.
(30) Strelow, J. M. A Perspective on the Kinetics of Covalent and Irreversible Inhibition. *SLAS Discovery* **2017**, *22*, 3−20.
(31) Bosc, N.; Meyer, C.; Bonnet, P. The Use of Novel Selectivity Metrics in Kinase Research. *BMC Bioinf.* **2017**, *18*, No. 17.
(32) Zhao, Z.; Liu, Q.; Bliven, S.; Xie, L.; Bourne, P. E. Determining Cysteines Available for Covalent Inhibition Across the Human Kinome. *J. Med. Chem.* **2017**, *60*, 2879−2889.
(33) Lenk, L.; Alsadeq, A.; Schewe, D. M. Involvement of the Central Nervous System in Acute Lymphoblastic Leukemia: Opinions on Molecular Mechanisms and Clinical Implications Based on Recent Data. *Cancer Metastasis Rev.* **2020**, *39*, 173−187.
(34) Rios, A.; Rekoff, G.; Dinh, B.; Chen, L.; Wahed, A.; Nguyen, N. MCL-247: Durable Response of a Patient with a Mantle Cell Lymphoma Central Nervous System (CNS) Relapse to Treatment with a Bruton Tyrosine Kinase Inhibitor (BTKi) Monotherapy. *Clin. Lymphoma Myeloma Leuk.* **2020**, *20*, S259−S260.
(35) Snijder, B.; Vladimer, G. I.; Krall, N.; Miura, K.; Schmolke, A.-S.; Kornauth, C.; Lopez de la Fuente, O.; Choi, H.-S.; van der Kouwe, E.; Gültekin, S.; Kazianka, L.; Bigenzahn, J. W.; Hoermann, G.; Prutsch, N.; Merkel, O.; Ringler, A.; Sabler, M.; Jeryczynski, G.; Mayerhoefer, M. E.; Simonitsch-Klupp, I.; Ocko, K.; Felberbauer, F.; Müllauer, L.; Prager, G. W.; Korkmaz, B.; Kenner, L.; Sperr, W. R.; Kralovics, R.; Gisslinger, H.; Valent, P.; Kubicek, S.; Jäger, U.; Staber, P. B.; Superti-Furga, G. Image-Based Ex-Vivo Drug Screening for Patients with Aggressive Haematological Malignancies: Interim Results from a Single-Arm, Open-Label, Pilot Study. *Lancet. Haematol.* **2017**, *4*, e595−e606.
(36) Leverson, J. D.; Sampath, D.; Souers, A. J.; Rosenberg, S. H.; Fairbrother, W. J.; Amiot, M.; Konopleva, M.; Letai, A. Found in Translation: How Preclinical Research Is Guiding the Clinical Development of the BCL2-Selective Inhibitor Venetoclax. *Cancer Discovery* **2017**, *7*, 1376−1393.
(37) Roberts, A. W.; Huang, D. Targeting BCL2 With BH3 Mimetics: Basic Science and Clinical Application of Venetoclax in Chronic Lymphocytic Leukemia and Related B Cell Malignancies. *Clin. Pharmacol. Ther.* **2017**, *101*, 89−98.
(38) Byrd, J. C.; Furman, R. R.; Coutre, S. E.; Flinn, I. W.; Burger, J. A.; Blum, K. A.; Grant, B.; Sharman, J. P.; Coleman, M.; Wierda, W. G.; Jones, J. A.; Zhao, W.; Heerema, N. A.; Johnson, A. J.; Sukbuntherng, J.; Chang, B. Y.; Clow, F.; Hedrick, E.; Buggy, J. J.; James, D. F.; O'Brien, S. Targeting BTK with Ibrutinib in Relapsed Chronic Lymphocytic Leukemia. *N. Engl. J. Med.* **2013**, *369*, 32−42.
(39) Gleeson, M. P.; Hersey, A.; Montanari, D.; Overington, J. Probing the Links between in Vitro Potency, ADMET and Physicochemical Parameters. *Nat. Rev. Drug Discovery* **2011**, *10*, 197−208.
(40) Estupiñán, H. Y.; Wang, Q.; Berglöf, A.; Schaafsma, G. C. P.; Shi, Y.; Zhou, L.; Mohammad, D. K.; Yu, L.; Vihinen, M.; Zain, R.; Smith, C. I. E. BTK Gatekeeper Residue Variation Combined with Cysteine 481 Substitution Causes Super-Resistance to Irreversible Inhibitors Acalabrutinib, Ibrutinib and Zanubrutinib. *Leukemia* **2021**, *35*, 1317−1329.
(41) Lynch, T. J.; Kim, E. S.; Eaby, B.; Garey, J.; West, D. P.; Lacouture, M. E. Epidermal Growth Factor Receptor Inhibitor−Associated Cutaneous Toxicities: An Evolving Paradigm in Clinical Management. *Oncologist* **2007**, *12*, 610−621.
(42) Wen, T.; Wang, J.; Shi, Y.; Qian, H.; Liu, P. Inhibitors Targeting Bruton's Tyrosine Kinase in Cancers: Drug Development Advances. *Leukemia* **2021**, *35*, 312−332.
(43) von Hundelshausen, P.; Siess, W. Bleeding by Bruton Tyrosine Kinase-Inhibitors: Dependency on Drug Type and Disease. *Cancers* **2021**, *13*, 1103.
(44) He, M. Y.; Kridel, R. Treatment Resistance in Diffuse Large B-Cell Lymphoma. *Leukemia* **2021**, *35*, 2151−2165.
(45) Eichhorst, B.; Robak, T.; Montserrat, E.; Ghia, P.; Niemann, C. U.; Kater, A. P.; Gregor, M.; Cymbalista, F.; Buske, C.; Hillmen, P.; Hallek, M.; Mey, U. Chronic Lymphocytic Leukaemia: ESMO Clinical Practice Guidelines for Diagnosis, Treatment and Follow-Up. *Ann. Oncol.* **2021**, *32*, 23−33.

https://doi.org/10.1021/acsptsci.2c00163
ACS Pharmacol. Transl. Sci. XXXX, XXX, XXX−XXX

(46) Xu, W.; Yang, S.; Zhou, K.; Pan, L.; Li, Z.; Zhou, J.; Gao, S.; Zhou, D.; Hu, J.; Feng, R.; Huang, H.; Ji, M.; Guo, H.; Huang, J.; Novotny, W.; Feng, S.; Li, J. Treatment of Relapsed/Refractory Chronic Lymphocytic Leukemia/Small Lymphocytic Lymphoma with the BTK Inhibitor Zanubrutinib: Phase 2, Single-Arm, Multicenter Study. *J. Hematol. Oncol.* **2020**, *13*, No. 48.

(47) Burger, J. A.; Tedeschi, A.; Barr, P. M.; Robak, T.; Owen, C.; Ghia, P.; Bairey, O.; Hillmen, P.; Bartlett, N. L.; Li, J.; Simpson, D.; Grosicki, S.; Devereux, S.; McCarthy, H.; Coutre, S.; Quach, H.; Gaidano, G.; Maslyak, Z.; Stevens, D. A.; Janssens, A.; Offner, F.; Mayer, J.; O'Dwyer, M.; Hellmann, A.; Schuh, A.; Siddiqi, T.; Polliack, A.; Tam, C. S.; Suri, D.; Cheng, M.; Clow, F.; Styles, L.; James, D. F.; Kipps, T. J. Ibrutinib as Initial Therapy for Patients with Chronic Lymphocytic Leukemia. *N. Engl. J. Med.* **2015**, *373*, 2425−2437.

(48) Liclican, A.; Serafini, L.; Xing, W.; Czerwieniec, G.; et al. Biochemical Characterization of Tirabrutinib and Other Irreversible Inhibitors of Bruton's Tyrosine Kinase Reveals Differences in on - and off - Target Inhibition. *Biochimica et Biophysica Acta (BBA) - General Subjects* **2020**, *1864* (4), 129531.

(49) Wang, B.; Deng, Y.; Chen, Y.; Yu, K.; et al. Structure-Activity Relationship Investigation for Benzonaphthyridinone Derivatives as Novel Potent Bruton's Tyrosine Kinase (BTK) Irreversible Inhibitors. *Eur. J. Med. Chem.* **2017**, *137*, 545−557.

https://doi.org/10.1021/acsptsci.2c00163
ACS Pharmacol. Transl. Sci. XXXX, XXX, XXX−XXX